Center for Ophthalmology
Institute for Ophthalmic Research

Refined electrophysiological recording and processing of neural signals from the retina and ascending visual pathways

Inaugural-Dissertation
zur Erlangung des Doktorgrades
der Humanwissenschaften

der Medizinischen Fakultät
der Eberhard Karls Universität
zu Tübingen

vorgelegt von
Torsten Jakob Straßer

aus
Neuburg an der Donau

2016

Dekan	Professor Dr. med. Ingo B. Autenrieth
1. Berichterstatter	Professor Dr. med. Dr. hc. mult. Eberhart Zrenner
2. Berichterstatter	Professor Dr. Herbert Klaeren
Tag der Disputation	30.06.2016

For my family

It seems that perfection is attained,
not when there is nothing more to add,
but when there is nothing more to remove.

– Antoine de Saint-Exupéry

Table of Contents

List of abbreviations

aECG	HL7 annotated electrocardiogram. An XML-based medical record data format for ECG data
Ag/AgCl	Silver-sliver chlorid. Used in electrophysiology for electrodes
AIS	Arzt Information System. Tuebingen Physicians Information System
API	Application programming interface. Defines functionalities, inputs, and outputs of a software component
AR	Auto-regression
ASCII	American Standard Code for Information Interchange. Character encoding scheme
BCVA	Best-corrected visual acuity. Visual acuity after subjective refraction
BLOB	Binary large object. Collection of binary data stored as a single entity, usually in database management systems
BOLD	Blood oxygenation level dependent. Indirect measure the neuronal activity using the difference of the oxygenated relative to the deoxygenated hemoglobin
BSAF	Better swing application framework. A Java software framework for the development of Swing-based desktop applications
cAMP	Cyclic adenosine monophosphate. Second messenger in many biological processes, used for intracellular signal transduction
CCD	Charge-coupled device. Electronic device for the conversion of photons into electron charges
CDISC	Clinical Data Interchange Consortium
CSV	Comma (character) separated values. Data format for tabular data in plain text proposed in RFC 4180
CT	Computed tomography. Imaging technology using computer-processed combinations of X-ray images

Cz	Central zero, electrode position according to the International 10/20 system
DFC (or DPF)	Differential path length factor. Factor for compensating the difference between length of the light path and source-detector separation in near-infrared spectroscopy
DFT	Discrete Fourier transformation. Mathematical method to convert a finite list of equally spaced samples into coefficients of a finite combination of complex sinusoids. Used to transform data from the time domain into the frequency domain
DICOM	Digital Imaging and Communications in Medicine. A standard for handling, storing, printing, and transmitting information in medical imaging
dpt	Diopter. A unit of measurement of the optical power. Reciprocal to the focal length measured in meters (m^{-1})
DSL	Domain-specific language. Programming language specialized to a particular application domain
DTD	Document type definition. Defines the document structure of an XML document with a list of legal elements and attributes
DTL	Dawson-Trick-Litzkow electrode. Silver coated fiber electroded used for electroretinography
ECG	Electrocardiography or electrocardiogram. Recording of the electrical activity of the heart
ecgML	Electrocardiogram markup language. XML-based data format for electrocardiogram data acquisition and analysis
EDF	European Data Format. A standard file format designed for medical time series data
EEG	Electroencephalogram. Recording of the electrical activity of the brain
ElVisML	Electrophysiology of Vision Markup Language. Proposed XML-based standard format for visual electrophysiological data
EOG	Electrooculography or electrooculogram. Technique for measuring the corneo-retinal standing potential between the front and the back of the eye

EPI	Echo planar imaging. Imaging scheme used in functional magnetic resonance imaging for rapid brain scanning. Each RF excitation is followed by a train of gradient echos with diff-fferent spatial encoding
EPT	Electrically evoked phosphene thresholds. Threshold of the electrical current needed to induce visual impressions
ERG	Electroretinography or electroretinogram. Recording of the electrical potentials of the retina in response to light stimuli
ETDRS	Early Treatment of Diabetic Retinopathy Study. Commonly refers to eye charts developed as part of the study for determination of the visual acuity
FDA	Food and Drug Administration. Federal agency of the United States responsible for protection and promotion of public health
FFX	Fixed effects. Statistical model representing observed quantities in terms of explanatory variables treated as if they were non-random
fMRI	Functional magnetic resonance imaging. Neuroimaging technique measuring changes in blood flow
fNIRS	Functional near-infrared spectroscopy. Neuroimaging technique measuring changes in blood oxygenation
FO	Fast oscillations. Fast light induced changes of the electrooculogram
FOV	Field-of-view. The size of the two or three dimensional spatial encoding area of an MRI image
FrACT	Freiburg Visual Acuity and Contrast Test. Automated vision test implemented as a multi-platform computer program
FWHM	Full width half maximum. Expression of a function given by the difference between two extreme values of the independent variable at which the dependent variable is equal to half of its maxium
Fz	Frontal zero, electrode position according to the International 10/20 system

GC	Ganglion cell, here retinal ganglion cell. Type of neuron located near the inner surface of the retina.
GDF	General Data Format.
GoF	Gang of Four. Erich Gamma, Richard Helm, Ralph Johnson, and John Vlissides, authors of the highly influential book on software engineering "Design Patterns: Elements of Resusable Object-Oriented Software"
HHb	Deoxyhemoglobin
HL7	Health Level 7. Set of international standards for transfer of clinical and administrative data between software applicatons
HPPD	Hallucinogen persisting perception disorder. Disorder characterized by a continual presence of sensory disturbances caused by the use of hallucinogenic substances
HTML	Hypertext Markup Language. Standard markup language used to create web pages
iDSL4SigProc	Integrated domain specific langauge for signal processing. Java API for processing visual electrophysiological signals
IEEE	Institute of Electrical and Electronics Engineers. A professional association
INL	Inner nuclear layer. Layer of the retina containing bipolar, horizontal and amacrine cells
IOD	Information object definition. An object-oriented data model used to specify information about real-world objects. Part of the DICOM specification
IPL	Inner plexiform layer. Layer of the retina
IS	Inner segment. Part of a photoreceptor
ISCEV	International Society for Clinical Electrophysiology of Vision. Professional association
JDBC	Java Database Connectivity. API for manufacturer independent database access in Java
JVM	Java Virtual Machine. Execution environment Java programs
LCD	Liquid-crystal display. Display technology using light modulating properties of liquid crystals

LED	Light-emitting diode. Semiconductor light source (p-n junction diode)
LGN	Lateral geniculate nucleus. Relay center in the thalamus for the visual pathway, receiving information directly from retinal ganglion cells
LSD	Lysergic acid diethylamide. A psychedelic drug
MBLL	Modified Beer-Lambert Law. Relates the attenuation of light to the material properties it travels through. Modified for use in near-infrared spectroscopy
mfERG	Multifocal ERG. Technique for recording local ERG responses simultaneously from many regions of the retina
MITA	Medical Imaging & Technology Alliance. Lobby for manufacturers of medical imaging equipment
MNI	Montreal Neurological Institute and Hospital. Here: a 3-dimensional coordinate system (atlas) of the human brain
MRI	Magnetic resonance imaging. Medical imaging technique using magnetic fields and radio waves
NEMA	National Electrical Manufacturers Association. U. S. industry group representing designers and manufacturers of electrical equipment
NIR	Near-infrared. Sub-band of the infrared radiation (wavelength: 0.75 – 1.4 µm)
O_2Hb	Oxygenated hemoglobin
OCT	Optical coherence tomography. Medical imaging technique using light to produce 3-dimensional images from within optical scattering media based on interferometry
OD	Oculus dexter. Right eye
ODT	File format used be OpenOffice, StarOffice, and LibreOffice
ONL	Outer nuclear layer. Layer of the retina
OP	Oscillatory potentials. High frequency, low-amplitude wavelets on the ascending limb of the b-wave
OPL	Outer plexiform layer. Layer of neural synapses in the retina
OS	Outer segments. Part of a photoreceptor

OS	Oculus sinister. Left eye
OU	Oculus uterque. Both eyes
Oz	Occipital zero, electrode position according to the International 10/20 system
PACS	Picture and Archiving and Communication System. A system used in medical imaging to store, retrieve, distribute, analyze, and digitally process medical images
PDF	Portable Document Format. File format to store documents independent of application, hardware, and operating system
RANSAC	RANdom SAmple and Consensus. Iterative method to estimate parameters of a mathematical model
RAPD	Relative afferent pupillary defect. Also called Marcus Gunn pupil. Medical sign of lesions of the optic nerve observed during the swinging-flashlight test.
ReML	Restricted maximum likelihood. Particular form of the maximum likelihood estimation
RMS	Root mean square. Also known as quadratic mean. Calculated as the square root of the arithmetic mean of the square of the samples
ROI	Region of Interest. Selected subset of samples within a dataset identified for a particular purpose
RPE	Retinal pigment epithelium. Layer of the retina responsible for light absorption, epithelial transport, spatial ion buffering, visual cycle, phagocytosis, secretion, and immune modulation
RTF	Rich Text Format. Proprietary document file format
SCP	Service Class Provider. Part of the DICOM specification. Provider of a specific functionality
SCU	Service Class User. Part of the DICOM specification. Consumer of a specific functionality
SD	Standard deviation. Measure to quantify the amount of variation or dispersion of a set of data values
SGML	Standardized Generalized Markup Language. Meta-language for defining generalized markup languages

SNR	Signal-to-noise ratio. Measure comparing the level of the desired signal to the level of background noise
SO	Slow oscillations. Slow light induced changes of the electrooculogram
SOP	Service Object Pair Classes. Part of the DICOM specification. Combination of service class provider and service class user
SQL	Structured query language. Special-purpose programming language for managing data in relational database management systems
Sra	Scleral radius. Measure for the radii of the sclera
TE	Echo time. Used in MRI. The time between the application of radiofrequency excitation pulse and the peak of the signal induced in the coil
THC	Tetrahydrocannabinol. Psychoactive constituent (cannabinoid) of cannabis
TR	Repetition time. Used in MRI. Time from the application of an excitation pulse to the application of the next pulse
UCUM	Unified Code for Units of Measure. A code system intended to facilitate unambiguous electronic communication of quantities together with heir units
UML	Unified Modeling Language. General-purpose visual modeling language in software development
VA	Visual acuity. Measure of the spatial resolution of the visual processing system
VECP	Visual evoked cortical potentials. See VEP
VEP	Visual evoked potentials. Potential changes in the occipital EEG induced by visual stimulation
VR	Value representation. Part of the DICOM specification. Data type and format of values of a date element
W3C	World Wide Web Consortium. International standards organization for the World Wide Web
XDF	Extensible Data Format. XML-based general-purpose file format for multi-channel time series data

XHTML	Extensible Hypertext Markup Language. Extension of the Hypertext Markup Language
XLS	Excel binary file format. File format used by Microsoft Excel
XML	eXtensible Markup Language. Structured textual data format, which is both human- and machine-readable.
XPath	XML Path Language. Query language for selecting nodes from an XML document
XQuery	XML Query Language. Query and functional programming language for querying and transforming collections of XML documents
XSD	XML Schema definition. XML-based meta-language for the definition of XML-based languages

I INTRODUCTION

The human vision is a fantastic piece of evolution, starting with the transformation of photons into electrical potentials at the level of photoreceptors and the first image processing in the inner retina, continuing with the transmission of the information along the optic nerve to the visual cortex, where the further image processing and recognition is carried out.

Visual electrophysiology investigates the whole path of the information flow between the retina and the visual cortex. It is not only a valuable tool in the diagnosis of ophthalmological diseases, but also helps to explain how our brain works and why we see the world as we see it.

This thesis presents refined electrophysiological methods for recording and processing of neural signals from the retina and the ascending visual pathways. These methods include new stimulus paradigms, novel electrodes for the recording of electrophysiological signals, software for analyzing visual electrophysiological recordings, and multi-modal approaches, which combine visual electrophysiology and neuroimaging techniques.

The thesis presents approaches on how to deal with the huge amounts of data collected during studies, clinical trials, and the clinical routine, and presents approaches for an open and independent, future-proof way to store these data.

Each chapter of this thesis stands on its own, including an introduction, a description of the methods and results, and a discussion. However, the central theme of the thesis is the software ERG Explorer, which was developed for analyzing, visualization, and reporting of visual electrophysiological data. This software was used for all studies presented in the last chapter of the thesis.

II VISUAL ELECTROPHYSIOLOGY

1 From light to perception

Vision is probably the most important of our senses. It allows us to perceive our environment and to assimilate information from our surroundings.

The eye and the visual system is an extraordinary piece of evolution, which technology is not able to model in its effectiveness or complexity, even though there are similarities to modern digital cameras: The iris and the lens work like the aperture and objective, respectively, of a camera; the retina is comparable to charge-coupled devices (CCD), responsible for converting light into electrical signals.

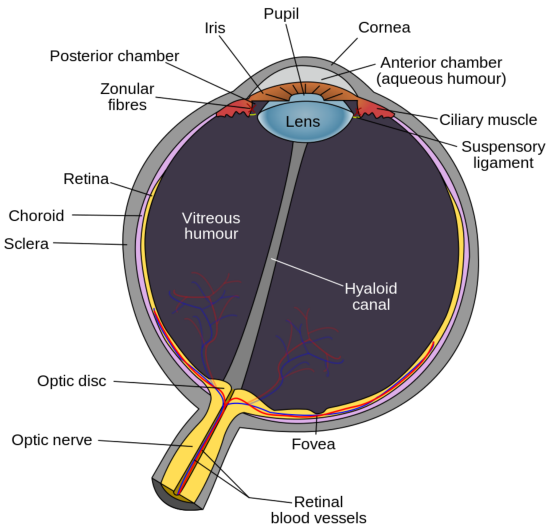

Figure 1: Schematic diagram of the human eye. Light is focused by the cornea. The iris of the eye controls the amount of light reaching the back of the eye by adjusting the size of the pupil. The eye's lens further focuses light. Through accommodation, this lens automatically focus on near objects. Light then reaches the retina, at the back of the eye, which converts optical images into electronic signals. The optic nerve then transmits these signals to the visual cortex. (Source: Wikimedia Commons, *Schematic diagram of the human eye*, 2007)

However, the retina is far more advanced than any available electronic device. Phototransduction, the conversion of light into electrical signals, is achieved by light sensitive proteins, controlling the opening or closing of ion channels in a photoreceptor, which is roughly analogous to a pixel of a CCD chip in its function of transforming light into electrical potentials.

The human retina contains about 126 million photoreceptors, far in excess of the number of pixels of a camera, which is about 20 megapixels, nowadays. The dynamic range of the retina covers about ten logarithmic units, whereby one single photoreceptors is able to detect a single photon of light.

The retina does not just simply transform light into electrical signals, but as neural tissue, the retina performs the first stages in image processing, compressing and digitizing the results of 126 million photoreceptors to send as digital spike trains along the 1.2 million fibers of the optic nerve to the brain.

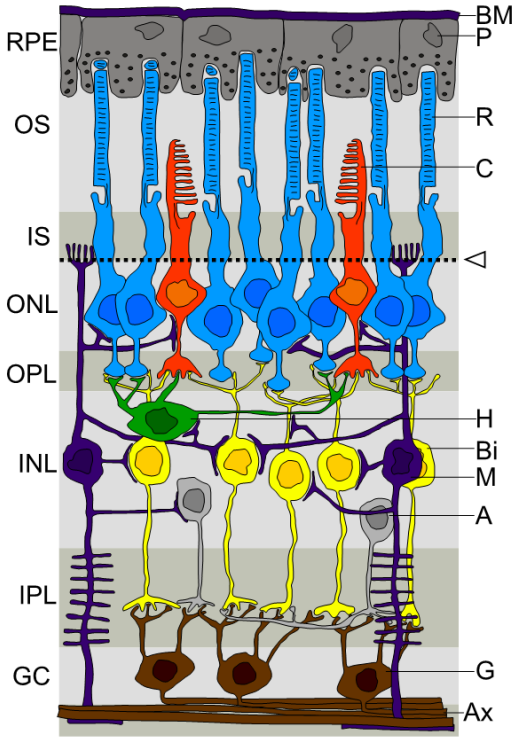

Figure 2: Layers and cells of the retina. The retinal pigment epithelium provides nutrition for the photoreceptors and recycles the outer segments of the photoreceptors. The inner segments connect to cells of the inner nuclear layer, where horizontal, bipolar, and amacrine cells perform a first image processing. Ganglion cell digitize the preprocessed information and send it along their axons to the optic nerve. (Source: Peter Hartmann, Wikimedia Commons, *Retina layers*, 2013)

A 250 micron thin, transparent tissue, the retina, in these terms works like a powerful micro-processor. It is structured in several layers (Figure 2), beginning with the retinal pigment epithelium (RPE), responsible for nutrition, the outer retina with the light sensitive photoreceptors (outer segments (OS), inner seg-

ments (IS)), and the inner retina where signals from receptors are compared before being sent to the higher visual centers (outer nuclear layer (ONL), outer plexiform layer (OPL), inner nuclear layer (INL), inner plexiform layer (IPL), ganglion cells (GC)). Figure 3 shows on the right an OCT image of the authors retina. The different layers of the retina can distinguished clearly. In the fundus image on the left, the green line indicates the position of the slice, crossing the center of the fovea.

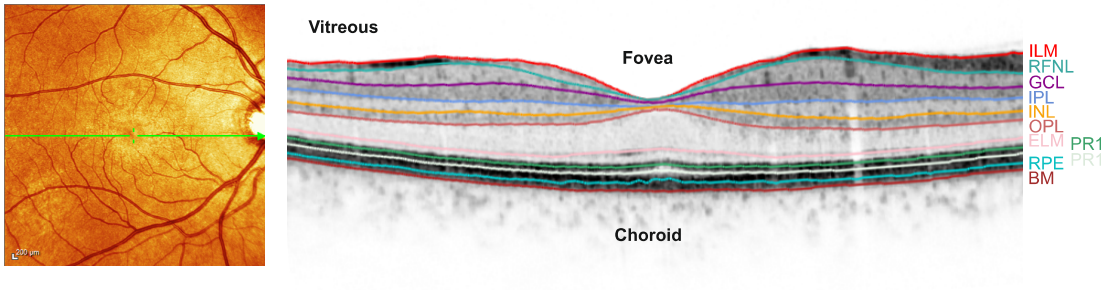

Figure 3: OCT image of the authors retina. The trough in the center of the image is the fovea, with the highest density of photoreceptors. The colored bands depict the single layers of the retina, e. g. nerve fiber layer (RFNL), ganglion cell layer (GCL), photoreceptors, (PR1, PR2), retinal pigment epithelium (RPE), and Bruch's membrane (BM). The green line in the fundus image on the left indicates the position of the slice. The fovea is in the center of the fundus image, the optic disc (blinds pot) can be seen on the right edge of the fundus image.

The optic nerve transmits information from both eyes via the optic chiasm, where the images are merged to a visual field, to the left and right, respectively, optic tract, and from there to the lateral geniculate nucleus and finally to the visual cortex of the brain. The visual association areas are responsible for higher order processing like motion or shape detection and assembles all the information to a picture of the environment.

Figure 4 depicts the image processing and recognition along the visual pathway in a simplified form.

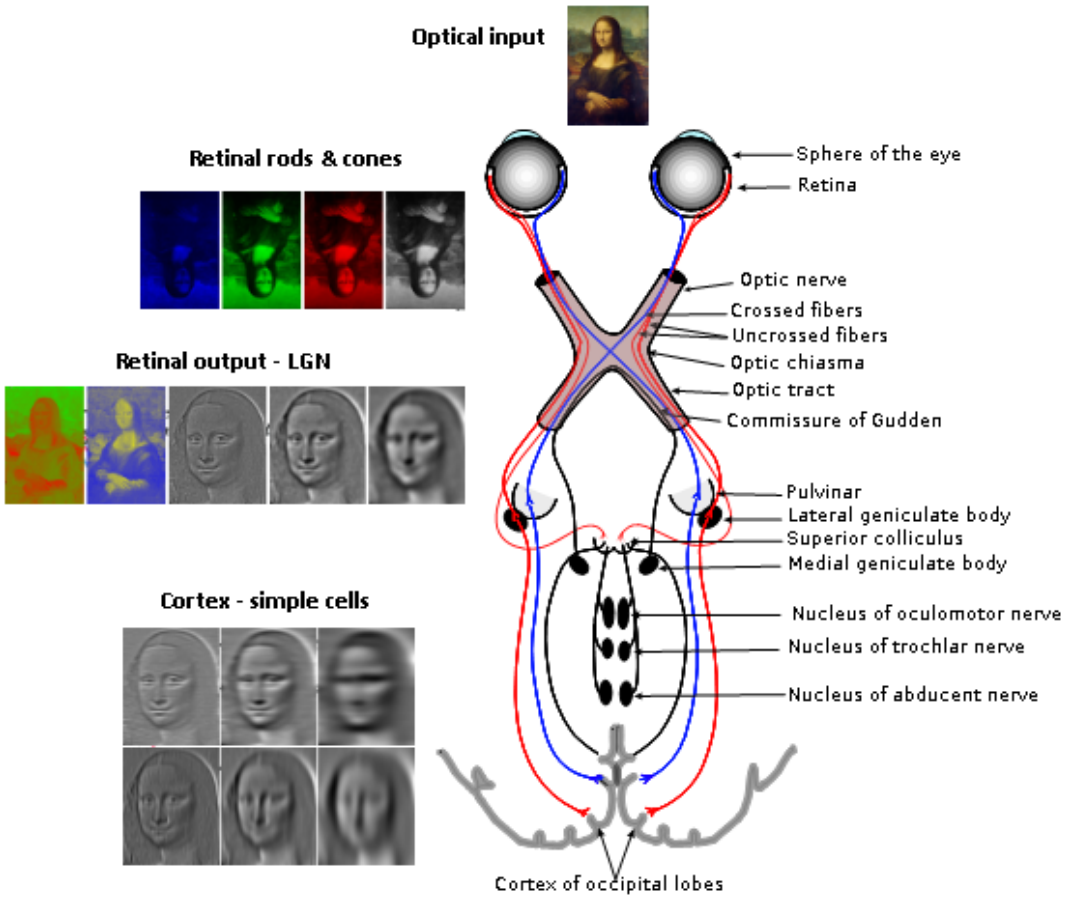

Figure 4: Simplified depiction of the image analysis by the human visual system. The photoreceptors act as spectral filters. The inner retina performs basic image processing like contrast enhancement. Additionally, the information is digitized and compressed before send along the optic nerve. The LGN correlates signals in space and time of both eyes, enabling three-dimensional perception. The visual cortex performs higher order image processing like face recognition. (Modified from: Karel Kulhavy, Wikimedia Commons, *Image analysis of Mona Lisa by the human visual system*, 2012)

2 Functional testing of the visual pathway

The fine tuned visual system is susceptible to damage. Impairments along the visual pathway can result in a slow degeneration (e.g. hereditary diseases, inflammation) or a sudden loss of vision (e.g. toxic, neoplasia, vascular insult).

To identify the cause of an unknown vision loss, the structure of the retina and the visual pathway can be assessed using imaging techniques, like optical coherence tomography (OCT) and magnet resonance imaging (MRI).

However, these techniques only detail the morphology of the reina and the visual pathway, respectively. In contrast, recording electrophysiological signals in response to visual stimuli allows for an objective and non-invasive assessment of the function of the visual pathway.

To investigate specific parts of the visual pathway, particular techniques are used: electroretinography (ERG), electrooculography (EOG), pattern ERG (PERG), visual evoked potentials (VEP). Figure 5 shows the different sources of the ERG, EOG, and PERG within the retina.

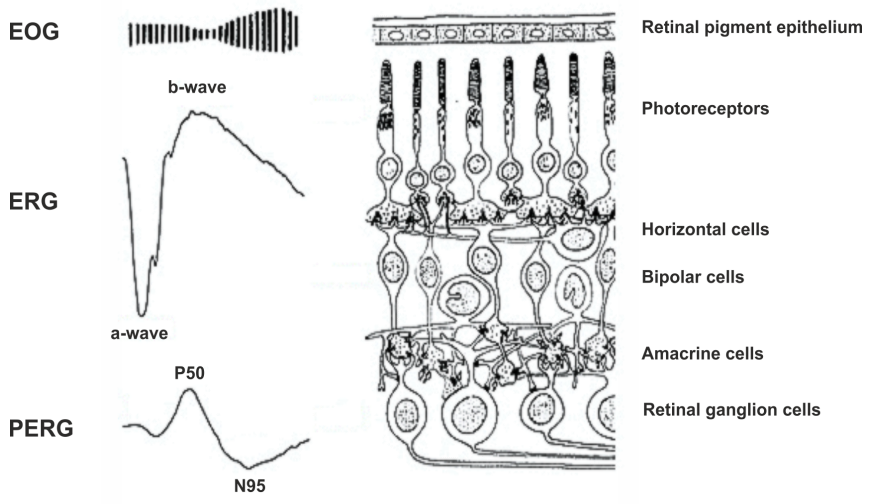

Figure 5: Sources of the electrooculogram, the electroretinogram and the pattern electroretinogram within the retina. The ERG is a response to brief light stimuli driven mostly by photoreceptors and the inner retina, whereas the PERG results from ganglion cells activated by contrasts of a pattern stimulus. The EOG is a slow change of the standing potential of the retinal pigment epithelium in response to long duration light stimulation. (Modified from: RP Fighting Blindness, *Structure of the retina*, http://www.rpfighting blindness.org.uk, 2015)

Registration of electrical potentials in response to visual stimuli is done using either skin electrodes (EOG, VEP), or different kinds of corneal electrodes (ERG). In Figure 6 the application of a corneal DTL electrode for recording an electroretinogram is demonstrated. The reference electrode is placed temporally, an earclip serves as ground electrode. Bach provides detailed instructions on how to mount DTL electrodes on his homepage[1].

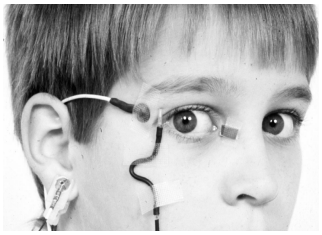

Figure 6: Application of a corneal electrode (DTL) for the recording of an electroretinograms. A thin silver coated nylon fiber is touching the cornea. The reference electrode is placed temporally. A earclip is used as ground electrode.

Figure 7: Two examples of Ganzfeld stimulators used for light stimulation in visual electrophysiology

Amplification and registration of the recorded potentials, as well as stimulus generation is carried out using commercial equipment, usually. Some tests (e.g. ERG), utilize a so called full-field stimulus (Figure 7); others use more complex patterned stimuli displayed on CRT or LCD monitors (e.g. PERG, VEP).

Figure 8 depicts the sources and the time course of the different components of the electroretinogram in response to a brief flash.

1 Preparation and Montage of DTL-like Electrodes. http://www.michaelbach.de/misc/dtl/index.html, last accessed 30.08.2015

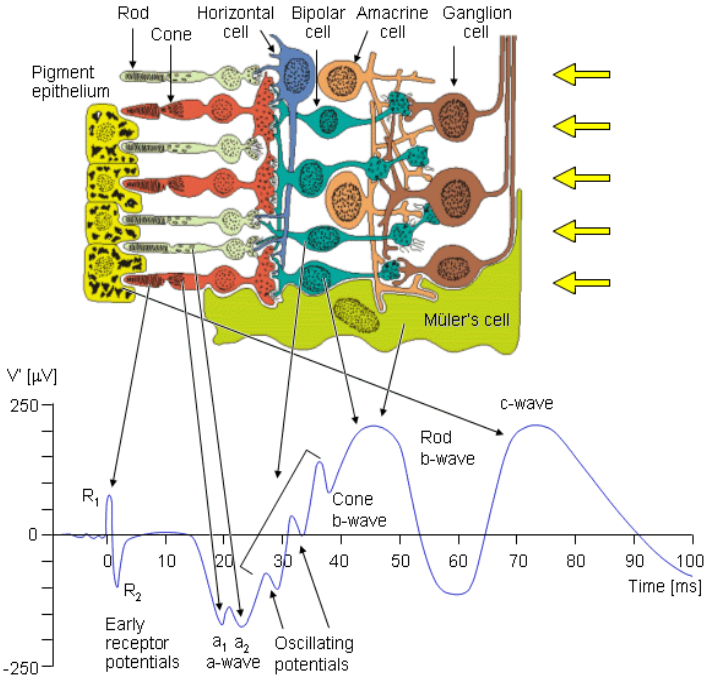

Figure 8: The cells of the retina and their response to a brief flash of light. The photoreceptors are the rods and cones in which a negative receptor potential is elicited. This drives the bipolar cell to become either depolarized or hyperpolarized. The amacrine cell has a negative feedback effect. The ganglion cell fires an action pulse so that the resulting spike train is proportional to the light stimulus level. (Source: *Electroretinogram*, in Bioelectromagnetism, J. Malmivuo and R. Plonsey, 1995 [349])

Investigating the different components of the electroretinogram allows virtually for a “dissection” of the retina: Each component can be assigned to one or more specific layers of the retina: The early receptor potential is the first component of an electroretinogram after a brief light stimulus. It is a biphasic potential change, which's size is direct related to the stimulus intensity. The early receptor potential contains information on the function of the outer segments of the retinal photoreceptors [2]. However, because of its short duration and small amplitude, it is difficult to measure.

The early receptor potential is followed by the so called a- and b-wave. The a-wave origins from extracellular radial currents [3] and provides information about the function of the photoreceptors in the retina. The exact source of the later b-wave is still subject of research. However, current research indicates that it originates in retinal cell that are post-synaptic to the photoreceptors, like bipolar cells. Another source of the b-wave are Müller cells, which generate elec-

trical currents through a change in their membrane potential in response to light induces changes in the ion concentration of the inner plexiform layer [4]. Since the b-wave appears already at very dim light levels – in contrast to the a-wave – and its amplitude is directly related to the intensity of the light stimulus, it is a measure mainly for the rod photoreceptor function.

Using bright light stimuli, small wavelets can be seen at the rising edge of the b-wave. These so called oscillatory potentials have their source in the interactions of different cells of the inner retina. Their exact source is not quite clear, however it is thought that they are generated in the inner plexiform layer [5], [6]. After band-pass filtering (75 – 300 Hz) of the electroretinogram the oscillatory potentials appear as four to five peaks whose amplitudes follow a spindle-like shape. Because of their origin, they permit conclusions about the state of the inner retina.

The c-wave is a reflection of the electrical potential change during hyperpolarization at the apical membrane of the retinal pigment epithelium [7]. The c-wave allows for examination of the function of the retinal pigment epithelium. However, for examining the retinal pigment epithelium the electrooculogram may be more suited [8].

Table 1 gives an overview of abnormalities in the electroretinogram in various diseases. Interestingly, a methanol intoxication is the only case where an "emergency" ERG would aid the diagnosis [9], [10].

Young et al. summarize current techniques, indications, and pitfalls of electrophysiological testing in a current review on electrophysiology in opthalmology [11]. Vincent et all give a review on pathognomonic ERGs in inherited retinal disorders [12].

Table 1: Various disease states with abnormal findings in the electroretinogram (Source: EyeWiki, [13])

Disease	Full-field ERG findings
Multiple evanescent white dot syndrome (MEWDS)	initially depressed a- and b-wave responses with return to normal values
Vitamin A deficiency	marked rod dysfunction and elevated threshold of rods and cones on dark adaptation
Cone dystrophy	markedly depressed photopic response and less affected scotopic response
Cancer associated retinopathy (CAR)	significantly reduced a-wave and b-wave amplitudes
Melanoma associated retinopathy (MAR)	extinguished rod responses, normal a-wave, reduced b-wave (electronegative ERG)
Retinitis pigmentosa	minimal or sub-normal a- and b-wave amplitudes (response primarily from cone system)
Congenital Achromatopsia (typical (rod) monochromat)	non-detectable cone response, normal or subnormal rod response
Congenital Hereditary Stationary Night Blindness (Schubert-Bornschein type)	normal scotopic a-wave with selectively reduced b-wave; implicit time of b-wave is approximately the same under scotopic and photopic conditions
Oguchi disease	normal photopic responses with predominantly reduced scotopic b-wave amplitudes
Fundus Albipunctatus	reduced scotopic amplitudes which improve to normal values after longer (variable) perior of dark adaptation
Stargardt Macular Dystrophy (Fundus Flavimaculatus)	extent of reduced a- and b-wave amplitudes depends on extent of fundus pigmentary changes; longer duration of dark-adaptation may be necessary for scotopic amplitudes to reach normal values
Best Vitelliform Macular Dystrophy	normal ERG responses with an abnormal EOG
Progressive Bifocal Chorioretinal Atrophy	subnormal 30-Hz flicker and single-flash scotopic responses
Fenestrated Sheen Macular Dystrophy	initially normal ERG responses with reduced scotopic and photopic responses in later stages
Familial Internal Limiting Membrane Dystrophy	reduced b-wave amplitudes
Gyrate Atrophy	significantly reduced or extinguished rod and cone responses

Choroideremia	reduced a- and b-wave amplitudes in both scotopic and photopic conditions; increased rod and cone b-wave implicit times
X-linked Juvenile Retinoschisis	reduced photopic and scotopic b-wave amplitudes
Autosomal Dominant Neovascular Inflammatory Vitreoretinopathy	selective reduction of b-wave amplitude
Autosomal Dominant Vitreoretinochoroidopathy	initially normal ERG with only mild to moderately reduced amplitudes in older patients
Familial Exudative Vitreoretinopathy	normal ERG responses (diminished oscillatory potentials may be observed)
Birdshot Retinochoroidopathy	selective reduction in b-wave amplitude more prominent in scotopic than photopic responses; delayed photopic and scotopic b-wave implicit times
Acute Zonal Occult Outer Retinopathy	ERG amplitudes vary from normal to subnormal with prolonged b-wave implicit times
Pseudo-Presumed Ocular Histoplasmosis Syndrome (Multifocal Choroiditis)	moderate to severely reduced rod and cone responses
Behcet Disease	initially loss of oscillatory potentials in flash ERG with subsequent reduction of b-wave amplitude
Sickle Cell Retinopathy	normal ERG in the absence of peripheral retinal neovascularization, reduced amplitudes of ERG components when peripheral retinal neovascularization is present
Takayasu Disease	initially decreased oscillatory potentials, later stages involve reduced a- and b-wave amplitudes
Carotid Artery Occlusion	reduced b-wave greater than a-wave amplitudes depending on extent and severity of occlusion
Central and Branch Artery and Vein Occlusions	reduced scotopic b-wave amplitudes in CRAO and CRVOs; slight b-wave reduction or normal ERG in branch retinal artery or vein occlusions
Hypertension and Arteriosclerosis	initially reduced oscillatory potentials followed by reduced a- and b-wave amplitudes
Chloroquine and Hydroxychloroquine toxicity	normal ERG responses unless presence of advanced retinopathy; cone function initially more affected than rod function

Thioridazine	decreased photopic and scotopic a- and b-wave responses depending on degree of fundus changes
Quinine	transiently decreased a- and b-wave amplitudes under both photopic and scotopic conditions with recovery after 24 hours
Methanol	reduced a- and b-wave amplitudes
Gentamicin	significantly reduced ERG amplitudes
Vitamin A deficiency	reduced ERG amplitudes particularly under scotopic conditions
Siderosis	initially a transient supernormal response then negative pattern followed by non-detectable response in severe cases (rod function more affected than cones; reduction of b-wave amplitude more than a-wave)

Whereas the electroretinography and the electrooculography allow for the examination of the function of the retina, visual evoked potentials (VEP) provide a means to measure the functional integrity of the ascending visual pathways. Visual evoked potentials are electrical potentials in the visual cortex, initiated by brief visual stimuli. VEPs are recorded using skin electrodes, applied at the forehead and at the scalp over the visual cortex. The most common stimulus used for eliciting visual evoked potentials is a checkerboard pattern, with one or two reversal per second. It provides a higher inter-subject reliability compared to only brief flashes [14].

Figure 9 depicts an example VEP recording of the author. The VEP is usually evaluated by measuring the amplitudes and peak times of the first negative trough (N75), the first positive trough (P100), and the second negative trough (N135). The numbers of the markers indicate the time of their appearance (75 ms, 100 ms, and 135 ms). The amplitude corresponds to the amount of axons conducting along the visual pathways, whereas the latency is affected by the myelin status of the visual pathway. Two of the main applications of visual evoked potentials are the diagnosis of multiple sclerosis and optic neuritis [15].

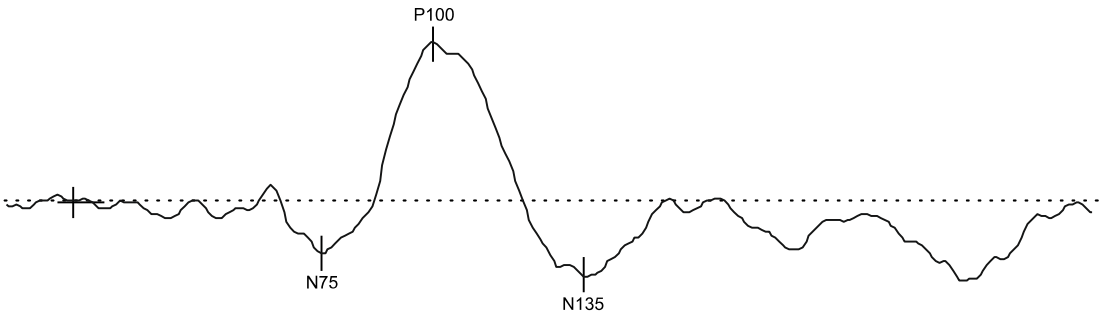

Figure 9: VEP recording in response to a pattern-reversal checkerboard stimulus of the author.

Visual evoked potentials can also be used as a tool for objective perimetry [16]–[18] and for an objective estimation of the visual acuity [19]–[21]. Additionally, VEPs are used in brain research to understand the processing of color, contrast, and motion in the brain [22]–[30].

More information on visual evoked potentials can be found in an overview on VEPs of Fahle and Bach [31]. Creel gives an introduction of the history of visual evoked potentials and provides case reports of several diseases affecting the VEP [32].

III PROCESSING VISUAL ELECTROPHYSIOLOGICAL SIGNALS

1 Diagnosys Espion electrophysiologic recording systems

According to its own statement, Diagnosys LLC is the leader in the field of ophthalmic electrophysiology[2]. The clinic for hereditary retinal degeneration runs in sum six electrophysiologic recording systems of Diagnosys, three Espion e^2 and three Espion e^3. The Espion e^3 system is the successors of the Espion e^{2}and provides, in addition to full-field ERG, pattern ERG, EOG, and VEP, multifocal ERG.

In the our setup, all six devices are using a central relational database management system, to store recordings. Therefore, these are accessible within the whole clinical network.

Additionally, the database is connected to the Tuebingen Physicians Information System (AIS), avoiding the need of manual entering patients information and providing access to examination results.

1.1 The structure of the Espion database

As mentioned earlier, the Diagnosys Espion electrophysiology systems use a relational database management system to store settings and recorded data. The database used, is the open-source relational database management system FirebirdSQL[3]. Besides the actual recorded waveforms, data like patient demographics, stimulation and acquisition settings as well as normative data and configuration parameters are stored in the database. The data are stored in several database tables, according to the relational data model, described first by Codd et al. [33], [34].

2 http://diagnosysllc.com/about/what-we-do, last accessed 01.07.2015
3 http://www.firebirdsql.org, last accessed 01.06.2015

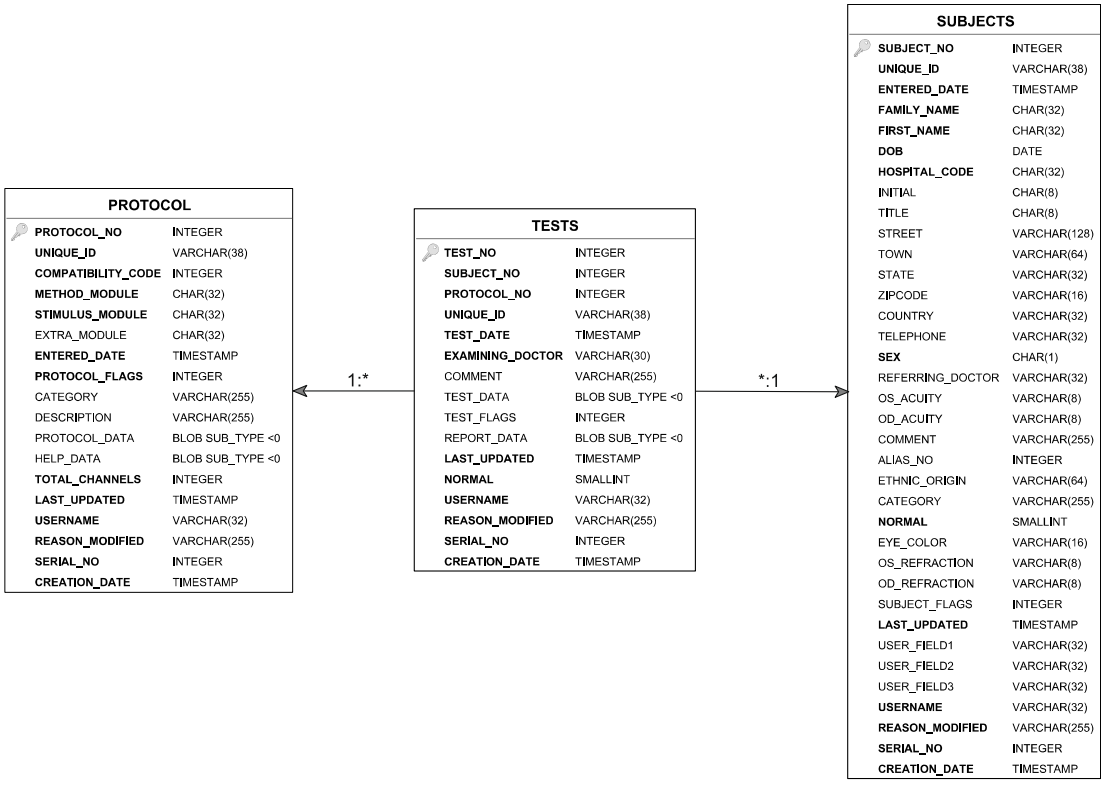

Figure 10: Entity-relationship diagram of the three main tables of th relational data model the Espion software uses to store electrophysiological recordings. Each examination stored in the table TESTS refers to one protocol, specifying acquisition and stimulus settings, and one subject, holding information on the patient, which underwent the examination, stored in the tables PROTOCOL and SUBJECTS, respectively. The relations between the tables are realized as foreign keys, referencing the primary key of the respective target table, thereby ensuring referential integrity

Figure 10 depicts the entity relationship diagram of the tree main tables PROTOCOL, TESTS, and SUBJECTS used by the Espion software. Details of an examination as well as the recorded waveform data belonging to it, is stored in the table TESTS. One entry in table TESTS refers to exactly one entry in table PROTOCOL and one entry in table SUBJECTS, whereas the first one contains settings for acquisition and stimulus parameters of the examination, the latter one demographic information on the subject, which underwent an examination, respec-

tively. Each of the tables contains a consecutively numbered integer value as primary key (denoted with a key in Figure 10). The relations between the tables are realized as foreign keys, referencing the primary key of the respective target table, thereby ensuring referential integrity.

From Figure 10 it is obvious, that not all details of an examination is stored as individual columns of the table TESTS. Instead, most of the data, including the actual waveform data, is stored within as a binary large object (BLOB) in the column named TEST_DATA. The reason to break with the relational data model for examination data, is due to the increased complexity of a data model modelling all details of an electrophysiological examination, and the resulting performance impact, as Richard Robson, founder and vice president of Diagnosys LLC, explained [35]. The same strategy is used to store protocol details in column PROTOCOL_DATA of table PROTOCOL.

During runtime, the Espion software uses the hierarchical or tree-like data structure depicted in Figure 11. When reading and writing, a mapping between the hierarchical and the relational data model takes place.

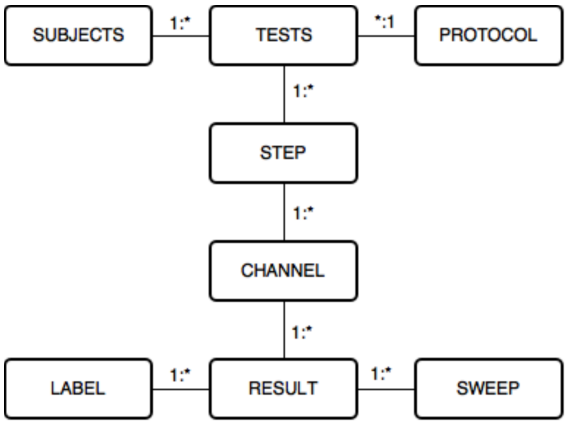

Figure 11: Data model used by the Espion software during runtime. Subjects, tests, and protocols are mapped to the corresponding tables in the database. All other entities are encoded as BLOB in the column TEST_DATA of table TESTS.

A test represents a single examination and is linked to a subject and a protocol. It consists of one or more steps, each depicting a specific set of stimulus param-

eters and acquisition settings, like recording time, number of channels, number of results and sweeps. Channels specify a specific electrode position and settings like notch filter or frequency filters. Results are averages of at least one ore more sweeps. Multiple results can be recorded. Associated to results are labels, which denote special points of interest like the a- or b-wave of a waveform. Sweeps represent the actual waveform data.

Except subject, protocol, and parts of the test data, all other data of this data structure are encoded as a set of consecutive records and stored as binary data in the column `TEST_DATA` of table `TESTS`. To reduce the amount of space required, the binary data are compressed using the deflate algorithm [36].

1.2 Accessing the Espion database

FirebirdSQL provides an implementation of the JDBC specification, called Jaybird[4], which allows access to data stored in the database management system using Java with SQL. Therefore, subject demographics as well as basic information about examinations are easy accessible. However, loading the actual recorded data is more complex, since, as mentioned before, these data are stored in a proprietary format in a BLOB. These data can be loaded from the table as a byte array in Java using SQL. Before any further processing the data first must be uncompressed. This is done using the inflate algorithm, which is part of the Java standard library[5].

The inflated byte array contains a series of consecutive records, representing the format of the data within the BLOB (Figure 12).

4 http://www.firebirdsql.org/en/jdbc-driver, last accessed 12.07.2015
5 http://docs.oracle.com/javase/7/docs/api/java/util/zip/Inflater.html, last accessed 12.07.2015

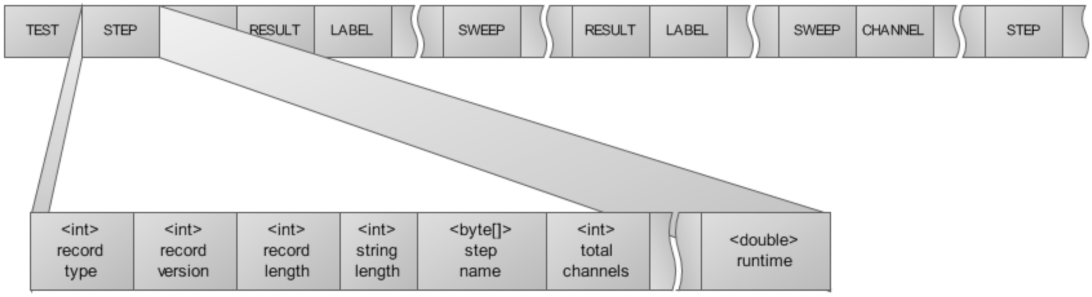

Figure 12: Organization of the data stored in the BLOB as consecutive records. Records have a variable length and are comprised of entries of specific data types.

Each record consists of a preamble describing the type (e. g. TEST, STEP, CHANNEL), the version, and the number of bytes of the record. Subsequently, chunks of data of specific data types are stored as series of bytes.

1.3 Reading records from the Espion database

Data input and output in Java is carried out with the stream API. Streams hide the complexity of the underlying data sources behind a simple API [37, Ch. 17]. Input streams inherit from java.io.InputStream, output streams from java.io.OutputStream. Both classes provide basic methods to read from or write to data sources, whereas the actual implementation specifics are left to derived classes.

Streams can be chained according to the pipes-and-filters pattern [38]: Each stream class implements either input, output, or a single processing step and forwards its result to the next stream in the chain.

In order to a read the examination data stored as records in the field TEST_DATA of the table TESTS, the new class RecordInputStream was implemented. RecordInputStream inherits from java.io.FilterInputStream, which is part of the Java SDK and ought to allow subclasses to transform data passing the

stream. Therefore, existing methods can be overridden or new methods can be introduced. Listing 1 shows the implementation of the class RecordInputStream.

```
1  public class RecordInputStream extends SwappedDataInputStream {
2      private int _lastRecordLength = -1;
3
4      public RecordInputStream(final InputStream is) {
5          super(new BufferedInputStream(is));
6      }
7
8      public IRecord nextRecord() throws RecordFormatException {
9          try {
10             if (_lastRecordLength != -1) {
11                 reset();
12                 read(new byte[_lastRecordLength]);
13             }
14
15             final int recordType = readInt();
16             if (recordType != -1) {
17               RecordType type = RecordType.valueOf((recordType >> 24) & 0xFF);
18
19               final int recordVersion = readInt();
20               final int recordSpare = readInt();
21
22               _lastRecordLength = readInt();
23
24               mark(_lastRecordLength);
25
26               // because of the first three readInt() (version, spare & length)
27               final int completeRecordLength = _lastRecordLength + 3 * 4;
28               return new Record(type, recordVersion, completeRecordLength, this);
29             } else {
30                 throw new RecordFormatException("Unknown record type.");
31             }
32         } catch (IOException e) {
33             throw new RecordFormatException(e);
34         }
35     }
36 }
```

Listing 1: Implementation of class RecordInputStream. The method nextRecord() read records sequentially from the underlying InputStream and returns the read Record object.

Instead of extending FilterInputStream directly, it extends SwappedDataInputStream (line 1), which performs a conversion between little endian and big endian byte-ordering. This is necessary, since the Java Virtual Machine (JVM) uses big endian internally, whereas the Espion software uses little endian. SwappedDataInputStream is part of the Apache commons-io library[6].

Within the constructor, the passed InputStream is wrapped in a java.io.BufferedInputStream (line 2); this implementation of a stream allows a "bookmark" to be set to a certain position in a stream, in order to jump back to it later. In method nextRecord(), this is used to mark the beginning of the current record (line 24). After reading the complete record, by using the length of the record read in line 22, the whole record is skipped (line 12). This ensures, that even if not the complete record was read, the correct position for reading the following record is set.

If the complete record is read from the underlying InputStream successfully, an object implementing the interface IRecord (Listing 2) is returned from the method nextRecord() (line 28).

```
1  public interface IRecord extends DataInput {
2      public RecordType getType();
3      public int getVersion();
4
5      public byte[] readByteArray(final int length) throws IOException;
6      public Color readColor() throws IOException;
7      public Date readDateTime() throws IOException;
8      public String readString() throws IOException;
9      public BitSet readBitSet() throws IOException;
10
11     public void skip(final int n) throws IOException;
12 }
```

Listing 2: The interface IRecord extends the interface DataInput by additional helper methods to return data from a data source.

6 http://commons.apache.org/proper/commons-io, last accessed 12.07.2015

The interface IRecord extends the interface DataInput[7], which provides methods for reading and reconstructing data in any Java primitive data type from a binary stream, by additional helper methods. The implementation delegates calls to these methods to the corresponding methods of the underlying InputStream.

```
1  // ...
2  final DataSource ds = new FBWrappingDataSource();
3  // ...
4  final Connection conn = ds.getConnection();
5  final Statement stmt = conn.createStatement();
6  final ResultSet rs = stmt.executeQuery("SELECT test_data FROM tests");
7
8  while (rs.next()) {
9   final Blob blob = rs.getBlob("test_data");
10  final InputStream is = blob.getBinaryStream();
11  final InflaterInputStream iis = new InflaterInputStream(is, new Inflater(true));
12  final RecordInputStream ris = new RecordInputStream(iis);
13  final IRecord record = ris.nextRecord();
14  if (RecordType.RECORD_ERG_TEST.equals(record.getType())) {
15   String protocolDescription = record.readString();
16   System.out.println(protocolDescription);
17  }
18 }
19 // ...
```

Listing 3: Short example of how to use the RecordInputStream to decode test data contained in the the column BLOB TEST_DATA of table TESTS.

Listing 3 demonstrates the use of the RecordInputStream with a short example: using the FBWrappingDataSource a connection to the FirebirdSQL database is created (line 2) and an SQL statement to retrieve the column TEST_DATA of the table TESTS is executed (line 6). The returned result set is iterated (line 8) and for each result, a chain of streams is instantiated (lines 10-12). Finally, the first record of the stream is fetched (line 14) and if its type equals to an ERG (line 14), the first chunk of data, which is the description of the protocol used for the selected test, is read and printed to the standard output (lines 15 & 16).

7 http://docs.oracle.com/javase/7/docs/api/java/io/DataInput.html, last accessed 12.07.2015

2 Generic data model for visual electrophysiological data

In the previous sections, the data model used by the Espion software for persisting electrophysiological recordings, as well as the access and the decoding of persisted data was described. In the following, a data model for visual electrophysiological data will be introduced and the process of initializing the model using data retrieved from the Espion database as stream of records will be described.

The data model is independent of a specific manufacturer, as its structure applies to visual electrophysiological data in general. Using the data model with other electrophysiologic system than the Espion system, can easily archived by implementing a software interface adapted to the data structures of the data source.

Figure 8 depicts an UML class diagram of the main interfaces of the generic data model for visual electrophysiological data. The data model is divided between interfaces representing the actual recorded data (ITest, IStep, IChannel, IResult, and ISweep), and interfaces representing meta information storing simulation and acquisition settings (IProtocol, IStepDefinition, IChannelDefinition. Therefore, a parallel hierarchy of interfaces exists, whereas interfaces representing actual data have a reference to their counterpart embodying meta-information (e. g. ITest – IProtocol, IChannel – IChannelDefinition).

A description of the single interfaces shown in Figure 13, together with their relations is listed in Table 2.

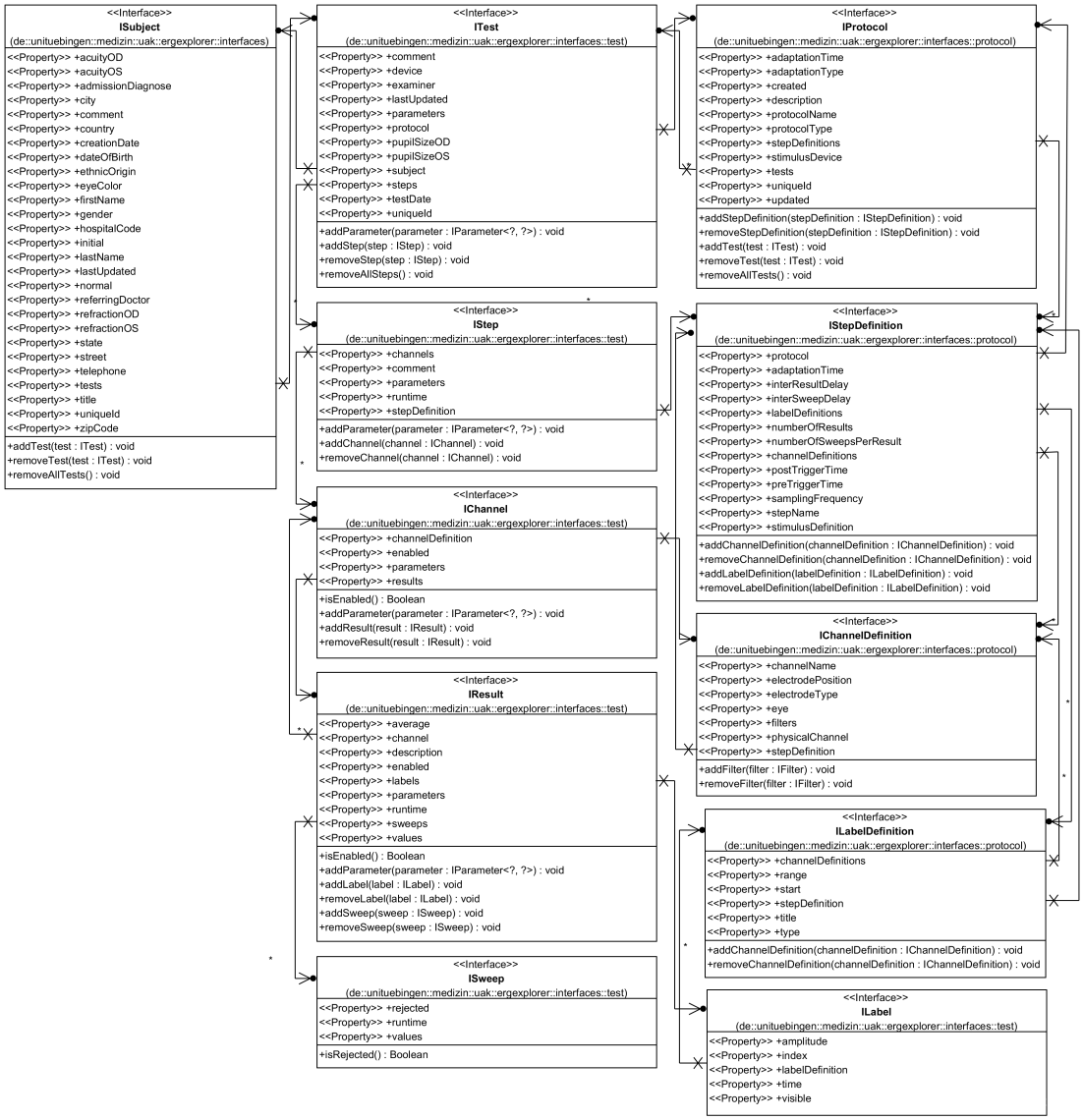

Figure 13: UML class diagram of the main interfaces of the generic data model for visual electrophysiological data. The data model is divided in interfaces representing the actual data and interfaces embodying meta-information, whereas the forme ones have references to their counterparts of the meta level.

Table 2: List of the main interfaces of the generic data model for visual electrophysiological data. The interfaces are divided into interfaces representing actual data and interfaces embodying meta-information. Interfaces representing actual data have a reference to their counterpart of the meta-data hierarchy, which are listed in the same row. The column references lists all interfaces referenced by the current interface.

Actual data			Meta data		
Interface	Description	references	Interface	Description	references
ISubject	Patient demographics	ITest (*)	-	-	-
ITest	Examination details	ISubject (1) IStep (*)	IProtocol	Represents an examination protocol. Container for a set of stimuli.	ITest (*) IStepDefinition (*)
IStep	Container for channels for one specific step in the protocol	ITest (1) IChannel (*)	IStepDefinition	Specific stimulus and acquisition settings for a step.	IProtocol (1) IChannelDefinition (*) ILabelDefinition (*)
IChannel	Container for results of belonging to one recording channel	IStep (1) IResult (*)	IChannelDefinition	Electrode positions, channel name, filter settings	IStepDefinition (1)
IResult	Averaged waveform data of corresponding sweeps	IChannel (1) ISweep (*) ILabel (*)	-	-	-
ILabel	Cursor on averaged waveform data	IResult (1)	ILabelDefinition	Cursor name and type, placement, channel assignment	IStepDefinition (1) IChannelDefinition (*)
ISweep	Waveform data		-	-	-

Values in brackets denote the cardinality of a relation: 1 = exactly one, * = zero, one, or many

2.1 Conversion between records and generic data model

As mentioned before, data is retrieved from the Espion database as stream of consecutive record, representing different pieces of information. In order to convert these records into the generic data model, a modified version of the builder pattern is used. As part of the so-called gang-of-four (GoF) design patterns, introduced by Gamma et al. in 1994 [38], it belongs to the group of creational patterns. It aims to separate a complex step-by-step creation of objects from their representation and is especially useful, if an internal state has to be kept during creation. A disadvantage of the builder pattern is, that for each object to be created, an own builder must exist. This leads to a large number of classes and a tight coupling between the resulting object and the builder as Eilebrecht and Starke state in their book about software design patterns [39].

The way the builder pattern is used to convert from records to the generic data model is different to the original GoF builder pattern. Instead of only one, in this implementation the builder returns two products. This follows from the separation of the generic data model between actual and meta data, whereas the sources for both are the same records. Additionally, according to the relations between the interfaces of the generic data model, a builder delegates the build process for dependent classes to subordinate builders. Figure 14 demonstrates the modified builder pattern as UML class diagram at the example of the concrete builder class StepBuilder.

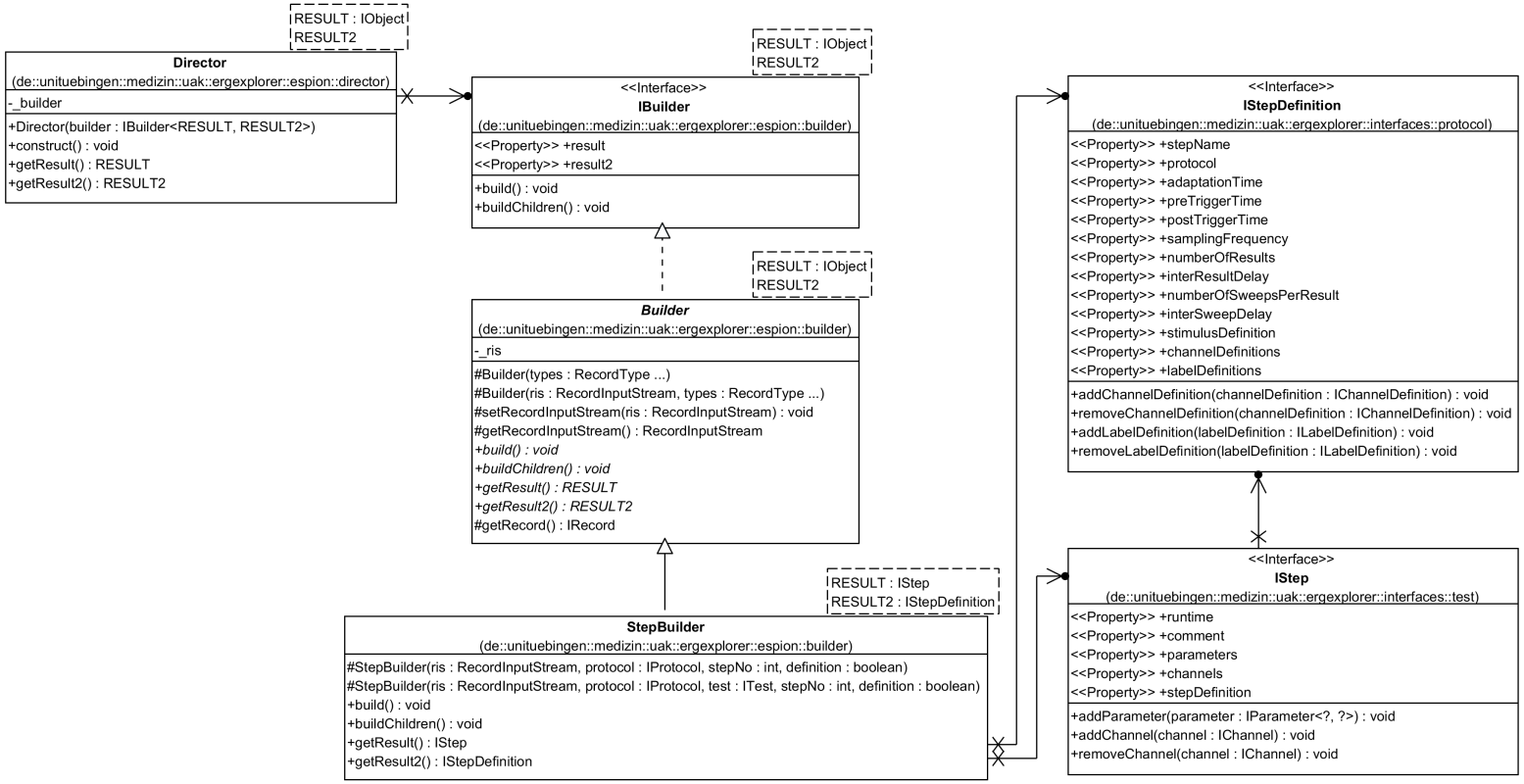

Figure 14: UML class-diagram of the implementation of the builder pattern at the example of the StepBuilder: The concrete builder inherits from the abstract builder and is responsible for creation and initialization of the implementations of the interfaces IStepDefinition and IStep using data provided by the RecordInputStream. For subsidiary objects (ILabel and IChannel), the StepBuilder delegates the creation to downstream builders in method buildChildren().

Listing 4 exemplifies the use of the builder pattern at the shortened implementation of the class StepBuilder, which is responsible for the creation and initialization of the implementation of the interfaces IStep and IStepDefinition. It also demonstrates the nested use the builders ChannelBuilder and LabelBuilder, to create the dependent implementations of the interfaces IChannel and ILabel, respectively.

```
1  public class StepBuilder extends Builder<IStep, IStepDefinition> {
2   private IStep _step;
3   private IStepDefinition _stepDefinition;
4
5   private final IProtocol _protocol;
6   private final ITest _test;
7   private int _totalMarks;
8   private int _totalChannels;
9
10  protected StepBuilder(RecordInputStream ris, IProtocol protocol, ITest test) {
11   super(RecordType.RECORD_ERG_STEP, ris);
12   _protocol = protocol;
13   _test = test;
14  }
15
16  public void build() throws BuilderException {
17    try {
18     final IRecord record = getRecord();
19
20     String name = record.readString(); // step name
21     _totalChannels = record.readInt(); // Number of channels
22
23     int adaptationTime = record.readInt(); // Adaptation Time in minutes
24     int resultDelay = record .readInt();
25
26     record.skip(getRecord().readInt()); // stimulusData
27     record.skip(getRecord().readInt()); // acquisitionData
28     record.skip(INTEGER_SIZE); // booleanFlags
29     int sampleTime = record.readInt();
30     Amount<Frequency> samplingFrequency = valueOf(1000000d / sampleTime,  HERTZ);
31    record.skip(INTEGER_SIZE); // totalPoints
32    record.skip(INTEGER_SIZE); // preTriggerPoints
```

```
33      record.skip(DOUBLE_SIZE); // xAxisLength
34      record.skip(DOUBLE_SIZE); // xAxisOffset
35      record.skip(DOUBLE_SIZE); // xAxisZero
36      record.skip(DOUBLE_SIZE); // totalTicks
37      record.skip(INTEGER_SIZE); // autoZeroPerformed
38
39      int preTriggerTime = record.readInt();
40      int postTrigerTime = record.readInt();
41      int sweepsPerResult = record.readInt();
42      int resultsPerRun = record.readInt();
43      int autoZeroPreTrigger = record.readInt();
44      int autoZeroRange = record.readInt();
45      record.skip(INTEGER_SIZE); // Print start time in ms
46      record.skip(INTEGER_SIZE); // Print range in ms
47
48      _totalMarks = record.readInt(); // Total markers
49      int stimulusPeriod = record.readInt();
50      getRecord().skip(record.readInt());
51
52      Date runTime = record.readDateTime();
53
54      _stepDefinition = new StepDefinition(_protocol);
55
56      _stepDefinition.setAdaptationTime(valueOf(adaptationTime,
                    NonSI.MINUTE).TO(SI.SECOND));
57      _stepDefinition.setPostTriggerTime(valueOf(postTrigerTime, SI.MICRO(SI.SECOND)));
58      _stepDefinition.setPreTriggerTime(valueOf(preTriggerTime, SI.MICRO(SI.SECOND)));
59      _stepDefinition.setNumberOfResults(resultsPerRun);
60      _stepDefinition.setSamplingFrequency(samplingFrequency);
61      _stepDefinition.setInterResultDelay(valueOf(resultDelay, SI.SECOND));
62      _stepDefinition.setStepName(name);
63      _stepDefinition.setNumberOfSweepsPerResult(sweepsPerResult);
64
65      _step = new Step(_test);

66      _step.setRuntime(runTime);
67      _step.setStepDefinition(_stepDefinition);
68    } catch (IOException e) {
69      throw new BuilderException(e.getMessage(), e);
70    }
71  }
```

```
72 public void buildChildren() throws BuilderException {
73   for (int i = 0; i < _totalMarks; i++) {
74    LabelDefinitionBuilder builder
        = new LabelDefinitionBuilder(getRecordInputStream(), _stepDefinition);
75
76    Director<ILabelDefinition, Void> director = new Director<>(builder);
77    director.construct();
78
79    ILabelDefinition labelDefinition = director.getResult();
80    _stepDefinition.addLabelDefinition(labelDefinition);
81   }
82
83   // create channels & channeldefinitions
84   for (int i = 0; i < _totalChannels; i++) {
85    ChannelBuilder builder = new ChannelBuilder(getRecordInputStream(), _step);
86
87    Director<IChannel, IChannelDefinition> director = new Director<I>(builder);
88    director.construct();
89
90    IChannel channel = director.getResult();
91    IChannelDefinition channelDefinition = director.getResult2();
92    if (channel != null) {
93     _step.addChannel(channel);
94    }
95    if (channelDefinition != null) {
96       _stepDefinition.addChannelDefinition(channelDefinition);
97    }
98   }
99
100   public IStep getResult() {
101     return _step;
102    }
103
104   public IStepDefinition getResult2() {
105     return _stepDefinition;
106    }
107   }
```

Listing 4: Implementation of a concrete builder according to the builder pattern at the example of the class StepBuilder.

The class StepBuilder extends the abstract class Builder using the interfaces IStep and IStepDefinition as template parameters of the parent class (line 1). These template parameters define the return type of objects created by this builder. Additionally to the RecordInputStream, which is inherited from the abstract Builder, the constructor defines two parameters of type IProtocol and ITest (line 10). These two parameters are used to link the created objects with their dependent classes, whereas the RecordInputStream is passed to the constructor of the parent class (line 11).

The method build() gathers the data from the current record (lines 20 – 53), which is later used to create and initialize the two resulting objects of type IStep and IStepDefinition (lines 54 – 63). The resulting objects can be accessed using the methods getResult() and getResult2() (lines 101 & 105).

Finally, dependent classes are created in method buildChildren(), by using the respective builder implementations (lines 72 – 98).

The use of the builder pattern allows for a separation between data model and initialization, which is especially beneficial in this rather complicated conversion between record-type data and the object model of the generic data model for visual electrophysiological data.

2.2 API usage

To simplify usage of the API and hide the complexity of database access and conversion of the record-type data to generic data model, the class EspionConnection provides set of easy to use methods, which are listed in Table 3.

Table 3: Methods provided by the class EspionConnection for hiding the complexity of database access.

Method	Return type	Description
getSubjectList()	List<ISubject>	Returns all subjects in the Espion database
getProtocolList()	List<IProtocol>	Returns all protocols in the Espion database
getTestList(ISubject)	List<ITest>	Returns all tests belonging to the specified subject
getTestList(IProtocol)	List<ITest>	Returns all tests based on the specified protocol
loadTest(ITest)	ITest	Returns a test by using a template object

Beside providing access to the Espion database, the class EspionConnection implements lazy loading and a caching strategy for tests and protocols already loaded by leveraging the (virtual) proxy pattern [38]. This helps to reduce the number nescessary database accesses.

```
1  final DataSource ds = new FBWrappingDataSource();
2  // data source initialization
3  final EspionConnection ec = new EspionConnection(ds);
4
5  for (final ISubject subject : ec.getSubjectList()) {
6    System.out.printf("%s, %s\n", subject.getLastName(), subject.getFirstName());
7
8    for (final ITest test : ec.getTestList(subject)) {
9      final IProtocol protocol = test.getProtocol();
10     System.out.printf("%tD: %s\n", test.getTestDate(), protocol.getProtocolName());
11   }
12 }
```

Listing 5: Retrieving subjects and associated tests from a JDBC datasource of the Espion database using the class EspionConnection.

The code example in Listing 5 uses the EspionConnection to load all subjects (line 5) and their associated tests (line 8) from the Espion database and prints the last- and first name of each subject, as well as the examination date and the name of the protocol used for the test (line 10).

3 An integrated domain specific language for post-processing and visualizing electrophysiological signals in Java

This text was published in the conference proceedings of the Annual International Conference of the IEEE Engineering in Medicine and Biology in 2010: T. Strasser, T. Peters, H. Jagle, E. Zrenner, and R. Wilke, "An integrated domain specific language for post-processing and visualizing electrophysiological signals in Java.," Conf. Proc. IEEE Eng. Med. Biol. Soc., vol. 1, pp. 4687–90, Jan. 2010.

3.1 Introduction

Electroretinography (ERG) records the summed electrical potentials arising in the retina during light stimulation, usually delivered by a full-field (Ganzfeld) stimulator. There are several components contributing to this summed response: photoreceptors (rods and cones) and various neural and non-neuronal cells of the inner retina. Therefore, the ERG is used as a non-invasive method for functional testing of the visual system and is a valuable tool for the precise diagnosis of retinal disorders.

The source of the electrical signals contained in the ERG is the movement of ions within the retina as a result of depolarization or hyperpolarization of cellular membranes of neurons, glial cells, and photoreceptors. This activity is measured indirectly with electrodes placed at the cornea.

Evaluation of an ERG usually includes identifying waveform components of interest of the voltage trace and measuring their amplitude and timing characteristics. Examples are the so called a- and b-wave which are denoted as A and B in Figure 15, which shows recordings performed under two different stimulus

conditions: (a) single flash, (b) 30 Hz flicker. The a-wave is the trough, the b-wave peak the following peak of the curve.

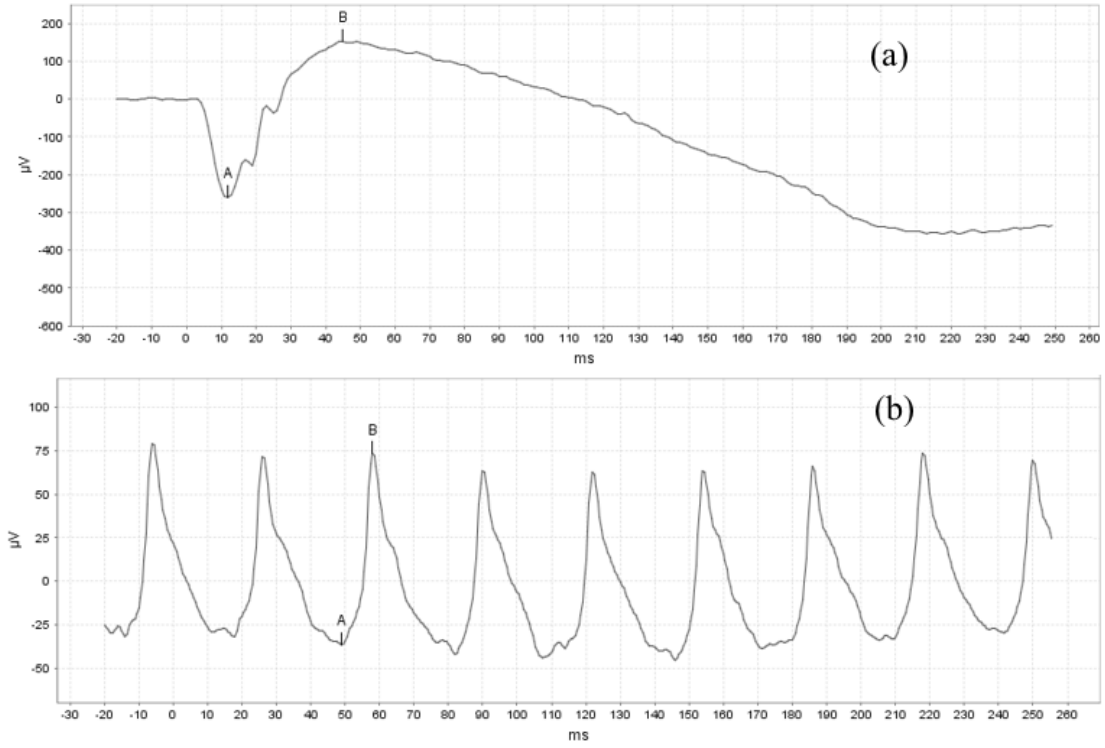

Figure 15: ERG responses for a single flash (a), and a flicker stimulus (b). The waveforms are annotated with markers (A- and B)

Nowadays, the evaluation of electrophysiological recordings is often performed by using built-in capabilities of electrophysiological devices. The devices usually provide widely used algorithms such as trend removal and averaging, or even more advanced algorithms like fast fourier transformation or band-pass filtering. However, many applications of electrophysiology require further processing for analyzing the recorded data. This further processing (or post-processing) is usually performed manually, using mathematical or statistical software packages like Mathworks Matlab, SAS JMP, WaveMetrics IGOR Pro or even

Microsoft Excel. This manual evaluation of recordings is a time consuming process and places high demands on the operator in order to guarantee reproducibility of results. It is also highly dependent on the electrophysiology device's capabilities for exporting measurements. In clinical routine and even more in clinical trials, a high demand for reproducible post-processing exists. Ideally, this post-processing should be generated without manual interaction, immediately after patient examination.

Another important point is the (graphical) presentation of recorded data. Most electrophysiological devices provide methods to generate printouts of waveforms and lists of markers set by an operator during the evaluation. These printouts are rarely customizable and are limited to the built-in evaluation algorithms. It is feasible to generate reports incorporating normative data, significance levels, and advanced evaluation results. This helps clinicians in interpreting results and supports specialized analysis used in clinical trials.

Last but not least, attempts for reducing paper-based information flow in hospitals are growing during recent years. Currently, many hospitals are using electronic information systems for managing patients data and documents, as well as examining results.

The previously stated problems have lead us to the development of a software framework, that can be used for analyzing and visualizing electrophysiological data. The primary intention of the framework is the post-processing of electrophysiological data such as produced by ERGs, visually evoked cortical potentials (VECP) or electrooculograms (EOG). It was developed as the basis of ERG Explorer [40], a software for analyzing and visualizing of visual electrophysiological data. Because, such a framework might be useful for other domains of electrophysiology, we have decided to develop it as an independent tool and provide it to the public. Hopefully, this will lead to an increasing num-

ber of implemented algorithms, therefore improving the use of the framework. Although, the framework can be used as standalone, its main benefit lies in its ease of integration into existing applications or systems.
First, we will describe the architectural principles of the framework, and then we will delineate its deployment and give examples, of its use.

3.2 The software framework

Goals

The framework is focused to provide a simple and quick way to implement signal post-processing, visualization, and reporting under an open-source license, making it easy to adapt to the specific needs of the user. The code is freely available on our website[8].
The main goals of the framework are:

- enable reuse of code
- extensibility by adding new processing methods
- ease of integration in own software
- adaptable to new application domains
- simple usage – fast learning curve

Implementation language

Although there are programing languages available which are focused on mathematical and/or statistical calculations like R (S) or Matlab, we have decided to use the general purpose language Java. Java was initially released in 1996 by Sun Microsystems and has advanced significantly since. Originally intended as an object oriented language for developing graphical user interfaces during the last

8 http://www.eye-tuebingen.de/zrennerlab, last accessed 20.07.2015

decade it has evolved into a language which is used in a wide range of application areas. The strength of Java results from the multitude of libraries available for almost any purpose, including many libraries intended for scientific usage. Together with the built-in capabilities of Java, performance can rival specialized languages like R (S) or Matlab in terms of scientific computing. Thus, the ability of Java to interface with almost any other device or system and the wide spread knowledge of the Java programming language led us to the decision to use Java as the implementation language of our framework.

3.3 Design and architecture

Utilized open-source libraries

As stated before, the framework uses several existing open source libraries, therefore taking advantage of best-of-breed solutions in specific problem domains. In detail these are:

- *JScience*[9], providing among others, a reference implementation for JSR-275: Units Specification, a linear algebra module, functions for symbolic calculations and analysis, real, rational and complex numbers and matrix operations
- *Apache Commons Math*[10], providing modules for statistics, linear algebra, numerical analysis, probability distributions, parametric estimation, differential and integral calculus
- *JFreeChart*[11], charting library (i. e. bar charts, x/y charts)
- *JasperReports*[12], reporting framework, providing template based mechanism for exporting to PDF, HTML, XLS, RTF, ODT, CSV, XML

9 http://jscience.org, last accessed 01.07.2015
10 http://commons.apache.org/proper/commons-math, last accessed 01.07.2015
11 http://www.jfree.org/jfreechart, last accessed 01.07.2015
12 http://community.jaspersoft.com/project/jasperreports-library, last accessed 01.07.2015

Framework architecture

The architecture of the framework leverages the pipes-and-filters architectural software pattern. This pattern provides a structure for processing streams of data. Each processing step is encapsulated in a filter component. The data is passed through pipes between filters [41].

Following this pattern, the framework is divided into the listed parts:

- *sources*, acting as data sources. Sources are responsible for transforming input data into a normalized data format, used by the framework. They represent the interfaces to external devices or applications
- *sinks*, delivering the processing results as single or multiple values
- *filters*, realizing the signal processing or transformation steps of the data
- *presentation*, responsible for visualization of the processing results as charts
- *reporting*, used to create meaningful reports based on processed data

The first three points of the above enumeration realize the pipes-and-filters pattern. This pattern is used in scenarios where data transformation is necessary. The most famous application of the pipes-and-filters pattern is text processing in UNIX shells: text documents can be processed by chaining several small applications, each of them with an exactly defined function. Another one is stream processing in the Java language itself: Streams, originating from different sources like files, network, or memory can be processed using various filters and later on stored using again specialized streams.

Sources, sinks and filters together build a so called *filter chain*, which is responsible for processing the data. A filter chain consists of one source, one sink, and one or more filters. The filters are combined in the order required to produce the desired results. It is also possible to add conditional branches to allow

for execution of filter based on variables or results of previous filters or filter chains. As mentioned perviously, the framework contains a set of filters.
Examples are:

- averaging
- interpolation
- fast fourier transformation
- Chebyshev frequency filter

New filters can easily be added to the framework by implementing the provided interfaces as described in the following chapter.

Sources provide the entry point to the filter chain. They are used to transform data from third party sites into the *normalized data format* which is used within the filter chain. The framework provides an example implementation for reading data from a character separated text file (CSV). For integration within custom software, a personalized implementation would usually be developed.

Sinks are used to deliver the results of the processing. Similar to sources, they can be used to create custom implementations and produce e. g. charts, CSV files, or spreadsheets.

To guarantee the smooth interaction of pipes-and-filters, it is necessary to define a contract between these parts of the framework. This is especially important when third party sites contribute custom implementations of filters and pipes.

This contract is based on the one hand on interfaces defined and provided by the framework and on the other hand on a command, normalized data format, used for exchanging data between pipes and filters, as well as input for the presentation and reporting component.

The normalized data format is independent from any data source related information; however adding extended information is possible, allowing the implementation of specialized filters, which are able to handle this information.
The normalized data format consists basically of time series data (i. e. points in time and the measured value) and the associated units of time points and values. The data format not only contains one time series but also list of them. This is due to the fact that electrophysiological recordings often consist either of multiple channels, of multiple sweeps of one channel, or even a combination of both.

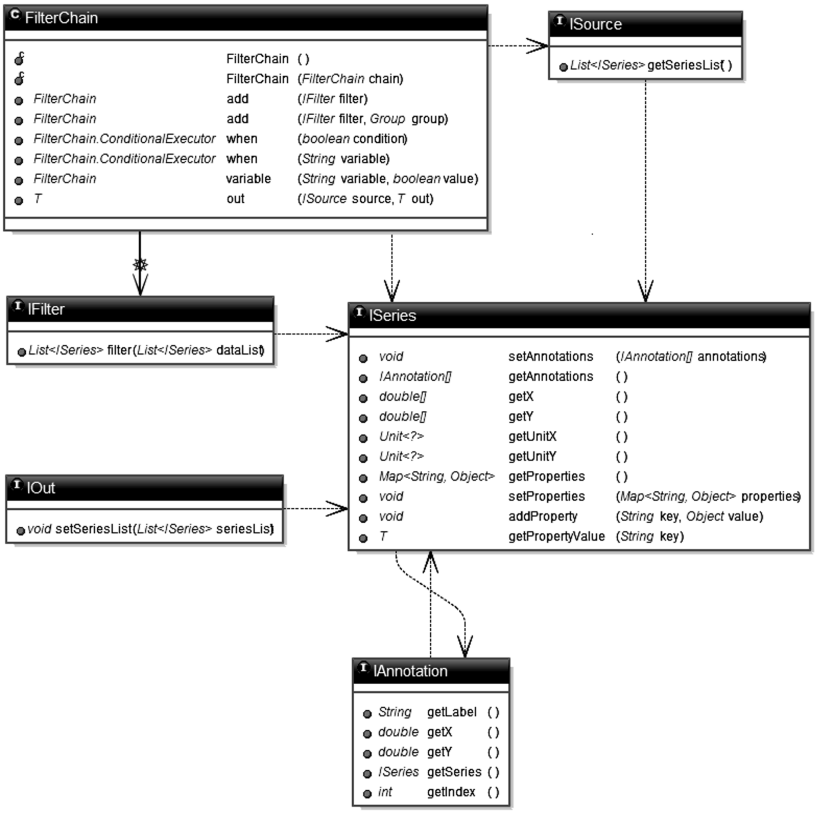

Figure 16: UML class diagram showing the interfaces and classes as well as their relationships of the iDSL4SigProc API. The FilterChain defines a list of filters, which are applied on data represented by a list of instances of the ISeries interface. Data are transformed into instances of ISeries using implementations of the interface ISource.

Figure 16 gives an overview of the most important interfaces and classes of the API. Every component is represented by a corresponding interface: sources (ISource), filters (IFilter), and sinks (IOut). The normalized data passed between filter implementations is realized as a list of objects implementing the interface ISeries. In addition to the time-series data, ISeries instances can contain annotations (IAnnotation) which may be used to annotate hot-spots like a- and b-waves of an ERG recording as mentioned in the introduction.

The remaining components, namely presentation and reporting, are implemented as sinks and therefore use the results of the processing both for visualization and reporting. The presentation component provides the possibility to create charts for displaying the processed data. The component leverages the visitor pattern [41] such, that visitors can be applied to a chart to control its appearance. Applied examples of the presentation and reporting components are given in the next chapter.

3.4 Integrated Domain Specific Languages

As previously described, the framework relies internally on both the software patterns pipes-and-filters and visitor. As an application programming interface (API) it leverages the concept of integrated domain specific languages (DSL).

Gamma et al. [38] describe a domain specific language as “a domain-specific language (DSL) is a programming language or executable specification language that offers, through appropriate notations and abstractions, expressive power focused on, and usually restricted to, a particular problem domain.”

A DSL requires a compiler or interpreter for execution. We decided to create a so called integrated or embedded DSL that uses the syntactic mechanisms of the base language [42], in this case Java. Using an embedded DSL has advantages as well as disadvantages, as described by Hudak [43]: on the one hand,

compilers and existing editors can be used, on the other hand the syntax of the DSL is less flexible because of constraints induced by the base language.
To implement the integrated DSL we are using the Java language features generics [44], and static imports [45] as well as a pattern called fluent interface. The idea behind fluent interface is, that a method of an object returns a reference of the object as its return value, allowing therefore the chaining of method calls at the same object [46]. Khan [47] describes how to leverage this concept to create simple DSLs. The class FilterChain embodies the fluent interface pattern for setting up the filter chain as well as special factory classes provided for each filter to configure the filter's settings.

3.5 Usage examples

```
1  new FilterChain()
2   .add(ArithmeticMeanFilter().build(), groupBy("CHANNEL_EYE"))
3   .add(ChebyshevFilter()
4    .bandpass(valueOf(75, HERTZ), valueOf(300, HERTZ),valueOf(1000,HERTZ))
5     .ripple(2).poles(4).build())
6   .add(RescaleFilter().y(MICRO(VOLT)).x(MILLI(SECOND)).build())
7  .out(new StepIn(test.getSteps().get(4)), XYChart())
8   .add(SeriesDecoratorVisitor()
9    .color("CHANNEL_EYE", OD, RED)
10   .color("CHANNEL_EYE", OS, BLUE).build())
11  .add(LegendVisitor().legendFromProperty("CHANNEL_EYE").alignBottom().build())
12  .add(TitleVisitor().title("Oscillatory Potentials").alignCenter().build())
13  .add(ClipVisitor().x(valueOf(-10, MILLI(SECOND)), valueOf(100, MILLI(SECOND))).build())
14 .show();
```

Listing 6: Using iDSL4SigProc to create a XY chart extracting the oscillatory potentials by using a Chebyshev band-pass filter on a single flash ERG. Before applying the band-pass filter, the single sweeps are grouped by the eye and then averaged. By using several visitors, the resulting chart is formated.

As stated before, we have developed an implementation of the source interface, which allows for importing of recordings directly from the database used by the electrophysiologic recording system. In this section we provide some examples for using the framework to process signals and visualize the results.

The example shown in Listing 6 uses one step of an ERG recording and applies a Chebychev band-pass filter, to extract the oscillatory potentials. An XY-chart is then created, formated, and displayed. Figure 17 shows the result of code in Listing 6.

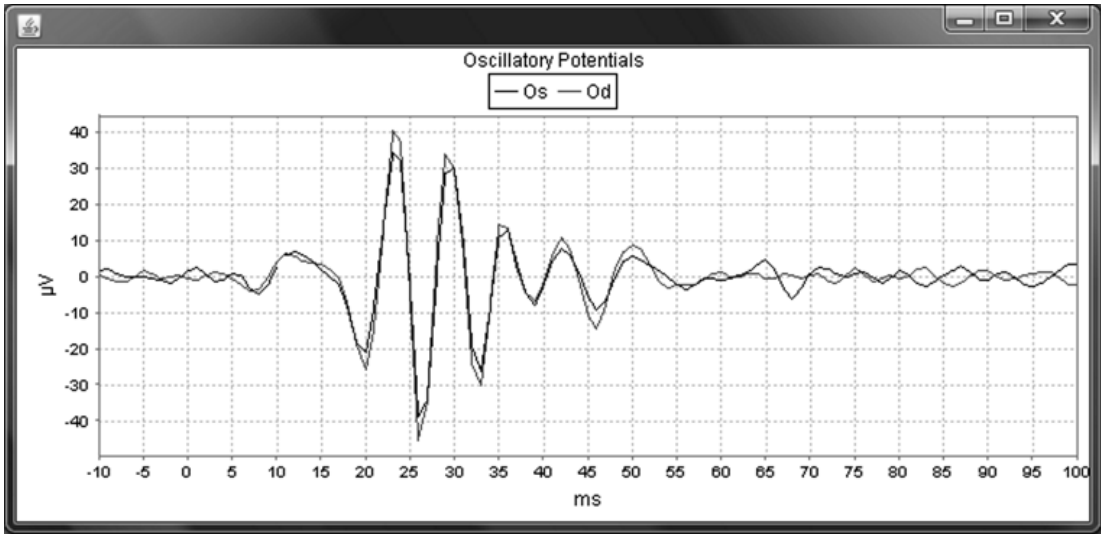

Figure 17: Oscillatory potentials extracted of a single flash ERG recording using a Chebyshev band-pass filter of iDSL4SigProc. The code to create this chart is shown in Listing 6.

A second example (Listing 7) demonstrates the application of the fast fourier transformation filter to an ERG, which used 9 Hz flicker as a stimulus. The code averages all sweeps recorded from the left eye and applies a linear de-trend and interpolates the number of data points to a power of two using spline estimation. Afterwards, the fast fourier transform is applied, in which the new sam-

pling frequency (caused by the interpolation) is specified, and the bar chart shown in Figure 18 is created to present the results.

```
1  new FilterChain()
2      .add(ChannelSelector().include(eye(OS)).build())
3      .add(ArithmeticMeanFilter().build())
4      .add(LinearDetrendFilter().build())
       .add(SplineInterpolationFilter().to(nextPowerOf2()).build())
5      .add(RescaleFilter().x(SECOND).build())
6      .add(FFTFilter().samplingFrequency(valueOf(1153.153, HERTZ)).amplitude().build())
7      .add(RescaleFilter().y(MICRO(VOLT)).build())
8  .out(new StepIn(test.getSteps().get(3)), BarChart())
9      .add(ClipVisitor().x(valueOf(0, HERTZ), valueOf(60, HERTZ)).build())
10 .show();
```

Listing 7: Using iDSL4SigProc to create a bar chart of the frequencies contained in an ERG recording. Before averaging the single sweeps of the recordings, the left eye is selected for analysis. Afterwards, a linear de-trend filter is applied and the number of data points is increased to a power of two by using spline interpolation. Finally, the fast fourier transform filter is applied and the results are presented as a bar chart.

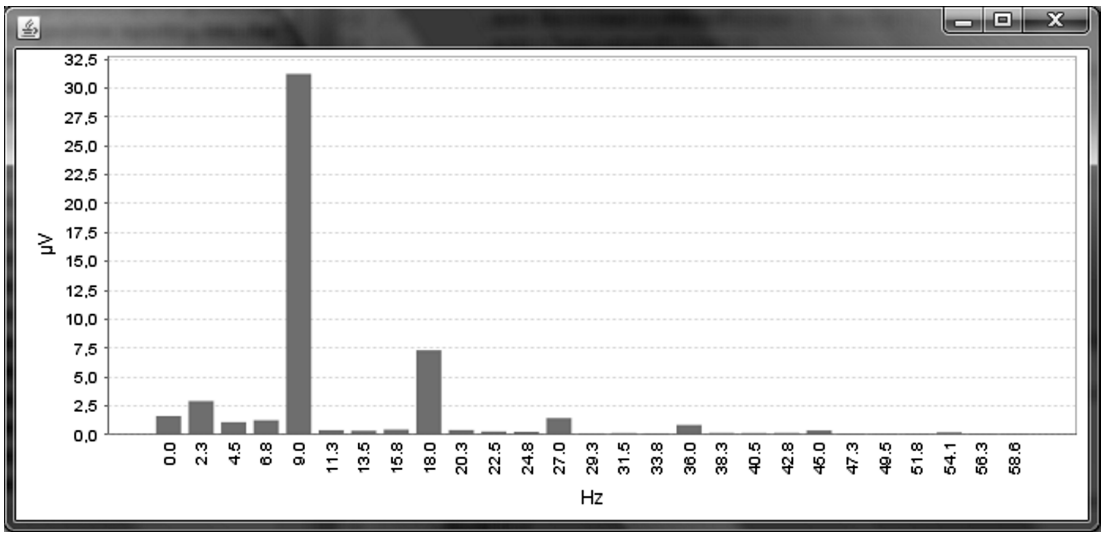

Figure 18: Result of the code shown in Listing 7: The bar chart shows the frequencies contained in an ERG recording, which used a 9 Hz flicker stimulus. The frequencies were calculated using the fast fourier filter of iDSL4SigProc.

3.6 Conclusion

Here we have presented a framework for the post-processing of electrophysiological data. The framework leverages design patterns such as pipes-and-filters and fluent interface. It provides an integrated domains specific language (DSL) allowing for a smooth learning curve and easy integration into existing software. The framework is the foundation of ERG Explorer which is used in the University Eye Hospital Tuebingen in clinical practice and in clinical trials.

4 ERG Explorer

4.1 Introduction

The role of signal processing in visual electrophysiology is of increasing importance. New stimulus paradigms with sophisticated analysis are published every year. However, several distinct communities are involved in clinical electrophysiology: Clinicians need easy to use tools and standardized results of visual electrophysiological examinations, whereas researchers are often using custom developed software for their analysis. Finally, in clinical trials, standardized analysis of a huge number of electrophysiological recordings is required. To cover these different requirements and to increase to become independent of proprietary a new software, the ERG Explorer, was developed.

4.2 Methods

The ERG Explorer was developed using the Java™ programming language, which allows for an independence of platform and operating system. It is based on the Better Swing Application Framework (BSAF)[13] which implements the infrastructure common to most desktop applications, like application life-cycle management, localization and internationalization, session state persistence, and an implementation of the model-view-controller pattern.

ERG Explorer features a plug-in system, which allows to work with visual electrophysiological data from different sources. The plug-in system is based on the Java ServiceLoader API [14]. Currently, three plug-ins are implemented: plug-in for importing electrophysiological recordings from the Espion database (described in section 1.2 of this chapter); a plug-in to read and write visual electro-

13 https://kenai.com/projects/bsaf/pages/Home, last accessed 01.09.2015
14 https://docs.oracle.com/javase/tutorial/ext/basics/spi.html, last accessed 02.09.2015

physiological data in ElVisML format (described in section 4 of chapter IV); a plug-in to a Reading Center software for the exchange of visual electrophysiological data in multi-center clinical trials [48].

Internally, ERG Explorer uses the generic data model for electrophysiological data (described in section 2 of this chapter) for the management of visual electrophysiological data.

Processing of data is done using iDSL4SigProc (section 3 of this chapter) which is in turn based on Apache Commons Math[15] for mathematical computations and JScience[16] for managing quantities together with their units.

Data visualization and charting is implemented using JFreeChart[17], reporting using JasperReports[18].

ERG Explorer is based completely on open source software and leverages many other software frameworks and libraries in addition to those mentioned.

4.3 Results

Basic functionality

ERG Explorer provides the basic functionality for the evaluation of visual electrophysiological data:

- Modification of existing cursors and creation of new cursors
- Auto-placement of cursors using peak-finding based on pre-defined time periods
- Manual removal of single sweeps contaminated with artifacts
- Creating and deleting averages

15 http://commons.apache.org/proper/commons-math, last accessed 02.09.2015
16 http://jscience.org, last accessed 02.09.2015
17 http://www.jfree.org/jfreechart, last accessed 02.09.2015
18 http://community.jaspersoft.com/project/jasperreports-library, last accessed 02.09.2015

- Exporting of amplitudes and implicit times of cursor for single recordings or all recordings based on a protocol as CSV data
- Exporting of waveform data (averages or single sweeps) for single recordings of all recordings based on a specific protocol as CSV data
- Exporting of charts as images for publications

Figure 19 depicts the main interface of ERG Explorer. The window on the top left provides access to subjects and recordings stored in the Espion database. The window on the bottom left shows single sweep data of an electroretinogram; single sweeps can be selected and excluded from the average. The window on the center shows the manual modification of a cursor representing the a-wave of an electroretinogram.

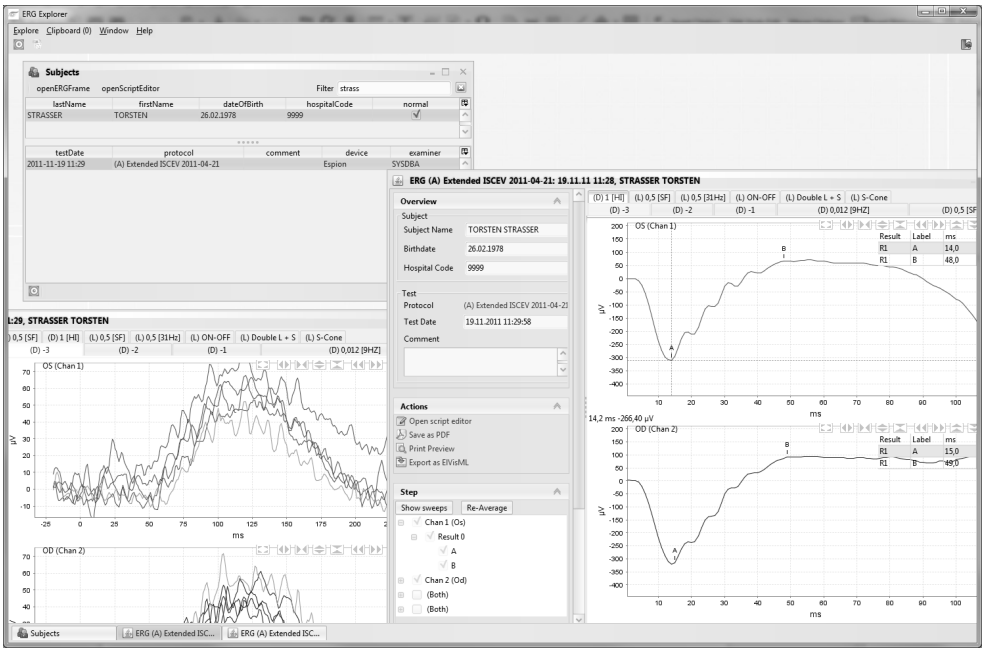

Figure 19: ERG Explorer provides native access to electrophysiological recordings stored in the Espion database. Basic functionality like setting cursors and creating averages of single sweeps is supported.

Peak-Finding

Beside a basic peak-finding based on pre-defined time periods, ERG Explorer implements two different automated peak-finding algorithms:

- Jacobson et al.: Auto-Threshold Peak Detection In Physiological Signals [49]
- Scholkmann et al.: An efficient algorithm for automatic peak detection in noisy periodic and quasi-periodic signals [50]

Figure 20 depicts the result of the peak-finding function based on the algorithm of Scholmann et al. [50] at the example of a sweepVEP of the author. Existing cursor definitions are automatically used for naming of the detected peaks and troughs.

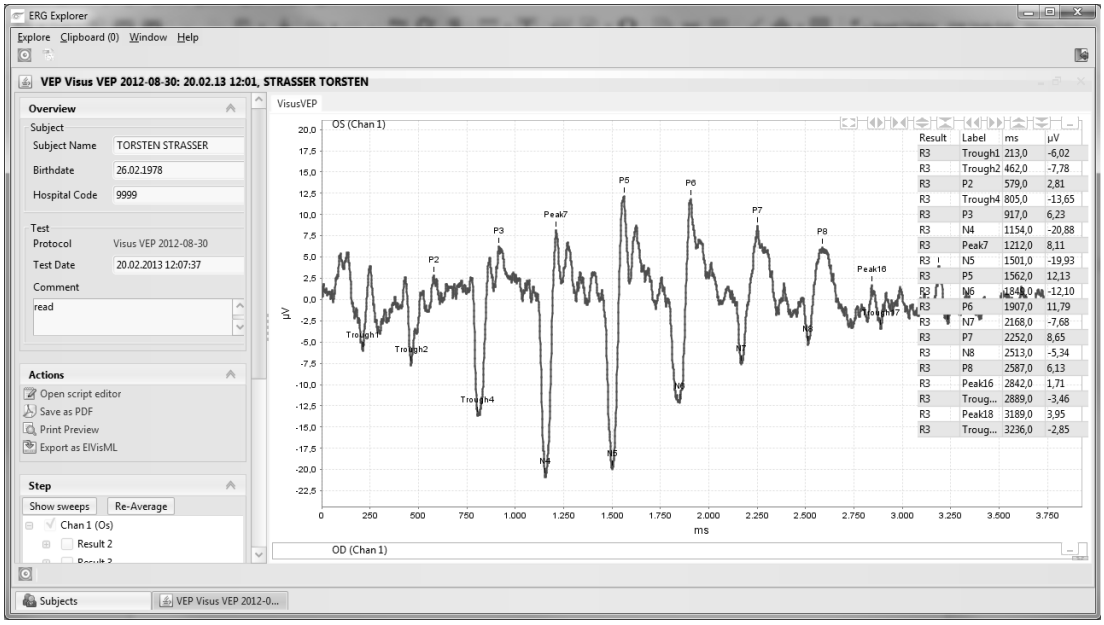

Figure 20: Result of the automated peak-finding function implementing the algorithm of Scholman et al. at the example of a sweepVEP of the author. If the used protocol defines cursors, the function automatically uses the naming of those

Detrending, filtering, and smoothing

ERG Explorer implements function for polynomial detrending (1st - 5th order) and digital filtering using an implementation of a Chebyshev filter (Figure 21).

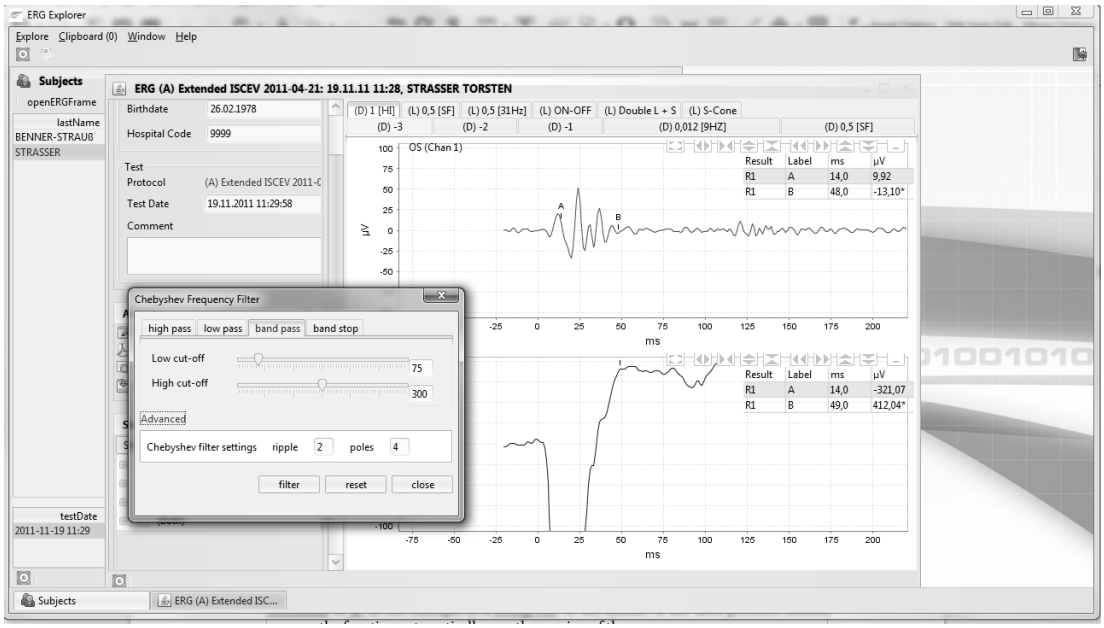

Figure 21: Application of a Chebyshev digital band-pass filter for extracting the oscillatory potentials of an electroretinogram. The filter was applied to the left eye (upper trace).

Detrending and smoothing of data is supported through an implementation of the Savitzky-Golay algorithm [51].

Specialized applications

Fourier analysis of flicker electroretinograms

The Fourier analysis allows for the evaluation of flicker electroretinograms in frequency space. A fast-fourier analysis as well as discrete fourier analysis were implemented in ERG Explorer and for the development of a ERG flicker stimu-

lus paradigm for “non-recordable” electroretinograms, published by Schatz et al. [52].

Intensity-Response curve calculation

A semi-automated estimation of the intensity-response (Naka-Rushton) function [53], [54] was implemented. The Naka-Rushton function allows to model the relationship between the strength of a flash stimulus and the amplitude of the b-wave using a sigmoid model (Equation 1).

$$\mathrm{R}(I) = \frac{R_{max} \cdot I^n}{I^n + K^n} \tag{1}$$

R_{max} is the asymptotic amplitude of the b-wave, K, the semi-saturation constant, is the intensity at which the b-wave amplitude is half of its asymptotic value and n determines the slope of the function at $I = K$ [55].

The implementation uses non-linear least-square optimization provided by Apache Commons Math for the estimation of the parameters of Equation 1. Figure 22 depicts the result of fitting the Naka-Rushton model to b-wave amplitudes in response to the flash strength at the example of an ERG of a rat.

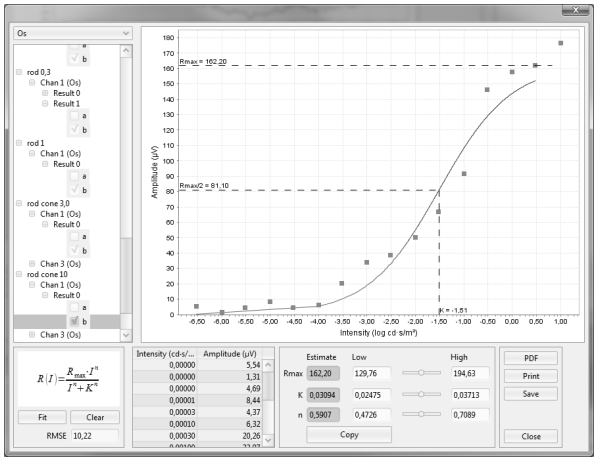

Figure 22: Results of a fit of the Naka-Rushton model to the b-wave amplitudes in response to the flash strength. The values for the parameters R_{max}, K, and n were estimated using non-linear least-square optimization. The data shown was collected during a drug study using rats.

The ERG Explorer was used, amongst other studies, in the study of Zobor et al., which assessed the cannabis-induced persisting perception disorder [56], where K was used as a measure for the retinal sensitivity.

Automated evaluation of the slow oscillations EOG

An automated analysis of the slow oscillations EOG [8] was developed and implemented in ERG Explorer. The analysis uses non-linear least-squares fitting of a model consisting of the sum of sine functions (Equation 2).

$$
\begin{aligned}
|\hat{a}| = \quad & \frac{2}{\pi} \cdot \frac{1}{1} \cdot \sin\left(2\pi 1 f t + \phi_1\right) \\
& \frac{2}{\pi} \cdot + \frac{1}{3} \cdot \sin\left(2\pi 3 f t + \phi_2\right) \\
& \frac{2}{\pi} \cdot + \frac{1}{5} \cdot \sin\left(2\pi 5 f t + \phi_3\right) \\
& \frac{2}{\pi} \cdot + \frac{1}{7} \cdot \sin\left(2\pi 7 f t + \phi_4\right) \\
& \frac{2}{\pi} \cdot + \frac{1}{9} \cdot \sin\left(2\pi 9 f t + \phi_5\right)
\end{aligned}
\tag{2}
$$

The absolute amplitude $\hat{a}$ for each trace of the EOG is estimated and plot versus the recording time. During the dark phase of the EOG, the amplitudes start to decrease until the reach the so called dark trough, whereas during the light phase the amplitudes increase until a so called light peak. Based the estimated amplitudes $\hat{a}$ for each trace two second order polynomial fits are applied for the amplitudes of the dark and the light phase, respectively, and the peak times and amplitudes of the dark trough and the light peak are calculated. Using the dark trough and light peak amplitude, the Arden ratio is calculated, finally.

Results of 52 healthy volunteers obtained using the described method and a manual evaluation of EOG showed no significant differences (Strasser et al. IOVS2015; 462). The calculated norm ranges were comparable to values re-

ported by Entenmann [57]. Interestingly, a similar approach were published independently by Sarossy et al. just recently [58]. Figures 23 and 24 depict the analysis of the slow oscillations EOG using ERG Explorer.

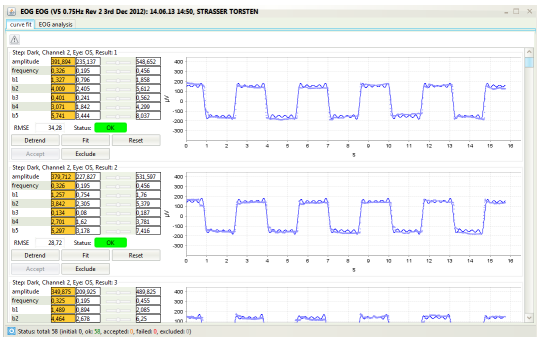

Figure 23: Fitting the sine-based model to the single traces of the slow oscillations EOG.

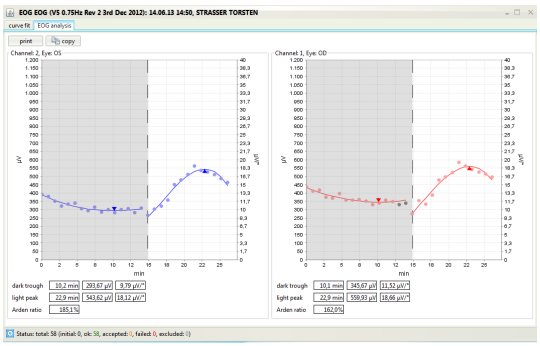

Figure 24: Estimation of the dark trough and light peak amplitudes and peak times using 2nd order polynomials and calculation of the Arden ratio.

Automated evaluation of the fast oscillations EOG

A novel automated analysis of the fast oscillations EOG [57] was developed and implemented in ERG Explorer: the fast oscillations EOG is smoothed using an ADSR (attack, decay, sustain, release) filter, and a sinusoidal model is fit to the resulting waveform using non-linear least-squares regression. Finally, the peak-to-trough ratio was calculated. The results showed significant higher values in comparison to those obtained with the built-in analysis of the Espion software (Strasser et al. IOVS2015; 462). Norm ranges established from 25 healthy volunteers using the novel method were in the same range as values reported by Entenmann previously [57]. Figure 25 depicts the results of the fast oscillations EOG analysis using ERG Explorer.

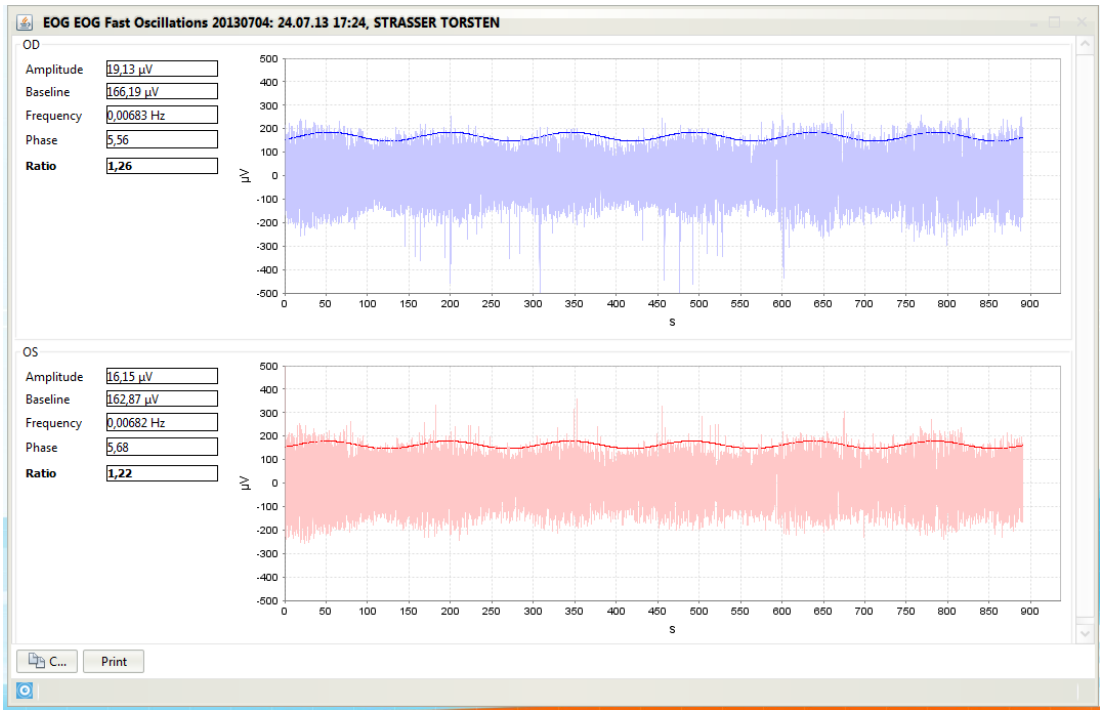

Figure 25: Results of the fast oscillations EOG analysis. The faint colored waveforms represent the raw EOG recording. The strong colored sinusoidal curves represent the result after application of ADSR filter and fitting a 2nd order model.

Reporting

For the clinical routine, reports for common electrophysiological examinations were developed. The reports are created using ERG Explorer and provide a presentation of the results of electrophysiological in a clear and standardized form.

The generation of the reports is based on iDSL4SigProc and the JasperReports library. Using the JasperStudio® (Jaspersoft Corporation, San Francisco, CA, USA)[19], templates for the different reports were defined. Within the XML-based templates, placeholders for charts were defined and iDSL4SigProc code for the chart generation is embedded into the template. During runtime, the JasperReports library uses a data source based on the generic data model for vis-

19 http://community.jaspersoft.com/project/jaspersoft-studio, last accessed 05.09.2015

ual electrophysiological data for filling the template. During this process, the embedded code is executed and the charts are created. In addition to chart generation, it is possible to refer to single data elements included in the generic data model, by using an XPath-like language for querying Java objects, named Commons JXPath[20]. Figure 26 depicts a screenshot of JasperStudio during editing the template for the "Extended ISCEV A" report.

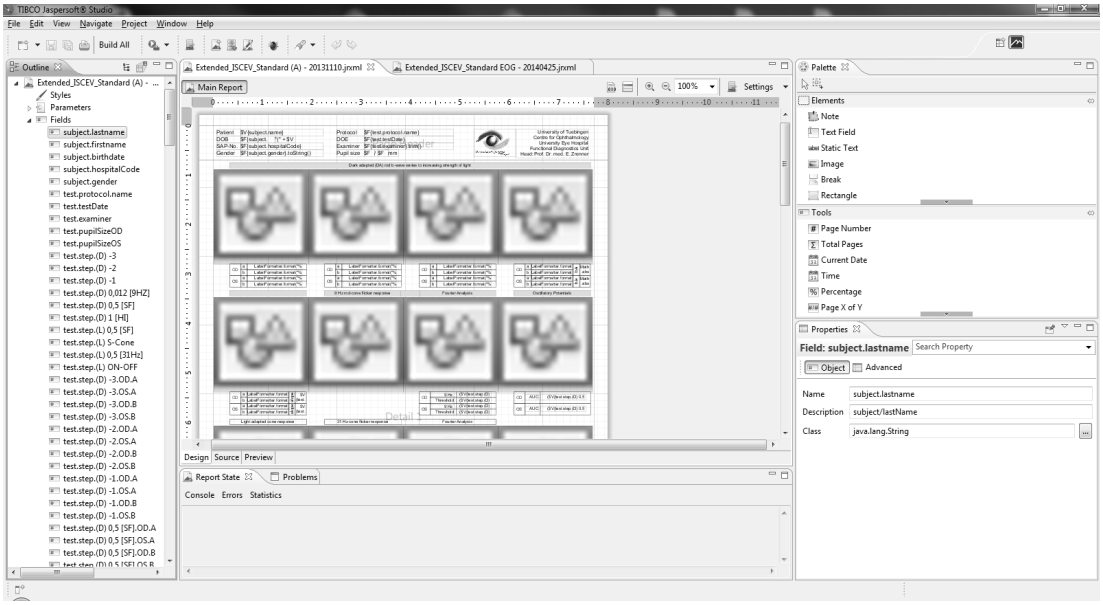

Figure 26: Screenshot of JasperStudio®. In the center, the template including the placeholders for the charts is depicted. At the left hand side, user defined variables are available. A property sheet showing the properties of the selected user defined variable "subject.lastname" is shown in the lower right corner. The XPath expression used to query the generic data model for the subjects lastname is entered in the field "description".

Listing 8 lists example code of a JasperReports template with embedded iDSL4SigProc code for chart generation. A variable named "subject.lastname" is defined in line 6. The XPath expression for querying the lastname of the subject is given in line 7. Lines 29 – 40 contain the placeholder for the chart with the embedded iDSL4SigProc code for the chart generation.

20 https://commons.apache.org/proper/commons-jxpath, last accessed 05.09.2015

```
<?xml version="1.0" encoding="UTF-8"?>
<jasperReport name="Extended_ISCEV_Standard (A) - 20100101" pageWidth="595" pageHeight="842" columnWidth="555" leftMargin="20" rightMargin="20" topMargin="15" bottomMargin="15" >
 <parameter name="IMAGE_SIZE" class="java.lang.Integer" isForPrompting="false">
  <defaultValueExpression><![CDATA[350]]></defaultValueExpression>
 </parameter>
 <field name="subject.lastname" class="java.lang.String">
  <property name="expression" value="subject/lastName"/>
  <fieldDescription><![CDATA[subject/lastName]]></fieldDescription>
 </field>
 <field name="test.step.(D) -3" class="IStep">
  <property name="expression" value="steps[stepDefinition/stepName=&amp;quot;(D) -3&amp;quot;]"/>
  <fieldDescription><![CDATA[steps[stepDefinition/stepName="(D) -3"]]]>
  </fieldDescription>
 </field>
 <pageHeader>
  <band height="50" splitType="Stretch">
   <staticText>
    <reportElement x="5" y="5" width="35" height="10"/>
    <text><![CDATA[Patient]]></text>
   </staticText>
   <textField evaluationTime="Report" isBlankWhenNull="true">
    <reportElement x="40" y="5" width="120" height="10" isPrintWhenDetailOverflows="true"/>
    <textFieldExpression><![CDATA[$V{subject.name}]]></textFieldExpression>
   </textField>
  </band>
 </pageHeader>
 <detail>
  <band height="745" splitType="Stretch">
   <image scaleImage="RetainShape">
    <imageExpression><![CDATA[new FilterChain()
  .add(ChannelSelector().exclude(channelNumbers(2, 3)).build())
  .add(RemovePreTriggerFilter().build())
  .add(RescaleFilter().x(SI.MILLI(SI.SECOND)).y(SI.MICRO(SI.VOLT)).build())
  .source(source($F{test.step.(D) -3}))
 .out(XYChart())
  .add(MarkerVisitor().build())
  .add(ClipVisitor().y(Amount.valueOf(-400, SI.MICRO(SI.VOLT)), Amount.valueOf(500, SI.MICRO(SI.VOLT))).build())
```

```
38  .add(SeriesDecoratorVisitor().color("CHANNEL_EYE", Eye.OD,
    Color.RED).color("CHANNEL_EYE", Eye.OS, Color.BLUE).build())
39 .render($P{IMAGE_SIZE}, $P{IMAGE_SIZE})]]></imageExpression>
40   </image>
41  </band> </detail>
42 </jasperReport>
```

Listing 8: Example of a JasperReports template using embedded iDSL4SigProc code for chart generation

On the following pages, the reports used in the clinical routine are presented: Figure 27 shows the report for the Extended ISCEV A protocol, which represents an electroretinogram including scotopic and photopic stimuli. The first row of the report shows ERG responses of the dark adapted retina to stimuli of light of increasing strength. Underneath the charts, values for amplitudes and implicit times of a- and b-wave are listed. Additional tests comprise ERG flicker responses (scotopic 9 Hz and photopic 30 Hz), oscillatory potentials, an On-Off response to a long duration stimulus and an s-cone specific stimulus using a blue flash on red background. For the two flicker responses, the results of a fourier analyses are shown in polar charts: the length of the arrows represent the amplitude of the harmonic frequency corresponding to the flicker frequency, whereas the angle of the arrow indicates the phase shift of the flicker response. Norm ranges are indicated by green rectangles or segments, respectively.

Figure 28 shows a similar report of the ISCEV A protocol used by the Visual Neurophysiology Service of the Wilmer Eye Institute at the Johns Hopkins.

Figures 29 and 30 show the reports for a pattern reversal VEP using two check-sizes and for a slow oscillations electrooculogram, respectively. Green rectangles indicate norm ranges.

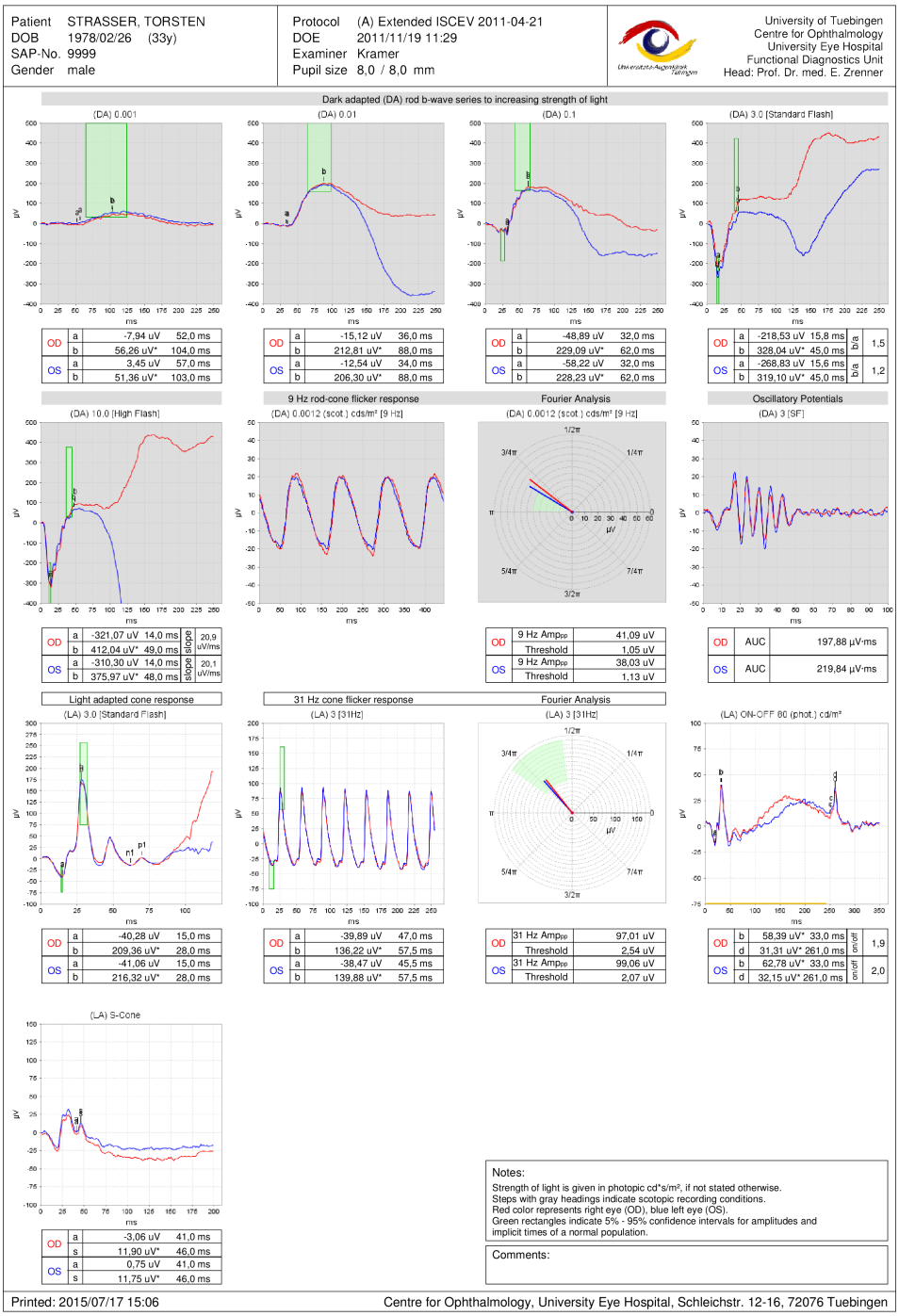

Figure 27: Report for the Extended ISCEV A protocol used at the Eye Hospital Tuebingen

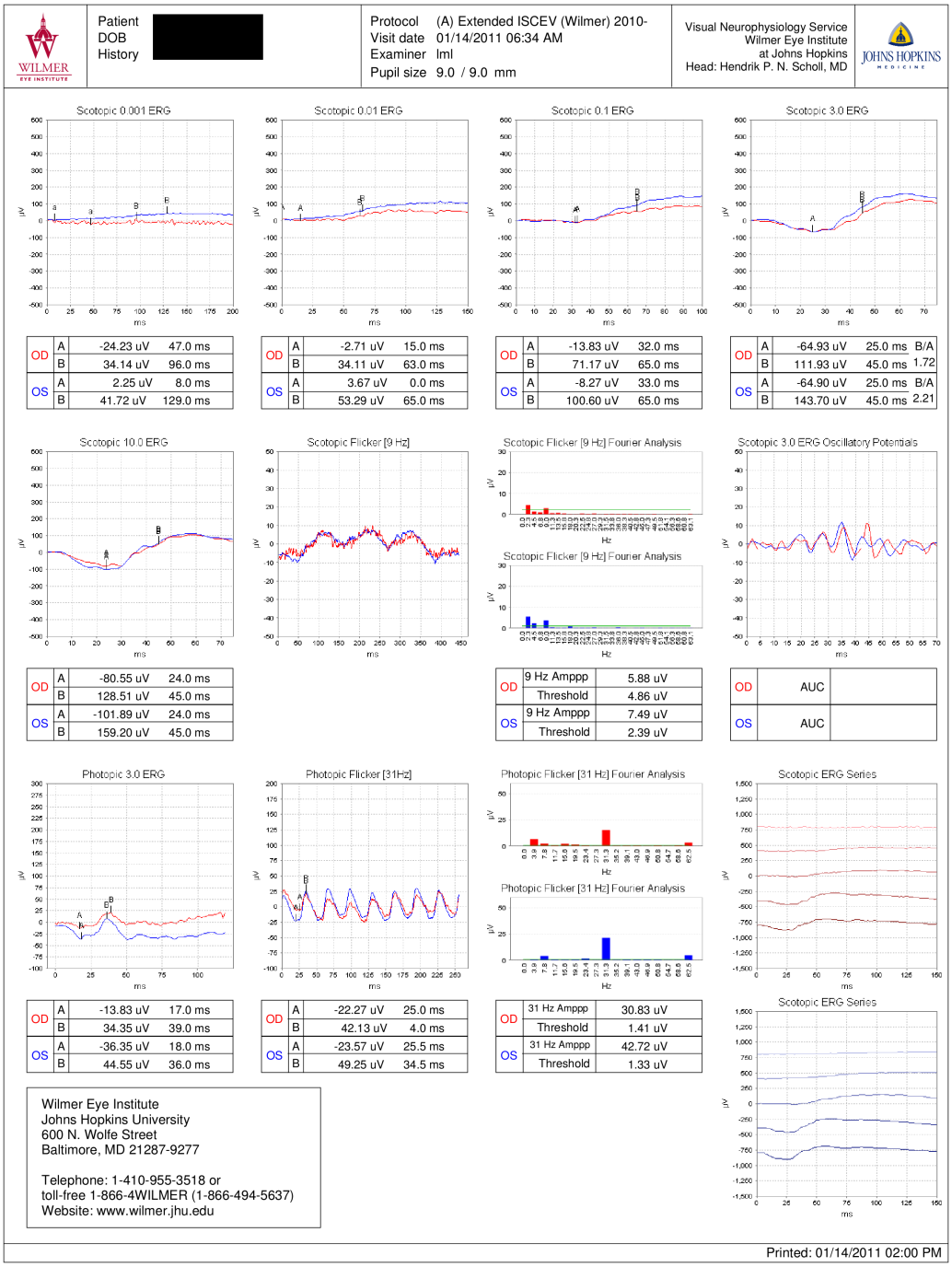

OD	A	-24.23 uV	47.0 ms	
	B	34.14 uV	96.0 ms	
OS	A	2.25 uV	8.0 ms	
	B	41.72 uV	129.0 ms	

OD	A	-2.71 uV	15.0 ms	
	B	34.11 uV	63.0 ms	
OS	A	3.67 uV	0.0 ms	
	B	53.29 uV	65.0 ms	

OD	A	-13.83 uV	32.0 ms	
	B	71.17 uV	65.0 ms	
OS	A	-8.27 uV	33.0 ms	
	B	100.60 uV	65.0 ms	

OD	A	-64.93 uV	25.0 ms	B/A
	B	111.93 uV	45.0 ms	1.72
OS	A	-64.90 uV	25.0 ms	B/A
	B	143.70 uV	45.0 ms	2.21

OD	A	-80.55 uV	24.0 ms	
	B	128.51 uV	45.0 ms	
OS	A	-101.89 uV	24.0 ms	
	B	159.20 uV	45.0 ms	

OD	9 Hz Amppp	5.88 uV
	Threshold	4.86 uV
OS	9 Hz Amppp	7.49 uV
	Threshold	2.39 uV

OD	AUC	
OS	AUC	

OD	A	-13.83 uV	17.0 ms	
	B	34.35 uV	39.0 ms	
OS	A	-36.35 uV	18.0 ms	
	B	44.55 uV	36.0 ms	

OD	A	-22.27 uV	25.0 ms	
	B	42.13 uV	4.0 ms	
OS	A	-23.57 uV	25.5 ms	
	B	49.25 uV	34.5 ms	

OD	31 Hz Amppp	30.83 uV
	Threshold	1.41 uV
OS	31 Hz Amppp	42.72 uV
	Threshold	1.33 uV

Figure 28: Report for the Extended ISCEV A protocol used at the Wilmer Eye Institute

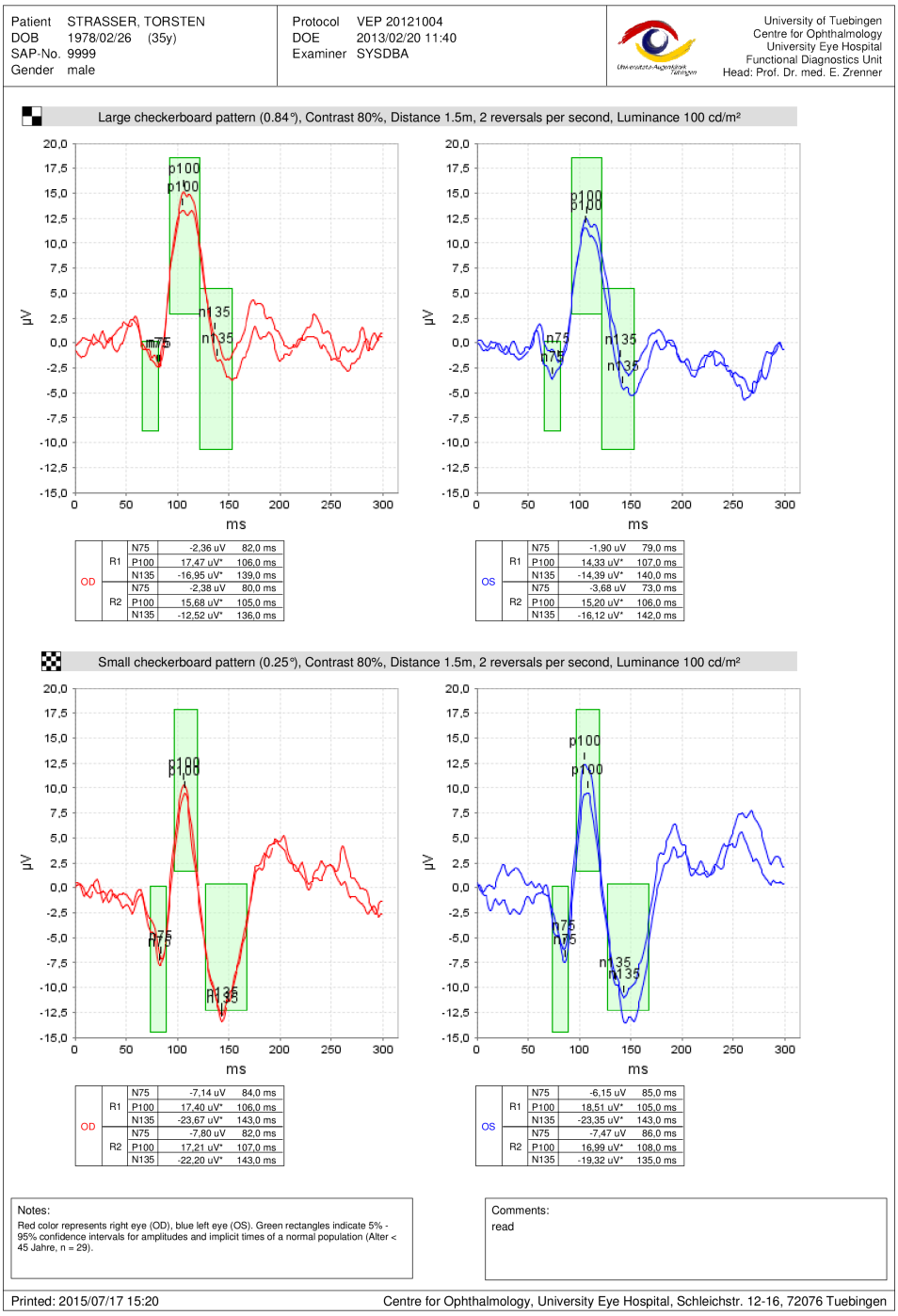

Figure 29: Report of a pattern reversal VEP using two check sizes

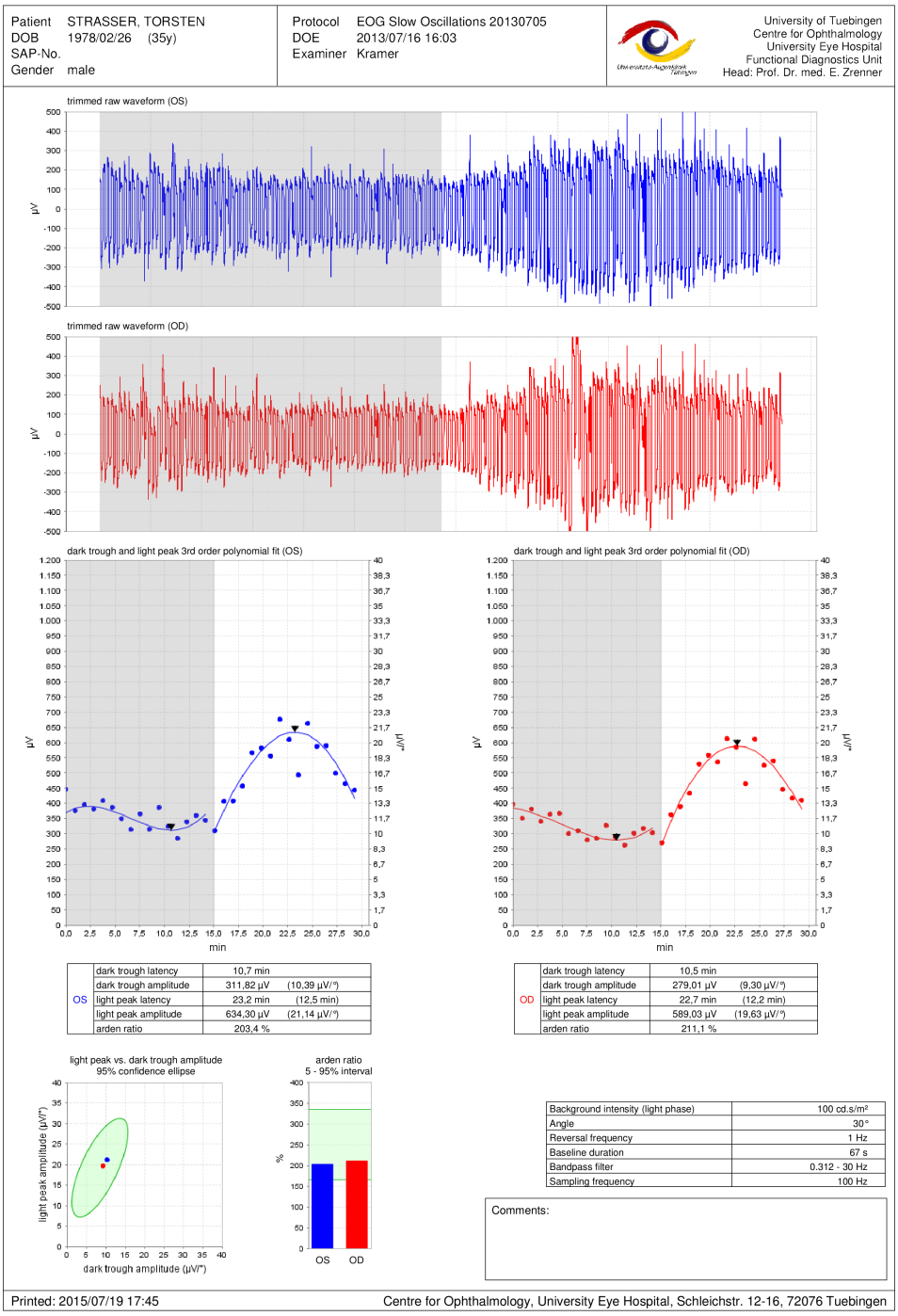

Figure 30: Report of the results of a slow oscillations electrooculogram

4.4 Conclusions

The ERG Explorer has been in use for several years in the clinical routine of the University Eye Hospital Tuebingen and the Wilmer Eye Institute at John Hopkins University. The developed standardized reports help the clinicians to reliably interpret the results of visual electrophysiological recordings.

The ERG Explorer was also successfully used in a number of studies [52], [56], including a multi-center clinical trial [48].

Because of its independence of proprietary software, the ERG Explorer allows for a rapid implementation of new analysis strategies and helps therefore in the translation of new methodologies from research into clinical routine.

IV STORAGE AND EXCHANGE OF VISUAL ELECTROPHYSIOLOGICAL DATA

1 The need for standardization

Since the results of visual electrophysiological examinations strongly depend on the acquisition settings and the stimulus parameters, it is important to use commonly accepted standards for the recordings, to allow meaningful comparison of results. The International Society of Clinical Electrophysiology of Vision (ISCEV), publishes standards and recommendations [59], [60], [8], [61], [14], for performing visual electrophysiological examinations; manufacturers of equipment for visual electrophysiology are supposed to incorporate those standards in their designs. However, up to now, no common standard exists for the exchange or storage of visual electrophysiological data. Information about acquisition settings and stimulus parameters are essential for a reliable interpretation of examination results. Therefore, these have to be stored along with the actual recordings. Up to now, completeness of storage relies on proprietary software solutions of the manufacturer of electrophysiological equipment.

It is to be expected, due to decreasing costs and improving capabilities of electro-physiological equipment, that the amount of data created in visual electrophysiology will increase in future. New developments try to incorporate functional data, gathered using electrophysiology, with structural information, originating from imaging technologies to gain more information about the information processing in the visual pathway and the brain [62], [63]. With the advent of gene therapies for hereditary eye diseases [64]–[66] and the improvements of retinal prosthesis [67]–[69], there is an increasing need for identification and recruitment of patient cohorts for these therapies, as well as for adequate functional efficacy endpoints for evaluation of their success. Further, it is a pre-requisite of any new treatment option, whether it be pharmacological,

gene therapy, cell-replacement therapy, etc. that the procedure is safe, and safety is demonstrated and evaluated objectively by electrophysiology.

Electrophysiology has an extensive diagnostic role in visual system disease as it can separate objectively the function of different cell types and layers within the retina; it can distinguish between localized loss of function and generalized dysfunction; it is increasingly used in the objective monitoring of treatment efficacy in inflammatory retinopathies; it has a privileged role in the investigation of pediatric patients with possible visual pathway problems where the patient may be unable to report their symptoms; and in the demonstration of abnormal intracranial visual pathway function. Many diseases have distinctive diagnostic signatures enabling accurate diagnosis when placed in a clinical context; in a few disorders, the ERG alone is pathognomonic.

Electrophysiology is also employed in drug development, both in preclinical and clinical trials, and in toxicity studies for safety and toxicity assessment.

However, access to visual electrophysiological data is often restricted to the performing lab and stored in proprietary data formats. When results are published, data are condensed to only a few parameters.

Especially in terms of long time archiving, this raises a major problem: A recent study has shown, that the availability of research data of published papers declines by 17 % per year [70]. Obviously, this is even worse with unpublished research.

2 Survey on existing data formats

Before considering a new standard data format it is advisable to review existing standards, wether they match the requirements and if not, investigate if it is possible to extend them.

Therefore, a survey on existing data formats for storage and exchange of electrophysiological data was conducted.

2.1 Data formats selected for comparison

Six data formats were selected as possible candidates for encoding visual electrophysiological data and evaluated according to the aforementioned criteria. The remaining formats listed by Schlögl [71] were not taken into consideration because of the lack of support by the electrophysiological community. The five selected formats are described briefly in the following:

- *The European Data Format plus (EDF+)* is a successor of the European Data Format (EDF) [72], which aims to overcome limitations in the original format. EDF was designed as a simple and flexible format for the exchange and storage of multichannel biological and physical signals.
- *The General Data Format (GDF)* [73] claims to incorporate the best features of other biomedical data formats and to try to avoid their limitations. It is mostly compatible with EDF and EDF+. Version v2.20 adds features like demographic information and optimizes data encoding.
- In 1993 the *DICOM* standard was extended by the *Supplement 30 "Waveform Interchange"* [74]. At present, the standard only supports a limited number of signals like the electrocardiogram, electroencephalogram and others. In order to support further modalities, new Information Object Definition (IOD) have to be implemented.
- *HL7* is the standard for electronic exchange of historical and administrative data in health services worldwide [75]. With the version 3.0 of the HL7 messaging standard, the standard switched from the previous binary format to an XML-based format. Part of this version is "HL7 annotated ECG" (aECG) [76].

Its main goal is the submission of biological data collected during clinical trials in an accurate and consistent way.

- *ecgML* is an XML-based data format for the exchange and storage of electrocardiographic data [75]. It is thus similar to the aforementioned HL7 aECG. However, ecgML focuses mainly on representing, exchanging and mining of ECG data.
- *XDF* aims to be a general purpose XML-based data format for multi-channel time series data [77]. Meta-information is stored as XML, whereas the actual time-series data are stored as chunks of binary data. It should not be confused with the equally named format developed by NASA.

2.2 Criteria for comparison

The data formats taken into consideration were compared based on the requirements for biomedical data formats described by Varri et. al. [78] and a set of criteria defined by Schlögl [71], which was extended by the following criteria to match the characteristics of visual electrophysiology and the requirements of modern software development:

- Platform and application independence

  Modern IT infrastructure is heterogeneous, therefore the data format should be independent of hardware and operating system.
- Unicode support

  In contrast to ASCII-based formats, using Unicode insures interoperability, portability, and multilingualism. This extends application life and broadens integration possibilities [79]. The Unicode Standard [80] is platform and vendor independent and has widespread industry support.
- Internationalization

  Internationalization comprises means of representing data with respect to

different languages, countries, or regions. Amongst others, this includes the formatting of currencies, dates and times (in respect to time zones), and numbers (e. g. decimal delimiters).

- Extensibility and versioning

  To address future needs, the data format must be extensible and provide a versioning scheme to maintain compatibility to data encoded with previous versions.

- Simple and self-descriptive

  The data format should be simple and self-descriptive in order to be easy to read and understand, even without special software. Long-term archiving is realized easier using self-descriptive data formats.

- Support for stimulus definitions

  In contrast to other electrophysiological examinations, in visual electrophysiology it is crucial to have detailed information about the stimuli used to elicit the recorded signals.

2.3 Results

None of the data formats taken into consideration could match all the previously described criteria, as Table 4 illustrates. No data format provides support for storing stimulus definitions; this is because the original focus of most formats on ECG, which does not require external stimuli.

DICOM and XDF provide means to extend the data format in order to include custom data like stimulus definitions, however, such an extension would be proprietary.

The survey showed a trend to leverage XML for new data formats and even for reworking existing formats into XML. This is understandable, taking into

account the support of features like Unicode support, internationalization, and platform independence, which XML provides inherently.

Table 4: Comparison of different data formats for electrophysiological data for their adherence to requirements for visual electrophysiology (adapted from [71])

	Format					
Selection criteria	EDF+	GDF	DICOM	HL7 aECG	ecgML	XDF
Multiple sampling rates	○[1]	✓	✓	✓	✓	✓
Multiple datatypes	✓	✓	○	✓	✓	✓
Physical units	✓	✓	✓	✓	✓	×
Events, annotations	✓	✓	✓	✓	✓	✓
Demographic information	○	○	✓	✓	✓	✓
Random access, streaming	✓	✓	×	○	○	○
Sensor positions	✓	✓	✓	✓	✓	✓
Single file	○[2]	○[2]	✓	✓	✓	✓
Vendor independence	✓	✓	✓	✓	✓	✓
Platform & application independent	○[3]	○[3]	○[3]	×[3]	×[3]	✓[3]
Unicode support	○[4]	×	✓	✓	✓	✓
Internationalization	×	×	×	✓	✓	✓
Extensibility / versioning	○[5]	○[5]	✓	✓	○	○[9]
Simple & self-descriptive	○[6]	○[6]	×	○[8]	✓	✓
Support for stimulus definitions	×	×	○[7]	×	×	○[9]

Adheres to requirements: completely (✓), partly (○), not (×)
[1]The sampling frequency is derived from the duration and the number of samples, whereas the duration should be a whole number of seconds; [2]Only one recording of one patient; [3]Mostly/only used for EEG and ECG; [4]Unicode is allowed only in annotations; [5]It is possible to define custom fields; [6]Only the header is human readable, the actual recorded data are binary encoded; [7]Storing of stimulus information is currently not supported. However, extension is possible; [8]Theoretically human readable, but overwhelming complex; [9]The format is based on XML, however its specification defines only a basic structure

In the following, the data formats evaluated will be described briefly for their adherence to the criteria used for comparison.

Despite the simple structure EDF+ as well as GDF, which makes them easy to implement, their extensibility is only limited. Both target mainly electrocardiography. EDF+ and GDF are binary formats, i. e. special software is required to

access data encoded in these formats. Furthermore, both formats lack the support of Unicode and internationalization.

DICOM is the probably the most accepted standard in medical imaging domain and medical informatics and is backed by a strong standardization organization, the National Electrical Manufacturers Association (NEMA). DICOM not only defines a data format, but also a complete infrastructure for implementing electronic health-care networks. Like EDF and GDF, DICOM is a binary format. It has a well-defined process for extending the format, but the process of certification of extensions is laborious.

HL7 annotated ECG and ecgML are both data formats based on the Extensible Markup Language (XML) and thus already fulfilling many of the criteria described above, like Unicode support, internationalization, vendor and platform independence, as well as human readability. However, both are focused on electrocardiography and not applicable for encoding visual electrophysiological recordings.

XDF, like HL7 annotated ECG and ecgML, is XML-based. However, it does not fully comply to the XML standard, as it stores time-series data as binary encoded chunks within the file. Therefore, it is not possible to open or edit data with common APIs or editors. XDF aims for easy extensibility by simply extending the XML part of the file. However, no specification beside the documentation in a wiki on the website is available, especially, there is no formal specification in a meta-language like DTD or XSD exists. Even if there is a plug in for the popular EEGLAB[21] software and MATLAB, XDF seems to be not widely used.

21 http://sccn.ucsd.edu/eeglab, last accessed 01.07.2015

2.4 Conclusions

None of the evaluated data formats matched all the requirements for encoding of visual electrophysiology recordings and therefore, is adequate to be applied in this particular field. Therefore, we decided to follow two different approaches, which are described in the rest of this chapter: First, we describe the extension of the DICOM supplement 30 “Waveform interchange” with a prototypic implementation, and second, a newly developed, XML-based data format for visual electrophysiology is detailed and several application examples of tis use are presented.

3 Integration of visual electrophysiological data with an open source DICOM viewer

This text was published in the conference proceedings of the IADIS International Conference e-Health in 2010: T. Strasser, M. Brenner, S. Hell, U. Oezleyen, U. Wiedemann, and M. Schmitz, "Integration of electrophysiological data of vision in an open source DICOM viewer," Proc. IADIS Int. Conf. e-Health 2010, pp. 279–282, 2010.

3.1 Introduction

Digital imaging and communications in medicine (DICOM) is a widely acknowledged standard in medical imaging and medical informatics. It provides the software interface and communication protocol for interchange of diagnostic and therapeutic information, images, and associated data of any kind. Medical devices with DICOM interfaces can be connected to share images and other information.

Since its introduction, the standard has continuously evolved to support new modalities and services. With supplement 30 "Waveform Interchange" [74], DICOM allows the interchange of waveform data, typically used for electroencephalograms or electrocardiograms.

In visual electrophysiology storage of data and its exchange is mostly based on the proprietary protocols of device vendors. In a previous project, software for vendor independent exchange of visual electrophysiology data based on DICOM was developed [81]. In the present project, an existing open-source DICOM viewer is extended to enable the display and analysis of data produced by vendor-independent software.

3.2 Digital Imaging and Communications in Medicine

The DICOM standard is managed by the Medical Imaging & Technology Alliance (MITA)[22], a division of the Association of Electrical and Medical Imaging Equipment Manufacturers (NEMA)[23]. Several working groups (21 as of February 2010) continuously evolve the standard to meet new requirements.

The current standard consists of 19 individual parts including the general structure (part 1), available information object definitions (IODs) (part 3), services class specifications (part 4), data structures and encoding (parts 5 & 6) and message exchange, network communication, and storage formats (parts 7, 8, 10 – 12). Additionally, there are several parts available which specify security and management issues and specific use cases [82]. For interoperability reasons, one of the most important parts is part 2: conformance, which defines rules that must be followed by device manufacturers and software developers to be compliant to the DICOM standard. Figure 31 shows the major sections of the DICOM specifications and their relationships.

Proposals for an extension of the DICOM standard, i. e. to integrate new modalities, are first added as supplements to the standard by one of the working groups and later reviewed by working group 6 (“base standard”) and eventually submitted for approval to the DICOM Voting Members.

22 http://www.medicalimaging.org, last accessed 08.07.2015
23 http://www.nema.org/pages/default.aspx, last accessed 08.07.2015

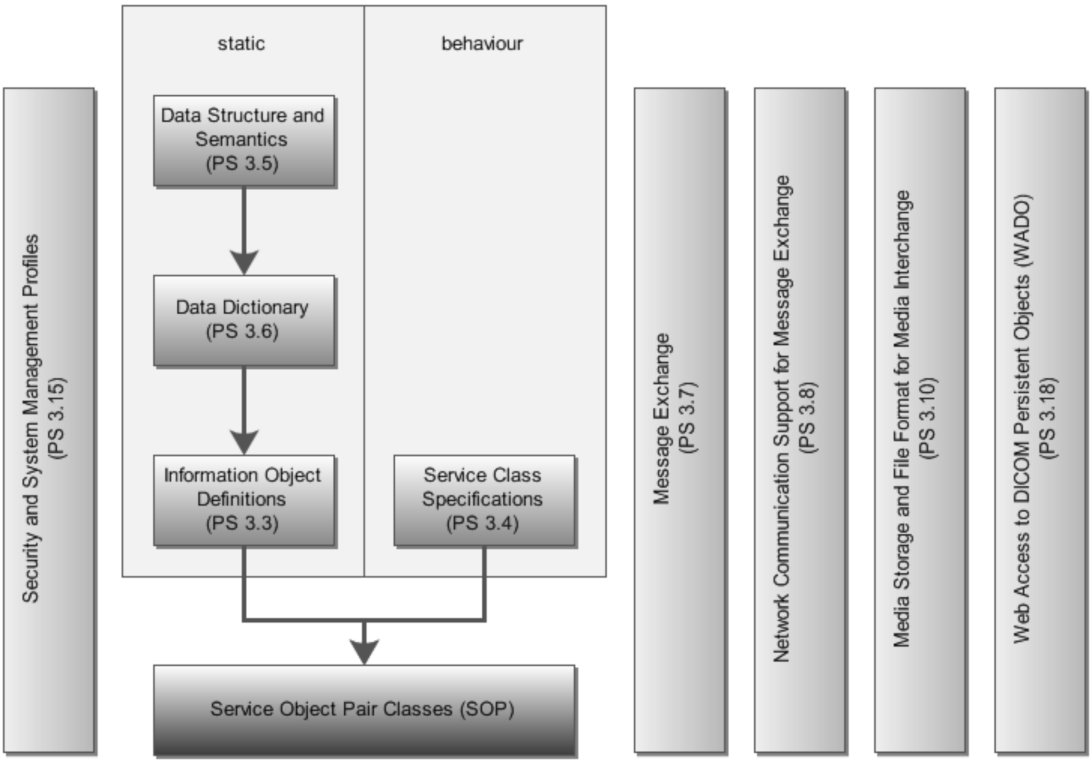

Figure 31: Major sections of the DICOM specifications and their relationships. PS 3.3 (Information Object Definitions), which defines data entities like the Patient IOD, is based on PS 3.6 (Data Dictionary) and PS 3.5 (Data Structure and Semantics), which specify reusable data structures and data types, respectively. Service Object Pair Classes (SOP) define a concrete interaction between a Service Class Provider (SCP) and Service Class User (SCU), which are defined by PS 3.4 (Service Class Specifications), involving a specific information object (IOD). The data exchange between an SCP and an SCU leverages accompanying services specified by DICOM. Amongst others, these are: PS 3.7 (Message Exchange), PS 3.8 (Network Communication Support), and PS 3.15 (Security and System Management Profiles).

The DICOM information model

The DICOM information model (Figure 32) follows the object-oriented paradigm. It includes information object definitions (IODs), that describe the type of data (e. g. patient demographics or examinations like CT, MRI), and service

classes, that specify operations available on each information object, i. e. query/retrieve, store, and print.

An information object definition is composed of data elements defined in the data dictionary (part 6) as shown in Figure 33.

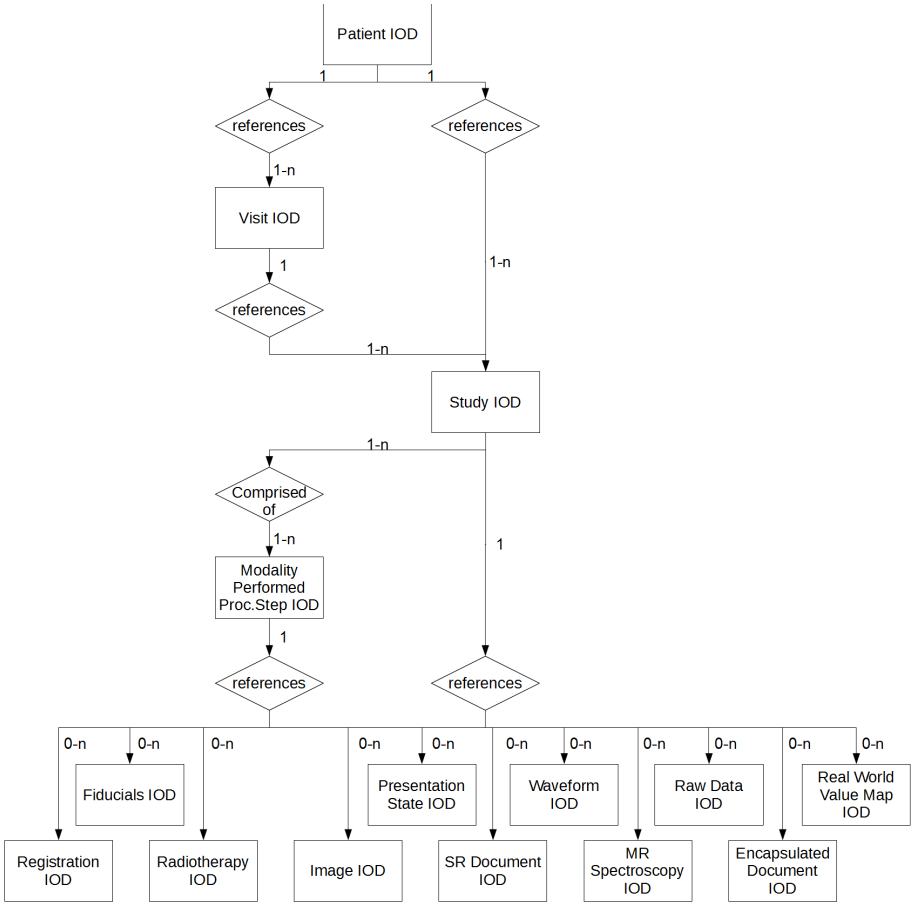

Figure 32: The DICOM information model. Information object definitions (IODs) are used to model real world scenarios (adapted from [348]).

Examples of data elements are shown Table 5. Each data element denotes a reusable piece of information and has a specific data type, called value representation (VR), defined in part 3 of the DICOM standard. Some of the available data types are listed in Table 6.

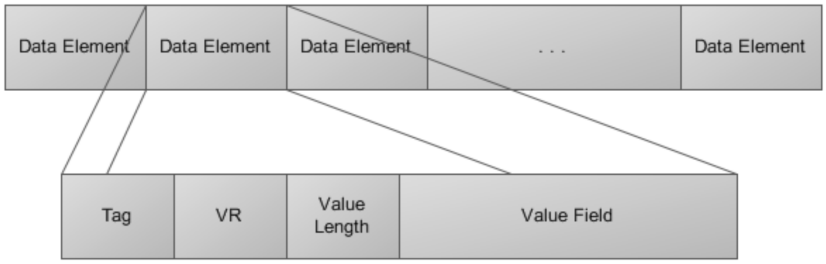

Figure 33: Structure of the Information Object Definition (IOD). An IOD is an object-oriented abstract data model to represent real-world objects built of of data elements holding the actual data.

Table 5: Examples of reusable data elements defined by the data dictionary in part 6 of the DICOM standard

Name	Tag	VR	VM
Patient's Name	(0010,0010)	PN	1
Patient ID	(0010,0020)	LO	1
Patient's Birth Date	(0010,0030)	DA	1
Patient's Sex	(0010,0040)	CS	1

Table 6: Examples of value representations (VR, data types) defined in part 6 of the DICOM standard.

VR	Description
CS	Code String
DA	Date
PN	Person Name
OB	Other Byte

Figure 34 depicts the major structures of the DICOM information model: A service object pair (SOP) is defined as the combination of a specific service class and an information object definition. Examples are “retrieve MRT examination“, or “print X-ray image”. SOPs can be grouped into classes, which make up an individual service class specification [83].

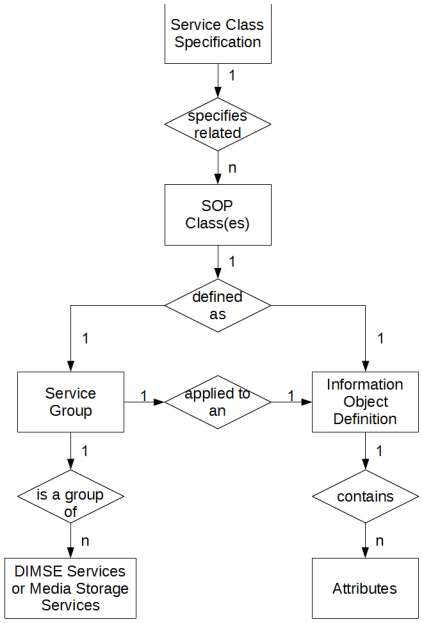

Figure 34: The Service Class Specification and the Information Object Definitions comprise the major structures of the DICOM information model. Service Object Classes define the participants and a specific action of an interaction, whereas Information Object Definitions exchanged data (adapted from [348]).

3.3 Extending the DICOM information model

Since the introduction of supplement 30 ("Waveform Interchange"), which became part of the standard in 2000, DICOM supports IODs for integrating waveform data into DICOM. This includes electrophysiological data like electrocardiograms (ECGs) and electroencephalograms (EEGs) as well as hemodynamic curve data, such as pressure flow signals [84]. At present, however, there is no IOD available to encode visual electrophysiological data in DICOM.

DICOM provides an extension mechanism by defining new IODs based on existing or even new data elements. In a previous project, we introduced a new IOD for storing electroretinogram data in DICOM and developed software for the integration of ERG devices into a clinical DICOM network.

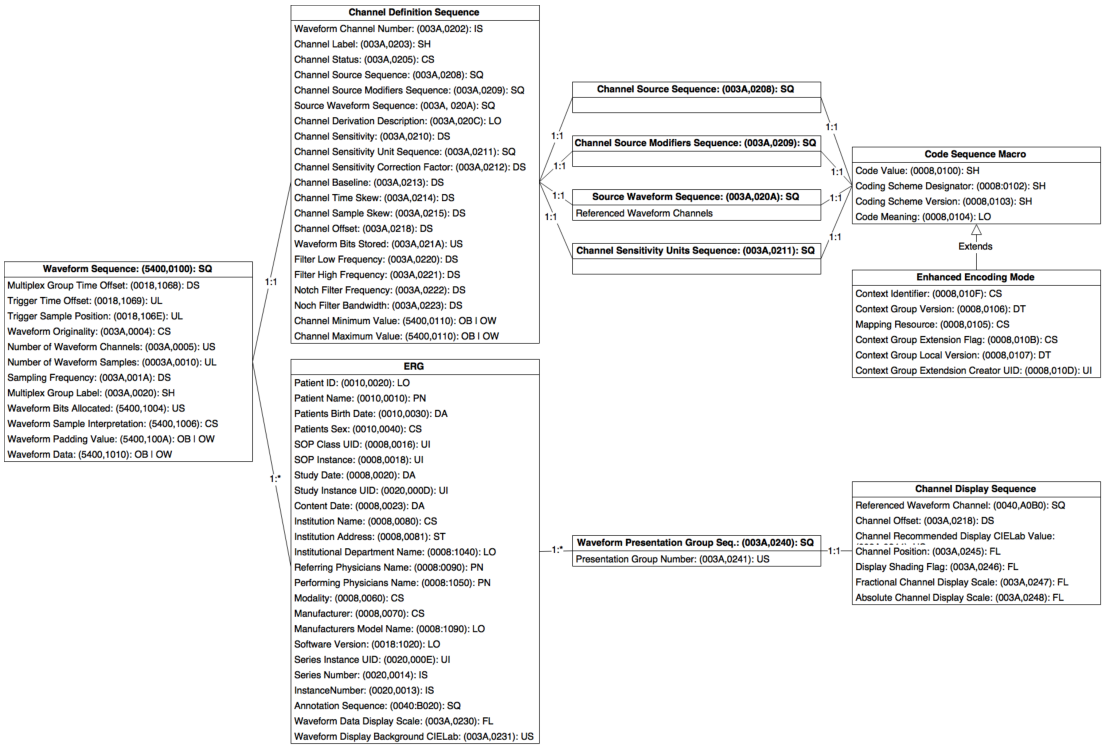

Figure 35: Entity-relationship diagram of the main parts of the new ERG IOD. It uses as many as possible existing value representations (VR) from the dictionary. However, some new value representations have to be introduced in respect to the specifics of visual electrophysiology.

In contrast to the existing IODs used for ECGs or EEGs, electroretinogram recordings not only contain the actual data but also incorporate recording specific stimulus parameters like flash intensity or flash duration. These requirements were taken into account during the development of the ERG IOD, where existing data elements were extended with new data types and even new data elements were created. Figure 35 depicts an entity-relationship diagram of the new ERG IOD.

For testing the new IOD we developed software based on the Pixelmed JAVA DICOM Toolkit[24]. The prototype implements a service class user (SCU) for the

24 http://www.pixelmed.com/#PixelMedJavaDICOMToolkit, last accessed 08.07.2015

ERG IOD and could be successfully used for storing ERG recordings in the open-source Picture and Archiving and Communication Systems (PACS) DCM4CHE[25] with DICOM interface [85].

3.4 Integration of the ERG IOD with an existing DICOM viewer

Since the developed ERG IOD is not part of the DICOM standard, it is not supported by software currently available for working with DICOM. Therefore, we extended the existing open-source Tudor DICOM Viewer[26], enabling it to to present and modify waveform information created during electroretinography. The Tudor DICOM Viewer is a simple but useful DICOM viewing application and is part of the Tudor DICOM Tools, a library written in Java that supports high-level DICOM operations. It not only provides means for displaying DICOM data but also implements features like store and send functionalities for communications with PACS equipment.

The Tudor DICOM Viewer leverages ImageJ[27] is a freely available image processing and analysis library for reading DICOM data [86]. This plug-in parses DICOM data and produces an image object which is then displayed in a frame of the Tudor DICOM Viewer. The plug-in was extended to accept DICOM data containing our new ERG IOD and to produce image data using the iDSL4SigProc library (see also chapter Fehler: Referenz nicht gefunden, 3), which are shown inside the Tudor DICOM viewer.

As well as testing with the open-souce Tudor DICOM Viewer, the ERG IOD was also tested with the LEADTOOLS DICOM Waveform SDK[28], a commercial

25 http://www.dcm4che.org, last accessed 08.07.2015
26 http://santec.tudor.lu/project/optimage/dicom/start, last accessed 08.07.2015
27 http://imagej.nih.gov/ij, last accessed 08.07.2015
28 https://www.leadtools.com/sdk/medical/dicom-waveform.htm, last accessed 08.07.2015

solution for developing DICOM applications. Since this software provides no easy means to register custom IODs, it does not support the access to information which is not part of the DICOM for Waveforms specification. However, the parts of the ERG IOD which comply to this specification, especially the waveform data itself, could be loaded successfully (Figure 36).

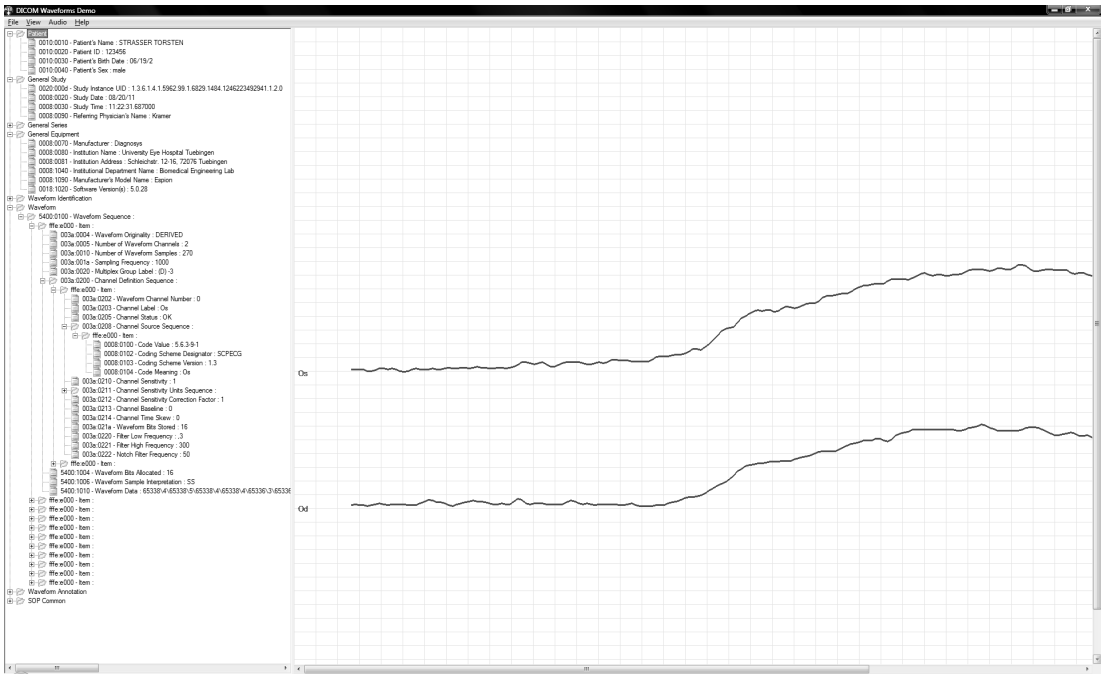

Figure 36: Viewing waveform data of an ERG recording stored as DICOM file using the LEADTOOLS Waveform SDK.

3.5 Conclusion

The developed prototype demonstrates the vendor-independent integration of visual electrophysiology data into a distributed e-Health network using PACS equipment based on DICOM, thus providing access to the advantages of existing DICOM infrastructure. In a previous project we introduced a new IOD with private attributes to map the extra data necessary for encoding and decoding ERG recordings.

Our current project extends existing DICOM software to enable the display and analysis of ERG recordings stored in the DICOM format.

For visualizing electrophysiological recordings of vision, we developed a plug-in for ImageJ to be used with the Tudor DICOM Viewer. This plug-in will soon be made available to the public.

ERG data stored as DICOM using the developed ERG IOD could also be loaded successfully in the commercial software the LEADTOOLS Waveforms SDK. A next step would be to submit a proposal for standardization of the ERG IOD.

4 Electrophysiology of Vision Markup Language

4.1 Introduction

Within the last decades, an ongoing process of standardization in the field of visual electrophysiology could be observed. The establishment of commonly used protocols defining parameters for stimulation and recording of electrophysiological examinations, has also led to a harmonization in the devices used for these examinations. This process was mainly driven by the International Society for Electrophysiology of Vision (ISCEV) ([2]–[6], and [34]). As a result, recordings from different sites became comparable, which is of increasing importance, especially in clinical trials.

The standardization consider stimulus parameters, acquisition settings, and recording conditions, but up to now there exists no standard for the storage and exchange of visual electrophysiological recordings. Although manufacturers of electrophysiological devices usually provide means for exporting data, these are often restricted to either proprietary, or simple ASCII-based formats (i. e. character separated values, CSV). Both have their drawbacks: whereas using the proprietary data formats of the manufacturers provides all necessary information regarding an examination, including used stimuli and recording settings, it requires special software to work with the data. This leads to a dependence on the manufacturer. In contrast, the second option allows for independent storage of data, but often lacks the detailed stimulus and acquisition parameters.

With the need for central reading in multi-center trials this becomes a major issue. The reading process usually requires the documentation of all details of an examination, to allow for properly monitoring compliance with study protocols, but should not depend on specific software to work with the data.

As described in chapter IV, section 2, standards for electrophysiological data do exist, e. g. for electroencephalography (EEG) or the electrocardiography (ECG). However, the scope of these standards is usually limited to their specific field of application. Common standards are also available, like GDF (General Data Format for Biosignals) [73], EDF (European Data Format) [88], [89], or HL7 aECG [76] and DICOM Supplement 30 "Waveform Interchange" [74]; as described earlier, these standards either do not match the requirements of visual electrophysiology, such as storing stimulus parameters, or they must be adapted, with considerable effort, which could lead to incompatible implementations, if not accepted widely.

Therefore, here we propose an open standard for the exchange of visual electrophysiological data, based on the eXtensible Markup Language (XML).
ElVisML has the following goals:

- Cover all relevant details of electrophysiological recordings so that they are completely comprehensible
- Independence from manufacturer, recording device, operating system, and application
- Self-descriptive
- Verifiability by specifying a strict syntax and grammar
- Leverage best-practices learned from existing similar standards in the electrophysiological domain
- Use of a well established terminology

The CARMEN consortium has published guidelines for the "Minimum Information about a Neuroscience investigation" (MINI) that should be reported about a data-set to facilitate computational access and analysis to allow a reader to interpret and evaluate the process performed and the conclusions reached. One

part of these guidelines focuses on data-sets in electrophysiology [90]. The design of ElVisML tries to satisfy these requirements.

4.2 Methods

XML as foundation of a data format for biomedical signals

The development of a new data format starts with a decision between two possible approaches: creating a binary format or a text-based format. Binary formats result generally in smaller files, thereby saving disk space and reducing transmission time (e. g. over network). However, they have the trade-off of being dependent on specialized software. Since neither disk space nor network speed play a big role anymore, human readability and simplicity is considered of much higher relevance than size.

In their comparison of existing data formats for body surface potentials maps, Bond et al. [91] state that during the last decade, an increasing number of XML-based data formats for electrophysiological signals in comparison to binary formats could be observed.

This trend is conveyed by regulatory guidance of the U.S. Food and Drug Administration (FDA) that requires the submission of ECG data in a standardized digital format instead of manufacturers' proprietary formats. FDA proposed an XML-based format [92] that is integrated into the HL7 messaging standard: the annotated ECG (aECG) file format [93]. Additionally, the FDA published requirements and instructions for the implementation of file formats based on XML [94]–[96].

For these reasons, XML was chosen as foundation for data format for visual electrophysiological data. XML is used in the majority of standards for data storage nowadays. Most industry players like Sun Microsystems, Microsoft Cor-

poration, IBM, and Oracle Corporation, as well as health-care organizations, like FDA, HL7, and the Clinical Data Interchange Consortium (CDISC), have committed to the use of XML.

The Extensible Markup Language (XML)

XML is a recommendation of the World Wide Web Consortium (W3C) [19]. It is a simplified subset of the Standard Generalized Markup Language (SGML).

XML provides a standardized approach for storing text-based data in a hierarchical structure and for adding meta data to data. These meta data annotate the actual data in form of tags: In XHTML, markup tags are used to define the presentation of text (e. g. bold or italic, text color, etc.). Beyond defining layouts, XML can add semantics to data, resulting in markup languages or XML dialects focused on specific domains of application.

```
1  <?xml version="1.0" encoding="UTF-8"?>
2  <Subjects>
3    <Subject id="1234">
4      <Firstname>Torsten</Firstname>
5      <Lastname>Straßer</Lastname>
6      <ContactInformation type="business">
7        <Street>Frondsbergstr. 23</Street>
8        <ZipCode>72070</ZipCode>
9        <City>Tübingen</City>
10       <Country>Germany</Country>
11     </ContactInformation>
12   </Subject>
13 </Subjects>
```

Listing 9: Example of an XML document containing contact details of a person

Listing 9 is a simple example of an XML dialect for contact details of persons. The actual information is enclosed with markup tags, adding semantic to it. Thereby, data becomes readable by humans as well as by software. Only a few rules for writing well-formed XML documents have to be followed: XML docu-

ments need a prolog, specifying the XML version and the used character set (line 1). The prolog is followed by a hierarchically nested markup tags.

An XML document is called well-formed, if it satisfies the following set of rules:

- Correct nesting of tags; beginning and end tags must match
- Hierarchical structure with only one single root
- Markup characters, such as “<”, “>”, “/”, and “&”, must be escaped according to the XML specification

If a document violates one of these rules, i. e. it is not well-formed, it is no XML. The example given in Listing 9 fulfills all rules and is therefore considered as well-formed.

A collection of markup tags (e. g. Subject, Firstname, Country) build up the vocabulary of an XML dialect. Tags allow for adding semantic information to data.

There are many software tools for processing XML-encoded data available such as editors, parsers, viewers, and libraries for almost any programming language. This simplifies the integration into existing software systems. To find more information about XML, the W3C website [97] is a good starting point.

XML Schema

As aforementioned, an XML dialect defines the vocabulary of a markup language based on the specific application domain. Similar to humans, different software programs can only communicate when they use the same vocabulary and grammar. The vocabulary and grammar have to be defined as a kind of dictionary, and all participants have to adhere strictly to it.

The XML standard does not include such a dictionary. Instead, XML schema languages close this loophole. Document Type Definition (DTD) and XML

Schema are the most common representative schema languages. They allow for the definition of a vocabulary (i. e. tags and attributes) and the hierarchical structure (the nesting of tags). XML Schema additionally supports the declaration of data types for the content of tags and attributes, and allows for the definition of relations between tags, therefore, extending the hierarchical concept of XML by referential integrity.

In addition to well-formedness, by using an XML schema language, XML documents can be checked for adherence to a particular schema. This process is called validation. A document valid if the validation was successful.
The validation consists of the following steps:

- Validation of the markup (the hierarchical structure of the document)
- Validation of the content of tags and attributes (data-types)
- Validation of integrity (relations between tags)

Van der Vlist [98] provides a comparison of available XML schema languages. We have decided to use XML Schema [99] as schema language for the specification of ElVisML. XML Schema, a recommendation of the W3C, is the de-facto standard for specifying XML dialects and has a great endorsement in industry. Unlike other schema languages, XML Schema is an XML dialect itself, having its schema defined in XML Schema.

XML Schema provides the basic concepts [100] for the definition of XML dialects, the facilities for describing structure and content [101], as well as data types supported [102].

XML Schema defines the hierarchical structure of the tags, their attributes, the cardinality of lists, and the data types of the content of tags and attributes. By using unique keys and key references, XML Schema allows the defining of references between tags, therefore, providing referential integrity similar to relational databases.

```
1  <?xml version="1.0" encoding="UTF-8"?>
2  <xs:schema xmlns:xs="http://www.w3.org/2001/XMLSchema"
       elementFormDefault="qualified">
3   <xs:element name="Subjects">
4    <xs:complexType>
5     <xs:sequence>
6      <xs:element name="Subject">
7       <xs:complexType>
8        <xs:sequence>
9         <xs:element name="Firstname" type="xs:string"/>
10        <xs:element name="Lastname" type="xs:string"/>
11        <xs:element name="ContactInformation">
12         <xs:complexType>
13          <xs:sequence>
14           <xs:element name="Street" type="xs:string"/>
15           <xs:element name="ZipCode" type="xs:integer"/>
16           <xs:element name="City" type="xs:string"/>
17           <xs:element name="Country" type="xs:string"/>
18          </xs:sequence>
19          <xs:attribute name="type" type="xs:string"/>
20         </xs:complexType>
21        </xs:element>
22       </xs:sequence>
23       <xs:attribute name="id" use="required" type="xs:string"/>
24      </xs:complexType>
25     </xs:element>
26    </xs:sequence>
27   </xs:complexType>
28  </xs:element>
29 </xs:schema>
```

Listing 10: Definition of an XML dialect defined using XML Schema at the example of address information.

Listing 10 presents an example for an XML dialect which could server as a schema of the example shown in Listing 9. The example illustrates one of the drawbacks of XML Schema: even for simple XML dialects, the definition of a schema may easily get overwhelming complex. In order to deal with this complexity, graphical representations of XML Schemata[29] became common and are

29 XML.com provides a comprehensive list of XML authoring tools: http://www.xml.com/pub/pt/3, last accessed 02.07.2015

supported by many software tools. Figure 37 depicts the graphical representation of the XML Schema of Listing 10 created with Altova XML Spy® (Altova GmbH, Vienna, Austria).

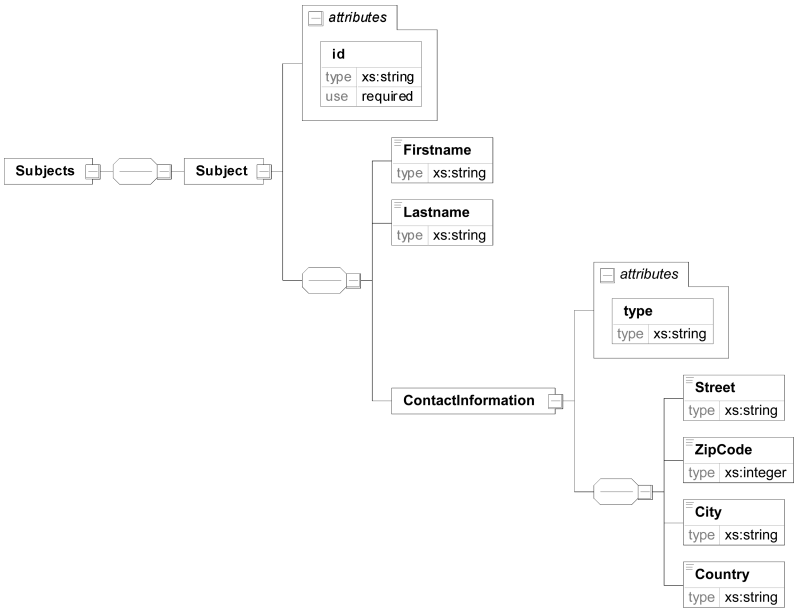

Figure 37: Graphical representation of the XML schema in Listing 10, created with Altova XMLSpy

A detailed discussion of XML Schema is beyond the scope of this work. Reference [99] is a starting point for more information about XML Schema.

Advantages of XML over CSV

The question of using CSV often arises during discussions about how to store data. Those favoring CSV argue that XML is overly complicated, takes a long time to process, and wastes a lot of space by obscuring the data with tags.

Some of these arguments hold true, especially the larger amount of space that is needed by XML compared to CSV. However, since disk space is cheap nowadays, and modern computers are fast, this is practically negligible.
CSV originally was designed for “flat”, record type data – but usually, data is not like this. A typical ERG recording session comprises of patient demographics,

information about the used stimuli and acquisition settings, and the actual recorded data. The structure of these data and their relations within them fit more to a hierarchical data model. Representation of hierarchical data as CSV is not easily possible, whereas XML inherently supports hierarchical data. Combined with a schema definition language, like XML Schema, specifying of referential integrity for parts of the data is possible.

One problem of CSV is dealing with special characters, like field separators, new lines, or quotes. No standard exists on this issue, although there are recommendations. The XML standard defines how to escape special characters. Additionally, XML allows to define the used character set and language of a document and supports Unicode, therefore, avoiding problems with language-specific characters, like German Umlauts.

The main benefit of XML, is its self-descriptiveness: all values stored in an XML document are enclosed in tags, describing their semantic, rendering it, especially useful for long-term storage: even if the software used to create the data is lost, it can still be opened with a simple text editor without loss of information ("Is this the left or the right eye?", "Are these values microvolts?"). Additionally, when used with a schema language, structural and syntactical correctness is validated, which is not possible using with other text-based formats like CSV.

Finally, a huge ecosystem for XML exists: XQuery [103] and XPath [104] provide means for querying XML documents similar to SQL for relational databases, XML databases allow for efficient storage and retrieval of XML [105], and XSLT [106] allows for the transformation of XML into almost any desired format. XML Editors allow for an easy editing and validation of XML documents and almost any programming language has built-in support for XML.

Referential integrity

The XML Schema specification of ElVisML uses references within an ElVisML document. Several entities have an attribute id for specifying a unique identifier to be referable by other elements. The referential integrity is enforced by leveraging unique constraints of XML Schema. Ids are required to be unique within an ElVisML document, but can be globally unique for exchange of data between different sites.

Representation of dimensional values

Storing quantitative measurements without accompanying units is not meaningful and may result worst case in useless data. This is even worse, when data is exchanged between different sites using different unit systems.

A prominent examples demonstrating this, is the loss of the Mars Climat Orbiter Mission in 1999. The loss was caused by a mismatch of the imperial and the metric system [107]. This accident could have been avoided by attributing the transferred numerical values with their appropriate units, which may have lead to an earlier detection of the conversion error. Modern software systems [108], should be designed to be able to do automated conversion between commensurable units.

For this reason, each numerical measurement value in ElVisML is represented as an entity with an attribute specifying the assigned unit as string, formatted according the Unified Code for Units of Measure [109].

Confidentiality and integrity

Medical records are considered highly confidential because of the very private, personal information they contain. In 1997, the National Research Council pub-

lished recommendations for protecting electronic health information [110]. Two of these apply for the design of ElVisML in particular:

> Protection of External Electronic Communications: Health care organizations need to protect sensitive information that is transmitted electronically over open networks so that it cannot be easily intercepted and interpreted by parties other than the intended recipient. To do so, organizations that transmit patient-identifiable data over public networks such as the Internet should encrypt all patient-identifiable information before transmitting it outside the organization's boundary.

and

> Electronic Authentication of Records: All health care organizations that use computerized electronic systems for order entry, discharge summaries, and other critical records should incorporate technologies for electronic signatures.

Confidentiality and integrity are crucial parts in the design of ElVisML. Confidentiality refers to limiting information access and disclosure to authorized users and preventing access by, or disclosure to unauthorized ones. Integrity refers to the trustworthiness of information resources. ElVisML leverages XML Digital Signature [111] and XML Encryption [112] to implement these requirements.

XML Signature allows to digitally sign a document to ensure that the document was sent by a trustworthy originator, and that it was not changed during transmission.

XML Encryption specifies a process for encrypting arbitrary, including not only XML. A whole XML document, single XML elements, or the content of an XML element can be encrypted. The original content is replaced by an

EncryptedData element, containing the encrypted data. XML Encryption works either with a symmetric or an asymmetric encryption algorithm.

4.3 Results

As the result from the need for a standardized format for the exchange and archiving of visual electrophysiological, a proposal for such a standard, namely ElVisML – the Electrophysiology of Vision Markup Language – was developed.

Following the previously described advantages, XML was used as the foundation of this standard, leveraging XML Schema for strict definition of its syntax and grammar.

Anatomy of ElVisML

Creating a new XML dialect can be a challenging task, especially when using XML Schema for its definition. There are many instructions available, which give advice and best practices on how to apply XML Schema and one can use existing standards as templates to realign [95], [96], [113], [114]. Unfortunately, sometimes these sources will give contradictory advices. In this case, a pragmatic approach was followed, since often there was not a definitive solution.

The implementation conformed to the recommendations given in [114], with exception of rule "6.1.7 No Uniqueness Constraints". Unique constraints are used in ElVisML to express references between different sections of a document, as will be described later.

An ElVisML document consists of three basic building blocks: Subjects, Protocols, and RecordingSessions, which are child elements of the root element ElVis. All of them are declared as optional to account for different use cases, e. g. exchange of patient information or protocol settings only, or exchange of a complete data-set including patient demographics, protocol settings and recorded

data. However, if the document contains a RecordingSession, the related Subject and Protocol elements must be present. Each of the main sections allows one or more child elements. It is possible to store several protocols, subjects, and recordings within one ElVisML file.

A detailed overview of the anatomy of ElVisML and examples on how to use it are given. As aforementioned, ElVisML is defined using XML Schema and therefore, it is easiest to depict its structure as graphical representation of the schema. All following figures illustrating the schema of ElVisML have been created using <oXygen/> XML Editor (Syncro Soft SRL, Craiova, Romania).

Figure 39 gives a graphical overview of the structure of ElVisML; Listing 11 exemplifies the minimum required information for a subject, a protocol, and a recordings session for a valid ElVisML document.

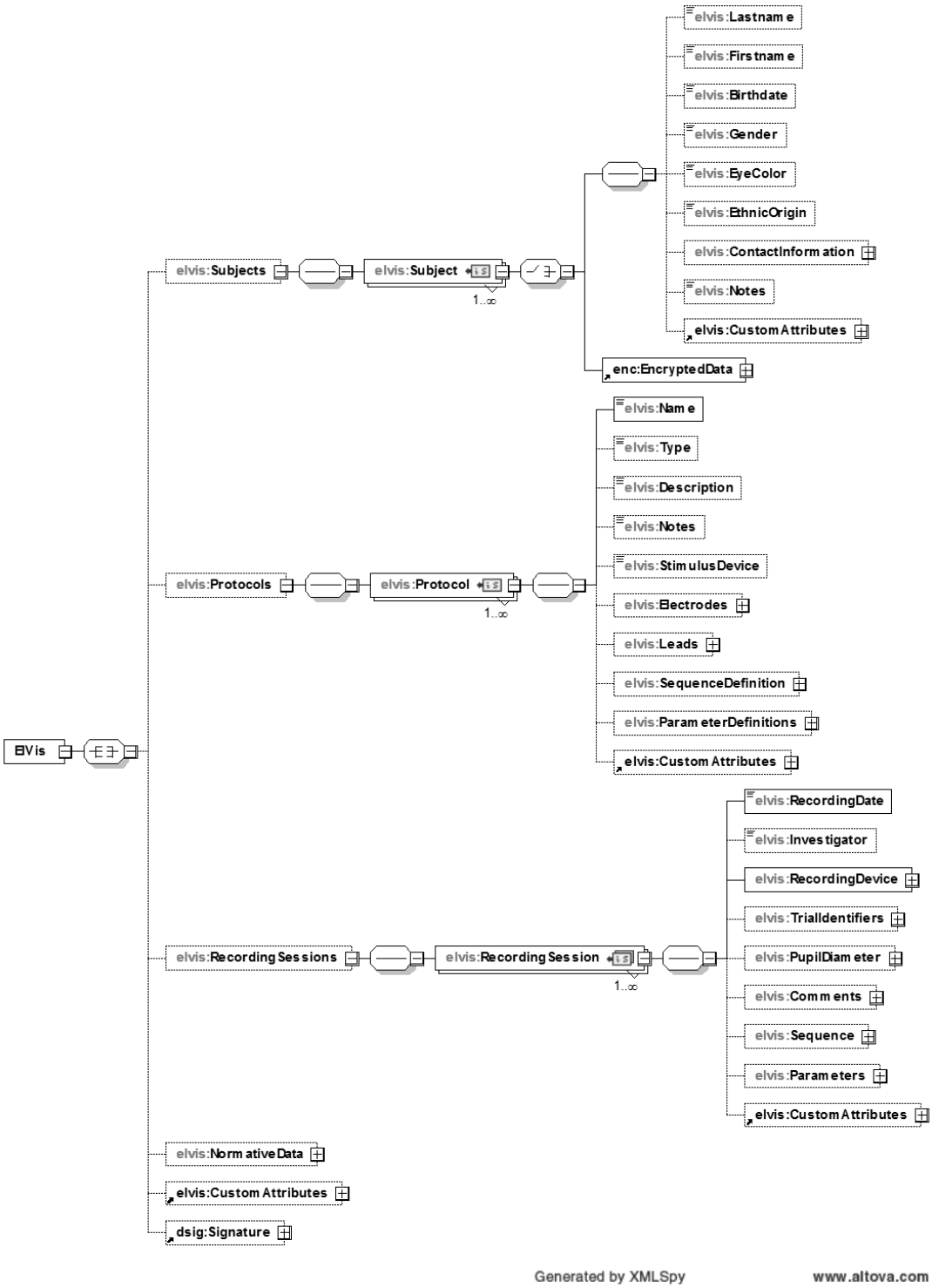

Figure 38: Graphical representation of the structure of ElVisML

```
1  <?xml version="1.0" encoding="UTF-8"?>
2  <elvis:ElVis xmlns:elvis="http://www.iscev.org/ElVisML-v1"
3    xmlns:xsi="http://www.w3.org/2001/XMLSchema-instance"
4    xsi:schemaLocation="http://www.iscev.org/ElVisML-v1 http://www.biomed-
   engineering.de/xsd/ElVisML-1.0.xsd"
5    creator="ERG Explorer" created="2010-10-13T15:32:12">
6    <elvis:Subjects>
7      <elvis:Subject id="S001"/>
8    </elvis:Subjects>
9    <elvis:Protocols>
10     <elvis:Protocol id="P001">
11       <elvis:Name>ISCEV A</elvis:Name>
12     </elvis:Protocol>
13   </elvis:Protocols>
14   <elvis:RecordingSessions>
15     <elvis:RecordingSession subjectRef="S001" protocolRef="P001">
16       <elvis:RecordingDate>2010-10-13T09:13:32</elvis:RecordingDate>
17       <elvis:RecordingDevice>
18         <elvis:DeviceName>Unobtainium 2000</elvis:DeviceName>
19         <elvis:Manufacturer>ACME Inc.</elvis:Manufacturer>
20       </elvis:RecordingDevice>
21     </elvis:RecordingSession>
22   </elvis:RecordingSessions>
23 </elvis:ElVis>
```

Listing 11: Example of an valid ElVisML document, containing the minimum required information for one subject with a recording session and the used protocol. The actual recorded data is not shown here.

Application of referential integrity

Listing 11 illustrates the application of referential integrity in ElVisML: a RecordingSession references the Protocol used for the recording, and the Subject, which underwent the examination. To enforce referential integrity, ElVisML relies on the concept of unique constraints of XML Schema. Entities can have unique ids assigned, which can be referenced by other entities. In XML Schema, such relations are defined using keys and keyrefs; Listing 12 shows the code necessary for the definition of the relations between a RecordingSession and the associated Subject and Protocol, respectively.

```
<xs:key name="SubjectKey">
 <xs:selector xpath="elvis:Subjects/elvis:Subject"/>
 <xs:field xpath="@id"/>
</xs:key>
<xs:key name="ProtocolKey">
 <xs:selector xpath="elvis:Protocols/elvis:Protocol"/>
 <xs:field xpath="@id"/>
</xs:key>
<xs:keyref name="RecordingSession2SubjectKeyRef" refer="elvis:SubjectKey">
 <xs:selector xpath="elvis:RecordingSessions/elvis:RecordingSession"/>
 <xs:field xpath="@subjectRef"/>
</xs:keyref>
<xs:keyref name="RecordingSession2ProtocolKeyRef" refer="elvis:ProtocolKey">
 <xs:selector xpath="elvis:RecordingSessions/elvis:RecordingSession"/>
 <xs:field xpath="@protocolRef"/>
</xs:keyref>
```

Listing 12: Enforcing referential integrity between RecordingSessions and associated Subjects and Protocols using XML Schema identity constraints

Table 7 lists important entities supporting referential integrity by defining an attribute id, and the entities referring to them.

Table 7: Entities of ElVisML supporting referential integrity

Element	Referenced by	Description
Subject	RecordingSession	A recording session is assigned to a subject
Protocol	RecordingSession	A recording session is performed using a protocol
StepDefinition	Step	Steps can use different stimulus and acquisition settings
ChannelDefinition	Channel	Channel specific settings (e. g. filter)
CursorDefinition	Cursor	Type of cursor, settings for automated placement
Average	References	Sweeps belonging to an average

Extensibility

ElVisML defines a minimum set of information to allow the unambiguous interpretation of electrophysiologic recordings of vision. However, device manufacturers often need specialized information not defined by ElVisM to ease the processing of the recordings. There may also requirements in clinical trials, which are not covered by the current version of the standard.

To meet these requirements, ElVisML provides the entity ExtendedAttributes as an optional child element of several entities of the standard. It acts as a wrapper for multiple Attribute elements and allows to store additional information, which are not part of the standard, as string based key-/value pairs. The Attribute element specifies an attribute key, that holds the name of the additional piece of data, whereas its value is stored as content of the element.

Listing 13 illustrates the use of ExtendedAttributes as part of the Subject element to store additional patient data.

```
1 <elvis:ExtendedAttributes>
2   <elvis:Attribute key="refractionOD">1.2 dpt</elvis:Attribute>
3   <elvis:Attribute key="refractionOS">1.4 dpt</elvis:Attribute>
4   <elvis:Attribute key="admissionDiagnose">RP</elvis:Attribute>
5   <elvis:Attribute key="uniqueId">4383-8855-137A-12C2-8013</elvis:Attribute>
6   <elvis:Attribute key="creationDate">1204624257000</elvis:Attribute>
7 </elvis:ExtendedAttributes>
```

Listing 13: An excerpt of the Subject element, illustrating the use of ExtendedAttributes to include additional information not part of the standard

In general the use of ExtendedAttributes is not recommended. Information stored as ExtendedAttributes is not part of the ElVisML standard and therefore, cannot be expected to be understood by other software. Especially, ExtendedAttributes should not be used to undermine restrictions of the ElVisML standard. As data of ExtendedAttributes are stored as string-based key-/value pairs, no

data types or unit information can be specified. When using ExtendedAttributes, implementers should follow the following advices:

- use them rarely
- do not use them to store data necessary for the interpretation of recordings
- use them meaningful with self-descriptive keys
- ignore ExtendedAttributes with unknown keys (do not modify or delete them)

Implementation of the representation of dimensional values

Each measurement value in ElVisML has assigned a unit in order to avoid ambiguousnesses. One example were such an ambiguousness may occur is the definition of a stimulus intensity: several different units exists therefor (e. g. candela (cd) or trolands (td)). Listing 14 exemplifies the use of the unit attribute at an excerpt of a stimulus definition encoded in ElVisML. Units are expressed as string, encoded according to the Unified Code for Units of Measure [35].

```
1 <elvis:Flash>
2   <elvis:FlashDuration unit="ms">4.0</elvis:FlashDuration>
3   <elvis:FlashStrength unit="cd*s*m^-2">3.0</elvis:FlashStrength>
4   <elvis:FlashColor>white</elvis:FlashColor>
5   <elvis:Fixation>true</elvis:Fixation>
6   <elvis:BackgroundLuminance unit="cd*m^-2">30.0</elvis:BackgroundLuminance>
7   <elvis:BackgroundColor>White-6500K</elvis:BackgroundColor>
8 </elvis:Flash>
```

Listing 14: Representation of numerical values with associated units. The units are encoded according to the Unified Code for Units of Measure

Implementation of confidentiality and integrity

As aforementioned, ElVisML leverages XML Signature and XML Encryption to ensure the integrity of documents and to protect sensitive information for unauthorized access.

XML Signature allows to digitally sign a document, therefore ensuring a trustworthy originator, as well as unmodified and complete transmission. ElVisML documents may include a Signature element, as a child of the root element ElVis, which stores the digital signature of a document (Listing 15).

```
1  <dsig:Signature>
2   <dsig:SignedInfo>
3    <dsig:CanonicalizationMethod Algorithm="REC-xml-c14n-20010315"/>
4    <dsig:SignatureMethod Algorithm="http://www.w3.org/2000/09/xmldsig#rsa-sha1"/>
5    <dsig:Reference URI="">
6     <dsig:Transforms>
7      <dsig:Transform Algorithm="xmldsig#enveloped-signature"/>
8     </dsig:Transforms>
9     <dsig:DigestMethod Algorithm="http://www.w3.org/2000/09/xmldsig#sha1"/>
10     <dsig:DigestValue>Rmsh25JxEoQN8eHFWH2UleqOLZw=</dsig:DigestValue>
11    </dsig:Reference>
12   </dsig:SignedInfo>
13  <dsig:SignatureValue>cPyQf … S4BRbYbdg==</dsig:SignatureValue>
14  <dsig:KeyInfo>
15   <dsig:X509Data>
16    <dsig:X509SubjectName>CN=Torsten Strasser,O=Institute for Ophthalmic
    Research,L=Tuebingen,ST=BW,C=de</dsig:X509SubjectName>
17    <dsig:X509Certificate>MIIDtjCCAp6gAw … Ge8KyXZW8 </dsig:X509Certificate>
18   </dsig:X509Data>
19   <dsig:KeyValue>
20    <dsig:RSAKeyValue>
21     <dsig:Modulus>wqpAR729Lv50tl … SqsigjBw==</dsig:Modulus>
22      <dsig:Exponent>AQAB</dsig:Exponent>
23    </dsig:RSAKeyValue>
24   </dsig:KeyValue>
25  </dsig:KeyInfo>
26 </dsig:Signature>
```

Listing 15: Digital signature of an ElVisML document

XML Encryption allows to encrypt whole XML documents, single XML elements, or the content of an XML element. The original content is replaced by an EncryptedData element, containing the encrypted data. XML Encryption can use symmetric or asymmetric encryption algorithms.

Since the Subject element contains sensitive patient data, it supports encryption of its content by specifying an optional EncryptedData element. After encryption, the content of the Subject element is therefore only accessible for users having the correct key (Listing 16).

```
27 <elvis:Subject id="S753172844" normal="false" externalIdentifier="4D48EDB1-013">
28   <enc:EncryptedData Type='http://www.w3.org/2001/04/xmlenc#Content'>
29     <enc:CipherData>
30       <enc:CipherValue>A23B4 … 5C56pAR729Lv5</enc:CipherValue>
31     </enc:CipherData>
32   </enc:EncryptedData>
33 </elvis:Subject>
```

Listing 16: ElVisML document after encryption with XML Encryption. The content of the Subject element is replaced by the encrypted data

4.4 Conclusions

Open standards like ElVisML help to ensure quality, validity, and integrity of visual electrophysiological data, provide manufacturer independent access, and long-term archiving in a future-proof format.

A number of manufacturers of equipment for visual electrophysiology, as well as the International Society for Clinical Electrophysiology of Vision (ISCEV) have expressed their support for the further development of ElVisML.

As part of a bachelor thesis supervised by the author [115], an interface between the generic data model for visual electrophysiological data, described in chapter II 2, and ElVisML was developed. This interface allows for reading and

writing ElVisML documents using ERG Explorer (chapter Fehler: Referenz nicht gefunden).

ElVisML was successfully applied in a multi-center clinical trial (two sites, 20 patients, four examinations per patient) as main data format for the exchange of ERG recordings between the sites, reading center, and the readers [48], [116]. Using ElVisML, an audit trail was realized by based on revisions of ElVisML documents, and automated conformance checks could be enforced during each step of the workflow using the data provided by ElVisML.

For an easy and platform independent visualization of ElVisML documents, a Web 2.0 application, ElVisWeb, was developed by students as part of their hands-on training supervised by the author. ElVisWeb is intended to facilitate the exchange of recordings on mailing lists like CEVnet[30] and to allow open access to data along with published articles.

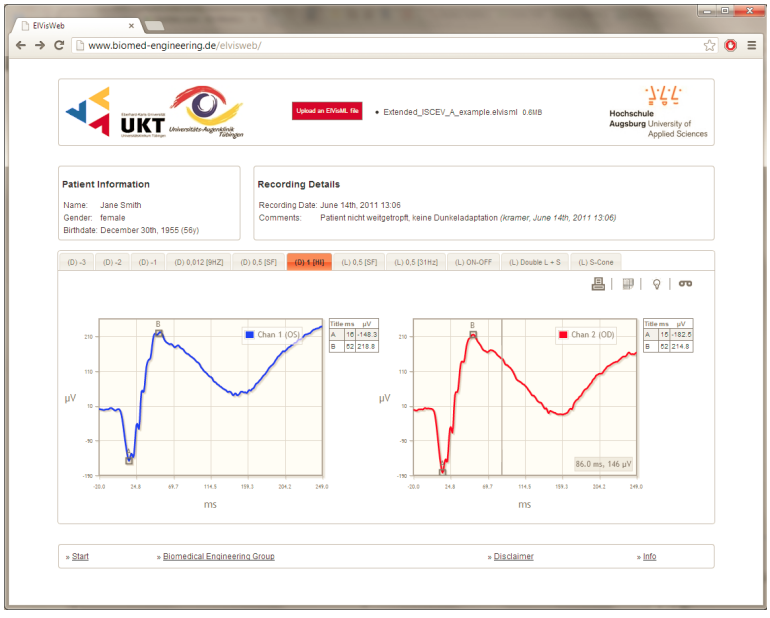

Figure 39: ElVisWeb, a Web 2.0 application for the visualization of visual electrophysiological data.

30 http://www.iscev.org/misc.html#CEVnet

V ELECTRODES

1 A novel contact lens electrode for recording the electrical potentials of the ciliary muscle during accommodation

This text is modified from a scientific report. A full paper (Clouse M., Schaeffel F., Strasser T., Zobor D., Zrenner E., alphabetical order) is in preparation.

1.1 Introduction

Accommodation is the ability of the eye to change its focus from distant to near objects: the lens alters its refractive power to maintain a clear and focused image on the retina [117]. The classical theory of accommodation, as published by Helmoltz in 1855 [118], proposes that the ciliary muscle moves forward in the eye during contraction, thereby releasing tension on the anterior zonular fibers and allowing the lens to curve and thicken as shown in Figure 40. This increases the optical power of the eye and allows it to focus on near objects. During disaccommodation, the ciliary muscle relaxes, which leads to the flattening of the lens.

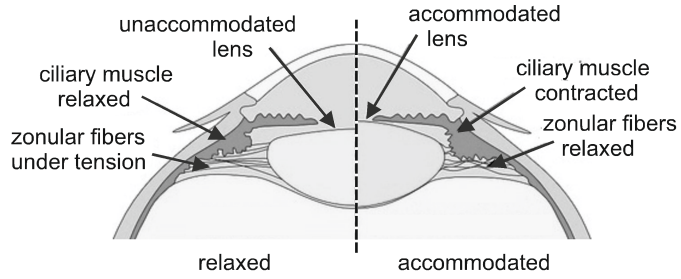

Figure 40: Accommodation in the normal eye. A contraction of the ciliary muscle leads to a relaxation of the zonular fibers, which leads to a more rounded shape of the lens. In contrast, a relaxation of the ciliary muscle puts tension on the zonular fibers, which allows the lens to flatten. Figure modified from: Azar D, Gatinel D, Hoang-Xuan T, ed. Refractive Surgery. Philadelphia: Mosby-Elsevier; 2006:501-510

In adolescents the eye can change the focus from infinity to about 7 cm [119]. However, the amplitude of accommodation declines with age steeply. By the fifth decade of life, the accommodative amplitude has declined so that the near point of the eye is farther than the reading distance. This phenomenon is called presbyopia.

A comprehensive review of the accommodation function of the human eye has been given by Toates in 1972 [120]. However, the pathophysiology of accommodation is still poorly understood [121]–[124].

There is only little known about the electrophysiological properties of the ciliary muscle, although its anatomical structure has been well-studied [125]–[128]. In 1955, Schubert et al. reported findings of corneal electrophysiological recordings obtained by the use of a contact lens electrode [125]. They described slow potential changes during accommodation of the eye and suggested that the ciliary muscle might be responsible for these potentials. The interpretation of the surface electrograms of the eye, however, seemed to be complex because of other extrinsic factors and artifacts (such as eye movements, pupil reflexes, activity of external ocular muscles, etc.). Therefore, direct exploration of the ciliary muscle with a thin needle electrode was considered necessary in order to characterize the isolated electrical activity of the ciliary muscle at rest and during accommodation of the eye. Such an attempt has been made by Hagiwara et al. in 1962 by using an Ag/AgCl needle electrode, which was directly inserted into the human ciliary muscle *in situ* and the recording of the action potential of the muscle was carried out [129]. Although the results were promising, this method was not carried forward in human studies, due to complications such as sympathetic ophthalmia.

Electrophysiological experiments on ciliary muscle activity have not been carried further for several decades. Therefore, there is a lack of conclusive experimental data. Here we introduce a novel bipolar contact lens electrode which allows for recording electrical potentials of the ciliary muscle during accommodation. The setup for a controlled testing of the accommodation is described. This work was part of a larger study, investigating the electrical responses of the ciliary muscle during accommodation. The electrical responses were recorded in young emmetropic, elderly presbyopic phakic, and pseudophakic subjects. Additionally, the effect of cycloplegia on the electrical responses were examined. Here, the results of electrophysiological recordings of ten emmetropic subjects are presented.

1.2 Methods

Participants

Our research followed the tenets of the Declaration of Helsinki [130] and the study was approved by the Ethics Committee of the University of Tübingen, Germany. Ten young healthy emmetropic subjects with a wide accommodation range were recruited from the faculty, staff, and student body of the University. All participants signed a written informed consent. The volunteers received an ophthalmological examination (including best corrected visual acuity, slit-lamp examination, measurement of the intraocular pressure, and funduscopy).
Inclusion criteria:

- Age between 18 and 35 years
- Full visual acuity without correction (= emmetropic, refractive error less than ± 0.5 D spheric and ± 0.75 D aspheric)
- Accommodation range > 6.0 D

- No ocular pathologies (especially no problems with accommodation)
- Written consent for study participation

Exclusion criteria:

- Women who were pregnant or nursing
- Health conditions, which would not allow longer measurements (e. g. problems with sitting, concentration, nervous cough, etc.)

Table 8: Participants of the study with age, gender and corrective lens used for the visual pathway.

Subject	Gender	Age	Corrective Lens (dpt)
AR	female	22	+ 0.5
CH	male	23	+ 0.5
CL	male	28	+ 0.5
ER	female	23	+ 0.5
KB	male	27	+ 0.5
NG	male	28	- 1.0
SD	male	21	N/A
SK	male	27	+ 0.5
YO	male	26	+ 0.5
ZL	male	27	- 0.75

Electrode development

A commercially-available scleral contact lens was modified: the Boston® XO_2 (hexafocon B, Bausch & Lomb GmbH, Heidelberg, Germany) is a gas permeable contact lens material composed of siloxanyl fluoromethacrylate copolymer. Boston XO_2 contact lenses are indicated for daily wear for the correction of refractive ametropia (myopia, hyperopia, astigmatism, and presbyopia) in aphakic and non-aphakic persons with non-diseased eyes. For our study, scleral lenses

with 20 mm diameters were chosen with three different Sra (scleral radius) parameters, resulting in a flatter lens, a standard lens, and a steeper lens (Sra = 13.25 / 12.5 / 11.75 mm). Two holes for contacting the leads were prefabricated by the manufacturer at 7 and 9 mm radii from the center of the lens (Figure 41).

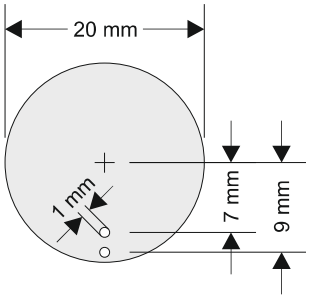

Figure 41: Dimensions of the processed Boston XO_2 contact lens electrode. Two wholes were drilled to allow for connecting the sputtered conductive surface on the inside of the lens with the leads.

After cleaning the lens with ethanol and drying, the holes were fitted with two small gold tubes to allow for the connection of the conducting surface with the leads. The tubes were fixed using a medical adhesive (EPO-TEK 354-T, Epoxy Technology, Inc., Billerica, MA, USA). To harden the adhesive, the lens was dried for 12 hours at a temperature of 80° Celsius. After fixing the rods, a conductive surface coating was deposited onto the inner surface of the lens using cathode sputtering. This resulted in two concentric, 150 nm thick, titanium-gold rings. The leads were connected to the tubes using a conductive adhesive (EPO-TEK H20E, Epoxy Technology, Inc., Billerica, MA, USA) and again dried for eight hours at 80° Celsius. Contacts to the leads were insulated using H20E adhesive and heat-shrink tubes. Finally, gold layers were sputter-deposited onto the inner surface of the lens to enable conductivity (Figure 42).

Figure 42: Inner and outer surface of the processed Boston XO2 contact lens after sputtering of the conductive surface and connecting the leads.

Visual target pathway

Accommodation targets consisted of five endo-illuminated perspex plates with the engraved letter "E", scaled in size to generate constant visual angles for the different viewing distances. The individual targets were illuminated by four small LEDs positioned in the corner of the perspex plates, which in turn were controlled by a custom-built circuit and a micro-controller (Atmel ATmega 8515, Atmel Corporation, San Jose, CA, USA) running a custom developed software. The nearest perspex plate was positioned at 20 cm (5 dpt), the most distant one at 2 m (0.5 dpt). The remaining three plates were placed at intermediate positions: 0.5 m (2.0 dpt), 0.4 m (2.5 dpt) and 0.286 m (3.5 dpt).

In order to minimize eye movements, accommodation targets were aligned as shown in Figure 43. To aid in alignment, the targets were rotated, changing the orientation of the "E.".

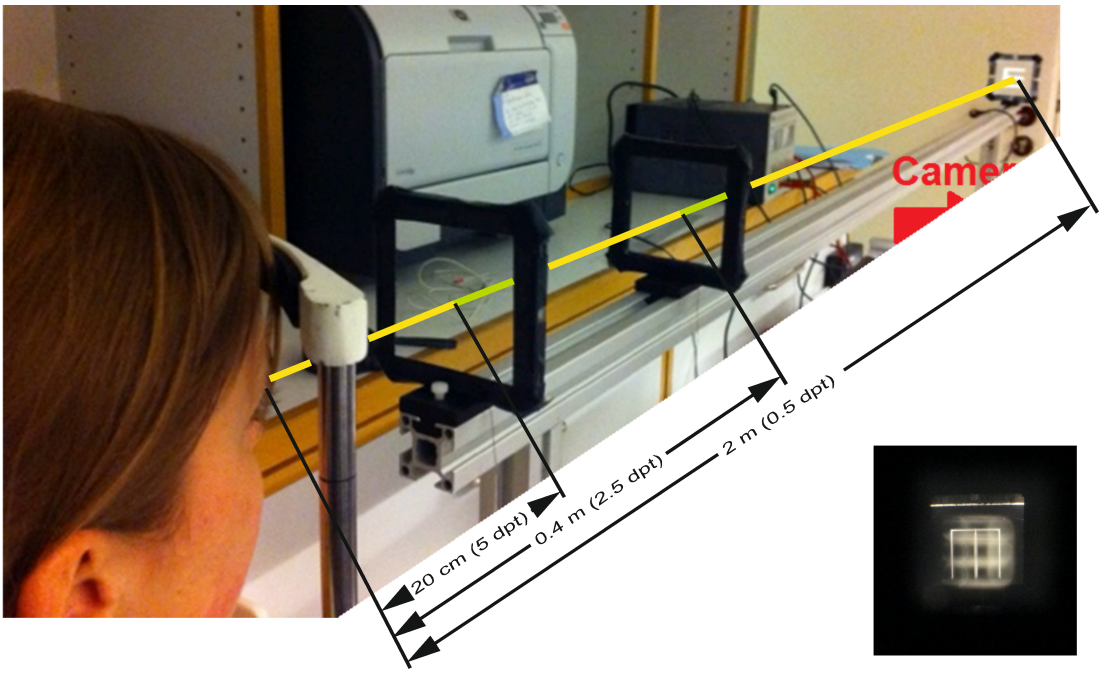

Figure 43: Visual target pathway: Five perspex plates with engraved illuminable "E"s were aligned along the optical axes of the eye, indicated by the yellow line in different distances (only three targets are shown). The image downright gives an impression of the subjects view.

Experimental setup

Electrical ciliary muscle activity was recorded on one eye by the bipolar contact lens electrode, while the contralateral eye was used for fixation and accommodation triggering. All measurements were carried out in an electrically shielded room, with standardized light condition that was checked before each measurement.

Local anesthetic eye drops (Novesine 0.4%) were applied three times at short intervals to the recorded eye in order to diminish corneal reflexes and irritation. The contact lens electrode was then filled with Vidisic gel for better contact and protection of the cornea.

A ground electrode was positioned at the center of the volunteer's forehead for electrical measurements, the contact lens electrode was placed centrally on the subject's eye, with the leads exiting the eye temporally.

The volunteer sat comfortably in a chair with his or her head positioned on a chin rest. The recorded eye was covered by a black patch attached to the chin rest in front of the eye to avoid disturbances due to blurred vision caused by the contact lens electrode.

The accommodation stimulus was introduced to the contralateral eye and the targets were aligned with the focusing eye for optimum test performance. Refraction was corrected to a distance of 2 m (0.5 dpt) with lenses placed in front of the fixating eye.

For each accommodation test, the far target at 0.5 dpt was first illuminated for ten seconds. An acoustic signal indicated the change of the target and the far target was turned off and one of the closer targets was illuminated for 15 seconds. Finally, a second acoustic signal indicated the change back to the distant target, which was illuminated for another 20 seconds.

To exclude possible influences of eye movements or pupil responses on the recorded electrical potentials of the ciliary muscle, additional recordings were done during forced eye movements and stimulation using a flash light, respectively (data not shown).

Data acquisition

The impedance and conductivity of the lens were tested each time before use with the help of a voltage generator that sent a known voltage to the electrode. This voltage was confirmed with a multimeter attached to the electrode leads.

Electrical signals were recorded with an electrophysiological recording system (Espion e², Diagnosys Ltd., Cambridge, UK). The start of a recording was triggered by the micro-controller using the Espion digital trigger input. The following acquisition settings were used: Sampling frequency: 1000 Hz, recording time 51000 ms, four sweeps per average, no linear drift removal, baseline removal (range 0 – 1000 ms), no band-pass filter.

Data analysis

The recorded data were smoothed using a Savitzky-Golay filter [51] (order = 4, window = 5000) to remove fast artifacts caused by eye movements. A linear detrend was applied using time intervals before (0 – 9 s) and after (30 – 39 s) accommodation. Some recordings showed a polarity reversal (negative response during accommodation period, see conclusions); in these cases, the amplitudes of the recording were inverted.

To measure the strength of the electrical potential induced by the change of accommodation, the root mean square amplitude (RMS) [131] was calculated for each target distance using Equation 3 in two time intervals: baseline [0 – 9] s and accommodation [14 – 25] s.

$$rms = \sqrt{\frac{1}{N} \sum_{t\,=\,start}^{end} x_t^2} \tag{3}$$

The RMS amplitude of the baseline interval is assigned to the target at the distance of 0.5 dpt.

Because of a large variation between the individuals, the RMS values were normalized to the maximum value of all target distances achieved by the individual.

1.3 Results

The new developed contact lens electrode was tolerated by all subjects and electrical responses of the ciliary muscle could be recorded from all subjects. Figure 44 depicts example recordings for different accommodation targets for one subject, KB.

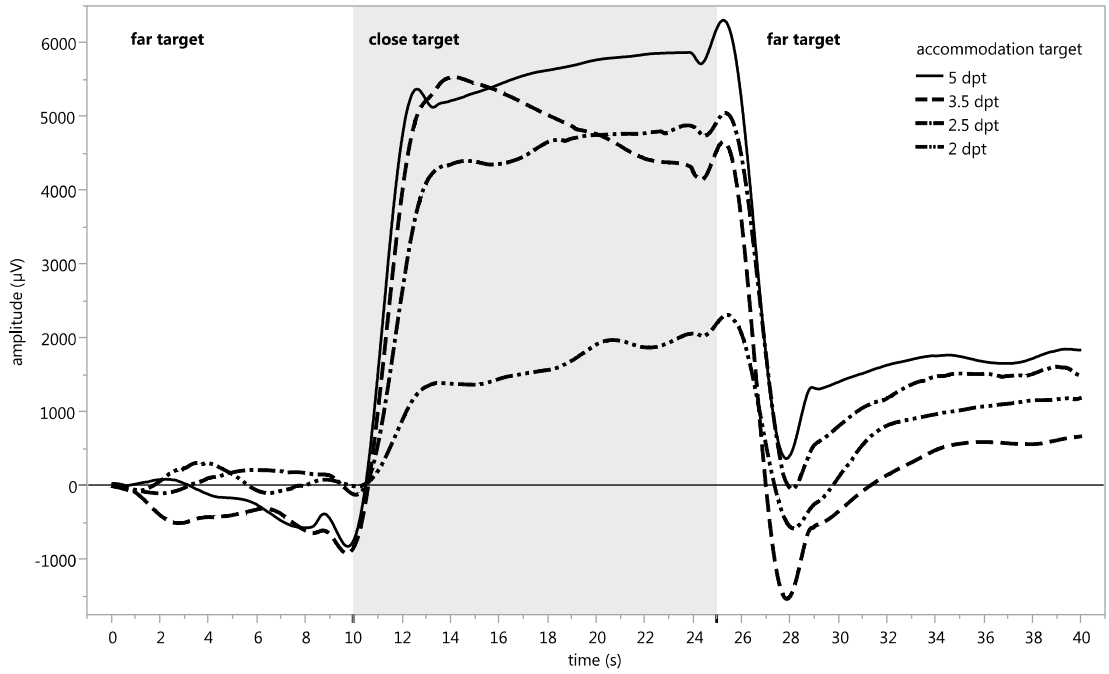

Figure 44: Electrical responses of the ciliary muscle of subject KB during accommodation to different targets. The grey area indicates the presentation of the near target. The far target was at a distance of 0.5 dpt. During accommodation to the near targets, the amplitude increases in relation to the distance of the target. Interestingly, there seems to be some over-/undershoot at the beginning and the end of the accommodation.

However, subject SD exhibited a high sensitivity to the recording electrode, leading to a noisy recording and subject ZL reported difficulties in accommodation. Nevertheless, recordings from both subjects could be included into the

analysis. Subject ER was excluded from further analysis because of a prevalence of blink artifacts and non-reliable responses.

Table 9 lists the root mean square amplitudes and the normalized rms amplitudes of all subjects in response to the different target distances.

Figure 45 shows a box-plot of the normalized rms amplitudes for each target distance over all subjects.

Table 9: RMS and normalized amplitude of all subjects for each target distance.

S.	rms amplitude (μV)					normalized rms amplitude (%)				
	0.5 dpt	2.0 dpt	2.5 dpt	3.5 dpt	5.0 dpt	0.5 dpt	2.0 dpt	2.5 dpt	3.5 dpt	5.0 dpt
AR	268.0	396.1	181.7	1638.3	**2026.2**	13	20	9	81	100
CH	112.0	339.4	347.9	694.9	**977.5**	11	35	36	71	100
CL	95.1	**662.4**	298.6	297.7	194.0	14	100	45	45	29
ER	*562.9*	***1190.9***	*910.2*	*374.2*	*824.4*	*47*	*100*	*76*	*31*	*69*
KB	212.2	1134.1	1141.7	2123.7	**2566.6**	8	5	44	83	100
NG	50.7	38.2	143.5	122.5	**188.4**	27	20	76	65	100
SD	80.0	527.0	723.1	178.6	**1465.4**	5	36	49	12	100
SK	204.6	1246.8	3921.7	4862.9	**4929.7**	4	25	80	99	100
YO	267.9	**830.2**	530.4	590.3	528.3	32	100	64	71	64
ZL	113.4	506.7	623.3	**1125.3**	439.9	10	45	55	100	39

Values in bold were used to calculated the normalized rms amplitude. Subject ER, in italics, was excluded from further analysis

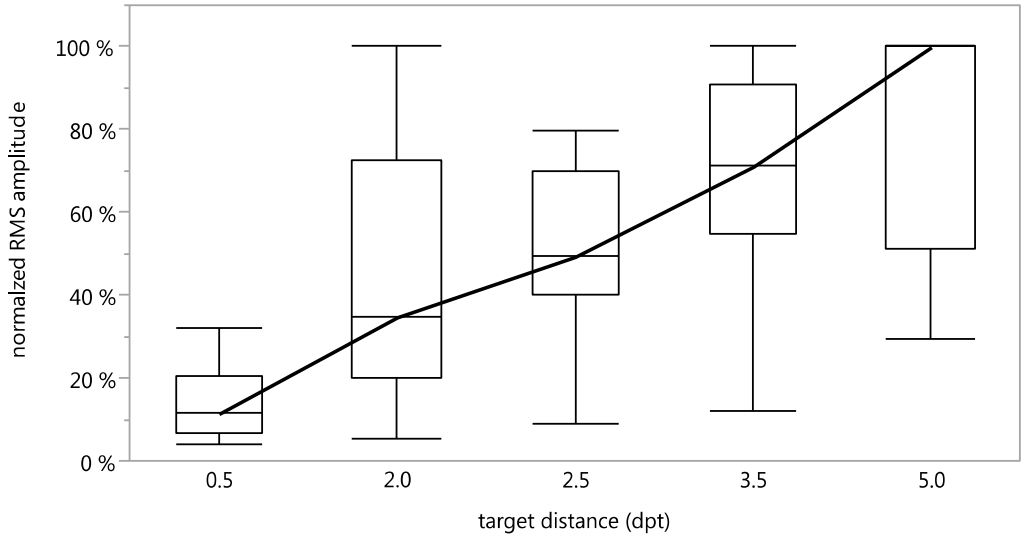

Figure 45: Normalized rms amplitudes of the electrical responses of the ciliary muscle during accommodation. Subject ER did not show reliable results and was excluded from the analysis. The rms amplitudes were calculated from the time intervals [14 – 25] s (2, 2.5, 3.5, 5 dpt) and [0 – 9] s (0.5 dpt), and normalized to the maximal response of each individual. With decreasing distance, the normalized rms amplitude increases, indicating a stronger activation of the ciliary muscle.

A one-way analysis of variance showed a significant effect of the target distance on the normalized rms amplitude ($F(4, 40) = 9.0698$, $p < .0001$).

Post hoc comparison using the Tukey HSD test revealed that the mean normalized rms amplitude for condition 0.5 dpt was significantly different to conditions 2.5 dpt, 3.5 dpt, and 5.0 dpt, and that condition 2.0 dpt was significantly different to condition 5.0 dpt. No significant differences were found between the other conditions. Mean values and standard errors for the single target distances are given in Table 10.

Table 10: Mean values and standard errors of the different target distances for post-hoc Tukey HSD test

Target distance	Mean value	Standard error	Difference to 0.5 dpt p-value	Difference to 2.0 dpt p-value
0.5 dpt	0.1402	0.0862	-	n. s.
2.0 dpt	0.4289	0.0862	n. s.	-
2.5 dpt	0.5094	0.0862	.0330	n. s.
3.5 dpt	0.6962	0.0862	.0004	n. s.
5.0 dpt	0.8134	0.0862	< .0001	.0024

n. s. = not significant

In two of the subjects, KB and SK, a sigmoidal model (Equation 4) could be fitted to the rms amplitudes in response to the target distance, using non-linear least squares fitting. KB and SK showed the highest rms amplitudes among all subjects.

$$rms_{est} = \frac{rms_{max} \cdot distance}{K^n + distance^n} \tag{4}$$

The sigmoidal model uses the following parameters: rms_{max} (µV) determines the maximum rms amplitude the curve converges to, K (dpt) is the half maximum of the sigmoid, and n controls how steeply the curve rises.

Figure 46 shows the results of the sigmoidal fit to the responses. Interestingly, the value of the half-maximum K (KB: K = 2.61 dpt; SK: K = 2.21 dpt) is similar in both subjects. However, the maximum amplitude rms_{max} in SK is about twice the maximum amplitude in KB. In four subjects, SD, NG, CH, and ZL, only a linear fit was possible, as shown in Figure 47. In the remaining subjects, AR, CH, and YO, no meaningful fit was possible.

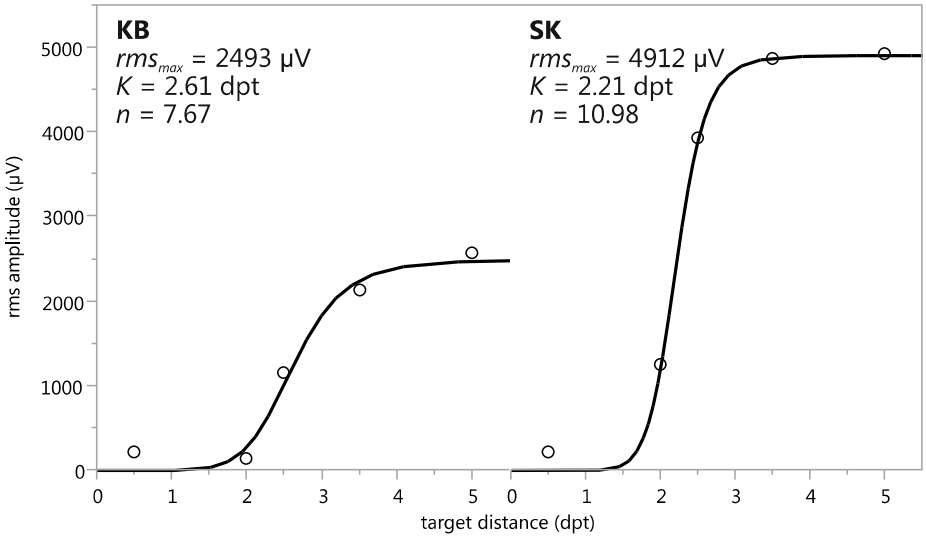

Figure 46: Fit of a sigmoidal model to the responses of KB and SK. Both subjects expressed the highest rms amplitudes of all subjects.

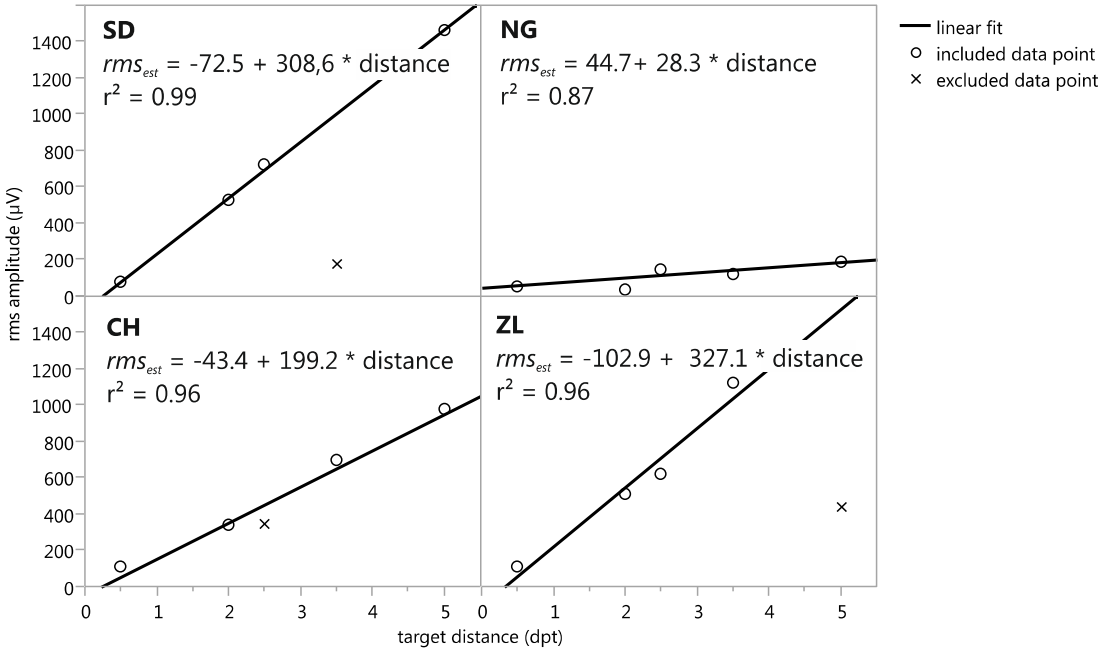

Figure 47: Linear fit to the responses of subjects SD, NG, CH, and ZL. Circles represent data points included in the fit, crosses represent excluded data points.

1.4 Discussion

Using the new developed electrode, it was possible to record electrical potentials of the ciliary muscle in response to accommodation. The shape of the recorded potentials conforms to those shown by Schubert in 1995 [75], whereas the amplitudes are in an order of a magnitude larger.

It was possible to record the electrical potentials in all subjects, however there was a high inter-subject variability in the size of the amplitudes. In one subject, no clear relation between the amplitudes and the target distances could be seen. In some recordings, a polarity reversal could be observed, resulting in a negative response to the accommodation. It is not clear though, what causes the variability of the amplitude sizes and the polarity reversal.

Using a flash light to induce a pupil response showed only a minor effect on the electrical potentials of the ciliary muscle. Likewise, eye movements result in short peaks in the signal, but do not have an effect on the overall shape of the response. This is consistent with the findings of Schubert [125]. Another possible confounding signal could arise from the retina through the illumination of the fixation targets. However, since the recorded signals in the experimental setup were in the range of millivolts, whereas retinal responses are typically in the range of microvolts, this signal would be negligible.

It is hypothesized that the inter-subject variability and the occasional polarity reversals are caused by a different recording position of the electrode relative to the ciliary muscle, which preferentially amplifies one part of the signal over the other (Figure 47). Keeping a stable recording position is aggravated by asymmetries in the shape of the eye: Asano-Kato et al. have found a pupil decentration in a considerable number of eyes [132]. Wildenmann and Schaeffel

reported a shift of the pupil decentration in relation to the pupil constriction [133].

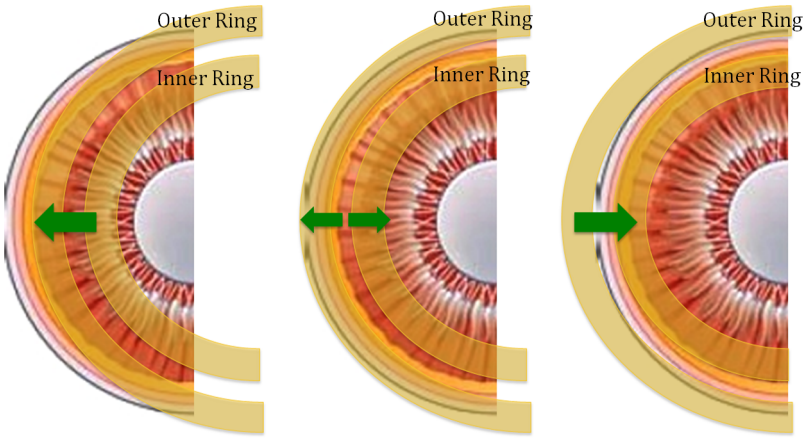

Figure 48: The hypothesized cause by which improper electrode placement over the ciliary body distorts the signal observed. The dominant electrical signal is indicated by a green arrow; the electrode rings are labelled.

Due to the variation in sizes and curvatures of the eyes [134], one or both conductive rings of the contact lens electrode may have poor contact to the surface of the eye, which may also account for lower amplitudes in some subjects. This corresponds to the reports of some of our subjects of poor fit (e. g. difficulty in keeping the electrode on the eye), or to the observation during the recording that the electrode was not correctly centered.

Fitting a stimulus-response model was only possible in six of the ten volunteers: in two subjects a sigmoidal model could be applied, whereas in the remaining four subjects, a linear relationship between the accommodation and the electrical response of the ciliary muscle was found. There is no apriori reason for using either a sigmoidal model or a linear model to describe the stimulus-response function of accommodation. However, both or similar functions can be found in several studies: Heath compared the influence of visual acuity

on the accommodative response of the eye [135]. His data suggests a linear dependency for best corrected visual acuity, but with an increased blur, the response functions became similar to a sigmoidal model; the stimulus-response curve shown by Toates [120] can be interpreted as a sigmoidal function; Ciuffreda et al. investigated the accommodative stimulus-response function in human amblyopia and found a linear relationship between stimulus and accommodation in normal subjects [136]. Rosenfield et al. divided the stimulus-response function into four regions – an initial non-linear region, a linear region, a transitional soft saturation region, and a hard saturation presbyopic region [137]. Their differentiation between different linear and non-linear regions also suggests a sigmoidal model.

1.5 Conclusions

With the help of improved measurement methods, our aim in this study was to apply the modern technique of electrophysiology to the ciliary muscle and its function, in an attempt to determine its characteristics non-invasively in human eyes.

This work describes the development of the novel contact lens electrode and the results obtained in healthy emmetropic young subjects; it provides a new technique for recording ciliary muscle activity in the human eye, which can be beneficial for further research on accommodation and could potentially be used to control an electrically-driven device for continuous refractive correction.

1.6 Acknowledgements

We are grateful to Dr. Hartmut Schulz of the workgroup for micropaleontology, Department of Geosciences, University of Tuebingen, for his support in the first tests of the sputter-coating of perspex surfaces, to Ralf Rudorf of Retina Im-

plant AG, who did the final sputter-coating of the contact lens, and to our workshop for providing the accommodative target as well as to Kevin Liedel, John Campin, Mark Zielke, and George Pettit for thorough discussion of the various problems throughout the course of this project. This study was supported by an investigator grant provided by ALCON.

2 A novel electrode made of a super absorbent polymer for preparation-free electrophysiological recordings: The marble electrode

In 2013, a patent was issued for the here presented electrode: T. Strasser; T. Peters; E. Zrenner. "Grundkörper, Halter, Kit und Elektrodenanordnung sowie Verfahren zur Herstellung". Eberhard-Karls-Universität, Universitätsklinikum Tübingen, assignee. Patent DE102012101337 B4. 31 Oct. 2013.

2.1 Introduction

Recording of VEPs is usually carried out using gold disc electrodes. To to obtain a good signal-to-noise ratio [138], extensive preparation of the patient is required, including cleansing and abrasion of the skin. Studies have shown, that the main source of impedance is the epidermis, which is composed of dead cells [139]. This preparation process is uncomfortable for the patient and after the recording, removing the gel residues often requires washing of the hair. Additionally, abrasion of the skin creates the potential risk of infections [140].

Figure 49: Marble electrode before and after soaking for several hours in water. When fully swollen, the marble electrodes consist of up to 99.9 % water and become therefor electrically conductive.

Marble electrodes are made of a super absorbant polymer (hydrogel), which is able to absorb water up to 500 times its weight. After swelling, the marble electrodes consist of up to 99.9 % of water (Figure 49), rendering them electrically

conductive. Zohuriaan-Mehr et al. gave a comprehensive of super absorbant polymers, their properties, and their applications [141].

In a previous study, we demonstrated the usability of a newly developed electrode, the marble electrode, for electroretinography in small animals (Figure 50) (Strasser et al. IOVS2012; 2462).

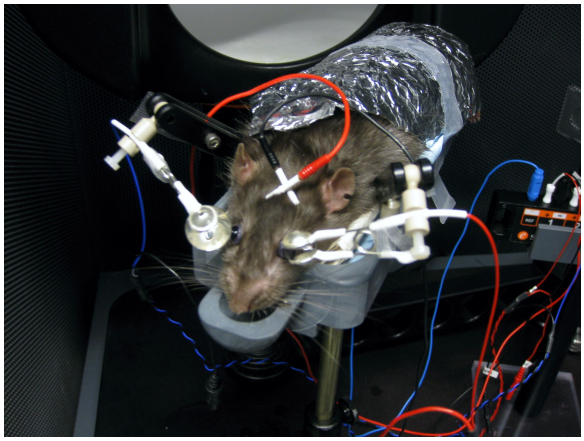

Figure 50: Using marble electrodes for electroretinography of small animals. The moisturized surface of the marble electrode prevents the eye from drying out. Marble electrodes are highly transparent and allow for passing light into the eye.

Based on the results of the previous study and reports of other groups, which have applied hydrogel electrodes for electroencephalography [142], [143], we have explored the application of the marble electrodes for the recording of visual evoked potentials.

2.2 Methods

Cup-like holders for the marble electrodes were manufactured by the workshop of the University Eye Hospital Tuebingen (Figure 51). These holders allow for mounting the marble electrodes at the scalp using a commercially available electrode cap (Figure 52). Inside the cup, a gold disc electrode connects the leads to the marble electrode. Holder and skin electrode can be reused, while the marble electrode can be disposed after use.

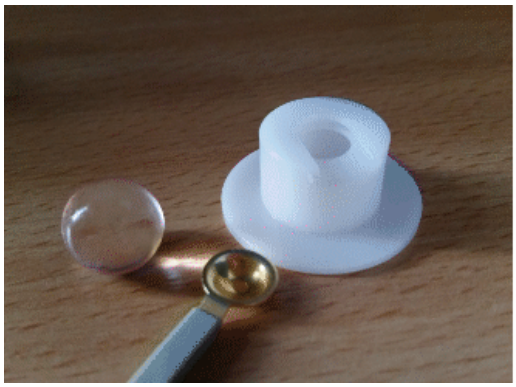

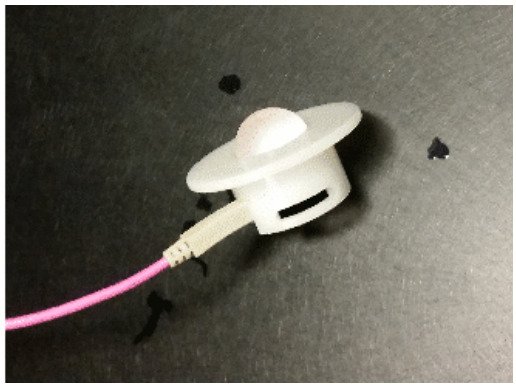

Figure 51: Cup-like holder manufactured by the workshop of the University Eye Hospital Tuebingen and a marble electrode. The holder allows for mounting the marble electrode at the scalp, while the connection to the amplifier and is realized using a conventional gold disc electrode. Cup-holders and skin electrodes can be reused; the marble electrode can be disposed after use.

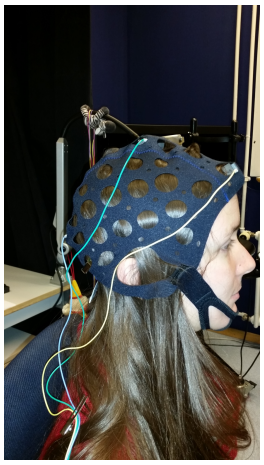

Figure 52: Volunteer prepared for a VEP recording using marble electrodes. The electrodes are mounted according to the ISCEV recommendations at OZ, FZ, and CZ using a electrode cap. No scalp abrasion was done.

To evaluate the usability of the marble electrode for recording VEPs and to examine the effect of high impedances on amplitudes and peak times of visual evoked potentials, pattern-reversal VEPs were recorded in seven healthy volunteers (six female, one male; age 22 – 54 years, mean 36.6 years) with best-corrected visual acuity according to the ISCEV standard [14]. VEPs were recorded with an Espion e² (Diagnosys Ltd., Cambridge, UK), the checkerboard stimulus was presented using a 21" CRT monitor (Model V999, Elonex, Birmingham, UK).

The marble electrodes were soaked in pure water for about six hours, until they were swollen to their maximal size.

In a first session, marble electrodes were used as active, reference, and, ground electrodes. No skin abrasion was performed. In a subsequent second session, the skin was cleaned using abrasive paste, and gold disc electrodes were applied using conductive paste. In both sessions, electrodes were mounted according to the International 10-20 system [14], [144]: active electrode at Oz, reference electrode at Fz, ground electrode at Cz.

Checkerboards of two check-sizes, 0.8° and 0.25°, were presented with a contrast of 80 % at a reversal rate of two reversal per second (onset 200 ms, offset 70 ms). VEPs were recorded using a sampling frequency of 1000 Hz and digitally bandpass-filtered (1.25 – 100 Hz). No notch filter was used. Post-trigger time was 300 milliseconds. Automated baseline correction was done using a 20 milliseconds pre-trigger period. Four averages, consisting of 64 single sweeps, were recorded for each check-size.

Cursors for N75, P100, and N135 [14] were placed using in the build-in peak-finding algorithm and manually corrected, if nescessary. Peak times and latencies of N75, P100, and N135 were exported using ERG Explorer for further analysis.

For assessment of the agreement between data obtained using conventional gold disc electrodes and marble electrodes, the limits of agreement of peak times and amplitudes were calculated using the Bland and Altman analysis [145]. Subsequently, the means of the differences were compared using paired-samples t-test statistics.

2.3 Results

VEPs could be recorded in all subjects using conventional gold disc electrodes and marble electrodes, regardless of the high impedances (between 40 – 80 kΩ) of the marble electrodes. Impedances of the gold disc electrodes were kept < 5 kΩ for all recordings. Single sweeps of recordings using marble electrodes showed a strong contamination with lines noise. However, the lines noise was almost completely removed by averaging of the 64 single traces. Figure 53 depicts the grand averages of 4 x 64 single traces for all subjects recorded using conventional gold disc electrodes (grey traces) and marble electrodes (black traces).

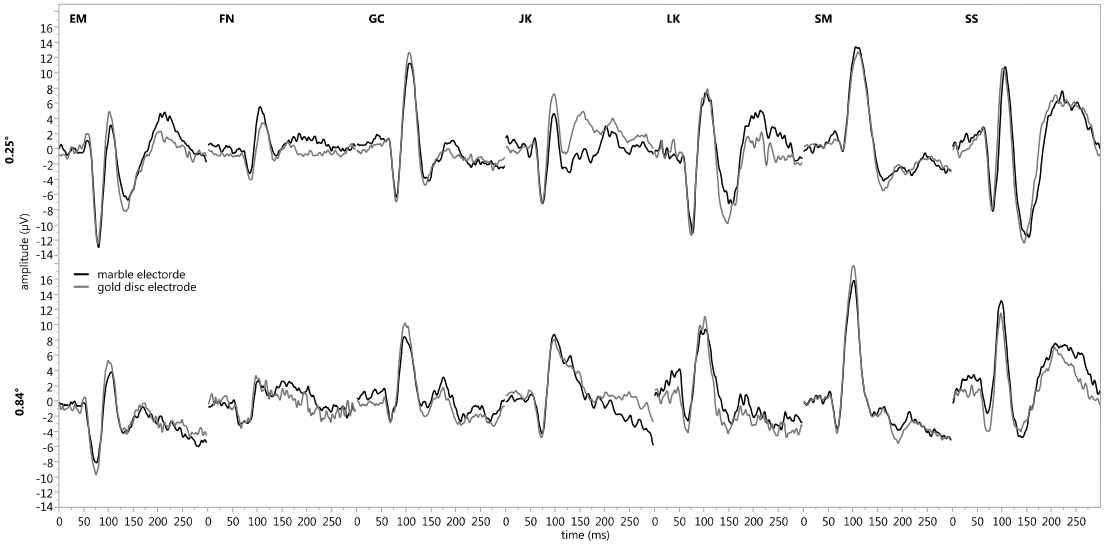

Figure 53: Individual VEP waveforms of the seven subjects (grand averages of 4 x 64 single sweeps). Recordings were done using conventional gold disc electrodes (grey traces) and marble electrodes (black traces). No cleansing or abrasion was used for the marble electrodes. Impedances were kept below 5 kΩ for recordings with gold disc electrodes, whereas it was about ten times higher for recordings with marble electrodes.

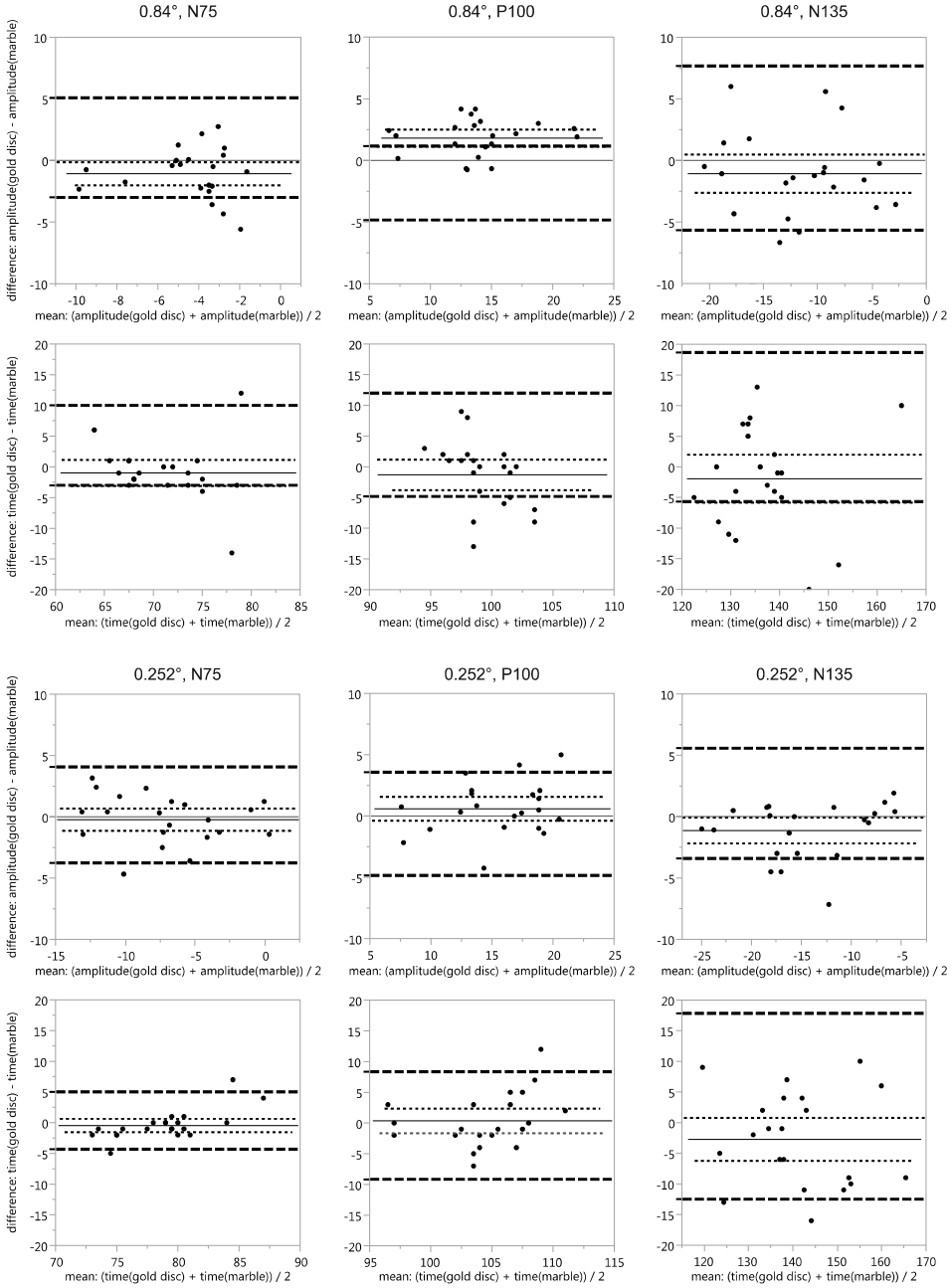

Figure 54: Comparison of amplitudes and peak times for N75, P100, and N135 for two check-sizes (0.84° and 0.25°), obtained using marble electrodes and conventional gold disc electrodes. The Bland-Altman plots show the relationship between the difference (Y-axis) and the mean (X-axis) of the results. Shown are the mean differences (solid black lines), the 95% confidence intervals (dotted lines) and the limits of agreement (dashed lines).

Table 11 lists mean and standard deviations for each cursor and check-sizes obtained using conventional gold disc electrodes and marble electrodes.

Table 11: Mean and standard deviation of VEP amplitudes and peak times of N75, P100, and N135, recorded using marble electrodes and conventional gold disc electrodes.

		Amplitude (µV) Mean ± SD		Peak time (ms) Mean ± SD	
Check-size	Cursor	Marble	Gold disc	Marble	Gold disc
0.84 °	N75	-3.84 ± 2.47	-4.88 ± 2.38	71.5 ± 5.4	70.6 ± 4.6
	P100	12.94 ± 3.97	14.79 ± 4.16	99.9 ± 4.4	98.7 ± 2.7
	N135	-11.16 ± 5.70	-12.19 ± 5.25	137.7 ± 10.1	135.9 ± 10.3
0.252 °	N75	-7.05 ± 4.45	-7.23 ± 4.07	79.0 ± 2.9	78.7 ± 4.6
	P100	15.25 ± 3.82	15.89 ± 4.34	104.3 ± 3.8	104.8 ± 5.2
	N135	-13.89 ± 5.71	-14.99 ± 6.18	142.5 ± 13.0	139.8 ± 12.1

N = 21, seven volunteers, four averages per subject

Paired-samples t-tests were conducted to compare the amplitudes and the peak times of each cursor for both check-sizes obtained using conventional gold disc electrodes and marble electrodes. The results of the paired-samples t-tests are given in Table 12.

A signifiant difference in the scores for amplitudes and peak times was seen only for the N75 and P100 amplitude for the check-size of 0.84° and for the N135 amplitude for the check-size of 0.252°. All other amplitudes and peak times did not show significant differences between conventional gold disc electrodes and marble electrodes. The limits of agreement (LoA), calculated according to Bland and Altman [145], are shown in Table 13.

Table 12: Results of the paired-samples t-tests comparing amplitudes and peak times obtained using conventional gold disc electrodes and marble electrodes. A significant difference was found for the amplitudes of N75 and P100 (0.84°) and N135 (0.252°)

		Amplitude		Peak time	
Check-size	Cursor	t-value	*p*-value	t-value	*p*-value
0.84 °	N75	-2.3055	.0320*	-0.8902	.3839
	P100	5.5771	< .0001***	-1.0395	.3110
	N135	-1.3883	.1803	-0.9885	.3347
0.252 °	N75	-0.4280	.6732	-0.7282	.4749
	P100	1.3705	.1857	0.44185	.6633
	N135	-2.1695	.0423*	-1.58512	.1286

N = 21, degrees of freedom = 20, * indicates p ≤ .05, ** p ≤ .01, *** p ≤ .0001

Table 13: Mean differences and 95 % confidence interval and Limits of Agreement between VEP amplitudes and peak times obtained using conventional gold disc electrodes and marble electrodes

		Amplitude			Peak time		
Check-size	Cursor	Mean difference	95 % CI	LoA	Mean difference	95 % CI	LoA
0.84 °	N75	-1.0381	-1.9774 -0.0988	-3.01 5.08	-0.9048	-3.0247 1.2152	-8.2 10.0
	P100	1.8519	1.1593 2.5446	-4.83 1.13	-1.2381	-3.7226 1.2464	-9.5 11.9
	N135	-1.0310	-2.5799 0.5190	-5.64 7.70	1.8788	-5.7763 2.0620	-15.0 18.7
0.252 °	N75	-0.1862	-1.0935 0.7212	-3.72 4.09	-0.3810	-1.4722 0.7103	-4.3 5.1
	P100	0.6419	-0.3351 1.6189	-4.85 3.56	0.4286	-1.5947 2.4519	-9.1 8.3
	N135	-1.0924	-2.1427 -0.0042	-3.43 5,.61	-2.6667	-6.1759 0.8426	-12.4 17.8

LoA = Limits of Agreement

2.4 Discussion

Visual evoked potentials have been recorded successfully in seven volunteer for two check-sizes using the newly developed marble electrodes and conventional electrodes. A Bland Altman analysis showed good agreement between the recordings of the marble electrodes and the conventional gold disc electrodes. Paired-samples t-tests did not show significant differences in amplitudes and peak times between recordings using conventional gold disc electrodes, except for N75 and P100 at a check-size of 0.84° and N135 at 0.252°. However, since the P100 amplitude is measured relative to the N75 amplitude [14], the significant difference of the N75 amplitudes may have led to a high significant difference of the P100 amplitude. The significant difference of the N135 amplitude may be explained by the inherent high variability of this parameter [146].

The mean differences of amplitudes and peak times between the conventional gold disc electrode and the marble electrode are in the range of the intra-subject variability published by several groups [147]–[152] and the limits of agreement were similar to those reported by Tello et al. for the repeatability of transient visual evoked potentials [153].

Interestingly, even though the single traces were strongly contaminated with lines noise, these artifacts could be removed almost completely using averaging, and had no effect on the measured amplitudes and peak times of the VEP. This is in line with the findings of Ferree et al. [140] and Kappenman and Luck [154], who found no significant difference between high impedance recordings and those with an impedance less than 5 kΩ, as recommended by ISCEV [59], [14].

Avoiding the need for cleansing and abrasion of the skin, increases patient comfort and significantly reduces the time for preparation. Additionally, it eliminates the risk of infection during abrasion of the skin [140]. Because the marble

electrode is disposed after the recording, time consuming disinfection or sterilization of the electrodes can be omitted as well.

In a previous study, we demonstrated the application of marble electrodes for the recording of electroretinograms in small animals (Strasser et al. IOVS2012; 2462). Additional use cases for the application of the marble electrode may be brain computer interfaces, since, in contrast to currently used electrodes, the marble electrode provides a higher wearing comfort (Surjo R. Sodekar, personal communication, June 2015).

Since marble electrodes consist of up to 99 % of water, they do not dry out, rendering them useful for long-time recordings, e. g. for brain computer interfaces or during functional magnetic resonance imaging.

Marble electrodes may also be used for trans-corneal electrical stimulation [155]. Several companies provide commercial devices (e. g. the OkuStim system, Okuvision GmbH, Reutlingen, German), which usually use modified versions of DTL electrodes [156]. These could be replaced by sterile marble electrode and therefore, ease the application for the patients.

2.5 Conclusions

This study has demonstrated, the potential of the marble electrode to replace conventional gold disc electrodes for the recording of visual evoked potentials. Using modern differential amplifiers and averaging, high-quality VEP recordings can be obtained without scalp abrasion. Their ease of use and their low costs may render them useful for other application domains, like brain computer interfaces or trans-corneal electrical stimulation.

VI SELECTED STUDIES

1 Ophthalmological assessment of cannabis-induced perception disorder: is there a direct retinal effect?

This text was published in Documenta Ophthalmologica in 2015: D. Zobor, T. Strasser, G. Zobor, F. Schober, A. Messias, O. Strauss, A. Batra, and E. Zrenner, "Ophthalmological assessment of cannabis-induced persisting perception disorder: Is there a direct retinal effect?," Doc. Ophthalmol., Jan. 2015.

1.1 Introduction

Hallucinogen persisting perception disorder (HPPD) is a temporary recurrence of disturbances in perception that are reminiscent of those experienced during one or more earlier intoxications with hallucinogens and includes many types of visual disturbances [157]–[169]. These perceptual changes can be halos around objects, difficulty in distinguishing between colors, alterations in color perception, geometric hallucinations, illusions that objects are moving or changing in size, "visual snow," or floaters [164], [165]. Some of these visual phenomena (e.g., floaters and afterimages) occur even in healthy subjects, who have never taken drugs [163], which makes the identification of HPPD difficult. Furthermore, the probability of developing HPPD after consuming a hallucinogen and its true prevalence are unknown, and the upper limit probably does not exceed 0.66 % according to literature [164].

Currently, although no effective treatment against these symptoms is available, some medications like diazepam or alprazolam seem to be helpful [167], [168]. It is generally recommended that patients should discontinue taking drugs and should also avoid caffeine and alcohol, which might have a negative

effect on HPPD [169]. In most of the cases, HPPD disappears spontaneously, but the duration can vary between individuals: Some patients have symptoms for months, but these can also last for years [161], [169]. Disturbances of visual perception following drug consumption are often unexplained, or symptoms can be misinterpreted [170].

Tetrahydrocannabinol (THC, marijuana, cannabis) is a psychotomimetic agent that induces impairment of sensory perception [157]–[160]. Although short-term effects on the visual system are well known [160], there is only little information on persisting visual disturbances [161], [162].

The activation of the cannabinoid receptors CB1 and CB2 in the visual cortex is certainly associated with the occurrence of perceptual changes [171], [172]. Nevertheless, there is evidence that direct activation of cannabinoid (CB) receptors in the retina can also play an essential role, since CB1 receptors have been found to be present in the retina as well [173], [174].

The activation of CB receptors has been associated with functional alterations in the three major retinal neurons: CB receptors were shown to reduce cyclic adenosine monophosphate (cAMP), which modulates voltage-dependent currents of cones [175], and therefore, they are suggested to modulate neurotransmitter release at the first synapse of the visual system [176]. A reciprocal inhibition of voltage-gated potassium currents by activation of cannabinoid CB1 in ON bipolar cells of goldfish retina has been reported [177], and at last, CBs can modify the excitability of retinal ganglion cells (RGC) [178]. All together, CBs might be able to mimic the light activation of photoreceptors, and therefore, CB1 and possibly CB2 expression may explain some of the CB-induced visual effects. Furthermore, the presence of CB receptors in human retinal pigment epithelium (RPE) has also been demonstrated [179], [180].

Some case reports mention normal retinal function in patients with HPPD [161], [162]; however, in none of them an extended electrophysiological evaluation was carried out. We hereby report detailed results observed in a patient, who claimed of cannabis-induced persisting perception disorder even after long period of marijuana abstinence. The results are compared with the findings of four heavy cannabis smokers without visual disturbances, serving as controls, and with our normative database.

1.2 Subjects

The research followed the tenets of the declaration of Helsinki, and the study was approved by the Ethics Committee of the University of Tübingen, Germany. Normal and control subjects were derived from the faculty, staff, and student body of the University, and the participating patient was recruited from the Department of Ophthalmology, University of Tübingen, Germany. All participants were included in the study after written informed consent. None of the subjects had suffered from psychotic symptoms or hallucinations before.

Patient

A 23-year-old male student complained of visual changes lasting for several years. He started smoking marijuana and cigarettes heavily at the age of 16 years. This period lasted uninterruptedly for about 4 years. Besides marijuana, he denied using any other drugs. He developed a persistent perception disorder despite discontinuing the use of cannabis a few months after the onset of his persistent visual symptoms. These included perception of visual snow, sperm-like whizzing dots, jittering lights, floaters, photophobia and visual discomfort, increased positive and negative afterimages, impaired night vision, increased halos, and starbursts around lights. These symptoms were so annoying that he

could not follow the lectures at the university. Besides a slightly elevated blood pressure, the clinical and neurological examinations including MRI did not reveal any altered result.

Controls

We recruited four young control subjects (one female, three male, mean age 25.5 years, range between 23 and 28 years) from our university, who considered themselves as heavy cannabis smokers, but denied any visual disturbances. The controls were otherwise healthy and had normal ophthalmological findings. Other drugs were not consumed.

1.3 Methods

A complete ophthalmological examination was carried out, including Snellen visual acuity, pupil reaction, Lanthony Panel D-15 color vision test, dark adaptation, visual field, and an extended electrophysiological examination.

Ganzfeld and multifocal ERGs were recorded according to the standards of the International Society for Clinical Electrophysiology of Vision (ISCEV) [60], [181], but additional stimuli were included to improve retinal function evaluation. All tests were performed using DTL electrodes with an Espion E² (Diagnosys LLC) recording device coupled with a ColorDome (Diagnosys LLC) as light source. After 30 min of dark adaptation, a series of responses to increasing flash intensities (4 ms—0.0001–10 cd.s/m2 in 0.5 log unit steps) were recorded, and the stimulus–response (S–R) functions modeled using the equation:

$$V(I) = \frac{V_{max} \cdot I^n}{(I^n + K^n)}$$

with the saturated b-wave amplitude V_{max}, the flash intensity K required for semi-saturation as a measure of retinal sensitivity, and the slope related exponent n [182].

With a question in mind, that the marijuana-induced alteration in CB receptor function may affect photoreceptor-RPE interaction, dark-adapted responses to a series of blue flicker (LED 470 nm) with an intensity of 0.03 cd.s/m² and frequencies between 5 and 30 Hz were recorded.

The light-adapted protocol (10 min of light adaptation to a background luminance of 30 cd/m2) included a single flash cone stimulus, ON–OFF measurements, and 30 Hz flicker (both: 4 ms, 3.0 cd.s/m²). In addition, responses to a flicker series with white stimuli of 3.0 cd.s/m² with increasing frequency from 5 to 45 Hz were included to investigate possible alterations in the temporal resolution of the cone retinal pathway.

Multifocal ERG (mfERG) was performed with a VERIS System (Version 5.1) using a Grass amplifier (model 12, Quincy, MA, USA) or with an Espion System (Diagnosys LLC). The stimulus, consisting of 61 scaled hexagonal elements covering a central visual field of 60 x 55°, was presented on a 19" monitor at a frame rate of 75 Hz at a distance of 32 cm from the subjects' eyes. Responses were amplified (200 000x), bandpass filtered (10–100 Hz), and analyzed according to ring averages.

Electrooculography (EOG) measurements were recorded with either the Tübinger EOG device or with the Espion E² (Diagnosys LLC) recording device coupled with a ColorDome (Diagnosys LLC) as light source in the controls according to the standards of ISCEV [8]. A fast oscillations protocol was included to extend functional evaluation of the RPE. The use of the two different devices was necessary due to modernization of the electrophysiology lab, but measure-

ment protocols were identical. Normal values were available for both devices, and results were compared with the appropriate data.

To test retinal sensitivity to electric stimulation, phosphenes were elicited by using a neurostimulator (Twister; Dr. Langer GmbH, Waldkirch, Germany) by means of DTL electrode as active electrode and a gold-plated cup electrode on the temporal skin connected to the negative pole. The neurostimulator was modified by the manufacturer to scale down current output. Impedance of the electrodes was tested using the built-in algorithm and at no time exceeded 5 kΩ. Measurements were performed in the dark; light was switched on periodically in order to avoid dark adaptation. Full darkness was necessary to perceive the very subtle phosphenes. A four-alternative forced-choice method was used for psychophysical determination of electrically evoked phosphene thresholds (EPT) in series of "biphasic positive" rectangular current pulses with duration of 1.0, 5.0, 25.0, and 50.0 ms [183].

Retrieved data were compared with the normal values obtained in the Centre for Ophthalmology—University of Tübingen Germany under standard conditions. The statistical analysis of the data was conducted by using the JMP 10 statistical software (SAS Institute Cary, North Carolina, USA).

1.4 Results

Patient

The ophthalmological examinations revealed hyperopia, although the patient had never needed glasses before. Best-corrected visual acuity was 1.25 (Snellen) on both eyes (RE: +2.0 sph -0.25 cyl 95°; LE: +1.75 sph -0.25 cyl 115°). The range of accommodation was six diopters on both eyes. Neuroophthalmic examina-

tions, color vision tests, and dark adaptation thresholds did not show any abnormalities. No relative afferent pupillary defect (RAPD) has been observed. Anterior segment and fundus appearance were completely normal, and intraocular pressure was 10 mmHg in both eyes.

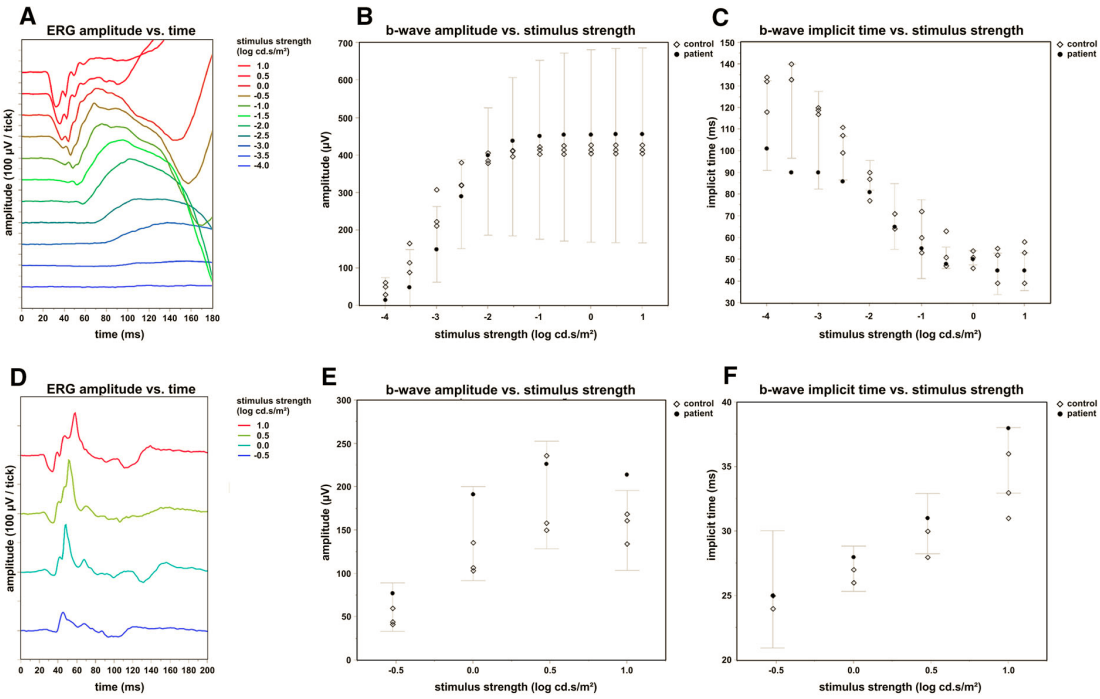

Figure 55: Ganzfeld ERG results. The scotopic (A) and photopic (D) ERG responses of the patient to increasing stimulus intensities showed normal waveforms. Scotopic b-wave amplitudes (B) and implicit times (C) were within normal limits for the patient and for all control subjects, such as amplitudes (E) and implicit times (F) of the photopic responses. The bars indicate the normal range, the filled circles represent results of the patient, and the diamonds represent results of the controls measured (n = 3) (From: Zobor, Strasser, et al., 2015)

Ganzfeld dark- and light-adapted ERG responses a- and b-wave amplitude and implicit times, oscillatory potentials and parameters V_{max} and K, light-adapted responses, single flash cone, ON–OFF responses, and all flicker frequencies were within normal ranges in both eyes (Figure 55). Multifocal ERG response amplitudes and implicit times were also normal.

The EOG showed a slightly reduced fast oscillations ratio (FO ratio = 1.08 and 1.15 on right and left eyes, respectively), and the slow oscillations EOG showed diminished trough standing potentials (6.0 and 6.45 µV/deg in the trough before onset of light) with a peak within the norm values (23.79 and 19.16 µV/deg) with Arden ratios of 3.967 and 2.97, respectively (14; Figure 56).

Table 14: EOG Results of the patient

			Normal range	
	OD	OS	N 5 % quantile	N 95 % quantile
Fast oscillation max. (µV/deg)	11.93	12.84		
Fast oscillation min. (µV/deg)	11.01	11.14		
Fast oscillation ratio	1.083[a]	1.152[a]	1.18	1.48
Slow oscillation (Arden)	3.967a	2.97	2.08	3.0
Peak (µV/deg)	23.79	19.16[a]	20.6	45.1
Trough (µV/deg)	6.0[a]	6.45[a]	9.2	19.2

The EOG showed slightly reduced fast oscillations ratios, and the slow oscillations showed diminished trough standing potentials with nearly normal peak values, resulting in higher Arden ratios for both eyes. The four control subjects were all within normal limits. The absolute values of the peak and trough standing potentials (in µV) can be calculated by multiplying the peak and trough values (given in µV/deg in the table) with 30 degrees, in accordance with the ISCEV Standards (From: Zobor, Strasser, et al., 2015)

N = normal, OD = right eye, and OS = left eye

[a] Pathologic result

The phosphene thresholds were considerably reduced (15; Figure 56), i. e., the patient needed less current to cause phosphene sensations in both eyes, in particular for pulses with long durations (50 ms) where the subject could refer visual sensations even by the minimal current that can be produced with the neuro-stimulator (0.001 mA).

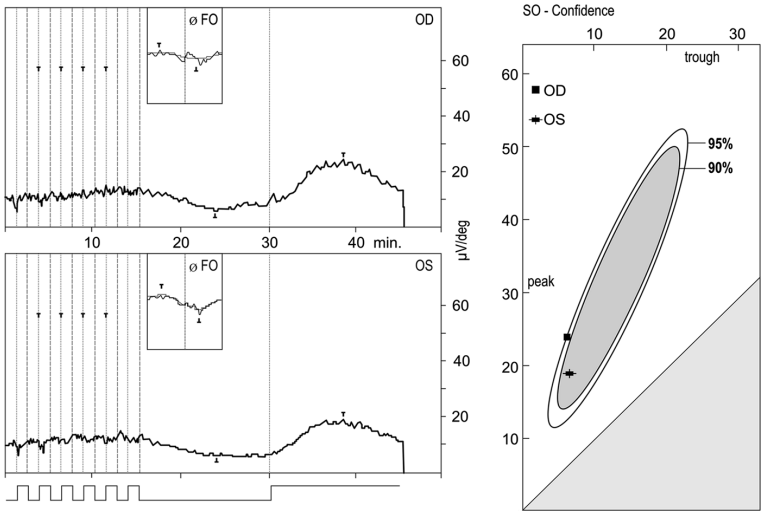

Figure 56: EOG results of the patient. While fast oscillations (FO) were reduced, slow oscillation (SO) ratios were rather above the normal limit due to reduced trough standing potentials and a peak within the norm values (From: Zobor, Strasser, et al., 2015)

Controls

Best-corrected visual acuity was 1.0 (Snellen) in the control subjects, and visual field tests showed normal results. Neuroophthalmic examinations, color vision tests, and dark adaptation thresholds were within normal limits.

Table 15: Electrically evoked phosphene threshold (EPT) results of the patient and control subjects

Pulse duration (ms)	Threshold (mA)						
	P1 OD/OS	C1 OD/OS	C2 OD/OS	C3 OD/OS	C4	N 5 % quantile	N 95 % quantile
1	0.2/0.3	0.05/.007	0.2/0.55	0.2/0.02[a]	n.a.	0.1	0.55
5	0.01[a]/0.02	0.07/0.2	0.14/0.18	0.02/0.02	n.a.	0.02	0.15
25	<0.0001[a]/0.0005[a]	0.1/0.07	0.036/0.055	0.026/0.03	n.a.	0.01	0.1
50	<0.0001 OU[a]	0.08/0.07	0.06/0.06	0.007[a]/0.018	n.a.	0.01	0.1

The EPTs of the patient were reduced, in particular for pulses with long durations (50 ms) causing visual sensations even at lowest possible currents of the neurostimulator. The control subjects did not reveal such alterations (From: Zobor, Strasser, et al., 2015)

n.a. = not available, N = normal, OD = right eye, OS = left eye, OU = both eyes
[a] Pathologic result

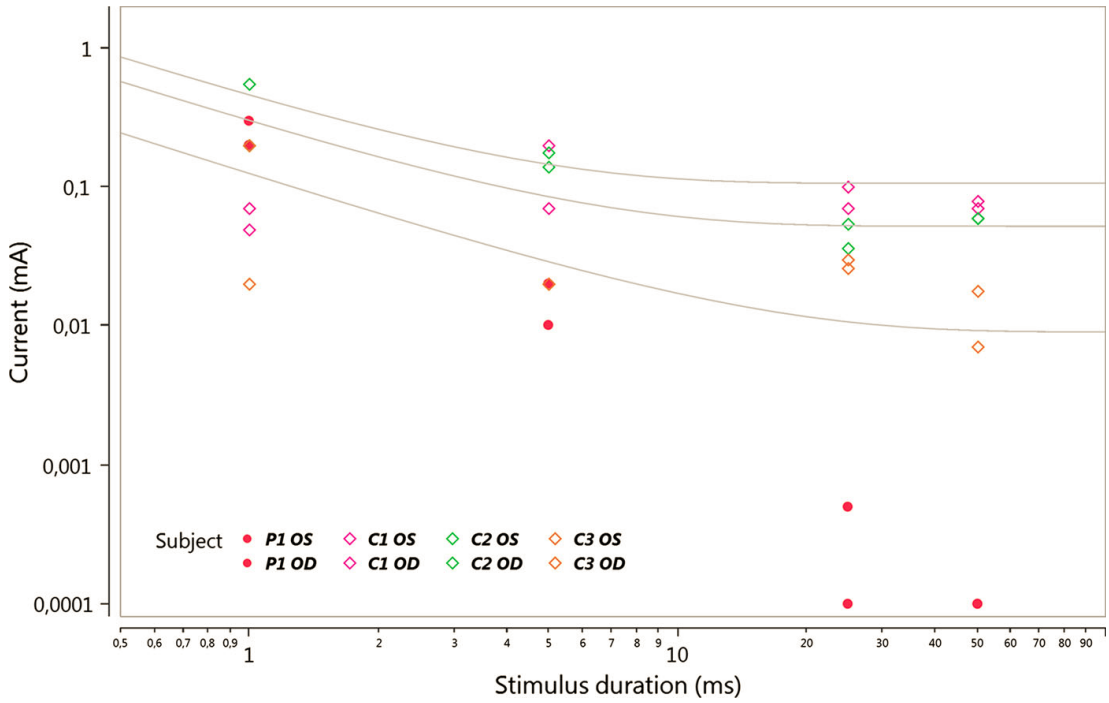

Figure 57: Strength–duration curve in a double-logarithmic representation of electrically evoked phosphene thresholds (EPT). We observed a massive reduction of phosphene rheobase in the patient, when measuring the threshold current required to elicit visual sensation. Control subjects - who denied any visual disturbances - showed normal EPT results. Red filled circles represent the EPT values of the patient, and empty diamonds (*pink*, *green*, and *orange*) show results of the control subjects (From: Zobor, Strasser, et al., 2015)

No RAPD was detected. Anterior segment and fundus appearance were completely normal, and intraocular pressure was within normal limits in every case. Ganzfeld and multifocal ERGs were not altered (Figure 55), and EPT measurements were also normal (15; Figure 57). The EOG measurements showed baseline values in the upper normal values of the fast oscillations in every control subject, and other parameters were inconspicuous.

1.5 Discussion

Different cannabis products, marijuana and hashish (concentrated form), are considered to be natural hallucinogens and are derived from the hemp plant (Cannabis sativa). Marijuana, a green herb from the flower, is considered a mild hallucinogen in comparison, for example, with LSD. Both drugs are usually smoked, and their effects include a feeling of relaxation, faster heart rate, the sensation that time is passing more slowly, and augmented sensory experiences concerning hearing, taste, touch, and smell.

Epidemiological studies show that marijuana is still a widely used illicit drug particularly in youth in many countries, and during the past decades, there is a growing interest on its potential side effects [184]–[187].

While the acute and short-lasting effects are relatively well described, questions and controversy remain on possible chronic and long-term effects. HPPD has been relatively well described for LSD [157], [166]–[168], [188], but it is not clearly known, whether cannabis can also provoke it. Diagnosis of cannabis-induced HPPD may be considered in rare cases following a full diagnostic workup to exclude other disorders, such as temporal lobe epilepsy or cortical tumor, presence of systemic disorders with cerebral effects, such as systemic lupus erythematosus, head trauma, intraocular pathology, and multiple sclerosis, or the use/interruption of other concomitant drugs or toxic exposures (heavy metals, insecticides, other aerosolized hydrocarbons, arsenic, and bromism) [160]–[162], [188].

The patient presented here did not show any systemic or ocular disorder, and as previously described in other reports [161], our standard ophthalmological examinations did not reveal any functional or morphological ocular alteration either. Responses in Ganzfeld and mfERG were also within normal limits, and

therefore, it seems reasonable to assume that the systems that are mostly responsible for the ERG response generation (phototransduction and postreceptoral signaling) in both rod and cone pathways are physiologically normal.

Surprisingly, alterations in two other electrophysiological examinations did show up. We observed a massive reduction of phosphene rheobase, when measuring the threshold current required to elicit visual sensation. Although there is ongoing debate on the exact site of electrical stimulation within the retina and some have argued that the photoreceptors are preferentially driven, evidence is emerging that photoreceptors and their synapses to bipolar cells are the preferential target because even retinas without any functioning photoreceptors can be stimulated within reasonable thresholds [183]. We know that CB1 receptor is expressed at the pre-synaptic site, where it inhibits voltage-gated Ca^{2+} channels and thus reduces the pre-synaptic neurotransmitter release, indicating that this receptor is an important regulator of synaptic transmission in the retina [189]. The markedly increased sensitivity to electrically evoked phosphenes in cannabis-induced HPPD suggests altered mechanisms of the signal transmission in the retina that may cause hyperexcitability, e.g., in response to the permanently ongoing spontaneous activity of neurons in the retina. A further alternative could be a reduced outer blood retinal barrier integrity that may account for the phosphenes being visible at low currents. Taken the RPE's resistance is low, the current could trigger bipolar cell activity more easily as the resistive path to the outer retina is reduced. Moreover, psychophysical examination involving central visual processing might also be associated with specific psychophysiological responses, since long-term heavy cannabis users show changes both in cortical and peripheral reactivity [190]–[192]. There-

fore, a direct effect of CBs on the retinal function is suggested to be involved in disturbances of the visual function experienced after drug consumption.

Further, clinically measurable alterations were observed in the EOG. We reported reduced trough standing potentials and reduced fast oscillations ratios in the patient. The EOG is an electrophysiological test of function of the outer retina and RPE in which the change in the electrical potential between the cornea and the ocular fundus is recorded during successive periods of dark and light adaptation. This potential is mainly generated by the RPE and depends on the ion permeability across its basal membrane [8]. So far, several different ion channel types have been suggested to be involved in the generation of these potentials: Cl^- channels and L-type channels of the neuroendocrine subtype seem to have an important role [8], [193]. Changes in the EOG in Best's disease caused by alterations of bestrophin-1, a Cl^- channel, indicate the involvement of Cl^- channel in the EOG [193]. Mice deficient of neuroendocrine L-type channels show reduced standing potential in direct measurements. Recently, Wei et al. [179] showed the presence of CB1 and CB2 receptors in human RPE cells, suggesting a key role for the endocannabinoid system in neurodegenerative disorders. As the RPE expresses both cannabinoid receptors, it is likely that the observed changes are due to cannabinoid-dependent modulation of the ion channels in the RPE. CB1 receptor is known to modulate different ion channels: such as inhibition of L-type channels [194] or activation of TRPV1 and TRPV2 cation channels [195]. L-type channels [196] and TRPV1 and TRPV2 channels are expressed by the RPE. In the RPE, it has been shown that cannabidiol leads to increase in intracellular free Ca^{2+} though activation of TRPV2 channels [180]. Thus, it is possible that acute stimulation of the RPE by reminiscent CB receptor agonists or their metabolites could be responsible for the observed changes by an increase in intracellular free Ca^{2+} which in turn can lead to activation of

ion channels such Ca^{2+}-dependent Cl^- channels in the basolateral membrane. Activation of Ca^{2+}-dependent Cl^- channels in turn is known to generate the increased basolateral Cl^- conductance which is the base for the light rise in the EOG [197]. This might explain the observed changes in the EOG. In addition to this acute effect, sustained effects are also likely to be responsible for the observation. There are several reports about long-term effects of prolonged stimulation by CBs in the neuronal system [198], which may be explained with changed ion channel gene expression dependent on modulation of Ca^{2+} channel activity. It should be noted that also stimulation of CB1 leads to an increased surface expression of TRPV2 channels, which would generate a long-term effect [199]. We presume that due to CB receptor overstimulation the basolateral membrane shows a lower Ca^{2+}-dependent Cl^- conductance, probably due to decreased L-type channel activity causing lower basal Ca^{2+} levels. This in turn decreases the activity of Ca^{2+}-dependent Cl^- channels and conductance for Cl^- of the basolateral membrane, which would explain in part the reduced standing potential and the reduced FO, since the same change in intracellular Cl^- in the RPE would result in less hyperpolarization of the basolateral membrane. Thus, we believe not in a direct contribution of Ca^{2+} in the generation of the FO but a changed generation of the FO due to less basal Ca^{2+}-dependent conductance of the basolateral membrane.

Another possible explanation for a reduced standing potential in the EOG could be a reduced resistance between the basal and apical membranes. The RPE cells are connected by tight junctions, so the resistance across the layer is quite high. These tight junctions are regulated by Ca^{2+} and Ca^{2+} homeostasis. Should Ca^{2+} homeostasis in cannabis users be abnormal, the reduced standing potential could also be explained by a reduced resistance between the basal and

apical membranes. Alternatively, should tight junctions be not affected, reduced FOs could occur, if the apical voltage would be approximately equal to the basal voltage with the consequence that there would be less shunt current to develop the light trough of the FOs.

Thus, the observed changes in the EOG might be related to a different ion channel expression profile in the RPE of the patients, which could also explain why the EOG results of control subjects were within normal limits and why there are limited studies on cannabis induced HPPD despite its widespread use. In some cases, HPPD appears to have a sudden onset after a single drug experience, strongly suggesting the drug played a direct role in triggering symptoms. But in other cases, people report gradual worsening of symptoms with ongoing drug use. It is possible that the prevalence of HPPD is underestimated by authorities because many people with visual problems relating to drug use either do not seek treatment or, when they do seek treatment, do not admit having used illicit drugs. Thus, it may be that HPPD occurs more often than is detected by the health care system.

However, the exact chain of events, possibly at multiple sites (retinal as well as cerebral) in cannabis induced HPPD, remains unexplained. The observations presented here in relation to electrophysiological events as well as in relation to Cl^- channels may contribute to the elucidation of the detailed mechanism. Up to now, there are no randomized controlled trials to investigate visual function or test treatment possibilities against HPPD regardless the hallucinogenic drug that caused it. EOG and EPT measurements could be useful tools to demonstrate retinal alterations in cannabis-induced HPPD.

2 A refined method for analyzing the sweepVEP for objective estimation of the visual acuity

2.1 Introduction

Visual acuity (VA) is one of the most important parameters for testing visual ability. Its preservation or improvement is the endpoint for most ophthalmic treatments. Additionally, many legal regulations (e. g. a driving licence) require a minimum visual acuity. Visual acuity is typically carried out with the help of visual acuity charts (ETDRS or Snellen) with optotypes with defined properties (shape, size, contrast) that the subject must identify from a fixed distance. This allows a simple and rapid determination of visual acuity. Alternatively, there are other, partially automated, methods for the determination of visual acuity, such as the Freiburg Visual Acuity and Contrast Test (FrACT) [200]. Common to these methods is the need for cooperation of the subject, so that only a subjective assessment of visual acuity is possible. This is a disadvantage in cases where subjects are not, willfully or unwillfully, able to cooperate (e. g., patients with functional vision problems, the mentally disabled, malingerers).

An objective method for determining visual acuity is based on the measurement of electrical potential changes in the visual cortex during visual stimulation, the so-called visual evoked (cortical) potentials (VEP or VECP). The visual stimulus is an achromatic checkerboard pattern, with varying field size and periodic stimulus contrast reversal. Visual acuity correlates with the measurable potentials as a function of field size and with the spatial frequency of the checkerboard pattern [201], [202]. The maximum resolvable spatial frequency is mainly limited by visual acuity, which can thus be determined. This method is

known as VEP acuity (or visual acuity VECP) and has been in clinical use since the 1980s. In the literature there are different methods of VEP acuity techniques with respect to the stimulus parameters (e. g., temporal configuration, contrast, spatial frequency), as well as in analysis of the measured potentials.

However, in general, visual acuity can be only determined with a degree of uncertainty using the VEP acuity method. This is due to inherent noise in electrophysiological recordings and because of anatomical variation between subjects (e. g., skull thickness, brain topography). The main objective of this work is to develop a new method for the objective assessment of visual acuity by optimizing the stimulus used in commercially available systems and by improving the methods of evaluation. The aim is to develop a simple but more reliable method for the objective assessment of visual acuity that can be carried out with standard equipment used routinely in the clinic.

2.2 Methods

Subjects

Thirty-five healthy subjects (age 18 – 69 years, mean 42 years, 20 males, 15 females), in total 67 eyes, participated in the study. None of the subjects exhibited ocular or systemic pathology, and a general ophthalmic examination and standard VEP, according to the ISCEV standard [14], showed no abnormalities.

For at least one eye of each subject, the best-corrected visual acuity (BCVA) was measured using visual targets (Snellen) presented with a projector (Chart Projector CP-500), and a sweepVEP was recorded. The measured best corrected visual acuity was better than 0.8 (decimal) in all subjects.

The sweepVEP was recorded monocularly. If both eyes of a subject were measured, the recordings were carried out sequentially.

Three subsets of the subjects were defined. Two of them underwent more detailed examinations: in subset A (n = 9, 17 eyes), vision was degraded artificially using plus lenses of increasing strength (+1 D, +2 D, +3 D). For each strength, visual acuity was measured and a sweepVEP was recorded.

In subset B (n = 7, 13 eyes), the visual acuity and sweepVEP were measured with best corrected as well as with uncorrected visual acuity.

Subset C (n = 19, 37 eyes) consists of the remaining subsets. Subjective visual acuity and SweepVEP were determined only with best corrected visual acuity.

All subjects gave informed consent for the study, and this research followed the tenets of the Declaration of Helsinki [130]. The protocol for this study was approved by the local ethics committee.

Visual Stimulation

The used stimulus paradigm is based on the sweepVEP, originally described by Hajek and Zrenner [19]. It extends the original paradigm by adding six more checkerboards, resulting in a total of eleven checkerboards with increasing spatial frequencies.

The check sizes of the checkerboards were calculated in logarithmically equidistant steps and rounded to the nearest whole-numbers of pixels. Using a viewing distance of 1.6 m and a desired visual angle of the checkerboards of about 5.7°, the following eleven dominant spatial frequencies (according to Fahle and Bach [31]) were selected for the checkerboards: 0.6, 0.9, 1.4, 2.1, 3.3, 4.9, 7.3, 10.4, 18.2, 24.4, and 36.5 cycles per degree (cpd).

The stimuli were generated using a custom Java™ based software, running on a notebook, and presented using a 21" CRT monitor (Model V999, Elonex, Birmingham, UK). The luminance of the white and dark checks of the checkerboards was controlled using a spectrometer (LS-100, Konica Minolta, Tokyo,

Japan) and set to a Michelson [203] contrast of 62 %. The space-averaged mean luminance during stimulus presentation and inter-stimulus intervals was ~ 30 cd/m².

Each checkerboard is presented for 40 ms, followed by a pause of 300 ms, resulting in a total duration of 3.74 s for the complete sequence. The sequence is repeated 50 times. To ensure subject alertness, random digits from 0 to 9 appear in random intervals at the center of the screen and the subject are asked report the number seen [20].

Figure 58 depicts the time course of the used stimulus paradigm and the spatial frequencies of the checkerboards along with an average of 50 single VEP responses of subject 53 (BCVA).

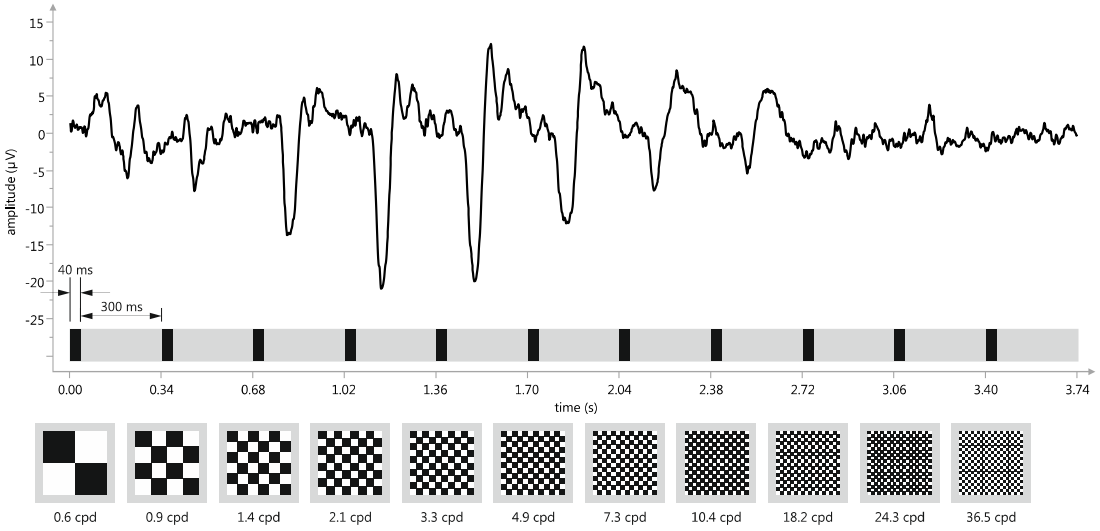

Figure 58: Time course and the eleven spatial frequencies of the used stimulus paradigm. Each checkerboard is presented for 40 ms (black rectangles), followed by an inter-stimulus interval of 300 ms. The space-averaged mean luminance was kept constant at 35 cd/m² during the complete sequence. The complete sequence was repeated 50 times. The chart shows an average of 50 single VEP responses to the full stimulus sequence.

Data Acquisition

The VEP was recorded using an electrophysiology recording system (Espion e², Diagnosys LLC, Cambridge, UK).

Gold-cup electrodes were mounted according to the ISCEV standard for VEP [14] using the International 10-20 system [204]: the active electrode was placed over the visual cortex at Oz, the reference electrode on the forehead at Fz. The ground electrode was placed on the vertex at Cz. Impedances were checked before the start of the recording and kept below 5 kΩ.

The signals were digitized with a sampling frequency of 1 kHz with 24 bits of resolution and filtered using a digital band-pass filter (0.625 – 100 Hz).

At the beginning of the recording of a trace, a trigger was sent to the stimulation software to start the stimulus sequence.

Data Analysis

Fifty band-pass filtered (0.625 – 100 Hz) traces were averaged to improve the signal-to-noise ratio, whereby the recording time of 3.74 s ensured the suppression of periodic hum noise [205]. The signals shows the typical “spindle” shape (Figure 58) [206].

Cursors were placed to the peak and troughs of the signal using an automated multi-scale based peak detection algorithm [50] implemented in ERG Explorer [40], and manually adjusted if necessary. Peak amplitudes were calculated relative to the preceding trough and exported along with the spatial frequencies of the checkerboards for further processing. Data were exported for further processing using iDSL4SigProc [207].

The exported peak amplitudes were plotted against the spatial frequency, and a model based on the generalized Ricker model (Equation 5) [208], [209] was fitted to the data using a nonlinear least-squares technique.

$$f(SF) = \left(A_{max} - A_{noise}\right) \cdot \left(\frac{SF}{SF_{max}}\right)^{shape} \cdot e^{1 - \left(\frac{SF}{SF_{max}}\right)^{shape}} + A_{noise} \qquad (5)$$

$$with\ A_{noise} > 0 \text{ and } 0 < shape < 2$$

The original model described by Ricker was modified to allow for a more descriptive interpretation of the estimated parameters: SF_{max} (cpd) is the spatial frequency at which the VEP amplitudes reach their maximum A_{max} (µV). A_{noise} (µV) represents the asymptotic amplitude of the spontaneous EEG amplitudes, here considered as background noise. The dimensionless parameter *shape* controls the "width" of the Ricker function. The value restrictions for the parameters noise and shape prevent a degradation of the model.

Equation 5 results in estimates for the spatial frequency of the maximal amplitude, the maximal amplitude, and the level of noise of the sweepVEP recording. However, there is no easy way to extract the limiting spatial frequency, used to estimate the visual acuity of the subject. In order to calculate the limiting spatial frequency, a second order polynomial is constructed using the estimated parameters A_{max}, and SF_{max}, as well as spatial frequency $SF_{max/2}$, at half the maximum amplitude A_{max} using the parabola vertex form:

$$f(SF) = \frac{\frac{A_{max}}{2} - A_{max}}{\left(\log 10(SF_{max/2}) - \log 10(SF_{max})\right)^2} \cdot \left(\log 10(SF) - \log 10(SF_{max})\right)^2 + A_{max} \qquad (6)$$

Equation 6 can be simplified to:

$$f(SF) = \frac{-\frac{A_{max}}{2}}{\left(\log_{10}(SF_{max/2}) - \log_{10}(SF_{max})\right)^2} \cdot \left(\log_{10}(SF) - \log_{10}(SF_{max})\right)^2 + A_{max} \tag{7}$$

The spatial frequency at half the maximum amplitude $SF_{max/2}$ is calculated using the inverse function of Equation 5:

$$SF_{max/2} = SF_{max} \cdot \sqrt[shape]{-W_{-1}\left(\frac{-e^{-1} \cdot \left(-\frac{A_{max}}{2} - A_{noise}\right)}{\left(A_{max} - A_{noise}\right)}\right)} \tag{8}$$

W_{-1} denotes the Lambert W function [210], also called omega function or product logarithm[31], which is the inverse of functions of the type $f(x) = x \cdot e^x$. Since the Lambert W function is not injective, only the left branch, indicated by the subscript -1, is used to calculate the corresponding spatial frequency $SF_{max/2}$ of the half of the maximum amplitude A_{max}.

Solving the quadratic Equation 7 for zero results in Equation 9, which gives the two spatial frequencies at the intersections of the second order polynomial with the abscissae.

$$SF_{\{1,2\}} = 10^{\log_{10}(SF_{max}) \pm \sqrt{2} \cdot \left(\log_{10}(SF_{max/2}) - \log_{10}(SF_{max})\right)} \tag{9}$$

Considering only the second solution of Equation 9, this leads to Equation 10 to calculate the limiting spatial frequency SF_0:

$$SF_0 = SF_{\{2\}} = 10^{\log_{10}(SF_{max}) + \sqrt{2} \cdot \left(\log_{10}(SF_{max/2}) - \log_{10}(SF_{max})\right)} \tag{10}$$

In addition to the limiting spatial frequency, using the estimated parameters of the modified generalized Ricker model, the quality of the recording can be de-

31 Most mathematical software packages include the Lambert W function. Implementations for several programming languages are available. Barry et al. [1] compare several approximations of the Lambert W function.

termined by defining a signal-to-noise ratio based on the maximum amplitude A_{max} and the level of *noise*. Therefore, a new parameter *SNR* is introduced in Equation 11:

$$SNR = 10 \cdot \log_{10}\left(\frac{A_{max}}{noise}\right) \text{dB} \tag{11}$$

This parameter allows the expression of the quality of a recording in a single common value. If the maximum amplitude decreases close to the noise level, the SNR will converge to 0 dB.

Statistical analysis

Nonlinear fitting and statistical analysis was carried out using JMP®, Version 11 (SAS institute Inc., Cary, NC).

A simple linear regression was used to predict the visual acuity based on the calculated limiting spatial frequency. The agreement between the predicted visual acuity and the subjective visual acuity was compared using a Bland-Altman plot [145], [211], [212] and a matched-pairs t-test of the means of the differences.

2.3 Results

The subjective visual acuity for the subjects of subset A with artificially degraded visual acuity are displayed in Table 16 and for subjects of subset B with uncorrected visual acuity in Table 17. All acuities are given in decimal units.

Table 16: Demographics and visual acuity for different levels of degradation of the visual acuity using plus lenses of 9 subjects of subset A. Missing entries were not collected for the subject.

			BCVA		+ 1 D		+ 2 D		+ 3 D	
subject	age	sex	OS	OD	OS	OD	OS	OD	OS	OD
02	31	f		1.0		0.7		0.4		0.16
15	48	f	1.5	1.25	0.63	0.63	0.4	0.4	0.16	0.16
18	18	m	1.6	1.6	0.8	0.8	0.2	0.2	0.1	0.1
27	42	f	1.25	1.25	0.8	0.8	0.32	0.32	0.16	0.16
29	25	m	1.0	0.9	0.4	0.4	0.16	0.2	0.1	0.1
30	28	m	1.25	1.25	0.7	0.7	0.4	0.4	0.2	0.2
40	23	f	1.0	1.0	0.4	0.7	0.2	0.32	0.08	0.16
51	27	m	1.0	1.0	0.4	0.4			0.16	0.16
53	35	m	1.0		0.63		0.25		0.1	

Values for visual acuity are specified in decimal notation.

Table 17: Demographics and visual acuity for uncorrected and best corrected visual acuity 7 subjects of subset B. Missing entries were not collected for the subject.

			uncorrected VA		BCVA	
subject	age	sex	OS	OD	OS	OD
4	27	f		0.32	1.0	1.0
6	57	m	0.32	0.32	1.25	1.25
11	60	f	0.7	0.4	1.0	1.25
16	43	m	0.4	0.3	1.0	1.25
26	69	f	0.5	0.5	1.0	0.9
35	50	m	0.4	0.4	1.25	1.25
57	68	m	0.4	0.4	1.25	1.25

Values for visual acuity are specified in decimal notation.

Transforming the visual acuities from the decimal scale to the logMAR scale reveals a linear relationship between visual acuity and the degree of degradation. The logMAR visual acuity is calculated from the decimal visual acuity using the following equation:

$$logMAR\ VA = -\log10(decimal\ VA) \tag{12}$$

Figure 59 shows a linear regression fit of the degree of artificial degradation of the visual acuity using plus lenses with the measured logMAR visual acuity of the subjects of subset A. A significant regression equation was found ($F(1, 57) = 537.44$, $p < .0001$). The predicted logMAR visual acuity is equal to -0.0678 + 0.3134 * degree of degradation in diopter. BCVA is taken as 0 diopter. As a rule of thumb, for each added diopter, the logMAR visual acuity increases about three times.

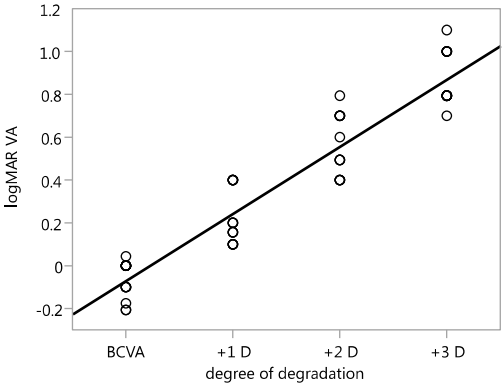

Figure 59: Measured visual acuity of subjects of subset A with BCVA and three degrees of artificially degraded visual acuity using plus lenses. A significant regression equation was found ($F(1, 57) = 537.44$, $p < .0001$), with an R^2 of .9041: logMAR VA = -0.0678 + 0.3134 * degree of degradation in diopter. As a rule of a thumb, for each diopter added, the logMAR visual acuity triplicates.

In Figure 60, a set of sweepVEP recordings of subject number 40 for best corrected visual acuity (top) and three degrees of artificially degraded visual acuity (from top to bottom: +1 D, +2D, +3 D) is shown. In each recording, a series of checkerboards with increasing spatial frequencies from 0.6 cpd to 36.5 cpd were presented for 40 ms, followed by a pause of 300 ms. The ticks at the abscissae indicate the start of the each stimulus presentation. The stimulation results in a typical “spindle” shape, whose maximum shifts to the left (i. e. to lower spatial frequencies) as the degradation of the visual acuity is increased.

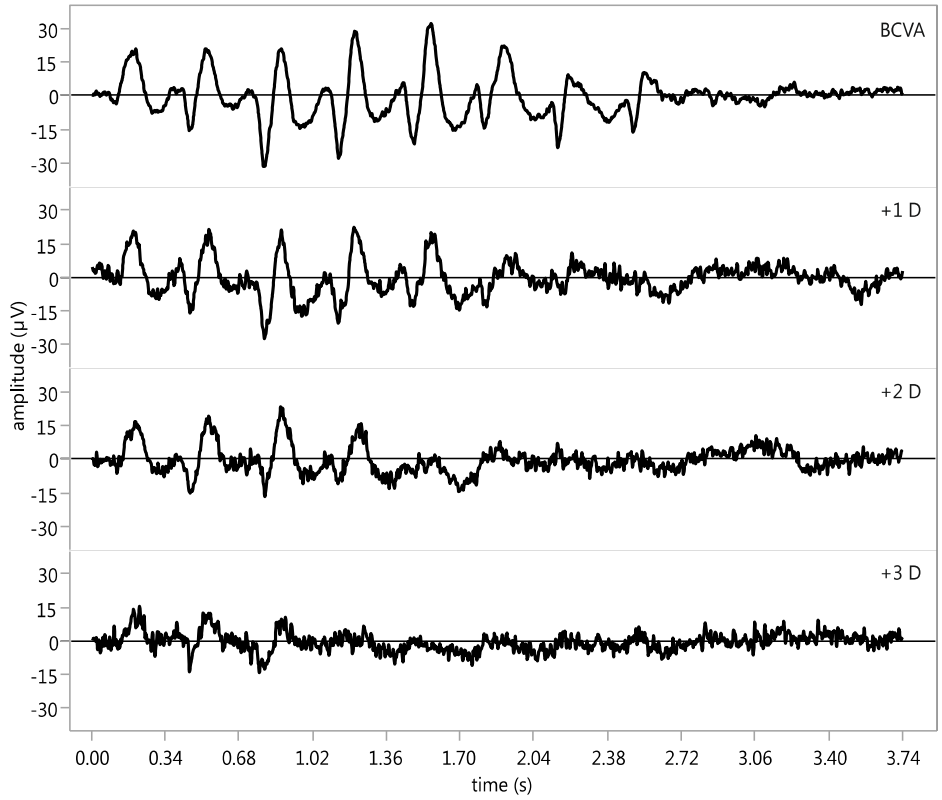

Figure 60: Original traces of sweepVEP recordings from subject number 40 with BCVA and three different degrees of artificially degraded visual acuity. All recordings show the typical "spindle" shape. However, with increasing degree of degradation, the amplitude decreases and the peak amplitude appears earlier at lower spatial frequencies. At higher spatial frequencies, single peaks cannot be distinguished from the spontaneous oscillations.

Figure 61 depicts the results of fitting the modified generalized Ricker model (dashed line) to the peak-to-trough amplitudes (circles) of the same subject. With an increase of the degradation of the visual acuity, the spatial frequency of the maximum response as well as its amplitude are are both decreasing. The level of noise does not change much. The figure also shows second order polynomial (solid line), calculated using the estimated parameters of the model, as well as the limiting frequency SF_o, which is determined as the second zero point of the parabola. The limiting spatial is decreasing as the degree of degradation is increased.

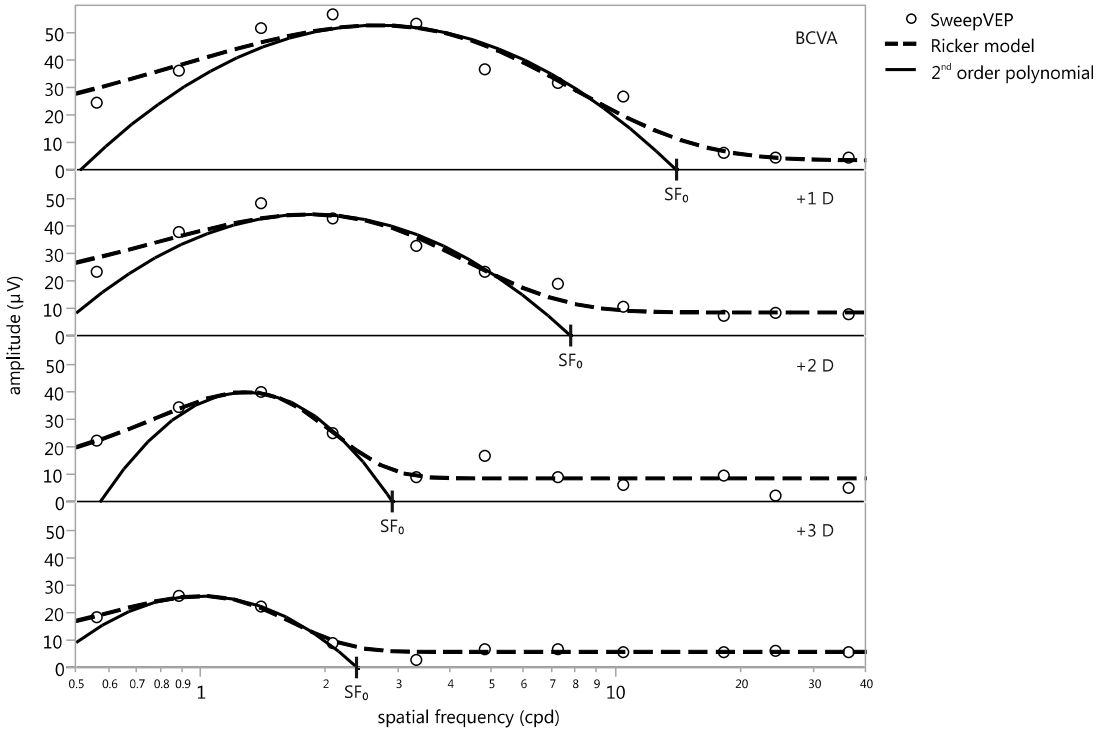

Figure 61: Tuning curves of subject number 40, recorded with BCVA and artificially degraded visual acuity. The recorded amplitudes of the sweepVEP are shown as circles. The dotted line represents the fitted Ricker model, the thick black line the second order polynomial, which was calculated using the estimated parameters of the Ricker model. The second zero point of the second order polynomial is used to determine the limiting spatial frequency SF_0. The SNR for the recordings were (from top to bottom): 12 dB, 7 d, 7 dB, and 6 dB.

The limiting spatial frequency was determined using the described method for all subjects of the subsets A and B and a simple linear regression between SF_0 and the subjective visual acuity was fit to the data. Figure 62 shows the results of the linear regression. The plot contains data of uncorrected visual acuity and best corrected visual acuity, as well as data of three degrees of artificially degraded visual acuity using plus lenses: circles indicated measurements with best corrected visual acuity, diamonds with uncorrected visual acuity, the other symbols represent measurements of artificially degraded visual acuity.

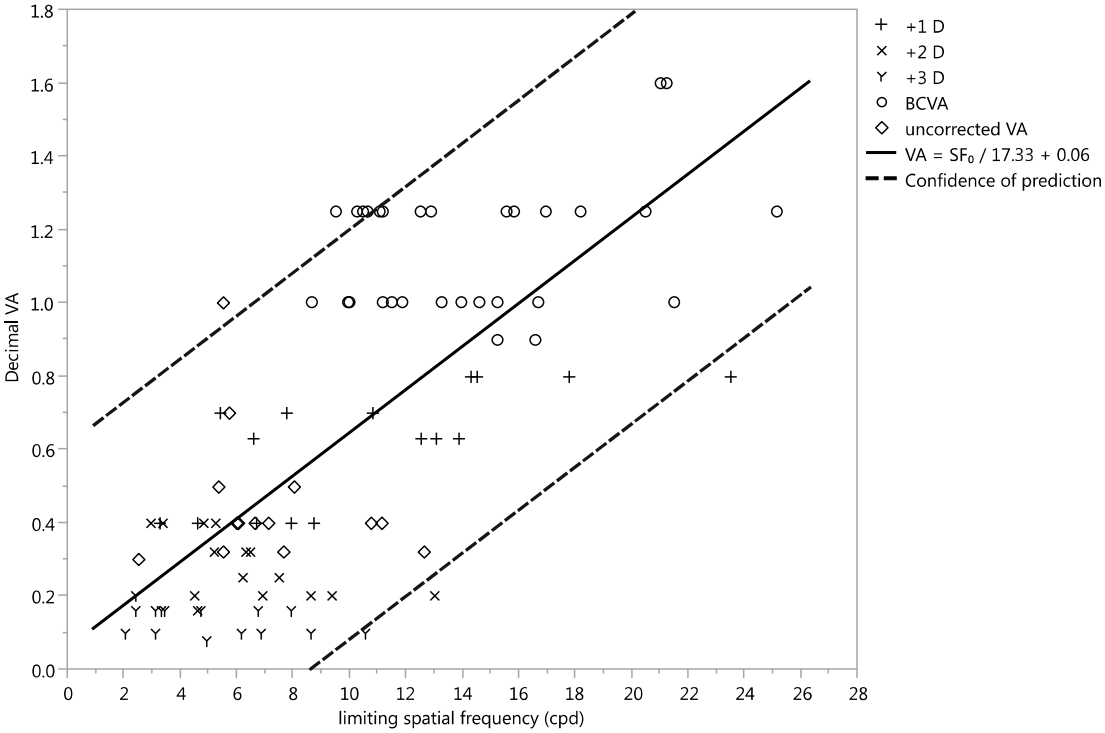

Figure 62: Relation between the limiting spatial frequency (SF_o) and the subjective visual acuity. A simple linear regression was calculated to predict the visual acuity based on the sweepVEP recordings of subgroups A and B. Circles indicated measurements with best corrected visual acuity, diamonds with uncorrected visual acuity. The other symbols represent measurements with different degrees of artificially degraded visual acuity using plus lenses. A significant regression equation was found ($F(1, 88) = 97.36$, $p < .0001$), with an R^2 of .5253. The predicted visual acuity is equal to 0.078 + 0.0577 * SF_o when SF_o is measured in cycles per degree. The visual acuity increases by about 0.5 per ten cycles per degree. The solid line shows the calculated regression, the dashed lines show the 95 % confidence limits of the prediction.

The solid black line represents the result of the simple linear regression, the dashed lines show the 95 % confidence limits of the prediction. A significant regression equation was found ($F(1, 88) = 97.36$, $p < .0001$):

$$VA = 0.0577 \cdot SF_o + 0.078, \text{ with } R^2 = .5253 \quad (13)$$

Equation 13 indicates an increase of the visual acuity of 0.5 per ten cycles per degree of the limiting spatial frequency. The visual acuity can be estimated by

dividing the limiting spatial frequency by 17.33, which is the reciprocal value of the coefficient in Equation 13. Using this equation, the limiting spatial frequency of a decimal visual acuity of 1.0 would be at about 16 cpd.

Based on Equation 13, the visual acuities of subjects of subset A and subset B were predicted using the calculated limiting spatial frequencies SF_o for each condition.

A linear regression (Figure 63) was calculated between subjective and predicted visual acuity. A significant regression equation was found ($F(1, 88) = 97.3621$, $p < 0.0001$), with an R^2 of .5253: subjective visual acuity = 4.98 x 10-8 + 0.9999 x predicted visual acuity. The coefficient of the regression corresponds almost exactly to the line of equality.

Figure 64 shows a Bland-Altman plot of the subjective and the predicted visual acuities of the subjects of the subsets A and B. The limits of agreement are [-0.5737, 0.5737].

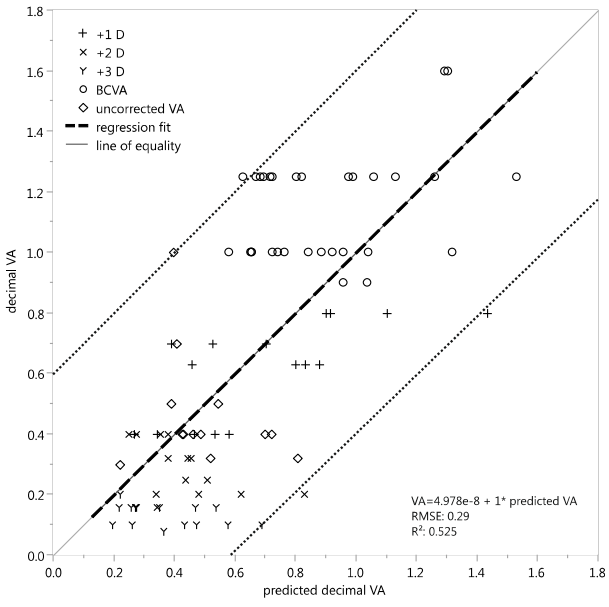

Figure 63: Regression plot of the predicted visual acuities on the X-axis and the subjective visual acuities on the Y-axis. Acuities are specified in decimal values. The diagonal solid line (gray) indicates the line of equality, the black dashed line shows the regression fitted to the data with the 95 % confidence intervals (dotted lines). The coefficient of the regression line (R^2 = .525) corresponds exactly to the line of equality.

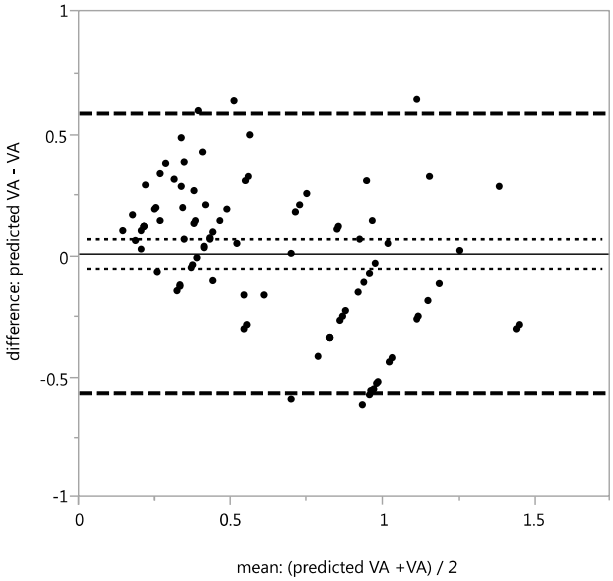

Figure 64: A Bland-Altman plot showing a comparison of the subjective and the predicted visual acuities (decimal) for subjects of subsets A and B. The plot shows the association of the mean (X-axis) and the difference (Y-axis) of the two results. The solid line represents the mean difference along with its 95 % confidence intervals (dotted lines). The dashed lines show the limits of agreement between the subjective and the predicted visual acuity.

A paired-samples t-test was conducted to compare the differences between the paired means of subjective and predicted visual acuity. The mean of the differences is 3.61×10^{-7} (95% confidence interval [-0.0613, 0.0613], standard error = 0.0309). The paired-samples t-test showed not a significant difference between the mean differences of subjective (mean = 0.6393) and predicted visual acuities (mean = 0.6393); $t(89) = 1.17 \times 10^{-5}$, $p = 1.0$.

The calculated SNR for all recordings was more than 4 dB, which corresponds to a maximum amplitude that is about 2.5 times higher than the noise level. A higher subjective visual acuity results in a better SNR, since the maximum amplitude is increased, whereas the level of noise does not change much. Figure 65 depicts the SNR for different ranges of subjective visual acuity for subjects of the subsets A and B. The SNR allows to classify recordings for quality. However, a definitive lower limit for the SNR still is to be defined.

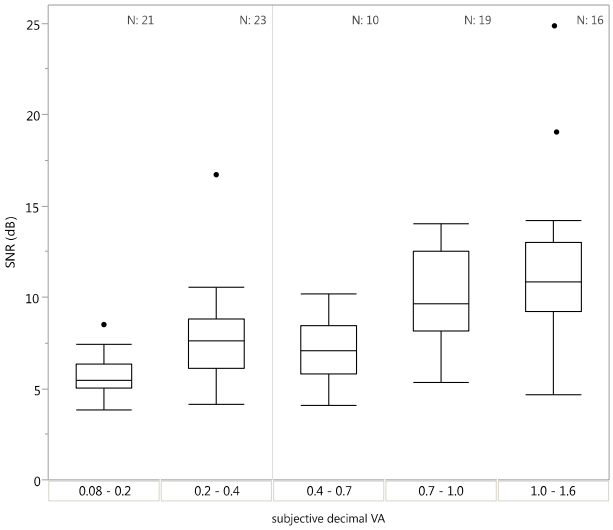

Figure 65: Signal-to-noise ratios calculated using the estimated parameters of the modified generalized Ricker model of subjects of subsets A and B. The SNR increases with the visual acuity and can therefore be used to judge the quality of a recording. As the maximum value of the amplitude converges to the noise level, the SNR converges to zero dB. In the data shown, the lowest SNR is about 4 dB, which means that the maximum amplitude is about 2.5 times higher than the noise level. A definitive lower limit for classifying recordings is still to be determined.

The regression function for predicting the visual acuity from the limiting spatial frequency (Equation 13) was used to predict the visual acuities of the subjects of subset C. For these subjects, subjective visual acuity and the sweepVEP was assed only with best corrected visual acuity. The subjective visual acuity was between 0.9 and 1.25 (0.9: n = 2, 1.0: n = 14, 1.25: n = 21). Figure 58 contrasts the subjective and the estimated visual acuities. The each line in the plot at the left side represents the correlation between subjective and estimated visual acuity for each single eye. The histograms at the right side describe the distribution of the acuities.

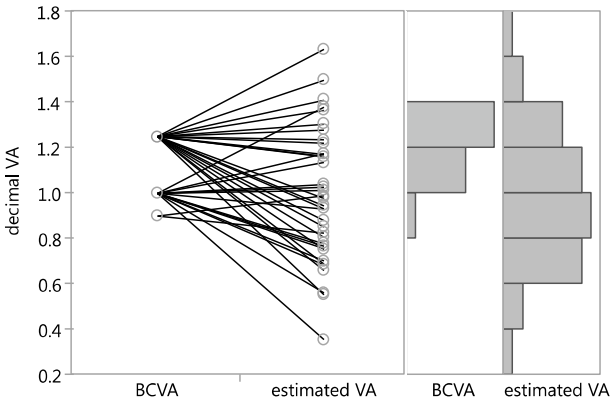

Figure 66: Comparison of the subjective and the predicted visual acuities with best corrected visual acuity for the subjects of subset C. In the plot on the left, lines indicate the correlation between subjective and predicted visual acuity for each eye. The histograms on the right describe the distribution of the subjective and the predicted visual acuity, respectively.

A direct comparison of the subjective and the predicted visual acuity indicates a high variability of the latter. However, examination of a histogram representation of the differences between the subjective and the predicted visual acuities (Figure 67), shows a median value of 0.09, with a 95 % confidence interval of [-0.38, 0.65].

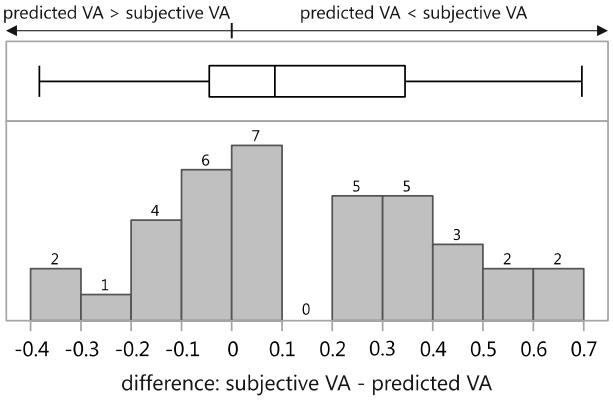

Figure 67: Histogram of the differences between subjective and predicted visual acuities (BCVA) for 37 eyes of subset C. The median difference is 0.09, with a 95 % confidence interval of [-0.38, 0.65] (decimal VA).

The confidence interval corresponds to the limits of agreement [-0.5737, 0.5737] resulting from the Bland-Altman plot (Figure 64) of the subjective and predicted visual acuities of the subsets A and B.

2.4 Discussion

In contrast to similar methods for estimating the visual acuity using visual evoked potentials, our methods uses almost twice as many spatial frequencies [19], [202], [20], [213], [214]. The reasons for this high number of spatial frequencies are first, that we experienced in clinical routine many young people with subjective acuities up to 1.8 (decimal). In his comparison of several methods of measuring the subjective visual acuity, Weseman also found a surprisingly high number of subjects with visual acuity up to 2.0 (decimal) [215]. These subjects can show peaks in the sweepVEP up to spatial frequencies of 30 cpd and more. Using Equation 13, the limiting spatial frequency for a decimal visual

acuity would be about 33 cpd. Since the highest spatial frequency of our used stimulus paradigm is 36.5 cpd, it is possible to cover the limiting spatial frequency even for subjects with very high visual acuities. In contrast to monitors common until a few years ago, modern display are able to present patterns with very high spatial frequencies, because of their high density of pixels.

Although the fitting of a linear or polynomial tuning curve [202], [19], [20], [206] to estimate the limiting spatial frequencies can also be performed with fewer spatial frequencies, using a higher number usually improves the quality of the fit. Additionally, it provides a means to estimated the level of "noise", which results from the spontaneous oscillations in the EEG. Therefore, the quality and the significance of the recorded sweepVEP can be judged.

The modified generalized Ricker model presented here makes use of this additional information through its tail convergence to the noise level at higher spatial frequencies. Since not only the significant responses to lower spatial frequencies are used for the fit, but also the "noisy" tail of the recording, the fit becomes more reliable and robust against outliers. Examples for such outliers are a sudden drop of the amplitude for a single spatial frequency. This was seen in a number of subjects during our study and was also described by others (Sven P. Heinrich, personal communication, June 2015), [214]. The cause for such a drop of the amplitude for a certain spatial frequency is still unclear. A relation to "double-peaks", which were recently described by Stothart et al. [216], may exist. Tyler et al. found indications, that the electrode placement may affect the appearance of double-peaks [214]. These double-peaks were also present in some of our subjects; however we did not observe a relation to the age of the subject.
Since visual acuity is closely related to contrast sensitivity, most methods [202], [19], [206] apply second order polynomial (parabola) tuning curves, which are determined psychophysically [217], [218], from direct recording of retinal gan-

glion cells [219], [220]. Several groups, including ours (Strasser et al. IOVS2014;5124), have investigated different functions to model the relationship between spatial frequencies and visual evoked potentials [20], [221]. Up to now only second order polynomials are used, with the exception of Bach et al, who use a linear regression to parts of the data [20].

However, a second order polynomial is not able to completely reflect the relationship between spatial frequency and amplitude. One would expect, that a fitted parabola would have its zero crossing at 0 cpd, which is not the case for most recordings. Additionally, a second order polynomial does not reflect the convergence to the baseline defined by the spontaneous EEG oscillations: the transition between clearly significant responses and background oscillations follows more the shape of an inverse exponential function, which corresponds to the neural tuning curves described by Dehaene [222]. Therefore, our goal was to find a model which fits the data more naturally.

The choice to use the generalized Ricker model for modeling the relation between spatial frequency and the sweepVEP peak-to-trough amplitude was done empirically. In contrast to a parabola its origin is at 0 cpd and it is able to model the spontaneous oscillations, defining the “noise” level.

The model was introduced 1994 by Ricker as a growth model to describe the growth of a population in context of stock and recruitment in fisheries [208]. Since the underlying mechanisms for processing stimuli of different spatial frequencies and its effect on the visual evoked potentials is not completely understood, justifying the application of the Ricker model faces us with the same problem as Ricker was confronted with.

In 1994 Ricker writes [208]:

> "Towards a theory of recruitment: The justification for using any reproductive curve must in the long run come from observations. However it would be most useful, if it were possible, to formulate some general theory of reproduction which might lead to a standard type of reproduction curve applicable in majority of situations."

The results of our study proved, that the Ricker model is able to describe closely the amplitudes of the sweepVEP in relation to the spatial frequencies of the presented checkerboards. Interestingly, Mannos et al. [223] used a Ricker model to blur images, even if they were not aware of this fact. Indeed, their used model is quite similar to the one we developed (Equation 6). In this study, blurred versions of images were created using their model, which then were graded for quality in comparison to the original image by independent raters. Based on the gradings, a transfer function was created, which was compared to published contrast-sensitivity functions. Mannos et al. found a considerable similarity between the transfer function and the contrast-sensitivity functions.

Stromeyer and Klein describe a transducer function to predict the detectability of test gradings added to an in-phase background with a harmonic grading as a function of the contrast, spatial frequency, and phase of test and background. From their results, they conclude that spatial frequency channels in human vision act as asymmetric edge mechanism, which might explain the reason, that the shape of their transducer function resembles the Ricker model remarkably, even if its derivation is different.

This gives us confidence to use the Ricker model to model the relationship between the spatial frequencies of the presented checkerboards and the sweepVEP peak-to-trough amplitudes.

One drawback of the introduced model is that it is not possible to easily derive the limiting spatial frequency based on the estimated parameters. As a compromise, we used the estimated parameters of the Ricker model to fit a second order polynomial. Even if a second order polynomial fit is common for estimating the limiting frequency, this is unsatisfactory. We have evaluated several different means of deriving the limiting spatial frequency based on the estimated parameters, including a line fit to the declining limb of the model, estimation of the highest reliable spatial frequency based on the amplitude of the noise level, and several transfer functions of the spatial frequency of the maximum amplitude SF_{max}. However, the described method leads to the best results regarding the agreement between subjective and predicted visual acuity. Finding a better derivation of the limiting spatial frequency based on the estimated parameters of the modified generalized Ricker model will be the subject of further research.

Using the estimated parameters of the modified generalized Ricker model creating the second order polynomial to calculate the limiting spatial frequency is preferable to directly fitting the parabola: since the modified generalized Ricker model uses all of the data, it tends to be more robust against outliers. A manual exclusion of data points is therefore not nescessary and is easier implemented than the heuristic approach used by Bach et al. [20]. However, during the analysis, extreme outliers had do be manually excluded in certain cases before fitting the Ricker model. This is due to the high sensitivity of the non linear least square regression to outliers. To avoid manual removal of outliers, several approaches can be used: one approach is to detect and remove outliers automatically using the method described by Motulsky and Brown [224] or use an alternative approach for fitting models to data like the random sample and consensus (RANSAC), introduced in 1981 by Fischler and Bolles [225], which is known to be more robust against outliers.

In contrast to the method proposed by Bach et al. [20], our method requires manual cursor placement. Although, it can be supported using peak-finding algorithms, a manual control and correction of the cursors are required. In this way, the method of Bach is superior to our method. However, Bachs method of using a fourier analysis to determine the amplitude of the first harmonic of the stimulus presentation frequency requires the use of a steady-state stimulus. This may lead to adaptation effects, as described by Heinrichs and Bach [226], which have to be taken into account. Moreover, malingerers could exploit the stimulus timing and deliberately defocus during stimuli with a high spatial frequency, which is not easily possible for the sweepVEP. In addition, pattern onset VEPs, like the sweepVEP, are less sensitive to poor fixation, eye movements, and deliberate defocusing [146].

The presented method allowed estimation of the limiting spatial frequency for all sweepVEP recordings, even when the visual acuity was drastically reduced by induced defocus using plus lenses. The limiting spatial frequency was closely related to the subjective visual acuity and by using a linear regression, an equation to predict the visual acuity based on the sweepVEP was found. When ignoring the small constant factor (0.078) of the regression, as a rule of thumb, the predicted visual acuity can be calculated from the limiting spatial frequency as follows: $VA = SF_0 / 17.33$. Interestingly, this value is close to the value described by Bach et al. [20]: They found a factor of 17.06 to convert between limiting spatial frequency and predicted visual acuity.

A linear regression line of subjective and predicted visual acuities corresponds closely to the line of equality (Figure 63). This corresponds to the small mean difference seen in a Bland-Altman plot of subjective and predicted visual acuities (Figure 64). However, the limits of agreement are with [-0.5737, 0.5737] rather wide. This is caused mostly by the high variability of the measured limit-

ing spatial frequency for best corrected visual acuity, which can be seen in Figure 63: the values for the best corrected visual acuity vary mostly between the three values 1.0, 1.25, 1.6, which correspond to the logarithmic size scale of optotypes. A finer scaling of the presented optotypes like the Freiburg Vision Test does (FrACT, [200]), would therefore probably result in values closer to the predicted visual acuity and to a smaller intervals of the limits of agreement. Additionally, König could show in her recent thesis [227], that the subjective visual acuity measured with ETDRS charts results in higher values than those obtained with the FrACT. For future studies we therefore recommend the use of FrACT for measuring the subjective visual acuity.

For subjects of the subset C, with best corrected visual acuity, we find a mean difference of only about 0.1 (decimal) between predicted and subjective visual acuity (Figure 67). However, this difference seems to depend on the value of the subjective visual acuity: the predicted visual acuity for subjects with good to high visual acuity is smaller than the subjective visual acuity, whereas the predicted visual acuity for subjects with a high induced defocus is overestimated. This dependency has been described also by Bach et al. [20]. The reason for the overestimation at low visual acuities and the underestimation at high visual acuities is currently unclear and will have to be addressed in future studies.

It is not clear, if the method presented here will give an accurate estimated of visual acuity in patients suffering from eye diseases as it does for normals and normals with artificially induced defocus. Artificially degrading the visual acuity using plus lenses allows only a limited simulation of poor vision resulting from eye diseases. Subjective visual acuity measurements in subjects of subset A showed a linear relation between the degree of degradation and the logMAR visual acuity (Figure 59), which is consistent with results from other studies [228], [229]–[231]. However, it is not clear, what effect an induced defocus has

on the visual system as a whole has. Mirzajani et al. found a reduction in the number of activated voxels and the strength of the BOLD signal using fMRI, which is related to an increase of induced defocus [232]. In a future study, we will use Bangerter occlusion foils to simulate degraded visual acuity. Bangerter foils affect the modulation transfer function as do plus lenses; but they do not exhibit spurious resolution and phase shifts [233], and may therefore be more suitable for simulating degraded visual acuity. However, Pérez at al. found a diff-fference between the denoted strength and the real optical characteristics of Bangerter foils, which has to be taken into account [233].

Bach et al. successfully estimated the limiting spatial frequency for patients suffering from cataract, epiretinal gliosis, corneal clouding, AMD, and chorioretinitis [20]. Further studies are in progress to investigate our method in patients suffering from a variety of eye diseases.

3 Assessment of “non-recordable” electroretinograms by 9 Hz flicker stimulation under scotopic conditions

This text was published in Documenta Ophthalmologica in 2011: A. Schatz, R. Wilke, T. Strasser, F. Gekeler, A. Messias, and E. Zrenner, “Assessment of ‘non-recordable’ electroretinograms by 9 Hz flicker stimulation under scotopic conditions.,” Doc. Ophthalmol., Dec. 2011.

3.1 Introduction

Electroretinography (ERG) is a well-established method for non-invasive, objective assessment of retinal function widely used in clinical practice and research [234]–[242]. In 1989, a basic standard protocol [International Society for Clinical Electrophysiology of Vision (ISCEV) standard] was adopted [243]. The protocol was intended to serve as a minimal protocol for the assessment of rod and cone function, which facilitated its wide use in laboratories and clinical settings around the world. The current ISCEV protocol [244] provides the basis for every-day’s clinical routine and allows for functional analysis of rod- and cone system responses.

Although these standards provide a valuable tool in the differential diagnosis of a number of retinal diseases [245], there are still a number of ERG techniques that are not covered by this standard. Some of them are widely used to further distinguish retinal responses and isolate responses generated by distinct retinal pathways, including short-wavelength cones, bipolar ON- and OFF-pathways, ganglion cells (photopic negative responses), and proximal retinal cells (scotopic threshold responses) [246]–[250]. Further, series of stimuli of varying in

stimulus strength or flicker frequency are used to fit models for examination of dynamic properties of cell groups in the visual system (e.g., Naka and Rushton fit [251]). All those specialized techniques have found important applications in clinical counseling and clinical trials.

Another application that demands specialized recording and analysis techniques is the measurement of patients with advanced retinal degeneration where standard ERG recordings are commonly found to be non-informative or not reliably discernible from noise. The small potentials in those ERG recordings generated by a grossly reduced population of retinal cells are often lower than the noise level. This leads to a profound decrease in signal-to-noise ratio (SNR) and implies serious methodological difficulties in clinical trials that rely on the inclusion and follow-up of patients with advanced stages of retinal degeneration [67], [252].

Motivated by this challenge a number of laboratories have proposed improved ERG techniques. Andréasson et al. [253] described the application of a filter setting to enhance SNR allowing the recording of small amplitude ERG. The photopic 30 Hz flicker has been used to obtain a high number of averages in a short examination time and to enhance the SNR [254]–[256]. Bach and Meigen [257] reported a method of data post-processing using discrete Fourier transformation (DFT) to quantify both the responses and noise signals in a steady state recording. This method allows for estimation of significance levels of the recorded response in comparison with background noise [258]. Another technique to estimate a significance level for "submicrovolt" recordings was described by Sieving et al. [259] and included a "cycle-by-cycle" analysis of a 32 Hz flicker response. An extraction of the harmonic information from each response of the 32 Hz flicker allowed the calculation of confidence intervals of the response and a noise distribution. In this work, we aimed at combining these

previously described approaches of generating a steady state response and specialized statistical analysis with an optimization of stimulus settings for the recording of low residual potentials in patients with advanced retinal degeneration under scotopic conditions. A new recording protocol was developed for the examination of patients with advanced retinal degeneration in clinical routine that is capable of detecting residual retinal functions under dark adapted conditions and to provide a surrogate marker of retinal function when other methods fail.

3.2 Methods

Subjects

Twenty-seven healthy subjects were included in the pilot study [mean age 28 ± 8.5 years standard deviation (SD)]. Initially, the range of optimal time-integrated luminance values was defined in 11 subjects and subsequently definite values were determined in 16 subjects.

Recordings of 922 patients (mean age 40.6 ± 18.3 years SD) were obtained from the outpatient clinic for hereditary retinal dystrophies at the Centre for Ophthalmology, University of Tübingen, where the new protocol (9 Hz flicker) was tested in clinical routine over a period of 5 years (2006–2011). ISCEV standard recordings as well as the new recordings described here, were obtained from all patients.

All study procedures complied with the Declaration of Helsinki and were approved by the University of Tübingen Ethics Committee. Informed and written consent was obtained from all healthy subjects after explanation of the nature and possible consequences of the study.

Electroretinography

ERG recordings were obtained using a Ganzfeld light source and a computer-based recording system (ColorDome® and Espion e²®, Diagnosys LLC, Cambridge, UK). Scotopic recordings were carried out after at least 30 min of dark adaptation and administration of two drops of tropicamide 0.5% (MydriatikumStulln®, Stulln, Germany). Gold cup electrodes (Gold Cup Electrodes, Viasys™ Healthcare, Madison, USA) were placed on both temples as reference and on the forehead as ground under dim red light. A drop of oxybuprocaine 0.4% (Novesine®, OmniVision, Puchheim, Germany) was applied for corneal anesthesia before positioning the Dawson-Trick-Litzkow [183], [260] electrodes. Impedance levels were checked to be below 5 kΩ at 25 Hz before and several times during measurement.

During the initial exploring stage of the pilot study, a range of stimuli varying in stimulus strength (log -5.92 to log 0.8 scot. cd s/m²) and wavelength (blue 470 nm, green 513 nm, red 635 nm) was tested for its effect on recorded waveforms, their amplitudes and the state of dark adaptation. In the subsequent optimizing stage of the pilot study, the protocol consisted of a series of 6 stimuli with increasing stimulus strengths (log -2.64 to log -1.4 scot. cd s/m² at 10 ms flash duration) and a series of 5 stimuli with increasing flash duration (6–14 ms at 0.012 cd s/m²).

Band-pass filtering between 0.3 and 300 Hz (Espion e²® built-in algorithm) was used for all standard ISCEV measurements. Extraction of oscillatory potentials (OP) was achieved using band-pass filtering between 100 and 300 Hz. During the measurements band-pass filtering was set to 1.25–30 Hz for the 9 Hz recordings to reduce noise sources clearly outside the expected frequency range of the response.

In clinical routine, the new 9 Hz flicker protocol consisted of 120 continuous sweeps with durations of 444 ms per sweep measured at 1 kHz sampling rate. This duration was chosen because it constitutes a multiple of the 9 Hz phase duration, and because it is short enough to avoid blinking artifacts. Each sweep was immediately inspected for artifacts and rejected by the system’s automated routine when the set acceptance margins of 250 µV were exceeded. Since the 120 sweeps were recorded continuously, typical noise sources like mains frequencies (50 or 60 Hz) were recorded with a fixed phase delay to the stimulus signal. Therefore, averaging the 120 sweeps can eliminate those noise sources effectively only if the phase duration of the signal is an odd divisor of the noise signal. This was the main reason for choosing 9 Hz rather than, for example, 10 Hz.

Paradigm of the pilot trial

Small retinal potentials are technically challenging to record due to the decreased SNR. The goal of the designed protocol had, therefore, to be threefold: (1) to increase retinal potentials by finding optimal stimulation conditions for the rod system, (2) to decrease noise in the recording by applying band-pass filtering [253], repetitive stimulation and averaging [261], [262], and (3) to isolate the signal in the frequency domain of the recording. Offline analysis of the signal in the frequency domain using DFT is a widely used approach and can also be used to estimate the amount of noise in the isolated frequency band [258]. This allows for the calculation of statistical significance levels of the detected signal according to the SNR.

Recovery of amplitude after bleaching and comparison with red light stimulation

The recovery of the 9 Hz amplitude after intense photo-bleaching during a time series under dark adapting conditions was recorded in one subject to test whether the stimulus strength applied in the 9 Hz protocol interferes with dark adaptation.

The response before bleaching was recorded according to the clinical protocol (30 min of dark adaptation, 9 Hz flicker, 0.012 scot. cd s/m² and 10 ms duration). Thereafter, the photopigment was bleached by exposure to 500 cd/m² white (6,500 K) light during 5 min. The 9 Hz protocol was then recorded immediately after bleaching and once every minute for 30 consecutive minutes using identical settings as used before bleaching. The amplitude was plotted against time after bleaching.

Finally, a red flash (635 nm) was used to compare the response with the blue stimulation. The cone pathway is more sensitive to red light. In contrast to the cone system, the rod pathway is more sensitive to blue light [263]. Therefore, an evident change in ERG waveform was to be expected when stimulation changed from blue to red light.

Signal processing and data analysis

A- and b-waves and respective implicit times were quantified according to ISCEV recommendations [264].

Data processing and analysis of the 922 patient measurements were performed using a self-programmed software [207] which allows for automated analysis of a large number of recordings with direct access to the ERG database

(Espion e²®, Diagnosys LLC, Cambridge, UK). The data processing steps of the software are described below:

Conditioning for DFT and averaging

In order to obtain the desired resolution in the DFT, six single sweeps of 444 ms were concatenated to form one long sweep with a total duration of 2,664 ms. The resulting 20 s long sweeps were then averaged. Finally, the sweep was detrended by fitting and subtracting a linear function to avoid low frequency artifacts in the DFT.

Discrete Fourier transformation (DFT)

The sweeps where transferred into frequency domain using standard DFT routines allowing for quick and easy identification of the 9 Hz component and its magnitude. The number of data points (n = 2,664) of the resulting average was increased by applying a spline interpolation to a power of two, which allows using the DFT procedure. Following the convention for measuring b-wave and 30 Hz flicker amplitudes from the minimum to the maximum, the amplitude of the 9 Hz response was calculated as twice the magnitude of the bin centered at 9.009 Hz (which is the exact stimulus frequency generated by the ERG system). Higher harmonics of this base frequency were not considered.

Statistical evaluation

The significance of the response was determined by evaluation of the SNR according to Meigen and Bach [258]. The method described by Meigen and Bach requires a recording duration of at least one second to have a sufficient high resolution of the signal in the frequency domain. This is the reason of the previously described joining of single sweeps. If the magnitude of the bin with the

expected signal exceeds the average noise signal by a factor of 2.82 the signal is significantly larger than noise with a P value of 0.05. All responses above this significance level were considered as valid signals and were used for descriptive statistics. ERG responses in the patient study were categorized as "non-recordable" if the photopic 31 Hz stimulation protocol showed no significant responses using the described DFT procedure, or b-waves of single flash responses were not identifiable (single flash rod response, scotopic and photopic response). After removal of all "non-recordable" recordings, 618 patient recordings remained. These patient measurements (618 patients and in total 1213 eyes) were used for calculation of correlation coefficients (Pearson's correlation coefficient) in order to assess any correlations between results from standard ISCEV ERG measurements and the new 9 Hz flicker response.

3.3 Results

Basic protocol settings

A blue light source of narrow bandwidth (standard blue light-emitting diode (LED), ColorDome® Ganzfeld, 470 nm) was chosen to stimulate rods and to diminish L- and M-cone (long- and middle-wavelength cones) interferences (19).

Pilot study

Stimulus series of increasing time-integrated luminances

It is apparent that the waveforms and the b-wave amplitudes follow a non-linear function in relation to stimulus strength under dark adapted conditions. A series of responses to a range of stimulus strengths (0.0000012–6.32 scot. cd s/m²) with 9 Hz recordings is shown in Figure 68a, respective b-wave amplitudes in Figure 68b. A first maximum of the b-wave amplitude was found at 0.01 scot. cd

s/m² followed by a decrease in amplitude and a second maximum at 2.52 scot. cd s/m² (Figure 68b). This double peak characteristic is in line with the findings of Scholl et al. [265] who showed suppression of retinal responses in the transition from predominantly rod- to cone-system driven responses. While the waveform around the first maximum was dominated by a pure b-wave, an a-wave was clearly visible near the second, brighter maximum where also oscillatory potentials became apparent (Figure 68a). In the frequency domain, it was observed accordingly that the clear dominance of the 9 Hz component at lower stimulation strength was lost in favor of higher harmonics (18 Hz, 27 Hz) at higher stimulation strengths closer to the second maximum (data not shown). Also, the phase delay of the 9 Hz flicker responses became gradually shorter with increasing stimulus strengths (data not shown). All that suggested a significant cone contribution at higher stimulus strengths in the range of the second maximum and indicated the suitability of the lower stimulus strength maximum for measurements of rod responses with the 9 Hz protocol. To further address this, the b-wave amplitudes were compared for two stimuli of different wavelengths, which were set to be isoluminant for the rod system, but not for the cone system. The second stimulus used here was of green light (LED light source, 513 nm). Due to the distinct spectral sensitivity of the rod versus the cone system (L- and M-cones), the green stimulus should evoke stronger responses from the cone system in comparison with the blue stimulus. Figure 68b shows that the b-wave amplitude found of both, green and blue stimuli are very well comparable at the first, dimmer maximum, whereas the green stimulus reaches the second maximum at lower stimulus strengths. This is in line with the assumption that the first maximum was dominated by rod-system response, whereas at the second maximum the cone system contributed significantly.

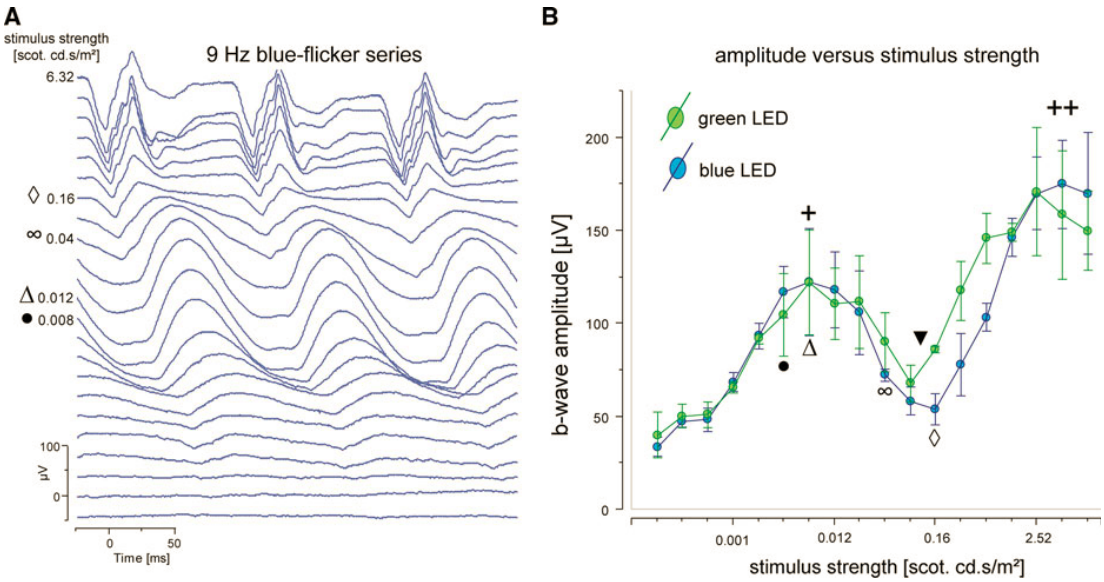

Figure 68: a Example of ERG measurements of the 9 Hz flicker stimulation with blue light (blue LED 470 nm), constant stimulus duration (10 ms) and rising stimulus strengths (from bottom 0.0000012 to top 6.32 scot. cd s/m²). Stimulus strengths marked on the left side of the ERG recordings indicate the highest 9 Hz amplitude of the DFT calculation (black filled circle 0.008 scot. cd s/m²); the first maximum b-wave amplitude (open triangle 0.012 scot. cd s/m²); the appearance of oscillatory potentials (infinite 0.04 scot. cd s/m²); the appearance of an a-wave in the ERG and the change of DFT frequency-dominance from 9 to 18 Hz (first higher harmonics [open diamond 0.16 scot. cd s/m²]). Note the change of ERG waveforms with higher stimulus strengths. **b** Series of stimulus strengths of the 9 Hz flicker with blue and green light stimulation (blue LED 470 nm, rod isoluminant green LED 513 nm). Recordings were performed in healthy subjects (n = 2) illustrated by means (line) and standard deviations (whiskers). The plot shows an identical first maximum in b-wave amplitudes for the blue and green stimulation (single plus). Higher stimulus strengths cause initially a reduction in b-wave amplitude. The lowest point of the b-wave decrease (filled inverted triangle) differs in stimulus strength between the green (lower stimulus strength) and blue stimulation (higher stimulus strength). Thereafter, with usage of higher stimulus strength a rapid rise of b-wave amplitudes is noticed to the second maximum (double plus). The marks described in a were added for orientation below the plot to illustrate the interrelation between ERG waveforms and amplitude (From: Schatz, Wilke, Strasser, et al., 2011)

For those reasons, further optimization of the stimulus strength was focused around the dimmer maximum of 0.01 scot. cd s/m². A much narrower range of stimulus strengths around this peak was measured in the subsequent optimiza-

tion study in 16 healthy volunteers. In 13 of 16 subjects (81 %), the maximum b-wave amplitude was at a time-integrated luminance of 0.012 scot. cd s/m² at 10 ms stimulus duration (Figure 69a, b).

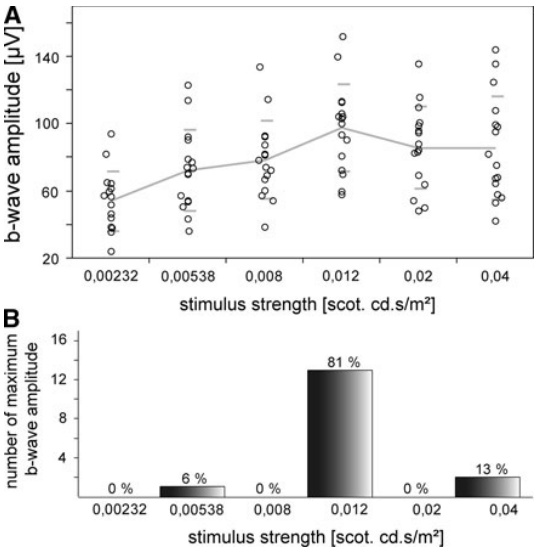

Figure 69: a Series of stimulus strengths of the pilot study in 16 subjects with a narrow range of stimulus strengths to optimize the 9 Hz flicker paradigm (fixed stimulus duration at 10 ms). Rings show the mean of both eyes of single subjects (n = 16). Descriptive analysis using means (connected line) and standard deviations (whiskers) show the distribution of amplitudes. The means are connected to illustrate the behavior of the b-wave amplitude at raising stimulus strengths (from 0.00232 to 0.04 scot. cd s/m²). The highest mean b-wave amplitude is found at the stimulus strength of 0.012 scot. cd s/m². **b** Distribution of stimulus strengths, which elicited maximum amplitudes (From: Schatz, Wilke, Strasser, et al., 2011)

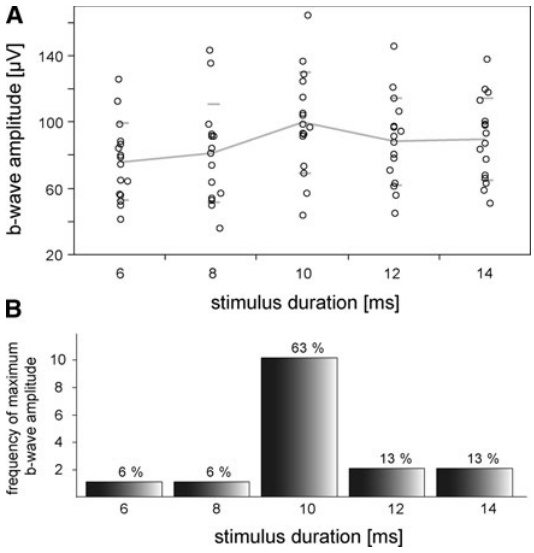

Figure 70: a Plots of amplitudes versus stimulus duration (ms) of 16 subjects (fixed stimulus strength at 0.012 scot. cd s/m²). Rings show the mean of both eyes of each subject (n = 16). Means and standard deviations (described in Figure 69a) illustrate the distribution of b-wave amplitudes at each duration-level. The highest mean b-wave amplitude is found at stimulus duration of 10 ms. **b** Distribution of stimulus durations, which elicited maximum b-wave amplitudes (From: Schatz, Wilke, Strasser, et al., 2011)

Stimulus series of increasing flash durations

Finally, in attempt to optimize the stimulus duration, duration series were performed using a constant stimulus strength of 0.012 scot. cd s/m². Stimulus duration of 10 ms yielded maximum b-wave amplitudes in 10 of 16 subjects (63 %) (Figure 70a, b). The mean amplitude of 32 measured healthy eyes was 97.56 ± 25.54 µV (SD) with an implicit time of the second peak of 191.67 ± 10.1 ms.

Response recovery after photopigment bleaching and comparison with red light stimulation

To test whether the stimulation parameters, in particular the prolonged and repetitive application of the light stimuli lead to an alteration of the dark adapted state the recovery of the 9 Hz amplitude was measured after photopigment bleaching. Figure 71a shows the series of 9 Hz recordings before bleaching, immediately after bleaching and up to 30 min recovery after bleaching. After a post-bleaching time of 25 min, the amplitude reached the same level as the response after 30 min of dark adaptation (Figure 71a, b).

Using red light stimulation (red LED 635 nm) instead of blue (470 nm), a time-integrated luminance of 0.005 and 0.012 cd s/m² showed a characteristic change in ERG waveform: a double-peaked waveform appeared. The second peak could be identified as an x-wave [266], [267], which is a contribution from the cone system to the scotopic ERG. In contrast, the blue LED provoked a sinusoid waveform with a single b-wave peak per cycle (Figure 72), which is a further indication of a rod response.

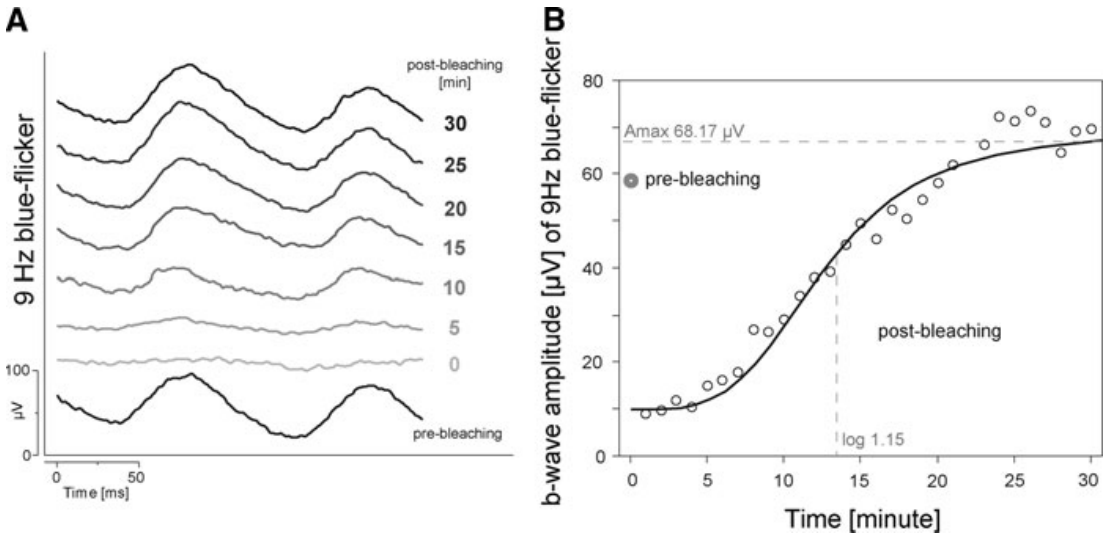

Figure 71: a 9 Hz flicker (0.012 scot. cd s/m² time-integrated luminance, 10 ms stimulus duration) recordings under dark adapted condition (pre-bleaching after 30 min of dark adaptation) and after a bleaching 500 cd/m² for 5 min (white 6500 K) with recording of 15 sweeps every minute for 30 consecutive minutes in darkness (post-bleaching). Post-bleaching recordings are shown in 5 min steps (0–30 min). **b** Plot of b-wave amplitudes versus time after bleaching of the described test procedure in a. 9 Hz amplitudes (rings) after bleaching are compared to the amplitude after 30 min of dark adaptation (thick ring = pre-bleaching). The continuous line (black) is fitted through all post-bleaching amplitudes to describe the recovery of amplitude after bleaching. The dotted lines indicate the maximum response of the fit (A_{max} 68.17 µV) and the time needed for half-recovery (t 14.13 min), respectively (From: Schatz, Wilke, Strasser, et al., 2011)

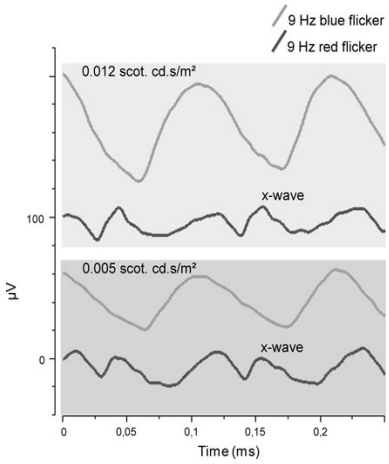

Figure 72: Comparison of 9 Hz flicker ERG waves elicited with different stimulation colors (blue LED, 470 nm, red LED, 635 nm) and time-integrated luminance of 0.012 scot. cd s/m² (upper panel) and 0.005 cd s/m² (lower panel). The main difference in the waveforms is the appearance of an x-wave in the red LED response as a sign of cone contribution to the recording (please note also the low amplitude of the red LED in comparison to the blue LED response) (From: Schatz, Wilke, Strasser, et al., 2011)

Patient study

The 9 Hz flicker paradigm with a time-integrated luminance of 0.012 scot. cd s/m² and stimulus duration of 10 ms (19) was used in clinical ERG examinations. 18 illustrates the correlation between the 9 Hz flicker amplitude and various parameters of the clinical ERG protocol. Strong correlations (>0.8) were found with all scotopic ERG recordings; except for the b-wave amplitude of the 0.001 cd s/m² stimulus and the a-wave amplitude of the 10 cd s/m² stimulus. The highest correlation is shown in Figure 73 for 0.01 cd s/m² with r = 0.87. For photopic ERG waves, only a moderate correlation was found (<0.8).

Table 18: Calculation of the Pearson's correlation coefficients (correlation) between the 9 Hz flicker amplitude (1. variable) and various amplitudes of the standard ERG measurement (2. variable) are listed with the significance level (P value) of the test

1 variable	2 variable	Correlation	*P* value
9 Hz amplitude	**(D) 10 cd s/m² a-wave ampl**	**-0.76**	<0.0001
	(D) 10 cd s/m² b-wave ampl	**0.84**	<0.0001
	(D) 3 cd s/m² a-wave ampl	**-0.8**	<0.0001
	(D) 3 cd s/m² b-wave ampl	**0.85**	<0.0001
	(D) 0.1 cd s/m² b-wave ampl	**0.86**	<0.0001
	(D) 0.01 cd s/m² b-wave ampl	**0.87***	<0.0001
	(D) 0.001 cd s/m² b-wave ampl	**0.7**	<0.0001
	(L) 3 cd s/m² a-wave ampl	*-0.53*	<0.0001
	(L) 3 cd s/m² b-wave ampl	*0.75*	<0.0001
	(L) 31 Hz amplitude	*0.69*	<0.0001

All waves measured under dark adapted condition are marked with a bold (D). The photopic measurements are marked with an italics (L). The ISCEV standard steps are underlined. The strongest correlation (*) is found for the rod b-wave amplitude [(D) 0.01 cd s/m2] of the standard ISCEV protocol (From: Schatz, Wilke, Strasser, et al., 2011)

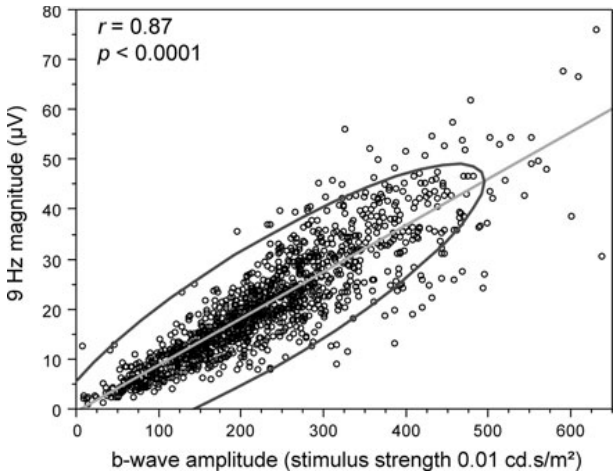

Figure 73: Plot of 9 Hz amplitude and the b-wave amplitudes of scotopic single flash responses (stimulus strength 0.01 cd s/m²). The line represents the linear fit of all measurements. The *ellipsoid* indicates the 95% density of all points. Pearson’s correlation coefficient is given by *r* (*r* = 0.87 at *P* < 0.0001) in the plot (From: Schatz, Wilke, Strasser, et al., 2011)

Two hundred and seventy-three patients of 922 patients included in the clinical study had non-recordable standard ISCEV ERG responses under dark adapted conditions (scotopic single flash stimulation from 0.001 up to 10 cd s/m²; Figure 74). In nearly one-third of those patients (30%, n = 82), a significant 9 Hz flicker response using the developed protocol was nevertheless obtainable. Thirty-eight percent (n = 114) of the cases with undetectable standard ISCEV rod responses (scotopic single flashes from 0.001 to 0.1 cd s/m²) still had a significant 9 Hz flicker ERG (Figure 74). In 256 cases, neither scotopic nor photopic responses were obtained from standard ISCEV recordings using single flash stimuli. Seventy-two (28%) of those cases presented a significant 9 Hz flicker ERG. By applying the DFT analysis to the photopic 31 Hz flicker recordings, an entirely non-recordable photopic ERG was found in 181 patients. In 16% of those patients, a significant 9 Hz flicker response was recorded successfully (Figures 74, 75). A representative example of a “non-recordable” standard ERG (59 years old woman with retinitis pigmentosa), but a significant 9 Hz flicker recording is shown in Figure 75.

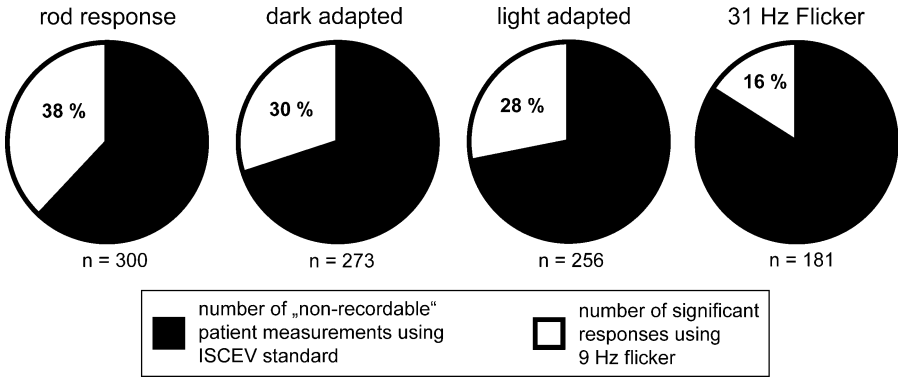

Figure 74: Patients with significant 9 Hz flicker responses as percentage of a population with "non-recordable" recordings using the ISCEV standard protocol. ISCEV rod responses included stimulus strengths up to 0.01 scot. cd s/m² (a total of 300 "non-recordable" measurements), scotopic ERG up to 10 scot. cd s/m² (n = 273), photopic ERG single flash responses with 3 phot. cd s/m2 under light adapted condition (n = 256) and 31 Hz flicker with 3 phot. cd s/m² (n = 181). Significance limits for steady state responses (9 and 31 Hz recordings) where determined as described in the methods (From: Schatz, Wilke, Strasser, et al., 2011)

3.4 Discussion

The aim of the current study was to develop a new ERG protocol to record and quantify residual rod ERG potentials in patients with advanced retinal degeneration where no responses can be discerned from noise when standard ISCEV protocols are employed. Theoretical considerations, as described in the following, led us to the development and the use of a 9 Hz flicker stimulus under dark adapted condition.

The 9 Hz flicker protocol

It may be sensible, especially in therapeutic interventional trials that are directed toward rod function in patients with advanced retinal degeneration, not to neglect the rod response when measuring residual ERG responses. The rod system under normal conditions exhibits larger amplitudes in comparison with

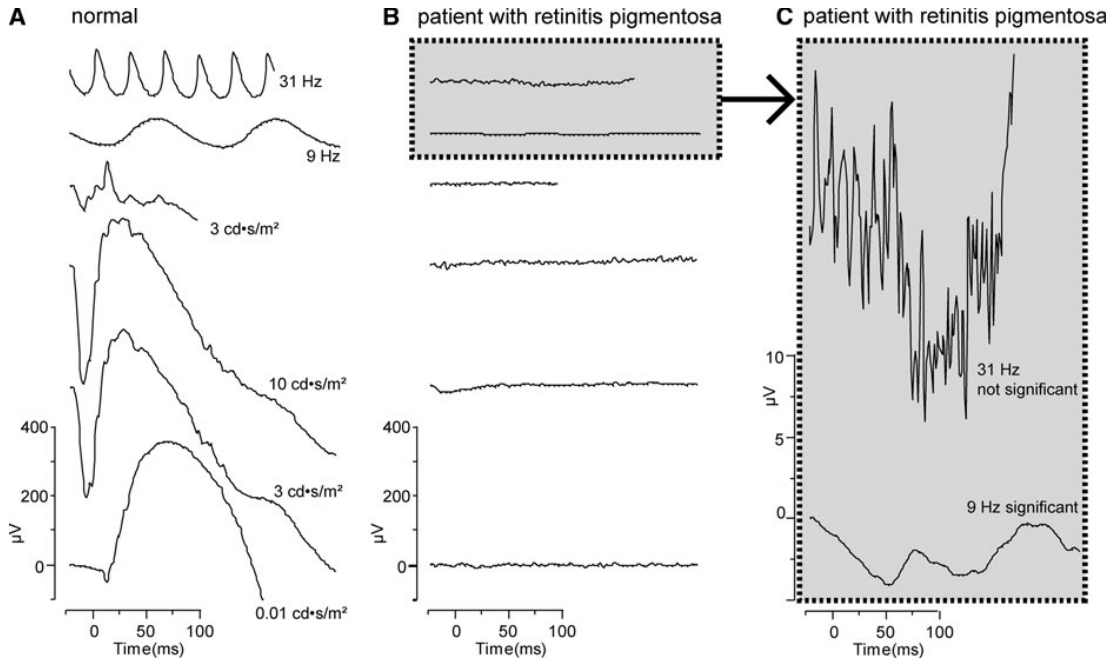

Figure 75: A clinical case of a patient with retinitis pigmentosa b and a significant 9 Hz flicker response as the only recordable ERG potential c in comparison with normal ERG a. Stimulation strengths are marked for the normal recordings (dark adapted 0.01 cd s/m², 3 cd s/m², 10 cd s/m² and 9 Hz flicker using 0.012 cd s/m² and 10 ms duration, and photopic single flash and 31 Hz flicker using 3 cd s/m² and a background illumination of 30 cd/m²). The scaling was changed for illustration of the 31 Hz and 9 Hz flicker recordings in c. The DFT amplitude of the 31 Hz flicker measurement was 1.6 µV, and the significance-threshold was 3.2 µV. Significance was reached in the 9 Hz flicker recording (DFT amplitude of 1.6 µV and a threshold of 1 µV) (From: Schatz, Wilke, Strasser, et al., 2011)

the cone system. A common finding in patients with retinal degeneration is photophobia or photoaversion [268]. This pathologically increased light sensitivity, which is frequently one of the first symptoms of retinal degenerations, renders ERG procedures with brighter stimuli highly uncomfortable, leading to blinking and motion artifacts sometimes prohibiting adequate recordings of such patients. It would be advantageous in those cases to rely on dimmer flashes that address mainly the rod system and—for the purpose of improved SNR by a large number of averages use flicker stimuli.

The rod system has a critical fusion frequency of approximately 28 Hz [269]. However, amplitudes decrease frequency-dependent from around 300 µV at 1 Hz to less than 5 µV at 15 Hz under dark adapted conditions. This decrease in rod amplitudes with raising frequencies has recently been shown for a silent substitution technique [270]. The slow pathway involving the rod bipolar cells is able to follow flicker stimulation only up to 15 Hz [271]. As described previously, averaging a high number of recordings (N) is needed to enhance the SNR [253], [258]. Averaging can reduce stochastic noise by a factor of 1/sqrt(N). Therefore, higher numbers are desirable. On the other hand, longer recording times also introduce more artifacts due to blinks or eye movements and long recording periods can also render a protocol inappropriate for use in clinical routine. The described protocol aimed at determining a good trade-off between generating high ERG amplitudes (the typical amplitude of the 9 Hz protocol is around 90 µV in healthy subjects (Figures 71a, 72a) in contrast to, for example, 15 Hz with less than 5 µV [265]), while still recording primarily a rod response in healthy volunteers, a high number of sweeps for averaging to improve SNR and keeping examination times short to be suitable for clinical routine. We believe the proposed protocol can be easily implemented into the clinical routine. The 9 Hz flicker protocol allows measuring of four amplitudes within a single recording time of 444 ms (duration per sweep). A sufficiently high number of 120 sweeps takes only 53 s (in total 480 amplitudes in less than a minute). Higher harmonics of the 9 Hz flicker do not superimpose the mains frequency (50 or 60 Hz, respectively). Additionally, the identification of rod ERG amplitudes can be more easily achieved compared with a single flash response due to the characteristic waveform consisting of several periodical amplitudes (Figures 68, 71, 72). On the other hand, the steady state signal characteristics allow for observer-independent determination of the amplitude by Fourier analysis making cursor set-

ting and inter-observer variability obsolete, which is of particular significance in multicenter clinical trials. The blue LED (470 nm) was chosen to minimize contributions of the cone system, which has been shown exemplarily using a red LED (635 nm) stimulus instead. A clear x-wave as reported by prior studies was noticed in the 9 Hz flicker ERG waves under stimulation with red light (Figure 72) [266], [267], [271], [272]. The x-wave is a sign of cone contribution to the rod ERG. The blue LED elicited a mainly rod mediated amplitude in contrast to the red LED.

Optimized stimulation settings

The final protocol after optimization in the pilot study implies a stimulus strength of 0.012 scot. cd s/m² and a 10 ms stimulus duration using blue light of 470 nm (Table 19). These settings provided the highest amplitudes under 9 Hz flicker stimulation while still mainly addressing the rod system, at least in healthy subjects. This is demonstrated in Figure 68, where signs of transition from rod dominated response to a cone dominated response are evident. However, the exact stimulus strength and duration are not critical as long as they are within the ranges of significance. The maximal amplitude in the characteristic line [amplitude versus stimulus strength or duration (Figures 68, 69, 70)] seemed to be the best indicator to discover optimal stimulation settings. The stimulation settings (Table 19) were optimized in healthy subjects rather than in patients with retinal degenerations because of the variances in ERG recordings in patients with various degenerative processes and different stages of disease progression, which would have prevented standardized testing conditions.

Definition of the 9 Hz flicker response

Table 19: The 9 Hz flicker protocol settings in detail

Description	9 Hz flicker
Averages per result	4
Acquisition	
Sample frequency	1000 Hz
Sweep pre-trigger time	0 ms
Sweep post-trigger time	444 ms
Sweeps per result	30
Drift removal	On
DC off-set removal	On: 0 ms
Stimulus	
Pulse frequency	9 Hz
Pulse duration	10 ms
Stimulus strength	0.012 scot. cd s/m²
Stimulus color	Blue (479 nm)
Background luminance	0 cd/m²
Channels (1 and 2)	
Filter low frequency cut-off	0.3 Hz
Filter high frequency cut-off	30 Hz

The characteristic changes in amplitude and waveform obtained in stimulus strength series and blue versus green stimulation (Figure 68) in combination with the kinetics of the photopigment bleaching test suggests that the 9 Hz flicker paradigm records a rod system dominated response in healthy subjects. Similar to the kinetics of single flash responses published by Cameron et al. [273], the 9 Hz amplitude showed an increase during dark adaptation, even when continuously recording 15 averages each minute (Figure 71a, b). It is evident that the 9 Hz protocol might not be confined to rod system responses in patients with retinal degeneration as it is in healthy subjects. Nevertheless, in the present study with over 900 unselected patients from clinical routine, we found the strongest correlation between the 9 Hz amplitude and the rod b-wave amplitude according to ISCEV standard [0.01 cd s/m² (Figure 73, 18)]. This finding suggests that the 9 Hz flicker response represents a rod response even in patients with retinal degenerations. The lower correlation coefficients for the photopic ERG responses

in comparison with the scotopic ERG responses further support this notion. Certainly, it cannot be ruled out that the 9 Hz recording consists in some instances, in particular in patients with isolated rod dystrophies, of significant cone-system contributions. In such instances, analysis of higher harmonics or visual inspection of the waveform should reveal such cone contributions by the characteristic x-wave formation (Figure 72). Recording ERGs in patients with advanced retinal degeneration is a challenging task. Hence, we do not declare the 9 Hz paradigm as a rod response in patients; it is actually a marker for residual potentials and can be derived by the rod or cone system referring to the character of the retinal disease.

Results in patients

The use of the 9 Hz flicker protocol in patients with advanced retinal degeneration revealed a new possibility to assess retinal rod dominated function even when ISCEV standard ERG responses were “non-recordable” (Figures 74, 75). Especially in patients with impaired rod function, the 9 Hz flicker protocol can provide the only objective assessment of retinal function. Thirty-eight percentage of 273 cases with “non-recordable” standard scotopic ERGs of our patients still exhibited a significant 9 Hz flicker response (Figure 74). Even if the standard ERG was “non-recordable” including the DFT analysis of the 31 Hz flicker protocol, a significant 9 Hz flicker response was detected in 16% of these patients (Figures 74, 75). The precise proportion of recordable responses depends on the applied statistics. Here, we chose to use the method published by Meigen and Bach [258], for its ease of use. We acknowledge that using a multivariate analysis instead and calculating proper Hotelling T^2 statistics may have resulted in slightly different results.

However, we would not recommend using the 9 Hz flicker protocol as a substitute of the photopic 30 Hz flicker, rather as an extra test. Our analysis showed that both protocols complement each other and together allow better assessment of retinal function in clinical or study conditions.

3.5 Conclusion

The proposed protocol has been successfully applied in clinical routine and revealed rod dominated responses in patients where the ISCEV standard protocol could not detect any rod response. This protocol (Table 19) prolonged clinical routine ERG recording sessions only slightly, so that we have actually added it to our standard set of ERG recordings for patients with retinal dystrophies. Analysis of results can be achieved by standard techniques, which are readily available and can be performed automatically in an offline post-processing step. Further should investigate correlations with other parameters of visual function (e.g., dark adaptation, visual field, optical coherence tomography and fundus autofluorescence) and with genotypes of examined patients. We believe that the 9 Hz flicker can successfully be applied in clinical trials where other objective or subjective means to assess retinal function including standard ISCEV ERG and perimetry fail. In these cases, the 9 Hz flicker may provide the only marker to objectively follow up changes in retinal function, which is essential in therapeutical trials treating advanced stages of retinal dystrophies.

4 A BOLD venture: comparison of VEP with functional near-infrared spectroscopy and functional magnetic resonance imaging for assessment of visual acuity

A full paper (Erb M., Fallgatter A. J., Häußinger F., Hillerkuss D., Lisowski L., Nasser F., Scheffler K., Schneider S., Strasser T., Zrenner E., Zobor D., alphabetical order) is in preparation.

4.1 Introduction

Visual evoked potentials (VEP) were first described in the 1930 [274] and have been used since the 1960s to investigate the visual pathway [275]. VEPs allow for functional testing of the optic nerve and the visual cortex and are therefore an important tool in neurology and ophthalmology [276]–[281]. In 1995, the International Society for Clinical Electrophysiology of Vision (ISCEV) published the first standard for visual evoked potentials [282], in which visually evoked cortical potentials are elicited by periodically alternating an achromatic checkerboard of a specific spatial frequency. It is not surprising though, that with the advent of neuroimaging techniques like functional magnetic resonance imaging (fMRI) or functional near-infrared spectroscopy (fNIRS), this stimulation paradigm became also popular in this domain [283]–[293].

Campbel and Maffei found in the 1970 evidence for the existence of size detectors in the visual system [201]. In the same year, Harter and White described a relation between the VEP amplitude and the check-size as a function of visual acuity [202] and later, Legge described the temporal and spatial properties of

the human vision [294]. Special neurons in the visual cortex act as localized spatial frequency filters [214], [295], [296]. A number of methods making use of the relation between VEP amplitude and spatial frequency of checkerboards for the estimation of the visual acuity, were proposed since then [19], [20], [206], [297]–[300]. Almoqbel et al. reviewed the current literature on visual acuity estimation using VEP [301] and Kurtenbach et al. compare three current methods with psychophysically determined visual acuity [21].

Several studies have investigated the sources of visual evoked potentials and the spatial frequency tuning of the visual cortex using functional magnet resonance imaging [220], [287], [28], [25].

FMRI and fNIRS both measure changes in the level of blood oxygenation (BOLD, [293]) of the cerebral blood flow in response to stimulation [302], whereas the EEG is a direct measure of the neural activity based on electrical potentials. However, they are related, as demonstrated by many studies [303]–[305]. Shibasaki gives a comprehensive overview of current neuroimaging techniques and their relation to electrophysiology [304].

An increasing number of studies has evaluated the results of synchronous recording of either VEP and fMRI [306], [307], or VEP and fNIRS [308]–[310] using checkerboard, dart board or windmill patterns, or sinusoidal gratings. However, up to now, there are only a limited number of studies investigating the efffect of visual acuity on the BOLD effect. Zaletel et al. compared the cerebral blood flow velocity responses and VEP amplitudes to gratings of different contrast [309]. Leguire et al. found a relationship among contrast sensitivity, visual acuity, and cortical activation recorded using fMRI [311], and Mirzajani et al. describe a significant effect of lens-induced degradation of the visual acuity on the visual cortex [232].

The aim of our study was to compare the effect of stimulation using checkerboards with different spatial frequencies to the neural activity measured with fNIRS and fMRI with visual evoked potentials and to evaluate the estimation of the visual acuity based on the BOLD effect.

4.2 Methods

Participants

Ten healthy subjects (six males, four females, age 19 – 63 years, mean 35.7 ± 12.7 (SD) years) participated in the study. None of the subjects exhibited ocular or systemic pathology, and a general ophthalmic examination showed no abnormalities. A VEP according to the ISCEV standard [14] was within the norm ranges for all subjects. Best corrected visual acuity (BCVA) was measured using visual targets (Snellen) presented with a projector (Chart Projector CP-500) and was better than 1.0 (decimal) in all subjects. Additionally, the visual acuity was measured using Landolt C optotypes with the Freiburg Visual Acuity Test (FrACT) [200] (Table 20).

All subjects underwent fNIRS and simultaneous steady-state pattern onset VEP [19], [20]. Five subjects underwent an additional fMRI scan. Stimulation was monocularly (right eye) for all examinations with best corrected visual acuity.

All subjects gave written informed consent and were financially rewarded for their participation. The research followed the tenets of the declaration of Helsinki [130], and the study was approved by the Ethics Committee of the University of Tübingen, Germany.

Table 20: Overview of the participants. Best corrected visual acuity was measured using ETDRS charts and FrACT.

				BCVA		FrACT Landolt C VA	
Subject	Sex	Age	Examination	OS	OD	OS	OD
AL	female	28	fNIRS, fMRI	1.0	1.0	1.01	1.15
NS	male	36	fNIRS, fMRI	1.0	1.0	1.33	1.46
EK	female	64	fNIRS	1.0	1.0	0.86	1.37
IN	male	44	fNIRS	1.0	1.0	1.14	1.18
CH	male	24	fNIRS, fMRI	1.0	1.0	1.06	1.77
ZL	male	28	fNIRS, fMRI	1.0	1.0	1.05	1.37
AW	female	35	fNIRS, fMRI	1.0	1.0	1.09	1.34
PH	male	44	fNIRS	1.0	1.0	1.19	1.14
SD	male	18	fNIRS	1.0	1.0	1.53	1.32
NB	female	28	fNIRS	1.0	1.0	1.23	0.92

Visual acuities are denoted as decimal values

Data acquisition

Methodological background of the functional near-infrared spectroscopy

Functional near-infrared spectroscopy makes use of the relative good transparency of biological tissue to near-infrared light in the spectral range of 650 – 1000 nm. This so called "optical window" [312] was proposed in 1977 by Franz Jöbsis as a means of in vivo measurement of blood oxygenation [313]. Near-infrared light of these wavelengths can penetrate the skull and is absorbed by oxygenated [oxyHb] and deoxygenated hemoglobin [de-

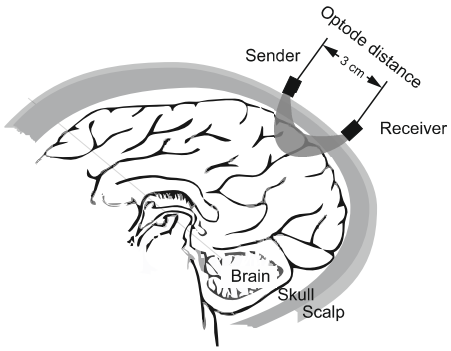

Figure 76: Schematic illustration of the diffusion of near-infrared light trough skull, scalp and brain. The photons travel along a "banana-shaped" path

oxyHb], depending on the used wavelength. This allows for an indirect quantification of the neural activity based on neuro-vascular coupling of the cerebral blood flow [314], [315]. However, due to scattering, the depth of penetration is limited to a few centimeters and assessment of the hemodynamic response is restricted to essentially cortical functions [308], [316]–[318]. Based on the absorption of the near-infrared light, the change in oxygenation and deoxygenation, respectively, is calculated using the modified Beer-Lambert law [319], [320]. Changes in oxy- and deoxygenated hemoglobin are determined by calculating the difference between a resting and a stimulation period. The quantity obtained is scaled in mmol*mm, implying the dependence on the path length of the NIR light in the brain. The path length is determined, on the one hand, by the inter-optode distance, on the other hand, by the differential path length factor (DFC), which may vary according to factors like the specific wavelength of the NIR light and the tissue type, but also on the gender and the age of the subject [321], [322].

A brief review on the history of fNIRS is given by Ferrari and Quaresima [323], whereas Strangman et al. review the application of NIRS for non-invasive neuroimaging [324]. Wolf et al. give a general overview of the application of NIRS for brain studies [325] and describes the progress of NIRS for clinical applications [326].

fNIRS

An ETG-4000 Optical Topography System (Hitachi Medical, Japan) was used to measure the concentration change of oxy-Hb and deoxy-Hb at a rate of 10 Hz. This device uses two wavelength of light (695 nm and 830 nm) to calculate the concentration changes with the Modified Beer-Lambert law (MBLL) [327]–

[329]. An 11 × 3 measurement patch provided by Hitachi was mounted to the participant's heads using an optode cap, with channel 37 placed on Oz (emitter 19 above and collector 26 below Oz, respectively), according to the International 10-20 system [204] (Figure 77b).

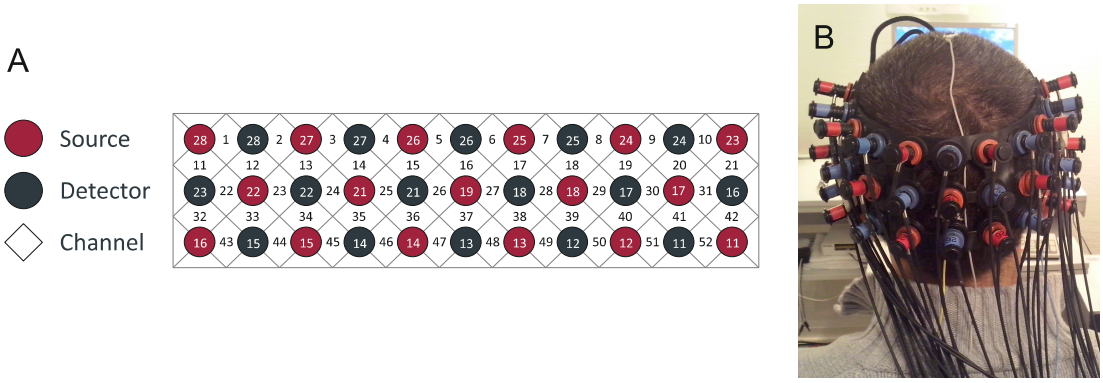

Figure 77: A: Configuration of the 33 optodes in the measurement patch resulting in 52 recording channels. Red circles represent emitter, blue circles receiver optodes, respectively. A pair of an emitter and a receiver comprises a channel. B: The measurement patch mounted on the head of a participant. Channel 37 is placed over Oz. An Ag/AgCL skin electrode is placed on Oz (active electrode, not seen in the picture) for the simultaneous recording of the VEP. Additional electrodes are mounted at Fz (reference electrode) and Cz (ground electrode).

Seventeen emitters and sixteen detectors were positioned alternate in each patch, for a total of 33 probes, resulting in 52 measurement channels (Figure 77a). The distance between an emitter-detector pair was 3 cm. The sampling rate was 10 Hz.

The ETG-4000 was located in a sound-proofed and electromagnetically shielded room. Room light was dimmed during the recording to about 500 lx.

VEP

VEPs were recorded simultaneously with fNIRS using a BrainAmp DC amplifier (Brain Products GmbH, Gilching, Germany) from Ag/AgCl cup electrodes,

placed according to the ISCEV recommendations [14] using the International 10-20 system [204] (active electrode Oz, reference electrode Fz, ground electrode Cz). Signals were acquired with a sampling frequency of 1 kHz and filtered online with a band-pass filter of 0.1-1000 Hz. Impedances were kept below 5 kΩ for all recordings.

fMRI

Structural and functional MRI images were acquired using a 3 Tesla MAGNETOM Prisma system (Siemens, Germany) with a 20-channel head coil.

High resolution T1-weighted structural imaging data were acquired using a MPRAGE sequence with the following settings: 176 sagittal slice of 1 mm thickness; repetition time (TR) = 2300 ms; echo time (TE) = 3.03 ms; inversion time (TI) = 1100ms; flip angle = 8°; field-of-view (FOV) = 240 x 256 mm^2; voxel size = 1.0 x 1.0 x 1.0 mm^3. Parameters for fMRI data acquisition using a BOLD sensitive gradient echo planar imaging (EPI) sequence were: TR = 2000 ms; TE = 30 ms; flip angle 90°; FOV = 192 x 192 mm^2; voxel size = 2.0 x 2.0 x 2.0 mm^3; base resolution = 96; number of slices = 31. The measured volume was placed around the occipital pole (including the primary visual cortex).

Stimulus paradigm and experimental design

Visual stimuli were presented using LCD monitors: for fNIRS an EIZO FlexScan L887 (Eizo Nanao Technologies, Japan) with a resolution of 1600 x 1200 at 20.1", and for fMRI an MR-compatible monitor, OptoStim (medres, medical research GmbH, Cologne, Germany) with a resolution of 2560 x1 600 at 30", and, in the case of fMRI, viewed via an adjustable mirror. The stimulus paradigm was implemented using Presentation (Neurobeharioral Systems Inc., Berkeley, CA,

USA) Specific description of the stimulation paradigm is given below. Participants were required to maintain fixation on the central point throughout the whole recording.

The stimulus paradigm uses onset checkerboard patterns with different spatial frequencies based on the sweepVEP technique, introduced by Hajek and Zrenner [19].

The time course of the hemodynamic response is in the order of a magnitude slower compared to visual evoked potentials: the onset of the response after stimulation begins, takes about 1-2 s [330], [331], and at sustained stimulation, it reaches a plateau at about 20 s [330]. After the end of the stimulation, it takes 4-6 s for the hemodynamic response to return to the baseline [330], [331]. To account for these dynamics of the hemodynamic response, the stimulus paradigm was modified to a block design. In a block design, a stimulus is presented for several seconds, followed by a resting period. The response is then determined as the deviation between the resting and stimulation period. This is known as "subtraction paradigm" [332]. Alternating repetition of the stimulation and resting blocks results in an increase in the signal-to-noise ratio and statistical power [333], [334], [335]. Within a block, either a static or a steady-state stimulus can be used [334]. Block designs are suited best for detecting amplitude diffferences of the hemodynamic response between different conditions [336].

The final stimulus design (Figure 78) uses five stimulation blocks of 21 s duration. The blocks are preceded and followed by ten seconds resting period, which determines the baseline of the hemodynamic response. Each block is repeated three times. The order of the blocks is randomized.

During each block a checkerboard using one of five spatial frequencies is presented as a steady-state pattern onset stimulus: the checkerboard (iso-luminant, 35 cd/m², Michelson contrast 70 %) is shown 60 times for 50 ms, followed

by a 300 ms pause. The size of the checkerboards is about 8 ° visual angle at a distance of 1.6 m for fNIRS and 2 m for fMRT, respectively. These values were chosen to be similar to the original stimuli of Hajek and Zrenner [19], but adjusted to comply with the frame rate of the LCD monitors used to present the stimulus. During the pauses, the checkerboard was rotated by 6 °, resulting in six complete rotations within one block. This “flip-book”-like stimulus was chosen to elicit a higher activation by additional stimulation of motion and orientation dependent channels. The block design combined with a steady-state stimulation within a block allows for a synchronous recording of visual evoked potentials and the hemodynamic response using fNIRS and fMRT, respectively.

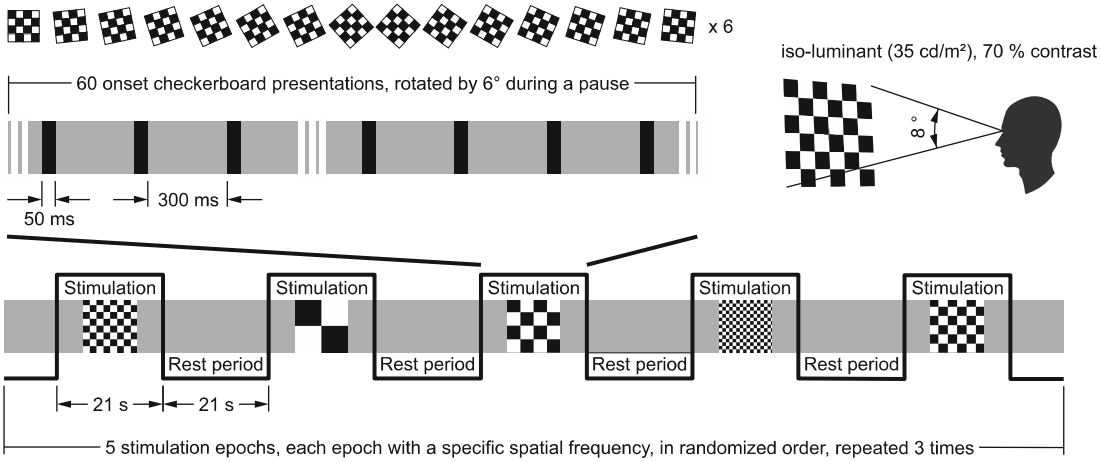

Figure 78: Block design of the visual stimulation. Each block presents an iso-luminant (35 cd/m²) steady-state onset checkerboard stimulus (50 ms presentation, 300 ms pause, ~ 2.86 Hz, 60 repetitions) of a specific spatial frequency (0.5, 1.4, 3.3, 7.0, 9.7 cpd), with a Michelson contrast of ~70 %. The size of the checkerboard is about 8° visual angle in a distance of 1.6 m (fNIRS & VEP) or 2 m (fMRI). The five blocks are repeated three times in randomized order, resulting in a total recording time of 10.5 min. Between the single blocks, a rest period of 21 s allows for the return of the hemodynamic response to its baseline. Within one block, checkerboards are presented for 50 ms, followed by a pause of 300 ms. During pauses, the checkerboards are rotated by 6°, resulting in six complete rotations per block.

Data analysis

VEP

Recorded traces were exported using BrainVision Analyzer (Brain Products GmbH, Gilching, Germany) in VHDR format and imported into EEGLAB Version 13.4.4b [201] running on Matlab (Release 2014a, The Mathworks, Inc., Natick, Massachusetts, USA). After binning, event related potentials were extracted and evaluated using the EEGLAB plugin ERPLAB Version 4.0.3.1 [202], and the peak-to-trough amplitude between the first negative trough (N1) and the first positive peak (P1) was measured.

fNIRS

The continuous wave form data were exported using the Hitachi software as CSV data. All further analysis of the data was conducted using NIRS-SPM Version 4R1 [200] and SPM Version 8 [32], running on Matlab R2014a.

Before imported into NIRS-SPM, the exported data were transformed using a custom Matlab script, since instead of exporting a continuous stimulus period, the Hitachi software changes the block design to only two single events at the beginning and at the end of the block [337].

Spatial registration of the channel positions was done using MNI coordinates of the channel obtained in a previous project using a neuronavigation system (LOCALITE GmbH, St. Augustin, Germany). The first level specification uses the hemodynamic response function [330] as basis set. To remove artefacts, caused by e. g. motion, heartbeat, respiratory noise, etc, the data were detrended using the wavelet minimum description length (Wavelet-MDL) method [338] and low-pass filtered with a hemodynamic response function

32 http://www.fil.ion.ucl.ac.uk/spm/software/spm8

(pre-coloring, [339]), as recommended by Ye et al. [340]. Correction for serial correlations (pre-whitening) was not applied. Based on the general linear model (GLM) beta values for the change of the oxygenated hemodynamic response were estimated using t-contrasts for each spatial frequencies [340]–[342]. To control for the family-wise error rate, *p*-value correction using expected Euler characteristics was applied [340]. A detailed description of the statistical analysis of fNIRS data can be found in the comprehensive review of Tak and Ye [343].

fMRI

The processing was done using SPM Version 12[33], running on Matlab R2014a. Functional MR scans were first motion corrected for movements up to 6 mm using a realignment procedure, taking into account the interaction between the Bo field (susceptibility) and the movement parameters, and then co-registered with the anatomical scans.

Parameters for the nonlinear transformation to the MNI space were determined with the unified segmentation procedure executed with the anatomical scans and then applied to the functional images. The last preprocessing step was smoothing with a Gaussian filter of 8 mm full width at half maximum (FWHM).

The periodic alternation of the block design was convolved with a hemodynamic response function (HRF) to yield the regressor for the design matrix of the general linear model (GLM). A high-pass filter with a cutoff of 128 s was included to the model to remove low frequent drifts, and serial correlations were accounted for by using an autoregressive AR(1) model for pre-whitening. Data

33 http://www.fil.ion.ucl.ac.uk/spm/software/spm12

from all stimulus conditions and subjects were included to a fixed effects (fFX) group analysis (1st level).

Functional maps were generated by simple Student *t*-tests comparing stimulation versus rest periods. A *p*-value threshold at $p < .05$ with family-wise error correction (FWE) for multiple tests was used to determine regions of activation.

Region of interest

A region of interest (ROI) was defined for fMRI analysis, based on structural and functional features: visual stimulation results in an activation in the visual cortex [284], [286], [287], [30], [344]. With the visual cortex as a starting point, a group analysis of all subjects was evaluated using an F-contrast, which included all stimulus conditions (spatial frequencies). The area with the strongest activation over all stimulus conditions and subjects was chosen as center of the ROI.

The ROI was defined as a sphere with its center at the right OCP occipital pole (according to the Talarachi atlas [345], MNI coordinates: [26, -96, 8]), and a radius of 6 mm. ROI selection was performed using MarsBaR version 0.44 [346].

For the fNIRS analysis, the following channels matching the ROI defined for fMRI were selected: channel 17, 27, 28. 37, 38, 39, 48, and 49. However, the penetration depth of near-infrared radiation is restricted to about 25 mm [347].

4.3 Results

fNIRS results

Figure 79 shows the averaged changes in oxygenated and deoxygenated hemoglobin versus time in response to a checkerboard stimulus with a spatial frequency of 3.3 cpd at the example of subject AW. Channel 37 is placed at Oz. Channels located close to the visual cortex show a strong increase in [oxyHb] and a during visual stimulation and a corresponding decrease in [deoxyHb].

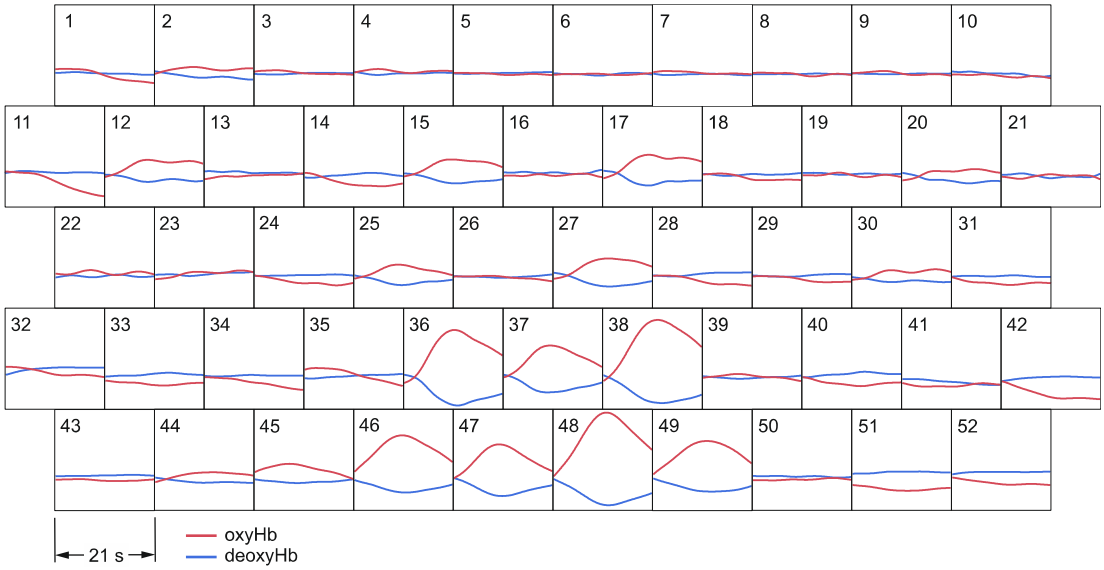

Figure 79: Averaged fNIRS results of changes of [oxyHb] (red traces) and [deoxyHb] (blue traces) versus time (s) of subject AW in response to a checkerboard stimulus with a spatial frequency of 3.3 cpd. Each box represents one channel of the measurement patch. Channel 37 is placed at Oz. Channels close to the visual cortex show a strong increase of [oxyHb], which reaches its maximum at about 10 s, whereas [deoxyHb] decreases simultaneously.

Using GLM analysis, beta weights of the hemodynamic response function were estimated for each subject and condition and activation maps were created using t-values of betas significantly different between stimulation and rest period.- Figure 80 presents the activity maps for all subjects and spatial frequencies.

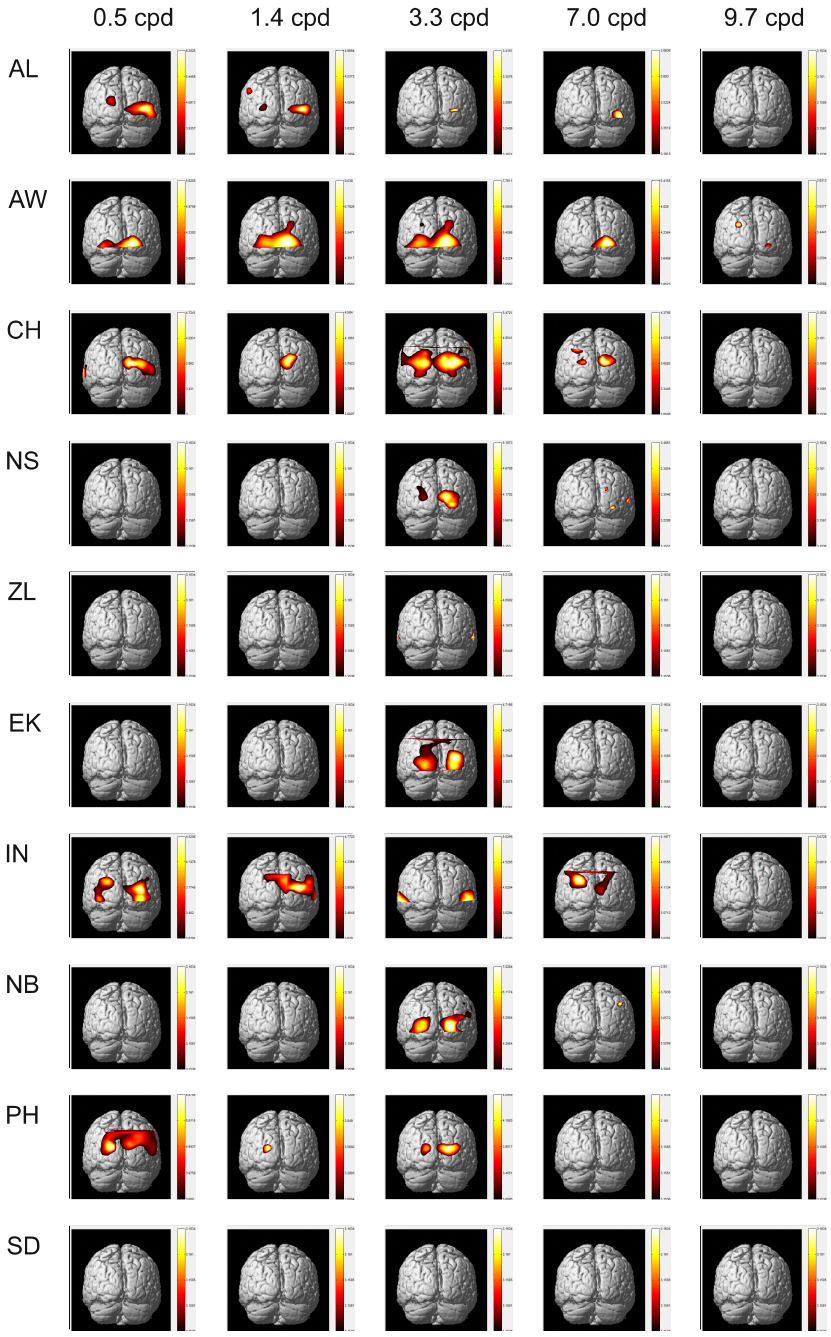

Figure 8o: Activity t-value heat maps for each subject. Colored areas indicate a significant change of [oxyHb] compared to the baseline. Each column represents a specific spatial frequency used for stimulation. Most subjects show an increase of activation with a peak at 3.3 cpd. However, two subjects (SD, ZL) showed no significant activation at all. It should be noted, that the scale of the activation is different for each subject and condition.

Figure 81 shows the relation between the spatial frequency of the checkerboard stimuli and the averaged beta values of channels part of the ROI. It should be noted, that significant as well as not significant values were included. Most subjects show an increase of the activation in relation to the spatial frequency, with a peak at 3.3 cycles per degree. However, some subjects show only weak or even a negative activations.

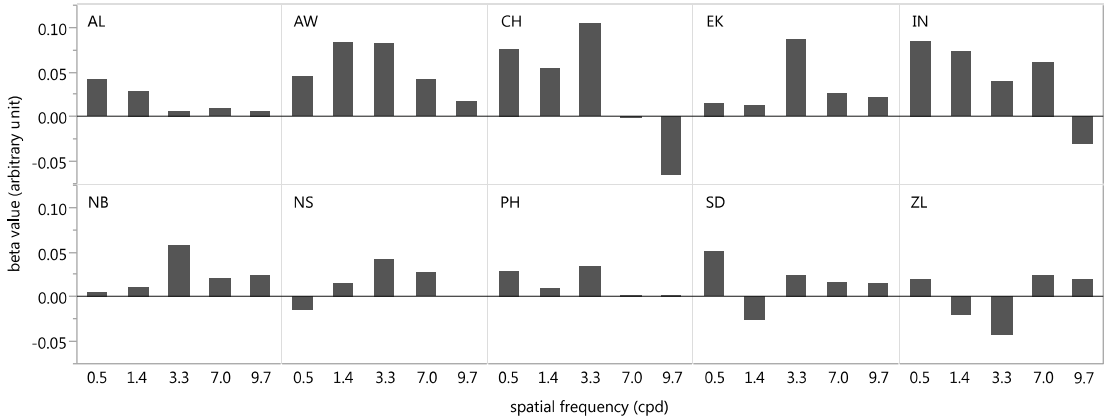

Figure 81: Beta values of [oxyHb] averaged over channels part of the ROI (channels 17, 27, 28. 37, 38, 39, 48, 49). It should be noted, that significant as well as not significant beta values were included.

VEP results

The visual evoked potentials, recorded synchronously to the fNIRS measurements, show the expected relation between the amplitudes and the spatial frequency of the checkerboard stimuli: with increasing spatial frequency, the trough and the peak become larger until they reach a maximum at a certain spatial frequency, after which they start to decline again [19]. Figure 82 depicts the time course of the visual evoked potentials in relation to the spacial frequency of the stimulus for each subject.

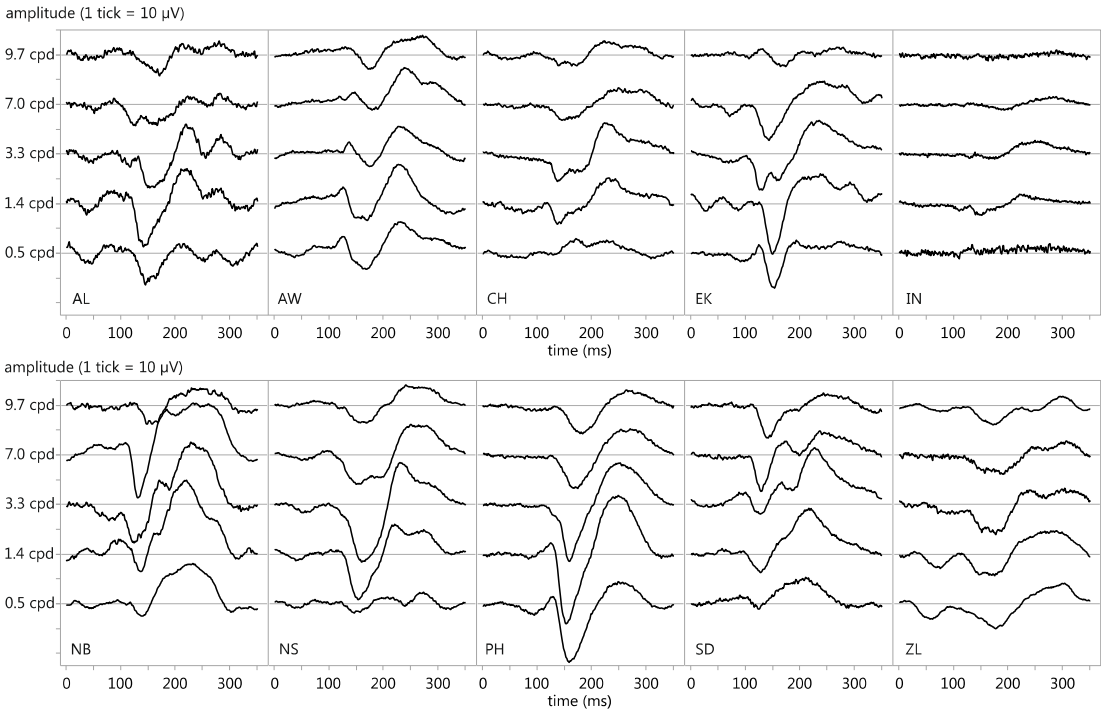

Figure 82: Time course of the visual evoked potentials of each subject in relation to the spatial frequency of the checkerboard stimuli.

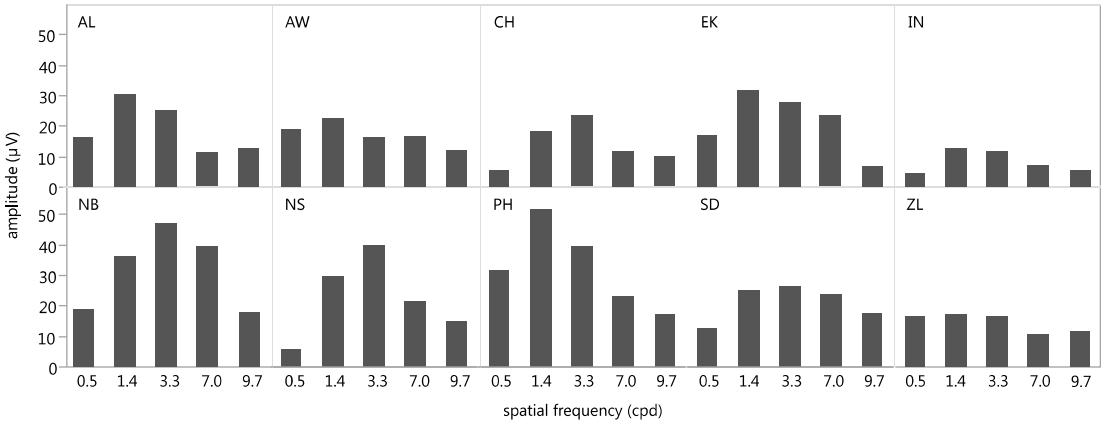

Figure 83: The size of the amplitude between the first negative trough and the following positive peak in relation to the spatial frequency of the checkerboard stimuli. All subjects show an increase of the amplitudes until a certain frequency, after which they start decline again.

Figure 83 presents the peak-to-trough amplitude in relation to the spatial frequency of the checkerboard stimuli. All subjects show the expected increase of the amplitudes until a certain spatial frequency, after which they start to decrease again.

fMRI results

In Figure 84, the BOLD response, measured using fMRI, in relation to the spatial frequency of the checkerboard stimuli is shown for the five subjects, which underwent a fMRI scan.

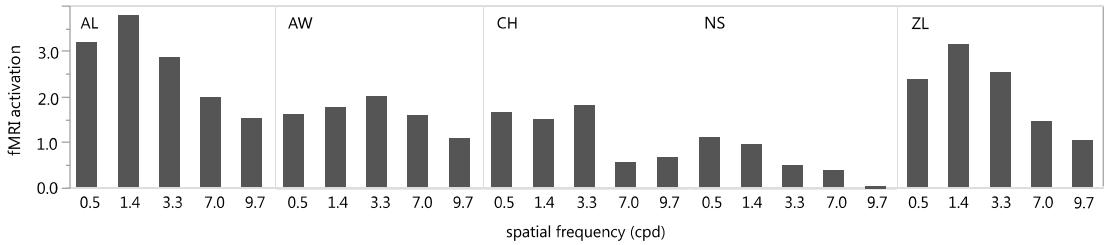

Figure 84: BOLD response of the right OCP occipital pole (ROI: sphere with a center at MNI coordinates: [26, -96, 8] and a radius of 6 mm) of the five subjects which underwent an fMRI scan, in relation to the spatial frequency of the checkerboard stimuli. The same pattern as in fNIRS and VEP can be seen: a increase of the signal until a maximum at a certain frequency, followed by a decline of the signal

Figure 85 shows functional maps of the five subjects which underwent a fMRI scan, during the stimulation with checkerboards of increasing spatial frequency. All subjects show increased activation of the visual cortex in relation to the spatial frequency of the stimuli.

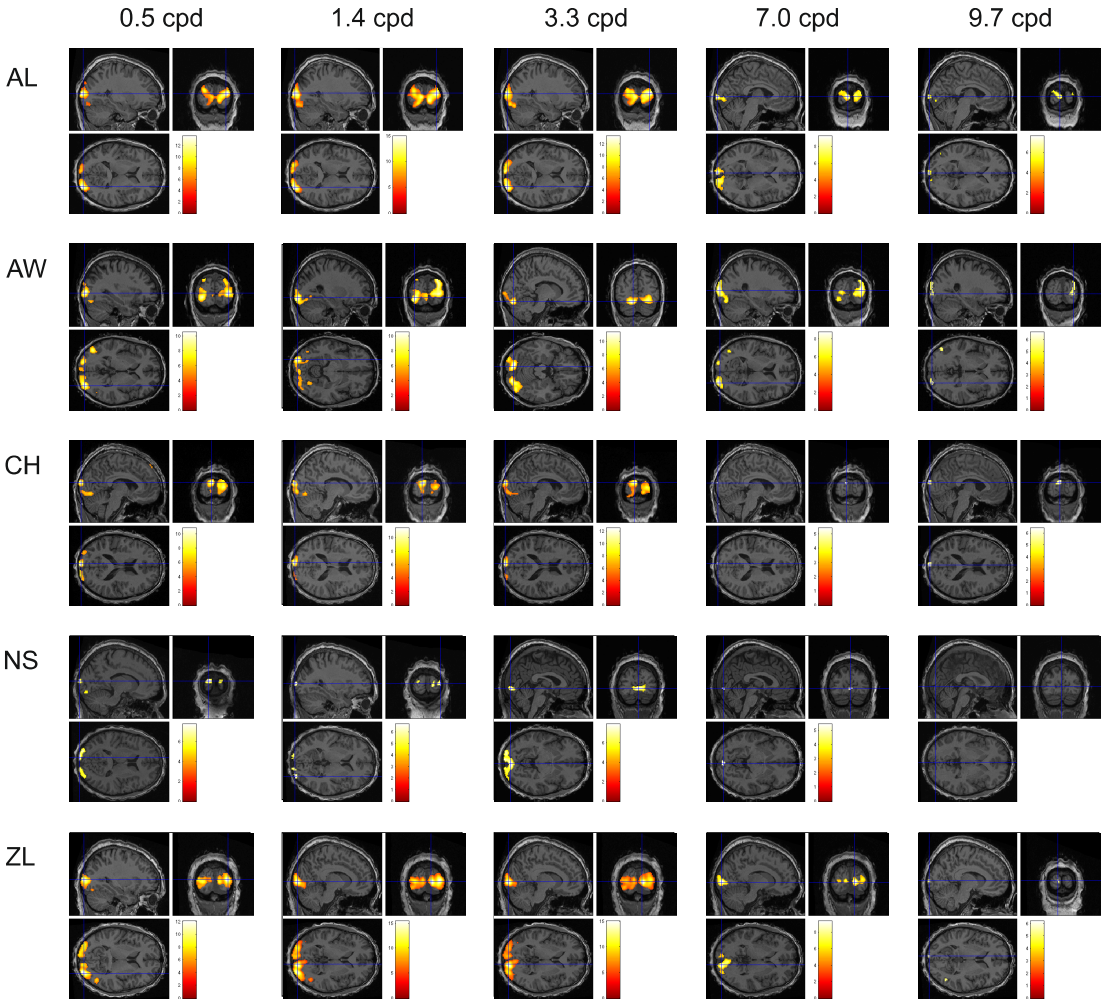

Figure 85: Functional maps of the subjects during the stimulation using checkerboard with different spatial frequencies. Most subjects show statistically significant ($P < 0.05$) activation in the primary visual cortex. The signal intensity increases in relation to the spatial frequency of the checkerboard stimulus, up to a certain frequency. The slices were chosen according to voxel expressing the highest response within the ROI for each subject. Only significant voxels are colored, whereas the color-scale is different for each subject and spatial frequency.

Estimation of the limiting spatial frequency

A non-linear least-squares fitting of a second order polynomial (Equation 14) was applied to the data shown in Figures 81, 83, and 84.

$$F(sf) = p_0 + p_1 \cdot (\log10(sf) - sf_{max}) + p_2 \cdot (\log10(sf) - sf_{max})^2 \quad (14)$$

Figure 86 provides an overview of the fitted second order polynomials for fMRI, fNIRS and VEP.

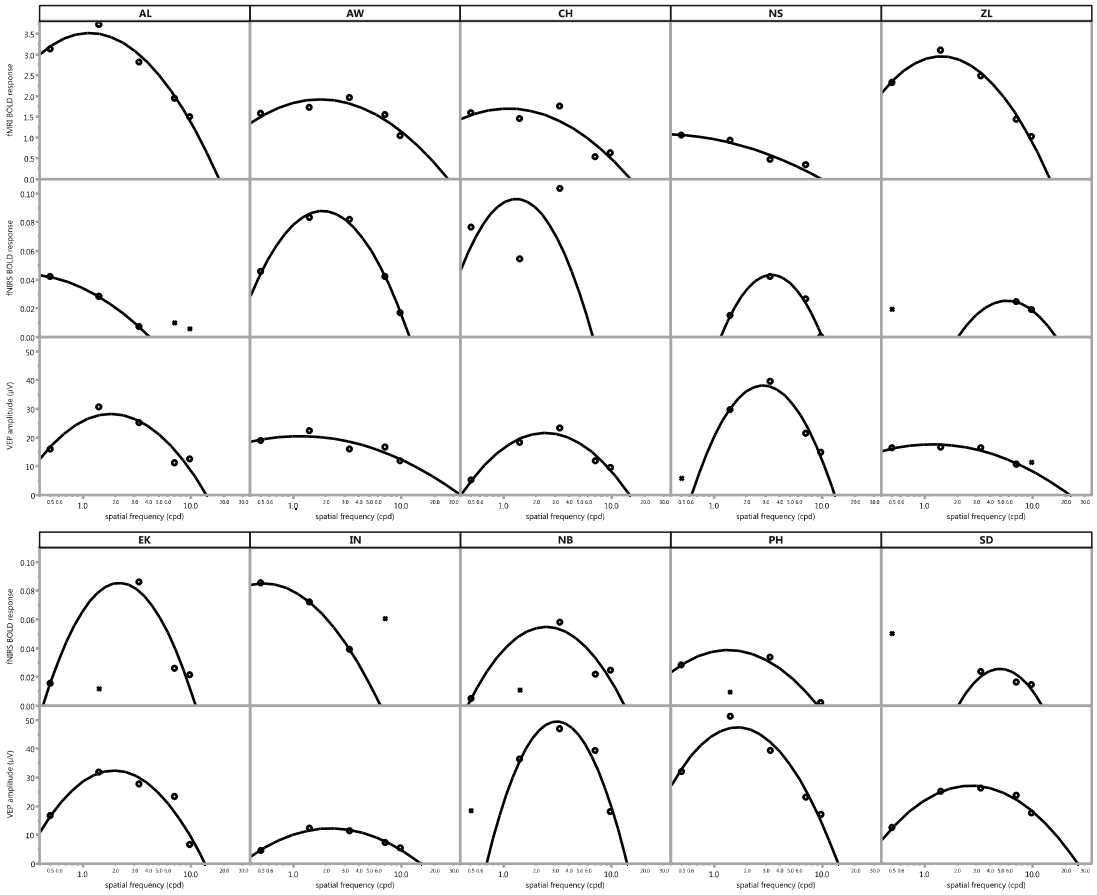

Figure 86: Results of a non-linear least-squares fit of a second order polynomial for the determination of the limiting spatial frequency. Data points included into the fit are represented by circles, excluded data points as crosses. The y-axis represent the peak-to-trough amplitude for VEPs and the BOLD response in arbitrary units for fMRI and fNIRS.

The limiting spatial frequency was determined as the second zero point of the polynomial using Equation 15 [19].

$$SF_0 = 10^{\left(sf_{max} - \frac{p_1 + \sqrt{(p_1^2 - 4 \cdot p_2 \cdot p_0)}}{(2 \cdot p_2)}\right)} \quad (15)$$

Table 21 lists median values and 5 – 95 % quantiles of the determined limiting spatial frequency for fMRI, fNIRS, and VEP. Single results are depicted in the box plot in Figure 87.

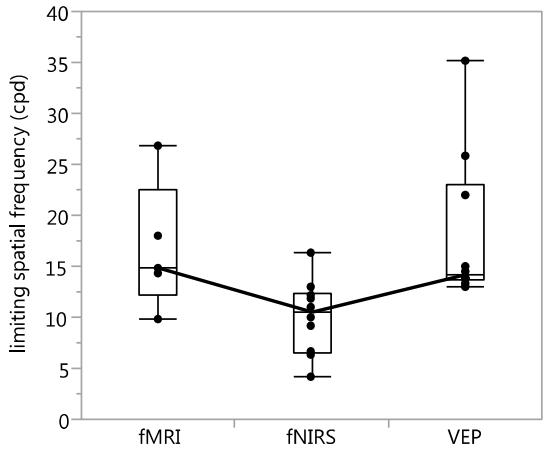

Figure 87: Box plot of the limiting spatial frequency obtained with fMRI, fNIRS, and VEP

Table 21: Median, 5 %, and 95 % quantiles of the determined limiting spatial frequency obtained with fMRI, fNIRS, and VEP

	n	Median (cpd)	Q 5 % (cpd)	Q 95 % (cpd)
fMRI	5	14.9	9.9	26.8
fNIRS	10	10.5	4.2	16.4
VEP	10	14.2	12.9	35.1

Limiting spatial frequencies obtained using fNIRS were lower in all subjects compared to those obtained by fMRI and VEP.

Figure 88 depicts the agreement between the limiting spatial frequencies obtained using fNIRS, fMRI, and VEP as Bland-Altman plots [145] of the difference versus the mean of the limiting spatial frequencies for each combination of recording techniques. The limits of agreement are: fNIRS / fMRI: [-22.4, 8.3]; VEP / fMRI: [-7.6, 13.3]; VEP / fNIRS: [-5.0, 21.0].

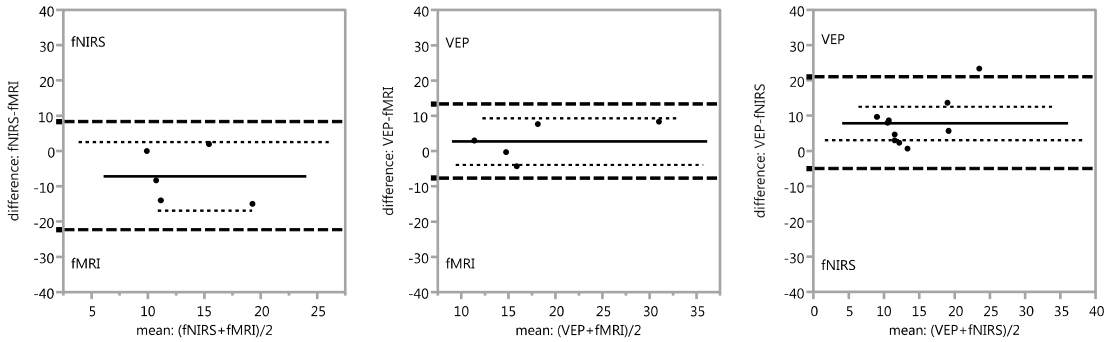

Figure 88: Agreement between the limiting spatial frequencies obtained using the different techniques fNIRS, VEP, and fMRI. The Bland-Altman plot shows the differences vs. the mean values of limiting spatial frequencies of the three pairs fNIRS / fMRI, VEP / fMRI, and VEP / fNIRS. Only the limiting spatial frequencies obtained using VEP and fNIRS show a significant difference. However, the limits of agreements (broken lines) are rather wide in all cases. It should be noted, that the numbers for comparison are only low (fNIRS / fMRI: n = 5; VEP / fMRI: n = 5; VEP / fNIRS: n = 10).

Because of the small number of subjects and the non-normal distribution of the differences, Wilcoxon Signed-Ranks tests for each combination of recording techniques were conducted: For fNIRS / fMRI, the Wilcoxon Signed-Ranks test indicated that median of the limiting spatial frequencies obtained using fNRIS scores (median = 10.5 cpd) were not significantly different to the limiting spatial frequencies obtained using fMRI scores (median = 14.9 cpd) ($Z = -4.5$, $p = .3125$).

For VEP / fMRI, the Wilcoxon Signed-Ranks test indicated that median of the limiting spatial frequencies obtained using VEP scores (median = 14.2 cpd) were not significantly different to the limiting spatial frequencies obtained using fMRI scores (median = 14.9 cpd) ($Z = 3.5$, $p = .4375$).

For VEP / fNIRS, the Wilcoxon Signed-Ranks test indicated that median of the limiting spatial frequencies obtained using VEP scores (median = 14.2 cpd) were significantly higher than the limiting spatial frequencies obtained using fMRI scores (median = 10.46 cpd) ($Z = 27.5$, $p = .0010$).

4.4 Conclusions

We demonstrated a relationship between the spatial frequency of a presented checkerboard and the activation measured in the visual cortex using fNIRS and fMRI. The obtained results were comparable to those of the sweepVEP and may be of clinical use in patients, were an electrophysiological examination is not possible. FNIRS has been proven to be a useful tool for investigating the visual pathway.

4.5 Acknowledgement

This work was supported by the fortüne-programme of the Faculty of Medicine Tuebingen (grant number: 2188-0-0).

SUMMARY

English

The purpose of this thesis was the development of refined methods for recording and processing of neural signals of the retina and ascending visual pathways. The first chapter describes briefly the fundamentals of the human visual system and the basics of the functional testing of the retina and the visual pathways. The second and third chapters are dedicated to the processing of visual electrophysiological data using the newly developed software ERG Explorer, and present a proposal for an open and standardized data format, ElVisML, for future proof storage of visual electrophysiological data. The fourth chapter describes the development and application of two novel electrodes: First a contact lens electrode for the recording of electrical potentials of the ciliary muscle during accommodation, and second, the marble electrode, which is made of a super-absorbant polymer and allows for a preparation-free recording of visual evoked potentials. Results obtained in studies using the both electrodes are presented. The fifths and last chapter of the thesis presents the results from four studies within the field of visual electrophysiology. The first study examines the ophthalmological assessment of cannabis-induced perception disorder using electrophysiological methods. The second study presents a refined method for the objective assessment of the visual acuity using visual evoked potentials and introduces therefore, a refined stimulus paradigm and a novel method for the analysis of the sweep VEP. The third study presents the results of a newly developed stimulus design for full-field electrophysiology, which allows to assess previously non-recordable electroretinograms. The last study describes a relation of the spatial frequency of a visual stimulus to the amplitudes of visual evoked potentials in comparison to the BOLD response obtained using functional near-infrared spectroscopy and functional magnetic resonance imaging.

German

Der Zweck dieser Dissertation war die Entwicklung verbesserter Methoden für die Aufzeichnung und die Verarbeitung von neuronalen Signalen der Netzhaut und der Sehbahn. Im ersten Kapitel werden kurz die Grundlagen des menschlichen Sehens und der funktionalen Untersuchung der Netzhaut und der Sehbahn mit Hilfe elektrophysiologischer Methoden beschrieben. Das dritte und vierte Kapitel befassen sich mit der Verarbeitung von elektrophysiologischen Messungen mit Hilfe der ihm Rahmen der Dissertation entwickelten Software ERG Explorer. Außerdem wird ein Vorschlag für ein offenes und standardisiertes Datenformat namens ElVisML für eine zukunftssichere Speicherung elektrophysiologischer Messungen vorgestellt. Im vierten Kapitel wird die Entwicklung von zwei neuartigen Elektroden beschrieben: Zuerst wird eine Kontaktlinsenelektrode zur Messung der elektrischen Potentiale des Ziliarmuskels während der Akkommodation vorgestellt; anschließend eine auf einem Superabsorber-Polymer basierende Elektrode beschrieben, die die Messung von visuell evozierten Potentialen ohne vorhergehende Reinigung der Haut erlaubt. Mit jeder Elektrode wurde jeweils eine Studie durchgeführt und die daraus erhaltenen Ergebnisse werden präsentiert. Im fünften um letztem Kapitel werden schließlich die Ergebnisse von vier Studien aus dem Gebiet der Elektrophysiologie des Sehens vorgestellt. In der ersten Studie werden die ophthalmologische Untersuchergebnisse von Cannabis-induzierter persistenter Wahrnehmungsstörung unter Zuhilfenahme von elektrophysiologischen Messungen beschrieben. Die zweite Studie eine verbesserte Methode zur objektive Abschätzung der Sehschärfe mit Hilfe visuell evozierter Potenziale und beschreibt die dafür verwendete neu entwickelte Auswertemethode vor. Die dritte Studie befasst sich mit einem neuen Stimulusparadigma für die Messung von Signalen in Patienten

trotz erloschenem ERG vor. In der letzten Studie wird der Zusammenhang zwischen der Ortsfrequenz eines visuellen Stimulus mit den Amplituden der visuell evozierten Potentiale im Vergleich zum BOLD Effekt, gemessen mit Hilfe der funktionellen Nahinfrarotspektroskopie und funktioneller Magnetresonanztomographie vorgestellt.

BIBLIOGRAPHY

[1] D. Barry, J.-Y. Parlange, L. Li, H. Prommer, C. . Cunningham, and F. Stagnitti, "Analytical approximations for real values of the Lambert W-function," *Math. Comput. Simul.*, vol. 53, no. 1–2, pp. 95–103, 2000.

[2] W. Müller and H. Töpke, "The early receptor potential (ERP)," *Doc. Ophthalmol.*, vol. 66, no. 1, pp. 35–74, 1987.

[3] W. a Hagins, R. D. Penn, and S. Yoshikami, "Dark current and photocurrent in retinal rods.," *Biophys. J.*, vol. 10, no. 5, pp. 380–412, 1970.

[4] H. Ripps and P. Witkovsky, "Chapter 7 Neuron — Glia interaction in the brain and retina," *Prog. Retin. Res.*, vol. 4, pp. 181–219, Jan. 1985.

[5] L. Wachtmeister, "Basic research and clinical aspects of the oscillatory potentials of the electroretinogram," *Doc. Ophthalmol.*, vol. 66, no. 3, pp. 187–194, Jun. 1987.

[6] L. Wachtmeister, "Oscillatory potentials in the retina: what do they reveal.," *Prog. Retin. Eye Res.*, vol. 17, no. 4, pp. 485–521, Oct. 1998.

[7] J. T. PEARLMAN, "The C-Wave of the Human ERG," *Arch. Ophthalmol.*, vol. 68, no. 6, p. 823, Dec. 1962.

[8] M. F. Marmor, M. G. Brigell, D. L. McCulloch, C. a Westall, and M. Bach, "ISCEV standard for clinical electro-oculography (2010 update).," *Doc. Ophthalmol.*, vol. 122, no. 1, pp. 1–7, Feb. 2011.

[9] a. D. Ruedemann, "The Electroretinogram in Chronic Methyl Alcohol Poisoning in Human Beings," *Trans. Am. Ophthalmol. Soc.*, vol. 59, pp. 480–529, 1961.

[10] M. T. Seme, P. Summerfelt, M. M. Henry, J. Neitz, and J. T. Eells, "Formate-induced inhibition of photoreceptor function in methanol intoxication.," *J. Pharmacol. Exp. Ther.*, vol. 289, no. 1, pp. 361–370, 1999.

[11] B. Young, E. Eggenberger, and D. Kaufman, "Current electrophysiology in ophthalmology," *Curr. Opin. Ophthalmol.*, vol. 23, no. 6, pp. 497–505, 2012.

[12] A. Vincent, A. G. Robson, and G. E. Holder, "Pathognomonic (diagnostic) ERGs. A review and update.," *Retina*, vol. 33, no. 1, pp. 5–12, 2013.

[13] U. R. Kumar and P. A. Karth, "Electroretinogram," *EyeWiki, American Academy of Ophthalmology*, 2015. [Online]. Available: http://eyewiki.aao.org/w/index.php?title=Electroretinogram&oldid=19643. [Accessed: 01-Sep-2015].

[14] J. V. Odom, M. Bach, M. Brigell, G. E. Holder, D. L. McCulloch, A. P. Tormene, and Vaegan, "ISCEV standard for clinical visual evoked potentials (2009 update).," *Doc. Ophthalmol.*, vol. 120, no. 1, pp. 111–9, Feb. 2010.

[15] W. B. Alshuaib, "Progression of visual evoked potential abnormalities in multiple sclerosis and optic neuritis.," *Electromyogr. Clin. Neurophysiol.*, vol. 40, no. 4, pp. 243–252, 2000.

[16] B. Bengtsson, "Evaluation of VEP perimetry in normal subjects and glaucoma patients.," *Acta Ophthalmol. Scand.*, vol. 80, no. 6, pp. 620–626, 2002.

[17] A. Klistorner and S. L. Graham, "Objective perimetry in glaucoma," *Ophthalmology*, vol. 107, no. 12, pp. 2283–2299, Dec. 2000.

[18] A. I. Klistorner and S. L. Graham, "Multifocal pattern VEP perimetry: Analysis of sectoral waveforms," *Doc. Ophthalmol.*, vol. 98, no. 2, pp. 183–196, 1999.

[19] A. Hajek and E. Zrenner, "[Improved objective visual assessment with visual evoked cortical potentials by rapid pattern stimuli sequences of different spatial frequency].," *Fortschr. Ophthalmol.*, vol. 85, no. 5, pp. 550–4, Jan. 1988.

[20] M. Bach, J. P. Maurer, and M. E. Wolf, "Visual evoked potential-based acuity assessment in normal vision, artificially degraded vision, and in patients.," *Br. J. Ophthalmol.*, vol. 92, no. 3, pp. 396–403, Mar. 2008.

[21] A. Kurtenbach, H. Langrová, A. Messias, E. Zrenner, and H. Jägle, "A comparison of the performance of three visual evoked potential-based methods to estimate visual acuity.," *Doc. Ophthalmol.*, vol. 126, no. 1, pp. 45–56, Feb. 2013.

[22] M. B. Hoffmann, A. S. Unsöld, and M. Bach, "Directional tuning of human motion adaptation as reflected by the motion VEP," *Vision Res.*, vol. 41, no. 17, pp. 2187–2194, 2001.

[23] A. Moskowitz and S. Sokol, "Effect of stimulus orientation on the latency and amplitude of the VEP.," *Invest. Ophthalmol. Vis. Sci.*, vol. 26, no. 2, pp. 246–8, Feb. 1985.

[24] R. Müller, E. Göpfert, M. Leineweber, and M. W. Greenlee, "Effect of adaptation direction on the motion VEP and perceived speed of drifting gratings," *Vision Res.*, vol. 44, no. 20, pp. 2381–2392, 2004.

[25] F. Di Russo, S. Pitzalis, G. Spitoni, T. Aprile, F. Patria, D. Spinelli, and S. a. Hillyard, "Identification of the neural sources of the pattern-reversal VEP," *Neuroimage*, vol. 24, no. 3, pp. 874–886, 2005.

[26] J. Gerling, T. Meigen, and M. Bach, "Shift of equiluminance in congenital color vision deficiencies: pattern-ERG, VEP and psychophysical findings.," *Vision Res.*, vol. 37, no. 6, pp. 821–6, Mar. 1997.

[27] M. Kuba, Z. Kubová, J. Kremláček, and J. Langrová, "Motion-onset VEPs: Characteristics, methods, and diagnostic use," *Vision Res.*, vol. 47, no. 2, pp. 189–202, 2007.

[28] L. Henriksson, L. Nurminen, A. Hyvärinen, and S. Vanni, "Spatial frequency tuning in human retinotopic visual areas.," *J. Vis.*, vol. 8, no. 10, pp. 5.1–13, 2008.

[29] J. Kremláček, M. Kuba, Z. Kubová, and J. Chlubnová, "Motion-onset VEPs to translating, radial, rotating and spiral stimuli," *Doc. Ophthalmol.*, vol. 109, no. 2, pp. 169–175, 2004.

[30] G. Bonmassar, D. P. Schwartz, a K. Liu, K. K. Kwong, a M. Dale, and J. W. Belliveau, "Spatiotemporal brain imaging of visual-evoked activity using interleaved EEG and fMRI recordings.," *Neuroimage*, vol. 13, no. 6 Pt 1, pp. 1035–43, Jun. 2001.

[31] M. Fahle and M. Bach, "Basics of the VEP," in *Principles and Practice of Clinical Electrophysiology of Vision*, J. Heckenlively and G. . Arden, Eds. London: MIT Press Cambridge, 2006, pp. 207–234.

[32] D. J. Creel, "Visually evoked potentials," *Webvision. Moran Eye Center*, 2015. [Online]. Available: http://webvision.med.utah.edu/book/electrophysiology/visually-evoked-potentials/. [Accessed: 01-Sep-2015].

[33] E. F. Codd, "A relational model of data for large shared data banks," *Commun. ACM*, vol. 26, no. 1, pp. 64–69, Jan. 1983.

[34] E. F. Codd, "Derivability, redundancy and consistency of relations stored in large data banks," *ACM SIGMOD Rec.*, vol. 38, no. 1, p. 17, Jun. 2009.

[35] R. Robson, "Personal Communication," 2010.

[36] P. Deutsch, "DEFLATE Compressed Data Format Specification version 1.3," 1996. [Online]. Available: http://www.rfc-editor.org/info/rfc1951. [Accessed: 20-Jun-2015].

[37] C. Ullenboom, *Java ist auch eine Insel*, 11th ed. Bonn: Galileo Computing, 2014.

[38] E. Gamma, R. Helm, R. E. Johnson, and J. Vlissides, *Design Patterns: Elements of Reusable Object-Oriented Software*, 1st ed. Amsterdam: Addison-Wesley Longman, 1995.

[39] K. Eilebrecht and G. Starke, *Patterns kompakt: Entwurfsmuster für effektive Software-Entwicklung*, 4th ed. Heidelberg: Spektrum Akademischer Verlag, 2010.

[40] T. STRASSER, R. WILKE, A. MESSIAS, and E. ZRENNER, "Erg explorer: a software for post-processing, analysing, and reporting of electrophysiological data," *Acta Ophthalmol.*, vol. 86, p. 0, Sep. 2008.

[41] F. Buschmann, R. Meunier, H. Rohnert, P. Sommerlad, and M. Stal, *Pattern-Oriented Software Architecture Volume 1: A System of Patterns*, 1st ed. West Sussex: John Wiley & Sons Ltd, 1996.

[42] A. van Deursen, P. Klint, and J. Visser, "Domain-specific languages," *ACM SIGPLAN Not.*, vol. 35, no. 6, pp. 26–36, 2000.

[43] P. Hudak, "Building domain-specific embedded languages," *ACM Comput. Surv.*, vol. 28, no. 4es, p. 196–es, Dec. 1996.

[44] S. Microsystems, "Generics." [Online]. Available: http://java.sun.com/j2se/1.5.0/docs/guide/language/generics.html.
[45] S. Microsystems, "Static Import." [Online]. Available: http://java.sun.com/j2se/1.5.0/docs/guide/language/static-import.html.
[46] M. Fowler and E. Evans, "MF Bliki: FluentInterface." [Online]. Available: http://www.martinfowler.com/bliki/FluentInterface.html.
[47] A. Khan, "Factories, Builders and Fluent Interfaces." [Online]. Available: http://aslamkhan.net/software-development/factories-builders-and-fluent-interfaces/.
[48] G. Lotz, "Design and Implementation of Reading Center Software for Multi-Center Clinical Trials," University of Tuebingen, 2011.
[49] A. L. Jacobson, "Auto-threshold peak detection in physiological signals," in *2001 Conference Proceedings of the 23rd Annual International Conference of the IEEE Engineering in Medicine and Biology Society*, vol. 3, pp. 2194–2195.
[50] F. Scholkmann, J. Boss, and M. Wolf, "An efficient algorithm for automatic peak detection in noisy periodic and quasi-periodic signals," *Algorithms*, vol. 5, no. 4, pp. 588–603, 2012.
[51] A. Savitzky and M. J. E. Golay, "Smoothing and Differentiation of Data by Simplified Least Squares Procedures.," *Anal. Chem.*, vol. 36, no. 8, pp. 1627–1639, Jul. 1964.
[52] A. Schatz, R. Wilke, T. Strasser, F. Gekeler, A. Messias, and E. Zrenner, "Assessment of 'non-recordable' electroretinograms by 9 Hz flicker stimulation under scotopic conditions," *Doc. Ophthalmol.*, vol. 124, no. 1, pp. 27–39, Feb. 2012.
[53] K. I. NAKA and W. A. H. RUSHTON, "S-POTENTIALS FROM COLOUR UNITS IN THE RETINA OF FISH (CYPRINIDAE)," *J. Physiol.*, vol. 185, no. 3, pp. 536–555, 1966.
[54] a. B. Fulton and W. a H. Rushton, "The human rod ERG: Correlation with psychophysical responses in light and dark adaptation," *Vision Res.*, vol. 18, no. 7, pp. 793–800, 1978.
[55] M. L. SEVERNS and M. A. JOHNSON, "The care and fitting of Naka-Rushton functions to electroretinographic intensity-response data," *Doc. Ophthalmol.*, vol. 85, pp. 135–150, 1993.
[56] D. Zobor, T. Strasser, G. Zobor, F. Schober, A. Messias, O. Strauss, A. Batra, and E. Zrenner, "Ophthalmological assessment of cannabis-induced persisting perception disorder: Is there a direct retinal effect?," *Doc. Ophthalmol.*, Jan. 2015.
[57] B. Entenmann, "Elektrookulographie," University of Tuebingen, 1996.

[58] M. G. Sarossy, M. H. a Lee, and M. Bach, “A fast automated method for calculating the EOG Arden ratio.,” *Doc. Ophthalmol.*, Mar. 2014.

[59] M. Brigell, M. Bach, C. Barber, K. Kawasaki, and a Kooijman, “Guidelines for calibration of stimulus and recording parameters used in clinical electrophysiology of vision. Calibration Standard Committee of the International Society for Clinical Electrophysiology of Vision (ISCEV).,” *Doc. Ophthalmol.*, vol. 95, no. 1, pp. 1–14, Jan. 1998.

[60] M. F. Marmor, a B. Fulton, G. E. Holder, Y. Miyake, M. Brigell, and M. Bach, “ISCEV Standard for full-field clinical electroretinography (2008 update).,” *Doc. Ophthalmol.*, vol. 118, no. 1, pp. 69–77, Feb. 2009.

[61] M. Bach, M. G. Brigell, M. Hawlina, G. E. Holder, M. a Johnson, D. L. McCulloch, T. Meigen, and S. Viswanathan, “ISCEV standard for clinical pattern electroretinography (PERG): 2012 update.,” *Doc. Ophthalmol.*, vol. 126, no. 1, pp. 1–7, Feb. 2013.

[62] E. Troeger, I. Sliesoraityte, P. Charbel Issa, H. N. Scholl, E. Zrenner, and R. Wilke, “An integrated software solution for multi-modal mapping of morphological and functional ocular data.,” *Conf. Proc. IEEE Eng. Med. Biol. Soc.*, vol. 2010, pp. 6280–3, Jan. 2010.

[63] T. Ganes and E. Kerty, “Multimodal evoked potentials, EEG and electroretinography in patients with dystrophia myotonica,” *Acta Neurol. Scand.*, vol. 78, no. 5, pp. 436–442, Nov. 1988.

[64] A. V Cideciyan, “Leber congenital amaurosis due to RPE65 mutations and its treatment with gene therapy.,” *Prog. Retin. Eye Res.*, vol. 29, no. 5, pp. 398–427, Sep. 2010.

[65] R. E. MacLaren, M. Groppe, A. R. Barnard, C. L. Cottriall, T. Tolmachova, L. Seymour, K. R. Clark, M. J. During, F. P. M. Cremers, G. C. M. Black, A. J. Lotery, S. M. Downes, A. R. Webster, and M. C. Seabra, “Retinal gene therapy in patients with choroideremia: initial findings from a phase 1/2 clinical trial,” *Lancet*, vol. 383, no. 9923, pp. 1129–1137, Mar. 2014.

[66] F. I. Al-Saikhan, “The gene therapy revolution in ophthalmology.,” *Saudi J. Ophthalmol. Off. J. Saudi Ophthalmol. Soc.*, vol. 27, no. 2, pp. 107–111, Apr. 2013.

[67] E. Zrenner, K. U. Bartz-Schmidt, H. Benav, D. Besch, A. Bruckmann, V.-P. Gabel, F. Gekeler, U. Greppmaier, A. Harscher, S. Kibbel, J. Koch, A. Kusnyerik, T. Peters, K. Stingl, H. Sachs, A. Stett, P. Szurman, B. Wilhelm, and R. Wilke, “Subretinal electronic chips allow blind patients to read letters and combine them to words.,” *Proc. Biol. Sci.*, vol. 278, no. 1711, pp. 1489–97, May 2011.

[68] L. da Cruz, B. F. Coley, J. Dorn, F. Merlini, E. Filley, P. Christopher, F. K. Chen, V. Wuyyuru, J. Sahel, P. Stanga, M. Humayun, R. J. Greenberg, and

G. Dagnelie, “The Argus II epiretinal prosthesis system allows letter and word reading and long-term function in patients with profound vision loss.,” *Br. J. Ophthalmol.*, vol. 97, no. 5, pp. 632–6, May 2013.

[69] A. T. Chuang, C. E. Margo, and P. B. Greenberg, “Retinal implants: a systematic review.,” *Br. J. Ophthalmol.*, Jan. 2014.

[70] T. H. Vines, A. Y. K. Albert, R. L. Andrew, F. Débarre, D. G. Bock, M. T. Franklin, K. J. Gilbert, J.-S. Moore, S. Renaut, and D. J. Rennison, “The availability of research data declines rapidly with article age.,” *Curr. Biol.*, vol. 24, no. 1, pp. 94–7, Jan. 2014.

[71] A. Schlögl, *Overview of data formats for biomedical signals*, vol. 25/4. Berlin, Heidelberg: Springer Berlin Heidelberg, 2009.

[72] B. KEMP, A. VARRI, A. ROSA, K. NIELSEN, and J. GADE, “A simple format for exchange of digitized polygraphic recordings☆,”*Electroencephalogr. Clin. Neurophysiol.*, vol. 82, no. 5, pp. 391–393, May 1992.

[73] A. Schlögl, “GDF - A general dataformat for biosignals,” *Structure*, pp. 1–15, Aug. 2006.

[74] ACR-NEMA, “DICOM Supplement 30: Waveform Interchange.” 1999.

[75] H. Wang, F. Azuaje, B. Jung, and N. Black, “A markup language for electrocardiogram data acquisition and analysis (ecgML).,” *BMC Med. Inform. Decis. Mak.*, vol. 3, p. 4, May 2003.

[76] “Health Leve Seven. HL7 Version 3 Standard: Regulated Studies - Annotated ECG,” 2003. [Online]. Available: http://www.hl7.org/V3AnnECG/foundationdocuments/welcome/index.htm.

[77] C. Kothe and C. Brunner, “XDF (Extensible Data Format),” 2012. [Online]. Available: https://code.google.com/p/xdf/. [Accessed: 01-Jul-2015].

[78] A. Varri, B. Kemp, T. Penzel, and A. Schlogl, “Standards for biomedical signal databases,” *IEEE Eng. Med. Biol. Mag.*, vol. 20, no. 3, pp. 33–37, 2001.

[79] T. Texin, “Benefits of the Unicode™ Character Standard,” 2003. [Online]. Available: http://www.i18nguy.com/UnicodeBenefits.html. [Accessed: 04-Jul-2015].

[80] J. D. U. C. Allen, *The Unicode standard 5.0*, Version 5. Upper Saddle River, NJ: Addison-Wesley, 2007.

[81] T. STRASSER, S. AVCU, V. KONEV, F. KORKMAZ, E. MANAV, T. SCHRECK, M. TAUKOVIC, R. WILKE, and E. ZRENNER, “Development of a software for the exchange of electrophysiological data of vision with PACS systems based on DICOM,” *Acta Ophthalmol.*, vol. 87, Sep. 2009.

[82] P. Mildenberger, M. Eichelberg, and E. Martin, “Introduction to the DICOM standard,” *Eur. Radiol.*, vol. 12, no. 4, pp. 920–927, Apr. 2002.

[83] H. Oosterwijk, *DICOM Basics*, 3rd ed. Aubrey, USA: Otech Inc., 2005.
[84] S. Xie, D. Yu, X. Wei, and K. Wang, "The semantic extension and storage of eecp hemodynamic waveforms based on dicom standard," *Med. Biol. Eng. Comput.*, vol. 46, no. 4, pp. 391–397, Apr. 2008.
[85] M. J. Warnock, C. Toland, D. Evans, B. Wallace, and P. Nagy, "Benefits of using the DCM4CHE DICOM archive.," *J. Digit. imaging Off. J. Soc. Comput. Appl. Radiol.*, vol. 20 Suppl 1, no. October, pp. 125–9, Nov. 2007.
[86] NIH, "ImageJ - Image Processing and Analysis in Java," 2010. [Online]. Available: http://rsbweb.nih.gov/ij/. [Accessed: 01-Jan-2010].
[87] D. L. McCulloch and R. Hamilton, "Essentials of photometry for clinical electrophysiology of vision.," *Doc. Ophthalmol.*, vol. 121, no. 1, pp. 77–84, Aug. 2010.
[88] B. Kemp, "European data format (EDF): Current availability and additional applications," *J. Sleep Res.*, vol. 11, p. 120, 2002.
[89] B. Kemp, "European data format 'plus' (EDF+), an EDF alike standard format for the exchange of physiological data," *Clin. Neurophysiol.*, vol. 114, no. 9, pp. 1755–1761, Sep. 2003.
[90] F. Gibson, P. G. Overton, T. V Smulders, S. R. Schultz, S. J. Eglen, C. D. Ingram, S. Panzeri, P. Bream, M. Whittington, E. Sernagor, M. Cunningham, C. Adams, C. Echtermeyer, J. Simonotto, D. C. Swan, M. Fletcher, and P. Lord, "Minimum Information about a Neuroscience Investigation (MINI): Electrophysiology," *Nat. Preced.*, pp. 1–7, 2009.
[91] R. R. Bond, D. D. Finlay, C. D. Nugent, and G. Moore, "XML-BSPM: an XML format for storing Body Surface Potential Map recordings.," *BMC Med. Inform. Decis. Mak.*, vol. 10, p. 28, Jan. 2010.
[92] W. Zareba, "New era for digital ECG: FDA requires digital ECG submission for tested drugs.," *Ann. Noninvasive Electrocardiol.*, vol. 7, no. 1, pp. 1–3, Jan. 2002.
[93] B. D. Brown and F. Badilini, "HL7 aECG implementation guide," 2005.
[94] B. Brown, M. Kohls, and N. Stockbridge, "FDA XML Data Format Design Specification," 2002. [Online]. Available: http://xml.coverpages.org/FDA-EGC-XMLDataFormat-C.pdf.
[95] B. Brown, M. Kohls, and N. Stockbridge, "FDA XML Data Format Requirements Specification," *Review Literature And Arts Of The Americas*, 2002. [Online]. Available: http://xml.coverpages.org/FDA-EGC-XML-Reqs-B.pdf.
[96] U. S. F. C. C. X. W. Group, "Draft Federal XML Developer ' s Guide," *Group*, 2002. [Online]. Available: http://xml.gov/documents/in_progress/developersguide.pdf. [Accessed: 01-Jan-2010].

[97] "Extensible Markup Language (XML)." [Online]. Available: http://www.w3.org/XML/.
[98] E. van der Vlist, "Comparing XML Schema Languages," 2001. [Online]. Available: http://www.xml.com/pub/a/2001/12/12/schemacompare.html.
[99] C. M. Sperberg-McQueen and H. Thompson, "XML Schema," 2000. [Online]. Available: http://www.w3.org/XML/Schema.
[100] D. C. (IBM) Fallside and P. Walmsley, "XML Schema Part 0: Primer Second Edition," 2004. [Online]. Available: http://www.w3.org/TR/xmlschema-0/.
[101] H. Thompson, D. Beech, M. Maloney, and N. Mendelson, "XML Schema Part 1: Structures Second Edition," 2004. [Online]. Available: http://www.w3.org/TR/xmlschema-1/.
[102] P. V. Biron and A. Malhotra, "XML Schema Part 2: Datatypes Second Edition," 2004. [Online]. Available: http://www.w3.org/TR/xmlschema-2/.
[103] S. Boag, D. Chamberlin, M. F. Fernández, D. Florescu, J. Robie, and J. Siméon, "XQuery 1.0: An XML Query Language," 2007. [Online]. Available: http://www.w3.org/TR/xquery/.
[104] J. Clark and S. DeRose, "XML Path Language (XPath)," 1999. [Online]. Available: http://www.w3.org/TR/xpath.
[105] A. Vakali, B. Catania, and A. Maddalena, "XML Data Stores: Emerging Practices," *IEEE Internet Comput.*, vol. 9, no. 2, pp. 62–69, Mar. 2005.
[106] J. Clark, "XSL Transformations (XSLT)," 1999. [Online]. Available: http://www.w3.org/TR/xslt.
[107] J. Oberg, "Why the Mars probe [accident investigation]," *IEEE Spectr.*, vol. 36, no. 12, pp. 34–39, 1999.
[108] G. Schadow, C. J. McDonald, J. G. Suico, U. Föhring, and T. Tolxdorff, "Units of measure in clinical information systems.," *J. Am. Med. Inform. Assoc.*, vol. 6, no. 2, pp. 151–62, 1999.
[109] G. Schadow and C. J. McDonald, "THE UNIFIED CODE FOR UNITS OF MEASURE," 2009. [Online]. Available: http://aurora.regenstrief.org/~ucum/ucum.html.
[110] P. Electronic, H. Information, M. Privacy, H. C. Applications, N. I. Infrastructure, P. Sciences, C. Isbn, T. Pdf, N. A. Press, and N. Academy, *FOR THE RECORD: PROTECTING ELECTRONIC HEALTH INFORMATION*. Washington, D. C.: National Academy Press, 1997.
[111] D. Eastlake, J. Reagle, D. Solo, F. Hirsch, T. Roessler, M. Bartel, J. Boyer, B. Fox, B. LaMacchia, and E. Simon, "XML Signature Syntax and Processing (Second Edition)," 2008. [Online]. Available: http://www.w3.org/TR/xmldsig-core/.

[112] D. Eastlake, J. Reagle, T. Imamura, B. Dillaway, and E. Simon, "XML Encryption Syntax and Processing," 2002. [Online]. Available: http://www.w3.org/TR/xmlenc-core/.
[113] D. Stephenson, "XML Schema best practices," 2004.
[114] N. T. A. Committee, "National Information Exchange Model Naming and Design Rules Version 1.3," 2008.
[115] M. Glaser, "Konzeption und Realisierung einer Java-basierten Schnittstelle zu ElVisML als Teil einer Software zur Analyse von elektrophysiologischen Untersuchungen des Sehens," University of Applied Sciences Augsburg, 2012.
[116] T. STRASSER, T. PETERS, and E. ZRENNER, "ElVisML: A little less conversation. Experiences with the Electrophysiology of Vision Markup Language in clinical routine and in a multi-center trial," *Acta Ophthalmol.*, vol. 89, Sep. 2011.
[117] A. J. Bron, R. C. Tripathi, and B. J. Tripathi, "The posterior chamber and ciliary body," in *Wolff's anatomy of the eye and orbit*, 8th ed., London: Chapman and Hall Medical, 1998, pp. 367–370.
[118] H. Helmholtz, "Ueber die Accommodation des Auges," *Albr. von Graefes Arch. für Ophthalmol.*, vol. 2, no. 1, pp. 1–74, Mar. 1855.
[119] M. Baumeister and T. Kohnen, "Current State of Accommodation Research," in *Cataract and Refractive Surgery*, Berlin, Heidelberg: Springer Berlin Heidelberg, pp. 101–110.
[120] F. M. Toates, "Accommodation function of the human eye.," *Physiol. Rev.*, vol. 52, no. 4, pp. 828–863, 1972.
[121] J. a. Mordi and K. J. Ciuffreda, "Static aspects of accommodation: age and presbyopia," *Vision Res.*, vol. 38, no. 11, pp. 1643–1653, Jun. 1998.
[122] J. a. Mordi and K. J. Ciuffreda, "Dynamic aspects of accommodation: age and presbyopia," *Vision Res.*, vol. 44, no. 6, pp. 591–601, Mar. 2004.
[123] M. A. Croft, A. Glasser, and P. L. Kaufman, "Accommodation and presbyopia.," *Int. Ophthalmol. Clin.*, vol. 41, no. 2, pp. 33–46, 2001.
[124] W. N. Charman, "Developments in the correction of presbyopia I: Spectacle and contact lenses," *Ophthalmic Physiol. Opt.*, vol. 34, no. 1, pp. 8–29, 2014.
[125] G. Schubert, "Aktionspotentiale des M. ciliaris beim Menschen," *Albr. von Graefes Arch. für Ophthalmol. Ver. mit Arch. für Augenheilkd.*, vol. 157, no. 2, pp. 116–121, 1955.
[126] H. Bornschein and G. Schubert, "Bestandpotential und Akkommodationszustand des menschlichen Auges," *Albr. von Graefes Arch. für Ophthalmol. Ver. mit Arch. für Augenheilkd.*, vol. 159, no. 1, pp. 45–51, 1957.

[127] M. ALPERN, P. ELLEN, and R. I. GOLDSMITH, "The Electrical Response of the Human Eye in Far-to-Near Accommodation," *Arch. Ophthalmol.*, vol. 60, no. 4, pp. 592–602, Oct. 1958.

[128] J. H. Jacobson, H. H. Romaine, G. P. Halberg, and G. Stephens, "The Electric Activity of the Eye During Accommodation," *Am. J. Ophthalmol.*, vol. 46, no. 5, pp. 231–238, Nov. 1958.

[129] H. Hagiwara and S. Ishikawa, "The Action Potential of the Ciliary Muscle," *Ophthalmologica*, vol. 144, no. 5, pp. 323–340, 1962.

[130] I. H. Subjects, "World Medical Association Declaration of Helsinki: ethical principles for medical research involving human subjects.," *J. Int. Bioethique*, vol. 15, no. 1, pp. 124–129, 2004.

[131] L. Arendt-Nielsen, J. Brennum, S. Sindrup, and P. Bak, "Electrophysiological and psychophysical quantification of temporal summation in the human nociceptive system.," *Eur. J. Appl. Physiol. Occup. Physiol.*, vol. 68, no. 3, pp. 266–273, 1994.

[132] N. Asano-Kato, I. Toda, C. Sakai, Y. Hori-Komai, Y. Takano, M. Dogru, and K. Tsubota, "Pupil decentration and iris tilting detected by Orbscan: Anatomic variations among healthy subjects and influence on outcomes of laser refractive surgeries," *J. Cataract Refract. Surg.*, vol. 31, no. 10, pp. 1938–1942, Oct. 2005.

[133] U. Wildenmann and F. Schaeffel, "Variations of pupil centration and their effects on video eye tracking," *Ophthalmic Physiol. Opt.*, vol. 33, no. 6, pp. 634–641, 2013.

[134] T. Eysteinsson, F. Jonasson, H. Sasaki, A. Arnarsson, T. Sverrisson, K. Sasaki, and E. Stefánsson, "Central corneal thickness, radius of the corneal curvature and intraocular pressure in normal subjects using non-contact techniques: Reykjavik Eye Study.," *Acta Ophthalmol. Scand.*, vol. 80, no. 1, pp. 11–15, 2002.

[135] G. G. HEATH, "The influence of visual acuity on accommodative responses of the eye.," *Am. J. Optom. Arch. Am. Acad. Optom.*, vol. 33, no. 10, pp. 513–524, 1956.

[136] K. J. Ciuffreda, S. C. Hokoda, G. K. Hung, and J. L. Semmlow, "Accommodative stimulus/response function in human amblyopia.," *Doc. Ophthalmol.*, vol. 56, no. 4, pp. 303–326, 1984.

[137] M. Rosenfield, K. J. Ciuffreda, G. K. Hung, and B. Gilmartin, "Tonic accommodation: a review. I. Basic aspects.," *Ophthalmic Physiol. Opt.*, vol. 13, no. 3, pp. 266–284, 1993.

[138] H. J. Scheer, T. Sander, and L. Trahms, "The influence of amplifier, interface and biological noise on signal quality in high-resolution EEG recordings.," *Physiol. Meas.*, vol. 27, no. 2, pp. 109–117, 2006.

[139] E. Huigen, a Peper, and C. a Grimbergen, "Investigation into the origin of the noise of surface electrodes.," *Med. Biol. Eng. Comput.*, vol. 40, no. 3, pp. 332–338, 2002.

[140] T. C. Ferree, P. Luu, G. S. Russell, and D. M. Tucker, "Scalp electrode impedance, infection risk, and EEG data quality," *Clin. Neurophysiol.*, vol. 112, no. 3, pp. 536–544, 2001.

[141] M. J. Zohuriaan-Mehr and K. Kabiri, "Superabsorbent Polymer Materials: A Review," *Polym. J.*, vol. 17, no. 6, pp. 451–477, 2008.

[142] R. J. Sclabassi, "Biopotential electrodes based on hydrogel," in *Proceedings of the IEEE 31st Annual Northeast Bioengineering Conference, 2005.*, 2005, no. C, pp. 69–70.

[143] N. A. Alba, R. J. Sclabassi, M. Sun, and X. T. Cui, "Novel hydrogel-based preparation-free EEG electrode.," *IEEE Trans. Neural Syst. Rehabil. Eng.*, vol. 18, no. 4, pp. 415–23, Aug. 2010.

[144] G. H. Klem, H. O. Lüders, H. H. Jasper, and C. Elger, "Report of the committee on methods of clinical examination in electroencephalography," *Electroencephalogr. Clin. Neurophysiol.*, vol. 10, no. 2, pp. 370–375, May 1958.

[145] J. M. Bland and D. G. Altman, "Statistical methods for assessing agreement between two methods of clinical measurement.," *Lancet*, vol. 1, no. 8476, pp. 307–10, Feb. 1986.

[146] "RECOMMENDED STANDARDS FOR VISUAL EVOKED POTENTIALS," *Clin. Neurophysiol.*, vol. 3 (Suppl.), pp. 54–70, 1986.

[147] B. S. Oken, K. H. Chiappa, and E. Gill, "Normal temporal variability of the P100.," *Electroencephalogr. Clin. Neurophysiol.*, vol. 68, no. 2, pp. 153–156, 1987.

[148] W. Joost and M. Bach, "Variability of the steady-state visually evoked potential: interindividual variance and intraindividual reproducibility of spatial frequency tuning.," *Doc. Ophthalmol.*, vol. 75, no. 1, pp. 59–66, 1990.

[149] S. Tobimatsu, H. Tomoda, and M. Kato, "Normal variability of the amplitude and phase of steady-state VEPs," *Electroencephalogr. Clin. Neurophysiol. - Evoked Potentials*, vol. 100, no. 3, pp. 171–176, 1996.

[150] S. Tobimatsu, "Transient and steady-state VEPs—reappraisal," *Int. Congr. Ser.*, vol. 1232, pp. 207–211, 2002.

[151] L. Lauritzen, M. H. Jørgensen, and K. F. Michaelsen, "Test-Retest Reliability of Swept Visual Evoked Potential Measurements of Infant Visual Acuity and Contrast Sensitivity," *Pediatr. Res.*, vol. 55, no. 4, pp. 701–708, 2004.

[152] J. Sarnthein, M. Andersson, M. B. Zimmermann, and D. Zumsteg, "High test-retest reliability of checkerboard reversal visual evoked potentials (VEP) over 8 months," *Clin. Neurophysiol.*, vol. 120, no. 10, pp. 1835–1840, 2009.

[153] C. Tello, C. G. V De Moraes, T. S. Prata, P. Derr, J. Patel, J. Siegfried, J. M. Liebmann, and R. Ritch, "Repeatability of short-duration transient visual evoked potentials in normal subjects," *Doc. Ophthalmol.*, vol. 120, no. 3, pp. 219–228, 2010.

[154] E. S. Kappenman and S. J. Luck, "The effects of electrode impedance on data quality and statistical significance in ERP recordings," *Psychophysiology*, vol. 47, no. 5, pp. 888–904, 2010.

[155] A. Schatz, T. Röck, L. Naycheva, G. Willmann, B. Wilhelm, T. Peters, K. U. Bartz-Schmidt, E. Zrenner, A. Messias, and F. Gekeler, "Transcorneal electrical stimulation for patients with retinitis pigmentosa: a prospective, randomized, sham-controlled exploratory study.," *Invest. Ophthalmol. Vis. Sci.*, vol. 52, no. 7, pp. 4485–4496, 2011.

[156] W. W. Dawson, L. Trick, and C. A. Litzkow, "Improved electrode for electroretinography," *Investig. Ophthalmol. Vis. Sci.*, vol. 18, no. 9, pp. 988–991, 1979.

[157] A. E. KRILL, A. M. WIELAND, and A. M. OSTFELD, "The Effect of Two Hallucinogenic Agents on Human Retinal Function," *Arch. Ophthalmol.*, vol. 64, no. 5, pp. 724–733, Nov. 1960.

[158] S. SHARMA and H. MOSKOWITZ, "EFFECT OF MARIHUANA ON THE VISUAL AUTOKINETIC PHENOMENON," *Percept. Mot. Skills*, vol. 35, no. 3, pp. 891–894, Dec. 1972.

[159] W. W. Dawson, C. F. Jiménez-Antillon, J. M. Perez, and J. A. Zeskind, "Marijuana and vision--after ten years' use in Costa Rica.," *Invest. Ophthalmol. Vis. Sci.*, vol. 16, no. 8, pp. 689–699, 1977.

[160] L. Levi and N. R. Miller, *Visual illusions associated with previous drug abuse.*, vol. 10, no. 2. 1990, pp. 103–110.

[161] G. L. Laffi and A. B. Safran, "Persistent visual changes following hashish consumption.," *Br. J. Ophthalmol.*, vol. 77, no. 9, pp. 601–602, 1993.

[162] M. C. Gaillard and F. X. Borruat, "Persisting visual hallucinations and illusions in previously drug-addicted patients," *Klin. Monbl. Augenheilkd.*, vol. 220, no. 3, pp. 176–178, 2003.

[163] H. D. Pomeranz and S. Lessell, *Palinopsia and polyopia in the absence of drugs or cerebral disease.*, vol. 54, no. 4. 2000, pp. 855–859.

[164] M. J. Baggott, E. Erowid, F. Erowid, and L. C. Roberston, "Prevalence of chronic flashbacks in hallucinogen users: a web-based questionnaire," in *CPDD annual meeting abstract 45*, 2006.

[165] D. H. Ffytche and R. J. Howard, "The perceptual consequences of visual loss: 'Positive' pathologies of vision," *Brain*, vol. 122, no. 7, pp. 1247–1260, 1999.

[166] J. W. Norton and J. J. Corbett, "Visual perceptual abnormalities: hallucinations and illusions.," *Semin. Neurol.*, vol. 20, no. 1, pp. 111–121, 2000.

[167] A. G. Lerner, E. Shufman, A. Kodesh, G. Kretzmer, and M. Sigal, "LSD-induced hallucinogen persisting perception disorder with depressive features treated with reboxetine: Case report," *Isr. J. Psychiatry Relat. Sci.*, vol. 39, no. 2, pp. 100–103, 2002.

[168] J. H. Halpern and H. G. Pope, "Hallucinogen persisting perception disorder: What do we know after 50 years?," *Drug and Alcohol Dependence*, vol. 69, no. 2. pp. 109–119, 2003.

[169] F. Grotenhermen, "The toxicology of cannabis and cannabis prohibition," *Chemistry and Biodiversity*, vol. 4, no. 8. pp. 1744–1769, 2007.

[170] J. S. Sunness, *Persistent afterimages (palinopsia) and photophobia in a patient with a history of LSD use.*, vol. 24, no. 5. 2004, p. 805.

[171] L. J. Sim-Selley, "Regulation of cannabinoid CB1 receptors in the central nervous system by chronic cannabinoids.," *Crit. Rev. Neurobiol.*, vol. 15, no. 2, pp. 91–119, 2003.

[172] I. Svíženská, P. Dubový, and A. Šulcová, "Cannabinoid receptors 1 and 2 (CB1 and CB2), their distribution, ligands and functional involvement in nervous system structures - A short review," *Pharmacology Biochemistry and Behavior*, vol. 90, no. 4. pp. 501–511, 2008.

[173] A. Straiker, N. Stella, D. Piomelli, K. Mackie, H. J. Karten, and G. Maguire, "Cannabinoid CB1 receptors and ligands in vertebrate retina: localization and function of an endogenous signaling system.," *Proc. Natl. Acad. Sci. U. S. A.*, vol. 96, no. 25, pp. 14565–14570, 1999.

[174] A. J. Straiker, G. Maguire, K. Mackie, and J. Lindsey, "Localization of cannabinoid CB1 receptors in the human anterior eye and retina.," *Invest. Ophthalmol. Vis. Sci.*, vol. 40, no. 10, pp. 2442–2448, 1999.

[175] S.-F. Fan and S. Yazulla, "Biphasic modulation of voltage-dependent currents of retinal cones by cannabinoid CB1 receptor agonist WIN 55212-2.," *Vis. Neurosci.*, vol. 20, no. 2, pp. 177–188, 2003.

[176] A. Straiker and J. M. Sullivan, "Cannabinoid receptor activation differentially modulates ion channels in photoreceptors of the tiger salamander.," *J. Neurophysiol.*, vol. 89, no. 5, pp. 2647–2654, 2003.

[177] S.-F. Fan and S. Yazulla, "Reciprocal inhibition of voltage-gated potassium currents (I K(V)) by activation of cannabinoid CB1 and dopamine D1

receptors in ON bipolar cells of goldfish retina.," *Vis. Neurosci.*, vol. 22, no. 1, pp. 55–63, 2005.

[178] M. R. Lalonde, C. A. B. Jollimore, K. Stevens, S. Barnes, and M. E. M. Kelly, "Cannabinoid receptor-mediated inhibition of calcium signaling in rat retinal ganglion cells.," *Mol. Vis.*, vol. 12, pp. 1160–1166, 2006.

[179] Y. Wei, X. Wang, and L. Wang, "Presence and regulation of cannabinoid receptors in human retinal pigment epithelial cells.," *Mol. Vis.*, vol. 15, pp. 1243–1251, 2009.

[180] R. Barro-Soria, J. Stindl, C. Müller, R. Foeckler, V. Todorov, H. Castrop, and O. Strauß, "Angiotensin-2-Mediated Ca2+ Signaling in the Retinal Pigment Epithelium: Role of Angiotensin-Receptor- Associated-Protein and TRPV2 Channel," *PLoS One*, vol. 7, no. 11, p. e49624, Nov. 2012.

[181] D. C. Hood, M. Bach, M. Brigell, D. Keating, M. Kondo, J. S. Lyons, M. F. Marmor, D. L. McCulloch, and A. M. Palmowski-Wolfe, "ISCEV standard for clinical multifocal electroretinography (mfERG) (2011 edition)," *Doc. Ophthalmol.*, vol. 124, no. 1, pp. 1–13, 2012.

[182] L. S. EVANS, N. S. PEACHEY, and A. L. MARCHESE, "Comparison of three methods of estimating the parameters of the naka-Rushton equation," *Doc. Ophthalmol.*, vol. 84, no. 1, pp. 19–30, Mar. 1993.

[183] F. Gekeler, A. Messias, M. Ottinger, K. U. Bartz-Schmidt, and E. Zrenner, "Phosphenes electrically evoked with DTL electrodes: A study in patients with retinitis pigmentosa, glaucoma, and homonymous visual field loss and normal subjects," *Investig. Ophthalmol. Vis. Sci.*, vol. 47, no. 11, pp. 4966–4974, 2006.

[184] S. T. Leatherdale, D. Hammond, and R. Ahmed, "Alcohol, marijuana, and tobacco use patterns among youth in Canada," *Cancer Causes Control*, vol. 19, no. 4, pp. 361–369, 2008.

[185] J. M. Wallace, T. A. Forman, B. J. Guthrie, J. G. Bachman, P. M. O'Malley, and L. D. Johnston, "The epidemiology of alcohol, tobacco and other drug use among black youth.," *J. Stud. Alcohol*, vol. 60, no. 6, pp. 800–809, 1999.

[186] J. Delva, J. M. Wallace, P. M. O'Malley, J. G. Bachman, L. D. Johnston, and J. E. Schulenberg, "The epidemiology of alcohol, marijuana, and cocaine use among Mexican American, Puerto Rican, Cuban American, and other Latin American eighth-grade students in the United States: 1991-2002," *Am. J. Public Health*, vol. 95, no. 4, pp. 696–702, 2005.

[187] L. Dierker, M. Stolar, E. Lloyd-Richardson, S. Tiffany, B. Flay, L. Collins, M. Nichter, M. Nichter, S. Bailey, and R. Clayton, "Tobacco, alcohol, and marijuana use among first-year U.S. college students: a time series analysis.," *Subst. Use Misuse*, vol. 43, no. 5, pp. 680–699, 2008.

[188] L. Hermle, M. Simon, M. Ruchsow, and M. Geppert, "Hallucinogen-persisting perception disorder," *Ther. Adv. Psychopharmacol.*, vol. 2, no. 5, pp. 199–205, Oct. 2012.

[189] P. Koulen and J. H. Brandstätter, "Pre- and Postsynaptic Sites of Action of mGluR8a in the mammalian retina.," *Invest. Ophthalmol. Vis. Sci.*, vol. 43, no. 6, pp. 1933–1940, 2002.

[190] K. Wölfling, H. Flor, and S. M. Grüsser, "Psychophysiological responses to drug-associated stimuli in chronic heavy cannabis use," *Eur. J. Neurosci.*, vol. 27, no. 4, pp. 976–983, 2008.

[191] L. A. Matsuda, S. J. Lolait, M. J. Brownstein, A. C. Young, and T. I. Bonner, "Structure of a cannabinoid receptor and functional expression of the cloned cDNA.," *Nature*, vol. 346, no. 6284, pp. 561–564, 1990.

[192] S. Munro, K. L. Thomas, and M. Abu-Shaar, "Molecular characterization of a peripheral receptor for cannabinoids.," *Nature*, vol. 365, no. 6441, pp. 61–65, 1993.

[193] H. C. Hartzell, Z. Qu, K. Yu, Q. Xiao, and L.-T. Chien, "Molecular physiology of bestrophins: multifunctional membrane proteins linked to best disease and other retinopathies.," *Physiol. Rev.*, vol. 88, no. 2, pp. 639–672, 2008.

[194] T. Endoh, "Pharmacological characterization of inhibitory effects of postsynaptic opioid and cannabinoid receptors on calcium currents in neonatal rat nucleus tractus solitarius.," *Br. J. Pharmacol.*, vol. 147, no. 4, pp. 391–401, 2006.

[195] D. G. Demuth and A. Molleman, "Cannabinoid signalling," *Life Sciences*, vol. 78, no. 6. pp. 549–563, 2006.

[196] S. Wimmers, L. Coeppicus, R. Rosenthal, and O. Strauss, "Expression profile of voltage-dependent Ca2+ channel subunits in the human retinal pigment epithelium.," *Graefes Arch. Clin. Exp. Ophthalmol.*, vol. 246, no. 5, pp. 685–692, 2008.

[197] R. P. Gallemore and R. H. Steinberg, "Light-evoked modulation of basolateral membrane Cl- conductance in chick retinal pigment epithelium: the light peak and fast oscillation.," *J. Neurophysiol.*, vol. 70, no. 4, pp. 1669–1680, 1993.

[198] T. Rubino and D. Parolaro, "Long lasting consequences of cannabis exposure in adolescence," *Mol. Cell. Endocrinol.*, vol. 286, no. 1–2 SUPPL. 1, 2008.

[199] S. Hassan, K. Eldeeb, P. J. Millns, A. J. Bennett, S. P. H. Alexander, and D. A. Kendall, "Cannabidiol enhances microglial phagocytosis via transient receptor potential (TRP) channel activation," *Br. J. Pharmacol.*, vol. 171, no. 9, pp. 2426–2439, 2014.

[200] M. Bach, "The Freiburg Visual Acuity test--automatic measurement of visual acuity.," *Optometry and vision science : official publication of the American Academy of Optometry*, vol. 73, no. 1. pp. 49–53, Jan-1996.

[201] F. W. Campbell and L. Maffei, "Electrophysiological evidence for the existence of orientation and size detectors in the human visual system.," *J. Physiol.*, vol. 207, no. 3, pp. 635–52, May 1970.

[202] M. R. Harter and C. T. White, "Evoked cortical responses to checkerboard patterns: effect of check-size as a function of visual acuity.," *Electroencephalogr. Clin. Neurophysiol.*, vol. 28, no. 1, pp. 48–54, Jan. 1970.

[203] A. A. Michelson, *Studies in Optics*. Chicago: University of Chicago Press, 1927.

[204] C. Neurophysiology, A. G. Copyright, A. Clinical, and N. Society, "Guideline 5: guidelines for standard electrode position nomenclature.," *Am. J. Electroneurodiagnostic Technol.*, vol. 46, no. 3, pp. 222–225, 2006.

[205] D. S. Ruchkin, "An analysis of average response computations based upon aperiodic stimuli.," *IEEE Trans. Biomed. Eng.*, vol. 12, no. 2, pp. 87–94, 1965.

[206] S. Heine, K. Rüther, J. Isensee, and E. Zrenner, "[Clinical significance of objective vision assessment using visually evoked cortical potentials induced by rapid pattern sequences of different spatial frequency].," *Klin. Monbl. Augenheilkd.*, vol. 215, no. 3, pp. 175–81, Sep. 1999.

[207] T. Strasser, T. Peters, H. Jagle, E. Zrenner, and R. Wilke, "An integrated domain specific language for post-processing and visualizing electrophysiological signals in Java.," *Conf. Proc. IEEE Eng. Med. Biol. Soc.*, vol. 1, pp. 4687–90, Jan. 2010.

[208] W. E. Ricker, "Stock and Recruitment," *J. Fish. Res. Board Canada*, vol. 11, no. 5, pp. 559–623, May 1954.

[209] L. Persson, K. Leonardsson, a M. de Roos, M. Gyllenberg, and B. Christensen, "Ontogenetic scaling of foraging rates and the dynamics of a size-structured consumer-resource model.," *Theor. Popul. Biol.*, vol. 54, no. 3, pp. 270–293, 1998.

[210] J. H. Lambert, "Observationes variae in mathesin puram," *Acta Helv. physico-mathematico-anatomico-botanico-medica*, vol. 3, pp. 128–168, 1758.

[211] J. M. Bland and D. G. Altman, "Measuring agreement in method comparison studies.," *Stat. Methods Med. Res.*, 1999.

[212] V. Chhapola, S. K. Kanwal, and R. Brar, "Reporting standards for Bland-Altman agreement analysis in laboratory research: a cross-sectional survey of current practice," *Ann. Clin. Biochem. An Int. J. Biochem. Lab. Med.*, vol. 0, no. 0, pp. 1–5, 2014.

[213] C. W. Tyler, P. Apkarian, D. M. Levi, and K. Nakayama, “Rapid assessment of visual function: an electronic sweep technique for the pattern visual evoked potential.,” *Investigative ophthalmology & visual science*, vol. 18, no. 7. pp. 703–13, Jul-1979.

[214] C. W. Tyler, P. Apkarian, and K. Nakayama, “Multiple spatial-frequency tuning of electrical responses from human visual cortex.,” *Exp. Brain Res.*, vol. 33, no. 3–4, pp. 535–550, 1978.

[215] W. Wesemann, “Sehschärfebestimmung mit freiburger visustest, Bailey-Lovie-Tafel und Landoltring-Tafel,” *Klin. Monbl. Augenheilkd.*, vol. 219, no. 9, pp. 660–667, 2002.

[216] G. Stothart, a. Tales, C. Hedge, and N. Kazanina, “Double peaked P1 visual evoked potentials in healthy ageing,” *Clin. Neurophysiol.*, vol. 125, no. 7, pp. 1471–1478, 2014.

[217] M. A. Georgeson and G. D. Sullivan, “Contrast constancy: deblurring in human vision by spatial frequency channels.,” *J. Physiol.*, vol. 252, no. 3, pp. 627–656, Nov. 1975.

[218] F. W. Campbell and J. G. Robson, “Application of Fourier analysis to the visibility of gratings.,” *J. Physiol.*, vol. 197, no. 3, pp. 551–566, 1968.

[219] C. Enroth-Cugell and J. G. Robson, “The contrast sensitivity of retinal ganglion cells of the cat.,” *J. Physiol.*, vol. 187, no. 3, pp. 517–552, 1966.

[220] K. D. Singh, a T. Smith, and M. W. Greenlee, “Spatiotemporal frequency and direction sensitivities of human visual areas measured using fMRI.,” *Neuroimage*, vol. 12, no. 5, pp. 550–564, 2000.

[221] M. Wolf, “Objektive Visusbestimmung mit Visuell Evozierten Potentialen,” Albert-Ludwigs-Universität Freiburg im Breisgau, 2006.

[222] S. Dehaene, “The neural basis of the c law: a logarithmic mental number line.,” *Trends Cogn. Sci.*, vol. 7, no. 4, pp. 145–147, 2003.

[223] J. Mannos and D. Sakrison, “The effects of a visual fidelity criterion of the encoding of images,” *IEEE Trans. Inf. Theory*, vol. 20, no. 4, 1974.

[224] H. J. Motulsky and R. E. Brown, “Detecting outliers when fitting data with nonlinear regression - a new method based on robust nonlinear regression and the false discovery rate.,” *BMC Bioinformatics*, vol. 7, p. 123, 2006.

[225] M. a. Fischler and R. C. Bolles, “Random sample consensus: a paradigm for model fitting with applications to image analysis and automated cartography,” *Commun. ACM*, vol. 24, no. 6, pp. 381–395, 1981.

[226] S. P. Heinrich and M. Bach, “Adaptation dynamics in pattern-reversal visual evoked potentials,” *Doc. Ophthalmol.*, vol. 102, no. 2, pp. 141–156, 2001.

[227] S. M. König, “Ein Vergleich von Early Treatment Diabetic Retinopathy Study (ETDRS) - Sehzeichentafeln, einer 8-Positionen-Landoltring-

Projektion und dem Freiburg Visual Acuity Test (FrACT)," University of Tuebingen, 2015.
[228] H. Radhakrishnan, S. Pardhan, R. I. Calver, and D. J. O'Leary, "Unequal reduction in visual acuity with positive and negative defocusing lenses in myopes.," *Optom. Vis. Sci.*, vol. 81, no. 1, pp. 14–17, 2004.
[229] T. W. Raasch, "Spherocylindrical refractive errors and visual acuity.," *Optom. Vis. Sci.*, vol. 72, no. 4, pp. 272–275, 1995.
[230] V. Kumaran, P. R. Mudvari, and R. Dhital, "Changes in Visual Acuity as a Function of Defocus Induced by Positive Lenses," *Int. J. Biol. Sci. Appl.*, vol. 1, no. July, pp. 7–10, 2014.
[231] F. Thorn and F. Schwartz, "Effects of dioptric blur on Snellen and grating acuity.," *Optom. Vis. Sci.*, vol. 67, no. 1, pp. 3–7, 1990.
[232] a Mirzajani, E. Sarlaki, H. H. Kharazi, and M. Tavan, "Effect of Lens-Induced Myopia on Visual Cortex Activity: A Functional MR Imaging Study.," *AJNR. Am. J. Neuroradiol.*, vol. 32, no. 8, pp. 1426–1429, 2011.
[233] G. M. Pérez, S. M. Archer, and P. Artal, "Optical characterization of bangerter foils," *Investig. Ophthalmol. Vis. Sci.*, vol. 51, no. 1, pp. 609–13, Jan. 2010.
[234] Y. Niwa, M. Kondo, S. Ueno, M. Nakamura, H. Terasaki, and Y. Miyake, "Cone and rod dysfunction in fundus albipunctatus with RDH5 mutation: An electrophysiological study," *Investig. Ophthalmol. Vis. Sci.*, vol. 46, no. 4, pp. 1480–1485, 2005.
[235] D. DiLoreto, J. R. Ison, G. P. Bowen, C. Cox, and M. del Cerro, "A functional analysis of the age-related degeneration in the Fischer 344 rat.," *Curr. Eye Res.*, vol. 14, no. 4, pp. 303–310, 1995.
[236] A. Messias, E. Zrenner, R. Tzekov, D. McGee, T. Peters, B. Wilhelm, A. Baryluk, R. Kubota, and F. Gekeler, "Single doses of all-trans-N-retinylacetamide slow down the ERG amplitude recovery after bleaching in rats.," *Doc. Ophthalmol.*, vol. 120, no. 2, pp. 165–74, Apr. 2010.
[237] G. Karpe, "Basis of clinical electroretinography," *Acta Ophthalmol.*, vol. 24 (suppl), pp. 1–118.
[238] C. Dalke, J. Löster, H. Fuchs, V. Gailus-Durner, D. Soewarto, J. Favor, A. Neuhäuser-Klaus, W. Pretsch, F. Gekeler, K. Shinoda, E. Zrenner, T. Meitinger, M. H. De Angelis, and J. Graw, "Electroretinography as a Screening Method for Mutations Causing Retinal Dysfunction in Mice," *Investig. Ophthalmol. Vis. Sci.*, vol. 45, no. 2, pp. 601–609, 2004.
[239] R. C. Siqueira, A. Messias, J. C. Voltarelli, I. U. Scott, and R. Jorge, "INTRAVITREAL INJECTION OF AUTOLOGOUS BONE MARROW–DERIVED MONONUCLEAR CELLS FOR HEREDITARY RETINAL DYSTROPHY," *Retina*, vol. 31, no. 6. pp. 1207–1214, 2011.

[240] M. Kondo, S. Ueno, C. H. Piao, Y. Miyake, and H. Terasaki, "Comparison of focal macular cone ERGs in complete-type congenital stationary night blindness and APB-treated monkeys," *Vision Res.*, vol. 48, no. 2, pp. 273–280, 2008.

[241] S. Viswanathan, L. J. Frishman, J. G. Robson, R. S. Harwerth, and E. L. Smith, "The photopic negative response of the macaque electroretinogram: Reduction by experimental glaucoma," *Investig. Ophthalmol. Vis. Sci.*, vol. 40, no. 6, pp. 1124–1136, 1999.

[242] N. V. Rangaswamy, L. J. Frishman, E. U. Dorotheo, J. S. Schiffman, H. M. Bahrani, and R. A. Tang, "Photopic ERGs in patients with optic neuropathies: Comparison with primate ERGs after pharmacologic blockade of inner retina," *Investig. Ophthalmol. Vis. Sci.*, vol. 45, no. 10, pp. 3827–3837, 2004.

[243] M. F. Marmor, G. B. Arden, S.-E. Nilsson, and E. Zrenner, "Standard for clinical electroretinography," *Doc. Ophthalmol.*, vol. 73, no. 4, pp. 303–311, Dec. 1989.

[244] M. F. Marmor, A. B. Fulton, G. E. Holder, Y. Miyake, M. Brigell, and M. Bach, "ISCEV Standard for full-field clinical electroretinography (2008 update)," in *Documenta Ophthalmologica*, 2009, vol. 118, no. 1, pp. 69–77.

[245] J. R. Heckenlively and G. B. Arden, Eds., *Principles and Practice of Clinical Electrophysiology of Vision*, 2nd ed. Cambridge: MIT Press, 2006.

[246] L. J. Frishman, "The scotopic threshold response," in *Principles and practice of clinical electrophysiology of vision*, J. R. Heckenlively and G. B. Arden, Eds. St. Louis: Mosby Year Book, 1991, pp. 121–124.

[247] L. J. Frishman and R. H. Steinberg, "Origin of negative potentials in the light-adapted ERG of cat retina.," *J. Neurophysiol.*, vol. 63, no. 6, pp. 1333–1346, 1990.

[248] M. Quigley, M. S. Roy, M. Barsoum-Homsy, L. Chevrette, J. L. Jacob, and J. Milot, "On- and off-responses in the photopic electroretinogram in complete-type congenital stationary night blindness," *Doc. Ophthalmol.*, vol. 92, no. 3, pp. 159–165, 1996.

[249] P. a Sieving, "Photopic ON- and OFF-pathway abnormalities in retinal dystrophies.," *Trans. Am. Ophthalmol. Soc.*, vol. 91, pp. 701–73, Jan. 1993.

[250] E. Zrenner and P. Gouras, "Blue-sensitive cones of the cat produce a rodlike electroretinogram," *Investig. Ophthalmol. Vis. Sci.*, vol. 18, no. 10, pp. 1076–1081, 1979.

[251] K. I. Naka and W. A. Rushton, "S-potential and dark adaptation in fish.," *J. Physiol.*, vol. 194, no. 1, pp. 259–269, 1968.

[252] E. L. Berson, B. Rosner, M. A. Sandberg, C. Weigel-DiFranco, R. J. Brockhurst, K. C. Hayes, E. J. Johnson, E. J. Anderson, C. A. Johnson, A. R.

Gaudio, W. C. Willett, and E. J. Schaefer, “Clinical trial of lutein in patients with retinitis pigmentosa receiving vitamin A.,” 2010.

[253] S. O. Andréasson, M. A. Sandberg, and E. L. Berson, “Narrow-band filtering for monitoring low-amplitude cone electroretinograms in retinitis pigmentosa.,” *Am. J. Ophthalmol.*, vol. 105, no. 5, pp. 500–503, 1988.

[254] H. E. Henkes, “Recent advances in flicker-electroretinography,” *Doc. Ophthalmol.*, vol. 18, no. 1, pp. 307–314, 1964.

[255] D. G. Birch and M. A. Sandberg, “Submicrovolt full-field cone electroretinograms: artifacts and reproducibility,” *Doc. Ophthalmol.*, vol. 92, no. 4, pp. 269–280, Dec. 1996.

[256] E. L. Berson, M. A. Sandberg, B. Rosner, D. G. Birch, and A. H. Hanson, “Natural course of retinitis pigmentosa over a three-year interval.,” *Am. J. Ophthalmol.*, vol. 99, no. 3, pp. 240–251, 1985.

[257] M. Bach and T. Meigen, “Do’s and don'ts in Fourier analysis of steady-state potentials,” *Doc. Ophthalmol.*, vol. 99, no. 1, pp. 69–82, 1999.

[258] T. Meigen and M. Bach, “On the statistical significance of electrophysiological steady-state responses,” *Doc. Ophthalmol.*, vol. 98, pp. 207–232, 2000.

[259] P. a Sieving, E. B. Arnold, J. Jamison, A. Liepa, and C. Coats, “Submicrovolt flicker electroretinogram: cycle-by-cycle recording of multiple harmonics with statistical estimation of measurement uncertainty.,” *Invest. Ophthalmol. Vis. Sci.*, vol. 39, no. 8, pp. 1462–9, Jul. 1998.

[260] W. W. Dawson, G. L. Trick, and C. A. Litzkow, “Improved electrode for electroretinography.,” *Invest. Ophthalmol. Vis. Sci.*, vol. 18, no. 9, pp. 988–91, Sep. 1979.

[261] E. DODT, “Cone Electroretinography by Flicker,” *Nature*, vol. 168, no. 4278, pp. 738–738, Oct. 1951.

[262] D. Regan, “Some characteristics of average steady-state and transient responses evoked by modulated light.,” *Electroencephalogr. Clin. Neurophysiol.*, vol. 20, no. 3, pp. 238–248, 1966.

[263] H. Davson, *Physiology of the Eye*, 5th ed. Basingstoke: Palgrave Macmillan, 1990.

[264] M. F. Marmor, A. B. Fulton, G. E. Holder, Y. Miyake, M. Brigell, and M. Bach, “ISCEV Standard for full-field clinical electroretinography (2008 update).,” *Doc. Ophthalmol.*, vol. 118, no. 1, pp. 69–77, Feb. 2009.

[265] H. P. Scholl, H. Langrová, B. H. Weber, E. Zrenner, and E. Apfelstedt-Sylla, “Clinical electrophysiology of two rod pathways: normative values and clinical application.,” *Graefes Arch. Clin. Exp. Ophthalmol.*, vol. 239, no. 2, pp. 71–80, 2001.

[266] S.-H. Lim and Y.-H. Ohn, "Study of blue and red flash in dark-adapted electroretinogram.," *Korean J. Ophthalmol.*, vol. 19, no. 2, pp. 106–111, 2005.
[267] R. G. Weleber, "The effect of age on the human rod and cone Ganzfeld electroretinograms," *Invest Ophthalmol Vis Sci*, vol. 20, pp. 392–399, 1981.
[268] A. A. Gawande, W. J. Donovan, A. P. Ginsburg, and M. F. Marmor, "Photoaversion in retinitis pigmentosa.," *Br. J. Ophthalmol.*, vol. 73, no. 2, pp. 115–120, 1989.
[269] A. Stockman, L. T. Sharpe, K. Rüther, and K. Nordby, "Two signals in the human rod visual system: A model based on electrophysiological data," *Vis. Neurosci.*, vol. 12, no. 05, p. 951, Sep. 1995.
[270] D. Cao, J. Pokorny, and M. a. Grassi, "Isolated mesopic rod and cone electroretinograms realized with a four-primary method," *Doc. Ophthalmol.*, vol. 123, no. 1, pp. 29–41, 2011.
[271] H. BORNSCHEIN, G. GOODMAN, and R. D. GUNKEL, "Temporal aspects of the human electroretinogram; a study of the implicit time-amplitude relationship of the B-wave.," *AMA. Arch. Ophthalmol.*, vol. 57, no. 3, pp. 386–392, 1957.
[272] E. L. Berson, P. Gouras, and M. Hoff, "Temporal aspects of the electroretinogram.," *Arch. Ophthalmol.*, vol. 81, no. 2, pp. 207–214, 1969.
[273] a M. Cameron, O. a R. Mahroo, and T. D. Lamb, "Dark adaptation of human rod bipolar cells measured from the b-wave of the scotopic electroretinogram.," *J. Physiol.*, vol. 575, no. Pt 2, pp. 507–526, 2006.
[274] D. Regan, "Some early uses of evoked brain responses in investigations of human visual function," *Vision Res.*, vol. 49, no. 9, pp. 882–897, 2009.
[275] S. Sokol, "Visually evoked potentials: Theory, techniques and clinical applications," *Surv. Ophthalmol.*, vol. 21, no. 1, pp. 18–44, Jul. 1976.
[276] P. Walsh, N. Kane, and S. Butler, "The clinical role of evoked potentials.," *J. Neurol. Neurosurg. Psychiatry*, vol. 76 Suppl 2, pp. ii16–i22, 2005.
[277] R. Kothari, P. Bokariya, S. Singh, and R. Singh, "Significance of Visual Evoked Potentials in the Assessment of Visual Field Defects in Primary Open-Angle Glaucoma: A Review," *Neurosci. J.*, vol. 2013, pp. 1–6, 2013.
[278] M. J. Aminoff and a L. Ochs, "Pattern-onset visual evoked potentials in suspected multiple sclerosis.," *J. Neurol. Neurosurg. Psychiatry*, vol. 44, no. 7, pp. 608–614, 1981.
[279] G. a Fishman, D. G. Birch, G. E. Holder, and M. G. Brigell, *Electrophysiologic testing in disorders of the retina, optic nerve, and visual pathway*, 2nd ed. San Francisco: Oxford University Press, 2001.
[280] M. J. Taylor and D. L. McCulloch, "Visual evoked potentials in infants and children.," *J. Clin. Neurophysiol.*, vol. 9, no. 3, pp. 357–372, 1992.

[281] G. E. Holder, R. P. Gale, J. F. Acheson, and A. G. Robson, "Electrodiagnostic assessment in optic nerve disease.," *Curr. Opin. Neurol.*, vol. 22, no. 1, pp. 3–10, Feb. 2009.

[282] G. F. a Harding, J. V. Odom, W. Spileers, and H. Spekreijse, "Standard for visual evoked potentials 1995," *Vision Res.*, vol. 36, no. 21, pp. 3567–3572, 1996.

[283] G. Krüger, a Kleinschmidt, and J. Frahm, "Dynamic MRI sensitized to cerebral blood oxygenation and flow during sustained activation of human visual cortex.," *Magn. Reson. Med.*, vol. 35, no. 6, pp. 797–800, 1996.

[284] S. a Engel, D. E. Rumelhart, B. a Wandell, A. T. Lee, G. H. Glover, E.-J. Chichilnisky, and M. N. Shadlen, "fMRI of human visual cortex," *Nature*, vol. 369, no. 6481, pp. 525–525, Jun. 1994.

[285] B. a. Wandell and J. Winawer, "Imaging retinotopic maps in the human brain," *Vision Res.*, vol. 51, no. 7, pp. 718–737, 2011.

[286] B. a Wandell, S. O. Dumoulin, and A. a Brewer, "Visual field maps in human cortex.," *Neuron*, vol. 56, no. 2, pp. 366–383, 2007.

[287] S. S. Kollias, "Investigations of the human visual system using functional magnetic resonance imaging (FMRI)," *Eur. J. Radiol.*, vol. 49, no. 1, pp. 64–75, 2004.

[288] A. Miki, J. C. Haselgrove, and G. T. Liu, "Functional magnetic resonance imaging and its clinical utility in patients with visual disturbances," *Surv. Ophthalmol.*, vol. 47, no. 6, pp. 562–579, 2002.

[289] T. Kato, a Kamei, S. Takashima, and T. Ozaki, "Human visual cortical function during photic stimulation monitoring by means of near-infrared spectroscopy.," *J. Cereb. Blood Flow Metab.*, vol. 13, no. 3, pp. 516–520, 1993.

[290] A. Miki, T. Nakajima, M. Takagi, T. Usui, H. Abe, C. S. J. Liu, and G. T. Liu, "Near-infrared spectroscopy of the visual cortex in unilateral optic neuritis," *Am. J. Ophthalmol.*, vol. 139, no. 2, pp. 353–356, 2005.

[291] M. a. Mcintosh, U. Shahani, R. G. Boulton, and D. L. McCulloch, "Absolute quantification of oxygenated hemoglobin within the visual cortex with functional near infrared spectroscopy (fNIRS)," *Investig. Ophthalmol. Vis. Sci.*, vol. 51, no. 9, pp. 4856–4860, 2010.

[292] S. Wijeakumar, U. Shahani, W. a Simpson, and D. L. McCulloch, "Localization of hemodynamic responses to simple visual stimulation: an fNIRS study.," *Invest. Ophthalmol. Vis. Sci.*, vol. 53, no. 4, pp. 2266–73, Apr. 2012.

[293] N. K. Logothetis, J. Pauls, M. Augath, T. Trinath, and a Oeltermann, "Neurophysiological investigation of the basis of the fMRI signal.," *Nature*, vol. 412, no. 6843, pp. 150–157, 2001.

[294] G. E. Legge, "Sustained and transient mechanisms in human vision: temporal and spatial properties.," *Vision Res.*, vol. 18, no. 1, pp. 69–81, 1978.
[295] C. F. Stromeyer and S. Klein, "Spatial frequency channels in human vision as asymmetric (edge) mechanisms," *Vision Res.*, vol. 14, no. 12, pp. 1409–1420, 1974.
[296] D. a. Pollen and S. F. Ronner, "Visual cortical neurons as localized spatial frequency filters," *IEEE Trans. Syst. Man. Cybern.*, vol. SMC-13, no. 5, pp. 907–916, 1983.
[297] D. E. Wiener, K. Wellish, J. I. Nelson, and M. J. Kupersmith, "Comparisons among Snellen, psychophysical, and evoked potential visual acuity determinations.," *Am. J. Optom. Physiol. Opt.*, vol. 62, no. 10, pp. 669–679, 1985.
[298] V. L. Towle and M. R. Harter, "Objective determination of human visual acuity from the visual evoked potential.," *Percept. Psychophys.*, vol. 25, no. 6, pp. 497–500, 1979.
[299] S. Sokol, "Measurement of infant visual acuity from pattern reversal evoked potentials," *Vision Res.*, vol. 18, no. 1, pp. 33–39, 1978.
[300] V. a. McBain, A. G. Robson, C. R. Hogg, and G. E. Holder, "Assessment of patients with suspected non-organic visual loss using pattern appearance visual evoked potentials," *Graefe's Arch. Clin. Exp. Ophthalmol.*, vol. 245, no. 4, pp. 502–510, 2007.
[301] F. Almoqbel, S. J. Leat, and E. Irving, "The technique, validity and clinical use of the sweep VEP.," *Ophthalmic Physiol. Opt.*, vol. 28, no. 5, pp. 393–403, Sep. 2008.
[302] J. J. Chen and G. B. Pike, "BOLD-specific cerebral blood volume and blood flow changes during neuronal activation in humans," *NMR Biomed.*, vol. 22, no. 10, pp. 1054–1062, 2009.
[303] S. a. Huettel, M. J. McKeown, A. W. Song, S. Hart, D. D. Spencer, T. Allison, and G. McCarthy, "Linking Hemodynamic and Electrophysiological Measures of Brain Activity: Evidence from Functional MRI and Intracranial Field Potentials," *Cereb. Cortex*, vol. 14, no. 2, pp. 165–173, 2004.
[304] H. Shibasaki, "Human brain mapping: Hemodynamic response and electrophysiology," *Clin. Neurophysiol.*, vol. 119, no. 4, pp. 731–743, 2008.
[305] O. J. Arthurs, E. J. Williams, T. a Carpenter, J. D. Pickard, and S. J. Boniface, "Linear coupling between functional magnetic resonance imaging and evoked potential amplitude in human somatosensory cortex," *Neuroscience*, vol. 101, no. 4, pp. 803–806, 2000.

[306] M. Bianciardi, F. Di Russo, T. Aprile, B. Maraviglia, and G. E. Hagberg, "Combination of BOLD-fMRI and VEP recordings for spin-echo MRI detection of primary magnetic effects caused by neuronal currents.," *Magn. Reson. Imaging*, vol. 22, no. 10, pp. 1429–40, Dec. 2004.

[307] S. Henning, K.-D. Merboldt, and J. Frahm, "Simultaneous recordings of visual evoked potentials and BOLD MRI activations in response to visual motion processing.," *NMR Biomed.*, vol. 18, no. 8, pp. 543–52, Dec. 2005.

[308] L. Rovati, G. Salvatori, L. Bulf, and S. Fonda, "Optical and electrical recording of neural activity evoked by graded contrast visual stimulus.," *Biomed. Eng. Online*, vol. 6, p. 28, Jan. 2007.

[309] M. Zaletel, M. Strucl, Z. Rodi, and B. Zvan, "The relationship between visually evoked cerebral blood flow velocity responses and visual-evoked potentials.," *Neuroimage*, vol. 22, no. 4, pp. 1784–9, Aug. 2004.

[310] H. Obrig, H. Israel, M. Kohl-Bareis, K. Uludag, R. Wenzel, B. Müller, G. Arnold, and A. Villringer, "Habituation of the Visually Evoked Potential and Its Vascular Response: Implications for Neurovascular Coupling in the Healthy Adult," *Neuroimage*, vol. 17, no. 1, pp. 1–18, Sep. 2002.

[311] L. E. Leguire, a. Algaze, N. H. Kashou, J. Lewis, G. L. Rogers, and C. Roberts, "Relationship among fMRI, contrast sensitivity and visual acuity," *Brain Res.*, vol. 1367, pp. 162–169, 2011.

[312] F. F. Jöbsis-vanderVliet, "Discovery of the Near-Infrared Window into the Body and the Early Development of Near-Infrared Spectroscopy," *J. Biomed. Opt.*, vol. 4, no. 4, p. 392, 1999.

[313] F. F. Jöbsis, "Noninvasive, infrared monitoring of cerebral and myocardial oxygen sufficiency and circulatory parameters.," *Science*, vol. 198, no. 4323, pp. 1264–1267, 1977.

[314] A. Villringer and B. Chance, "Non-invasive optical spectroscopy and imaging of human brain function," *Trends Neurosci.*, vol. 20, no. 10, pp. 435–442, Oct. 1997.

[315] L. H. Ernst, M. M. Plichta, E. Lutz, A. K. Zesewitz, S. V. Tupak, T. Dresler, A. C. Ehlis, and A. J. Fallgatter, "Prefrontal activation patterns of automatic and regulated approach-avoidance reactions - A functional near-infrared spectroscopy (fNIRS) study," *Cortex*, vol. 49, no. 1, pp. 131–142, 2013.

[316] G. Gratton, M. Fabiani, T. Elbert, and B. Rockstroh, "Seeing right through you: applications of optical imaging to the study of the human brain," *Psychophysiology*, vol. 40, no. 0048–5772, pp. 487–491, 2003.

[317] G. Gratton and M. Fabiani, "Dynamic brain imaging: Event-related optical signal (EROS) measures of the time course and localization of cognitive-related activity," *Psychon. Bull. Rev.*, vol. 5, no. 4, pp. 535–563, 1998.

[318] S. Lloyd-Fox, a. Blasi, and C. E. Elwell, "Illuminating the developing brain: The past, present and future of functional near infrared spectroscopy," *Neurosci. Biobehav. Rev.*, vol. 34, no. 3, pp. 269–284, 2010.

[319] L. Kocsis, P. Herman, and a Eke, "The modified Beer-Lambert law revisited.," *Phys. Med. Biol.*, vol. 51, no. 5, pp. N91–N98, 2006.

[320] F. Scholkmann, S. Kleiser, A. J. Metz, R. Zimmermann, J. Mata Pavia, U. Wolf, and M. Wolf, "A review on continuous wave functional near-infrared spectroscopy and imaging instrumentation and methodology.," *Neuroimage*, vol. 85 Pt 1, pp. 6–27, Jan. 2014.

[321] a Duncan, J. H. Meek, M. Clemence, C. E. Elwell, L. Tyszczuk, M. Cope, and D. T. Delpy, "Optical pathlength measurements on adult head, calf and forearm and the head of the newborn infant using phase resolved optical spectroscopy.," *Phys. Med. Biol.*, vol. 40, no. 2, pp. 295–304, 1995.

[322] A. Duncan, J. H. Meek, M. Clemence, C. E. Elwell, P. Fallon, L. Tyszczuk, M. Cope, and D. T. Delpy, "Measurement of Cranial Optical Path Length as a Function of Age Using Phase Resolved Near Infrared Spectroscopy," *Pediatr. Res.*, vol. 39, no. 5, pp. 889–894, May 1996.

[323] M. Ferrari and V. Quaresima, "A brief review on the history of human functional near-infrared spectroscopy (fNIRS) development and fields of application.," *Neuroimage*, vol. 63, no. 2, pp. 921–35, Nov. 2012.

[324] G. Strangman, D. a. Boas, and J. P. Sutton, "Non-invasive neuroimaging using near-infrared light," *Biol. Psychiatry*, vol. 52, no. 7, pp. 679–693, 2002.

[325] M. Wolf, G. Morren, D. Haensse, T. Karen, U. Wolf, J. C. Fauchère, and H. U. Bucher, "Near infrared spectroscopy to study the brain: an overview," *Opto-Electronics Rev.*, vol. 16, no. 4, pp. 413–419, 2008.

[326] M. Wolf, M. Ferrari, and V. Quaresima, "Progress of near-infrared spectroscopy and topography for brain and muscle clinical applications.," *J. Biomed. Opt.*, vol. 12, no. 6, p. 062104, 2007.

[327] S. R. Arridge, M. Cope, and D. T. Delpy, "The theoretical basis for the determination of optical pathlengths in tissue: temporal and frequency analysis.," *Phys. Med. Biol.*, vol. 37, no. 7, pp. 1531–1560, 1992.

[328] D. T. Delpy, M. Cope, P. van der Zee, S. Arridge, S. Wray, and J. Wyatt, "Estimation of optical pathlength through tissue from direct time of flight measurement.," *Phys. Med. Biol.*, vol. 33, no. 12, pp. 1433–1442, 1988.

[329] M. Hiraoka, M. Firbank, M. Essenpreis, M. Cope, S. R. Arridge, P. van der Zee, and D. T. Delpy, "A Monte Carlo investigation of optical pathlength in inhomogeneous tissue and its application to near-infrared spectroscopy.," *Phys. Med. Biol.*, vol. 38, no. 12, pp. 1859–1876, 1993.

[330] R. B. Buxton, K. Uludağ, D. J. Dubowitz, and T. T. Liu, "Modeling the hemodynamic response to brain activation," *Neuroimage*, vol. 23, no. SUPPL. 1, pp. 220–233, 2004.

[331] P. a Bandettini, E. C. Wong, R. S. Hinks, R. S. Tikofsky, and J. S. Hyde, "Time course EPI of human brain function during task activation.," *Magn. Reson. Med.*, vol. 25, no. 2, pp. 390–397, 1992.

[332] T. J. Grabowski and A. R. Damasio, "Investigating Language with Functional Neuroimaging," in *Brain Mapping: The Systems*, Elsevier, 2000, pp. 425–461.

[333] G. K. Aguirre and M. D'Esposito, "Experimental design for brain fMRI," in *Functional MRI*, C. T. W. Moonen and P. a Bandettini, Eds. Berlin, Heidelberg, New York: Springer, 2000, pp. 369–380.

[334] D. I. Donaldson and R. L. Buckner, "Effective paradigm design," in *Functional Magnetic Resonance Imaging*, P. Jezzard, P. M. Matthews, and S. M. Smith, Eds. Oxford: Oxford University Press, 2001, pp. 178–197.

[335] K. J. Friston, E. Zarahn, O. Josephs, R. N. Henson, and a M. Dale, "Stochastic designs in event-related fMRI.," *Neuroimage*, vol. 10, no. 5, pp. 607–619, 1999.

[336] M. W. L. Chee, V. Venkatraman, C. Westphal, and S. C. Siong, "Comparison of block and event-related fMRI designs in evaluating the word-frequency effect," *Hum. Brain Mapp.*, vol. 18, no. 3, pp. 186–193, 2003.

[337] M. A. Cloud, "RELIABLE FRONTAL CORTEX ACTIVITY FOR AN ORAL STROOP TASK USING FUNCTIONAL NEAR-INFRARED SPECTROSCOPY," University of Texas at Arlington, 2013.

[338] K. E. Jang, S. Tak, J. Jung, J. Jang, Y. Jeong, and J. C. Ye, "Wavelet minimum description length detrending for near-infrared spectroscopy," *J. Biomed. Opt.*, vol. 14, no. 3, p. 034004, 2009.

[339] K. J. Worsley and K. J. Friston, "Analysis of fMRI Time-Series Revisited—Again," *Neuroimage*, vol. 2, no. 3, pp. 173–181, Sep. 1995.

[340] J. C. Ye, S. Tak, K. E. Jang, J. Jung, and J. Jang, "NIRS-SPM: Statistical parametric mapping for near-infrared spectroscopy," *Neuroimage*, vol. 44, no. 2, pp. 428–447, 2009.

[341] A. J. a Nelder and R. W. M. Wedderburn, "Generalized Linear Models," vol. 135, no. 3, pp. 370–384, 2011.

[342] M. M. Plichta, S. Heinzel, A.-C. Ehlis, P. Pauli, and A. J. Fallgatter, "Model-based analysis of rapid event-related functional near-infrared spectroscopy (NIRS) data: a parametric validation study.," *Neuroimage*, vol. 35, no. 2, pp. 625–34, Apr. 2007.

[343] S. Tak and J. C. Ye, "Statistical analysis of fNIRS data: a comprehensive review.," *Neuroimage*, vol. 85 Pt 1, pp. 72–91, Jan. 2014.

[344] J. Warnking, M. Dojat, a Guérin-Dugué, C. Delon-Martin, S. Olympieff, N. Richard, a Chéhikian, and C. Segebarth, "fMRI retinotopic mapping--step by step.," *Neuroimage*, vol. 17, no. 4, pp. 1665–1683, 2002.

[345] J. Talairach and P. Tournoux, *Co-Planar Stereotaxic Atlas of the Human Brain*, 1st ed. Stuttgart: Thieme, 1988.

[346] M. Brett, J.-L. Anton, R. Valabregue, and J.-B. Poline, "Region of interest analysis using an SPM toolbox," in *8th International Conference on Functional Mapping of the Human Brain*, 2002.

[347] B. Chance, J. S. Leigh, H. Miyake, D. S. Smith, S. Nioka, R. Greenfeld, M. Finander, K. Kaufmann, W. Levy, and M. Young, "Comparison of time-resolved and -unresolved measurements of deoxyhemoglobin in brain.," *Proc. Natl. Acad. Sci. U. S. A.*, vol. 85, no. 14, pp. 4971–4975, 1988.

[348] "Digital Imaging and Communications in Medicine (DICOM) - Part 3: Information Object Definitions," Rosslyn, Virginia, USA, 2011.

[349] J. Malmivuo and R. Plonsey, *Bioelectromagnetism: Principles and Applications of Bioelectric and Biomagnetic Fields*, 1st ed. New York: Oxford University Press, Inc., 1995.

APPENDIX

1 ElVisML example

```
1  <?xml version="1.0" encoding="UTF-8"?>
2  <elvis:elvistrophysiology xsi:schemaLocation="ElVisML-0.5.xsd"
   xmlns:elvis="http://www.biomed-engineering.de/elvistrophysiology"
   xmlns:xsi="http://www.w3.org/2001/XMLSchema-instance">
3   <elvis:subjects>
4    <elvis:subject id="S-988443814" normal="false">
5     <elvis:firstname>Torsten</elvis:firstname>
6     <elvis:lastname>Anonymous</elvis:lastname>
7     <elvis:birthdate>1901-01-01+01:00</elvis:birthdate>
8     <elvis:gender>male</elvis:gender>
9     <elvis:extendedAttributes>
10     <elvis:attribute key="acuityOD">1.0</elvis:attribute>
11     <elvis:attribute key="acuityOS">1.0</elvis:attribute>
12     <elvis:attribute key="uniqueId">4CA58413-5F14-492C-8CB2-3665-9782</elvis:attribute>
13     <elvis:attribute key="lastUpdated">1286433736137</elvis:attribute>
14     <elvis:attribute key="creationDate">1161934822000</elvis:attribute>
15     <elvis:attribute key="SUBJECT_NO">132</elvis:attribute>
16    </elvis:extendedAttributes>
17   </elvis:subject>
18  </elvis:subjects>
19  <elvis:protocols>
20   <elvis:protocol id="P533075359">
21    <elvis:name>(A) Extended ISCEV 2010-01-13</elvis:name>
22    <elvis:type>ERG</elvis:type>
23    <elvis:description>(A) Extended ISCEV 2010-01-13</elvis:description>
24    <elvis:stimulusDevice>ColorDome</elvis:stimulusDevice>
25    <elvis:stepDefinitions>
26     <elvis:stepDefinition id="STD1767977284">
27      <elvis:name>(D) -3</elvis:name>
28      <elvis:adaptationTime unit="s">0.0</elvis:adaptationTime>
29      <elvis:preTriggerTime unit="micros">20000.0</elvis:preTriggerTime>
30      <elvis:postTriggerTime unit="micros">250000.0</elvis:postTriggerTime>
31      <elvis:samplingFrequency unit="Hz">1000.0</elvis:samplingFrequency>
32      <elvis:numberOfResults>1</elvis:numberOfResults>
33      <elvis:interResultDelay unit="s">0.0</elvis:interResultDelay>
34      <elvis:numberOfSweepsPerResult>5</elvis:numberOfSweepsPerResult>
35      <elvis:stimulus>
36       <elvis:erg>
37        <elvis:flash>
38         <elvis:flashDuration unit="ms">4.0</elvis:flashDuration>
```

```
39      <elvis:flashIntensity unit="cd*s*m^-2" type="photopic">0.0010</elvis:flashIntensity>
40      <elvis:flashColor>White-6500K</elvis:flashColor>
41      <elvis:fixation>true</elvis:fixation>
42      <elvis:backgroundLuminance unit="cd*m^-2"
    type="photopic">0.0</elvis:backgroundLuminance>
43      <elvis:backgroundColor>White-6500K</elvis:backgroundColor>
44      <elvis:extendedAttributes/>
45     </elvis:flash>
46    </elvis:erg>
47   </elvis:stimulus>
48   <elvis:channelDefinitions>
49    <elvis:channelDefinition id="CD-1058093463">
50     <elvis:name>Chan 1</elvis:name>
51     <elvis:eye>OS</elvis:eye>
52     <elvis:elvistrodeType>DTL</elvis:elvistrodeType>
53    </elvis:channelDefinition>
54   </elvis:channelDefinitions>
55   <elvis:cursorDefinitions>
56    <elvis:cursorDefinition id="LD2091977532">
57     <elvis:title>a</elvis:title>
58     <elvis:placement>
59      <elvis:start unit="ms">0.0</elvis:start>
60      <elvis:range unit="ms">75.0</elvis:range>
61      <elvis:type>trough</elvis:type>
62     </elvis:placement>
63     <elvis:channelDefinitions>
64      <elvis:channelDefinition>CD-1058093463</elvis:channelDefinition>
65     </elvis:channelDefinitions>
66    </elvis:cursorDefinition>
67    <elvis:cursorDefinition id="LD-590236315">
68     <elvis:title>B</elvis:title>
69     <elvis:placement>
70      <elvis:start unit="ms">80.0</elvis:start>
71      <elvis:range unit="ms">50.0</elvis:range>
72      <elvis:type>peak</elvis:type>
73     </elvis:placement>
74     <elvis:relativeTo time="false" amplitude="true">LD2091977532</elvis:relativeTo>
75     <elvis:channelDefinitions>
76      <elvis:channelDefinition>CD-1058093463</elvis:channelDefinition>
77     </elvis:channelDefinitions>
78    </elvis:cursorDefinition>
79   </elvis:cursorDefinitions>
```

```
  </elvis:stepDefinition>
 </elvis:stepDefinitions>
</elvis:protocol>
</elvis:protocols>
<elvis:tests>
 <elvis:test subject="S-988443814" protocol="P533075359">
  <elvis:date>2010-04-01T16:27:07.140+02:00</elvis:date>
  <elvis:comment>Pupils not dilated</elvis:comment>
  <elvis:pupilSize>
   <elvis:OD unit="mm">8.0</elvis:OD>
   <elvis:OS unit="mm">8.0</elvis:OS>
  </elvis:pupilSize>
  <elvis:device>
   <elvis:name>Espion</elvis:name>
   <elvis:version>5.0.28</elvis:version>
   <elvis:manufacturer>Diagnosys LLC</elvis:manufacturer>
  </elvis:device>
  <elvis:steps>
   <elvis:step stepDefinition="STD1767977284">
    <elvis:channels>
     <elvis:channel channelDefinition="CD-1058093463" enabled="true">
      <elvis:results>
       <elvis:result id="R-935392963">
        <elvis:data unit="nV">1062.0 520.0 -203.0 -13.0 -206.0 194.0 597.0 -39.0 811.0
 2772.0 1699.0 -810.0  ...</elvis:Values>
        <elvis:sampleTime unit="ms">0.9999999999999998</elvis:sampleTime>
        <elvis:cursors>
         <elvis:cursor id="L-1074885207" cursorDefinition="LD2091977532">
          <elvis:time unit="ms">58.999999999999986</elvis:time>
          <elvis:amplitude unit="nV">8650.0</elvis:amplitude>
          <elvis:extendedAttributes>
           <elvis:attribute key="index">79</elvis:attribute>
           <elvis:attribute key="preTriggerIndex">20</elvis:attribute>
           <elvis:attribute key="visible">true</elvis:attribute>
          </elvis:extendedAttributes>
         </elvis:cursor>
         <elvis:cursor id="L-1668424839" cursorDefinition="LD-590236315">
          <elvis:time unit="ms">107.99999999999997</elvis:time>
          <elvis:amplitude unit="nV">48744.99999999999</elvis:amplitude>
          <elvis:extendedAttributes>
           <elvis:attribute key="index">128</elvis:attribute>
           <elvis:attribute key="preTriggerIndex">20</elvis:attribute>
           <elvis:attribute key="visible">true</elvis:attribute>
```

```
122            </elvis:extendedAttributes>
123           </elvis:cursor>
124          </elvis:cursors>
125          <elvis:extendedAttributes>
126           <elvis:attribute key="description"/>
127           <elvis:attribute key="runtime">1270130818750</elvis:attribute>
128           <elvis:attribute key="enabled">true</elvis:attribute>
129          </elvis:extendedAttributes>
130         </elvis:result>
131        </elvis:results>
132       </elvis:channel>
133      </elvis:channels>
134      <elvis:extendedAttributes>
135       <elvis:attribute key="runtime">1270131287656</elvis:attribute>
136      </elvis:extendedAttributes>
137     </elvis:step>
138    </elvis:steps>
139    <elvis:extendedAttributes>
140     <elvis:attribute key="examiner">Strasser</elvis:attribute>
141     <elvis:attribute key="lastUpdated">1270124995765</elvis:attribute>
142    </elvis:extendedAttributes>
143   </elvis:test>
144  </elvis:tests>
145 </elvis:elvistrophysiology>
```

2 Fortüne-Study worksheets

2.1 Worksheet “Ophthalmic exam”

General information

*f*ortüne Study Worksheet (Volunteers)
Objective Assessement of Visual Acuity

Volunteer code _____

Date of Investigation _____

Physician _____

Family Name _____

First Name(s) _____

Date of Birth _____

Informend consent obtained? □ Yes □ No

Further pertinent information related to the Volunteer _____

_____

_____

Date _____

Signature _____

Version 2014-11-14 Page 1

Ophthalmic exam

BCVA (ETDRS)	RE	
	LE	
Slit lamp examination	RE	
	LE	
Autorefractor	LE	
	RE	
Funduscopy	RE	
	LE	
IOP	RE	
	LE	
FrACT – Landolt C Visual acuity	RE	
	LE	
FrACT – Contrast Grating (5 cpd)	RE	
	LE	

Notes

2.2 Worksheet “NIRS/EEG”

*f*ortüne Study NIRS/EEG Worksheet
Objective Assessement of Visual Acuity

Volunteer code _____

Date of Investigation _____

Eye tested (note reason if not OD) _____

Physician _____

Technician(s) _____

Family Name _____

First Name(s) _____

Date of Birth _____

Room brightness (lx) _____ Impedance (kΩ) _____

Export filename(s) prefix _____

Further pertinent information related to the Volunteer _____

Date and Signature _____

AUTHORS' CONTRIBUTIONS

This thesis was conducted at the Institute for Ophthalmic Research and the University Eye Hospital Tübingen, under supervision of Prof. Dr. med. Dr. mul. Eberhart Zrenner.

A novel contact lens electrode for recording the electrical potentials of the ciliary muscle during accommodation

The idea of using sputter-coating the conductive surface of the contact lens electrodes was developed by the author, based on previous works of Prof. Dr. Eberhart Zrenner and Dr. Ditta Zobor. First tests of sputtering were performed by the author with the support of Dr. Hartmut Schulz of the workgroup for micropaleontology, Department of Geosciences, University of Tuebingen. Recordings with volunteers were conducted by Dr. Ditta Zobor, Margaret Clouse, and the author, under supervision of Prof. Dr. Eberhart Zrenner. The setup for the experiment was developed by the author with support of Dominic Hillerkuss, based on ideas of Prof. Dr. Eberhart Zrenner and Dr. Ditta Zobor. The electrophysiological recording protocol was implemented by the author. Software of the micro-controller controlling the visual targets and triggering the electrophysiologic recording system was developed by the author. The described data processing and statistical analysis of data from volunteers were done by the author.

A novel electrode made of a super absorbent polymer for preparation-free electrophysiological recordings: The marble electrode

The idea of using super absorbent polymers in form of the marble electrodes was developed by the author. The cup-like holder were designed by the author and Susanne Kramer and manufactured by the workshop of the University Eye Hospital Tuebingen. Recordings were conducted by the author with the support

of Susanne Kramer. Data processing and statistical analysis of recorded VEPs was done by the author.

Ophthalmological assessment of cannabis-induced perception disorder: is there a direct retinal effect?

The study was planned and conducted by Dr. Ditta Zobor. The author contributed in implementing the electrophysiological recording protocols and prepared the electrophysiological processing, especially EOG data, for further statistical analysis, done by Dr. Ditta Zobor. Figures 55, 57 were created by the author.

A refined method for analyzing the sweepVEP for objective estimation of the visual acuity

The study was planed and conducted by the author. The stimulus paradigm, the required software, and the electrophysiologic recording protocol was developed by the author. Ophthalmic examinations were done by Dr. Ditta Zobor, Dr. Hana Langrova, and Dr. Fadi Nasser. Recordings were conducted by the author with the support of Dr. Hana Langrova, Dr. Fadi Nasser, and Gudrun Haerer. The presented approach of analysis sweepVEP data was developed by the author. All statistical analysis were done by the author.

Assessment of "non-recordable" electroretinograms by 9 Hz flicker stimulation under scotopic conditions

The study was planed and conducted by Dr. Andreas Schatz. The author contributed in implementing the electrophysiological recording protocols and prepared the data for further processing, especially the fourier analysis of the flicker ERGs. The author further contributed in methods and discussion.

A BOLD venture: comparison of VEP with functional near-infrared spectroscopy and functional magnetic resonance imaging for assessment of visual acuity

The grant application for the fortüne-Project was written by the author with support of Prof. Dr. Zrenner and Dr. Zobor. The study was planned and conducted by the author under supervision of Prof. Dr. med. Zrenner and Dr. Ditta Zobor. Ophthalmic examinations were done by Dr. Ditta Zobor, Dr. Hana Langrova, Dr. Fadi Nasser, and Lukasz Lisowski. The used stimulus paradigm was developed by the author with support of Dr. Michael Erb, Department of Biomedical Magnetic Resonance Imaging, University of Tuebingen, and Dr. Sabrina Schneider, Department of Psychiatry and Psychology, University of Tuebingen. The stimulus was implemented in Presentation by Dominic Hillerkuss under supervision of the author. Recordings were done by the author with support of Dr. Sabrina Schneider, Ramona Täglich, Lukasz Lisowski, and Dominic Hillerkuss (fNIRS), Dr. Michael Erb, Edyta Charyasz, Lukasz Lisowski, and Dominic Hillerkuss (fMRI), and Dr. Fadi Nasser and Dominic Hillerkuss (sweep-VEP). The analysis of the imaging data was developed by the author with the support of Dr. Sabrina Schneider and Florian Häußinger (fNIRS), and Dr. Michael Erb (fMRI), and performed by Dominic Hillerkuss under supervision of the author. Statistical analysis was performed by the author.

Ich versichere, das Manuskript selbständig verfasst zu haben und keine weitere als die von mir angegebenen Quellen verwendet zu haben.

PUBLICATIONS

Journal articles

D. Zobor; T. Strasser; G. Zobor; F. Schober; A. Messias; O. Strauss; A. Batra; E. Zrenner, "Ophthalmological assessment of cannabis-induced persisting perception disorder: Is there a direct retinal effect?," *Doc. Ophthalmol.*, Jan. 2015.

A. Schatz; R. Wilke; T. Strasser; F. Gekeler; A. Messias; E. Zrenner, "Assessment of 'non-recordable' electroretinograms by 9 Hz flicker stimulation under scotopic conditions," *Doc. Ophthalmol.*, vol. 124, no. 1, pp. 27–39, Feb. 2012.

Conference paper

T. Strasser; T. Peters; H. Jagle; E. Zrenner, R. Wilke, "An integrated domain specific language for post-processing and visualizing electrophysiological signals in Java.," *Conf. Proc. IEEE Eng. Med. Biol. Soc.*, vol. 1, pp. 4687–90, Jan. 2010.

T. Strasser; M. Brenner; S. Hell; U. Oezleyen; U. Wiedemann; M. Schmitz, "Integration of electrophysiological data of vision in an open source DICOM viewer," *Proc. IADIS Int. Conf. e-Health 2010*, pp. 279–282, 2010.

Patents

T. Strasser; T. Peters; E. Zrenner. "Grundkörper, Halter, Kit und Elektrodenanordnung sowie Verfahren zur Herstellung". Eberhard-Karls-Universität, Universitätsklinikum Tübingen, assignee. Patent DE102012101337 B4. 31 Oct. 2013.

Conference contributions

T. Strasser; K. Stingl; H. Langrová; N. Düzenli; A. Kurtenbach; E. Zrenner, "Comparison of automated evaluation of the fast and slow oscillations Electrooculogram and normative data", *Investigative Ophthalmology & Visual Science*, Vol. 56, 462, June 2015.

Torsten Strasser; Fadi Nasser; Gudrun Haerer; Ditta Zobor; Anne Kurtenbach; Eberhart Zrenner, "Objective Assessment of Visual Acuity using Visual Evoked Potentials - the Visus VEP revised", *Investigative Ophthalmology & Visual Science*, Vol. 55, 5124, April 2014.

T. Strasser; H. Langrová; A. Kurtenbach; D. Zobor; D. Hillerkuss; E. Zrenner, "Quick and easy light sensitivity assessment of the dark adapted eye: The Tuebingen Scotopic Threshold Test (TSTT)", *Investigative Ophthalmology & Visual Science*, Vol. 54, 3015, June 2013.

T. Strasser; T. Peters; A. Zhour; D. Akl; E. Zrenner, "A Novel Inexpensive And Preparation-free Wet Electrode For Recording Electroretinograms In Small Animals Based On Super-absorbent Polymers", *Investigative Ophthalmology & Visual Science,* Vol. 53, 2462., March 2012.

T. Strasser; T. Peters; E. Zrenner, "ElVisML: A little less conversation. Experiences with the Electrophysiology of Vision Markup Language in clinical routine and in a multi-center trial," *Acta Ophthalmol.*, vol. 89, Sep. 2011.

T. Strasser; A. Goldina; S. Lang; M. Lotter; M. Oder; T. Ostertag; M. Ulrich; M. Walter; D. Yildiz; T. Peters; E. Zrenner, "ElVisWeb: An interactive web-application for the visualzation of ERG recordings based on the Electrophysiology of Vision Markup Language," *Acta Ophthalmol.*, vol. 89, Sep. 2011.

T. Strasser; S. Avcu; V. Konev; F. Korkmaz; E. Manav; T. Schreck; M. Taukovic; R. Wilke; E. Zrenner, "Development of a software for the exchange of electrophysiological data of vision with PACS systems based on DICOM," *Acta Ophthalmol.*, vol. 87, Sep. 2009.

T. Strasser; R. Wilke; A. Messias; E. Zrenner, "ERG Explorer: a software for post-processing, analysing, and reporting of electrophysiological data," *Acta Ophthalmol.*, vol. 86, p. 0, Sep. 2008.

ACKNOWLEDGEMENT

First I would like to thank Professor Dr. med. Dr. mult. Eberhart Zrenner for beeing my supervisor for so many years. After so many years, I am still impressed by the amount of knowledge he owns and his proficiency in sharing this knowledge. I am convinced it is not possible to stop learning from him.

I also like to thank all the colleagues at the Institute for Ophthalmic Research and at the University Eye Hospital, who became my friends during all the years. There are so many people I have to thank, that I am sure that I will forget some of them. I would like to thank Dr. Robert Wilke for introducing me to the world of visual electrophysiology and to scientific conferences; Dr. Anne Kurtenbach, for her support in all projects and for proof-reading my thesis; Susanne Kramer for teaching me how to do high-quality electroretinograms; Dr. Tobias Peters, the best physician I now, who became a good friend of mine during the many nights we have together analyzed ERG recordings; Dr. Ditta Zobor for her patience in explaining me ophthalmology and the many studies we did together; Professor Frank Schaeffel, who is not getting bored about continuously explaining me the optics of the eye; Professors Bärbel & Helmut Wilhelm for introducing me into pupilography; Dr. Fadi Nasser, Dr. Lukasz Lisowski, Ulrike Fuchs, Gudrun Haerrer for the support in my studies; Dominic Hillerkuss for beeing the best Hiwi and bachelor student; Heval Benav, for doing the Ph. D. together (at least most of the time); Thomas-Wheeler Schilling and his group for their support in all the grant applications; Professor Dr. Rainer Kelch, who is responsible that I came to Tübingen; Richard Robson, for sharing the code of the Espion software with me, which without I could not have done all of this. Daniel Lindgren for many interesting discussions during conferences all over the world; Daniel Rathbun and his group members for sharing the office.

Finally, I would like to thank all people I might have forgotten to mention: All of you helped me a lot and without you, it would not have been so much fun!

CURRICULUM VITAE

Name	Torsten Straßer	
Geburtsdatum	26. Februar 1978	
Geburtsort	Neuburg a. d. Donau	
Beruflicher Werdegang	09 – 15	Projektleiter, STZ eyetrial, Tübingen
	09 – 10	IT Spezialist, STZ eyetrial, Tübingen
	08 – 15	Akademischer Mitarbeiter Universitäts-Augenklinik Tübingen
	04 – 15	Lehrbeauftragter HS Augsburg, Augsburg
	05 – 06	IT Spezialist, ProSiebenSat.1 Produktion GmbH, München
	03 – 05	IT-Consultant, ssb GmbH, München
	01 – 02	Webapplication Developer, Sapient GmbH, München
	00 – 01	Technical Projectmanager, Kabel New Media GmbH, München
Studium	07 – 15	Promotion (Dr. sc. hum), Universität Tübingen
	04 – 06	Informatik (Master), HS Augsburg
	98 – 03	Informatik (Diplom), FH Augsburg
Schulausbildung	94 – 96	Fachoberschule Ingolstadt
	90 – 94	Knabenrealschule der Herz-Jesu-Missionare Rebdorf Eichstätt
	86 – 90	Grund- und Teilhauptschule Nassenfels
Qualifikationen		IBM DB2 Certified Developer
		Certified Solution Architect SAP ERP 6.0
Auszeichnungen	13	EVER Travel-Grant (Best-Section Paper)
	10	Travel-Grant Neuro-Ophthalmologische Gesellschaft
	09	ISCEV Travel-Grant
	09	EVER Travel-Grant (Best-Section Paper)
	08	DFG Travel-Grant